HAL
archives-ouvertes.fr

Analysis and design of planar passive repeaters with quasi-endfire radiation for 60GHz indoor communications

Duo Wang

▶ **To cite this version:**

Duo Wang. Analysis and design of planar passive repeaters with quasi-endfire radiation for 60GHz indoor communications. Networking and Internet Architecture [cs.NI]. INSA de Rennes, 2015. English. <NNT : 2015ISAR0011>. <tel-01274849>

HAL Id: tel-01274849

https://tel.archives-ouvertes.fr/tel-01274849

Submitted on 16 Feb 2016

HAL is a multi-disciplinary open access archive for the deposit and dissemination of scientific research documents, whether they are published or not. The documents may come from teaching and research institutions in France or abroad, or from public or private research centers.

L'archive ouverte pluridisciplinaire **HAL**, est destinée au dépôt et à la diffusion de documents scientifiques de niveau recherche, publiés ou non, émanant des établissements d'enseignement et de recherche français ou étrangers, des laboratoires publics ou privés.

Thèse

THESE INSA Rennes
sous le sceau de l'Université européenne de Bretagne
pour obtenir le titre de
DOCTEUR DE L'INSA DE RENNES
Spécialité : Electronique et Télécommunications

présentée par
Duo WANG
ECOLE DOCTORALE : *MATISSE*
LABORATOIRE : *IETR*

Analyse et conception de répéteurs passifs plans à rayonnement quasi-latéral pour communications «indoor» à 60GHz

Ghaïs El Zein
Professeur à l'INSA de Rennes / Membre Invité

Thèse soutenue le 06/05/2015
devant le jury composé de :

Xavier BEGAUD
Professeur à l'Institut Mines-Télécom, Télécom ParisTech / Président
Claire MIGLIACCIO
Professeur à l'Université de Nice-Sophia Antipolis / Rapporteur
Jean-Marc LAHEURTE
Professeur à l'Université Paris-Est Marne-La-Vallée / Rapporteur
Raphaël GILLARD
Professeur à l'INSA de Rennes / Directeur de Thèse
Renaud LOISON
Professeur à l'INSA de Rennes / Co-encadrant

Analyse et conception de répéteurs passifs plans à rayonnement quasi-latéral pour communications «indoor» à 60GHz

Duo WANG

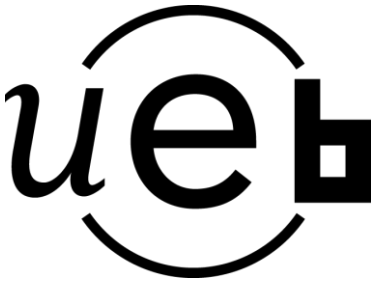

En partenariat avec

Document protégé par les droits d'auteur

Analyse et conception de répéteurs passifs plans à rayonnement quasi-latéral pour communications «indoor» à 60GHz

RÉSUMÉ

Table des matières

Résumé

1. Introduction

Le développement des systèmes sans fil se poursuit à grande vitesse. En particulier, il existe une grande demande pour des communications à haut débit, notamment pour les courtes et moyennes distances. Les protocoles traditionnels de communication sont incapables de supporter la transmission des données à très haut débit et, par ailleurs, le spectre en basses fréquences est saturé. Dans un tel contexte, la bande des 60GHz est préconisée. Grâce à son large spectre sans licence (57GHz à 64 GHz), elle permet un débit maximum de plus de 5Gbit/s [123-124]. Les communications à 60GHz sont notamment préconisées en environnement «indoor» où de nombreuses études sont rapportées [125-126]. Toutefois, d'un point de vue pratique, cet environnement est très contraignant (présence de murs et autres obstacles occultant) et la couverture radio y est difficile à assurer à cause des fortes atténuations, en particulier en absence de visibilité directe (NLOS) [127]. Par conséquent, l'utilisation de répéteurs peut constituer une solution appropriée pour améliorer de telles liaisons.

Dans cette thèse, on considère l'exemple typique d'une liaison sans visibilité directe dans le cas d'un couloir à angle droit ou d'un couloir en T (Fig. 1). Il s'agit alors de rétrodiffuser le signal émis par une borne d'émission (signal matérialisé par les lignes bleues) de façon à ce qu'il se propage dans les bras orthogonaux du couloir (lignes rouges). Le répéteur doit ainsi être conçu pour rayonner latéralement lorsqu'il est illuminé par une onde incidente sous incidence normale. Plusieurs contraintes sont prises en compte dans cette étude : d'abord, nos investigations se limitent aux répéteurs passifs [20-23], ceux-ci présentant l'avantage du faible coût et de la simplicité de mise en œuvre. Ensuite, le répéteur doit être facilement intégrable sur un mur pour limiter l'encombrement et les difficultés d'installation résultantes. Ainsi, ni les réflecteurs traditionnels tridimensionnels, comme le réflecteur parabolique [8-9] et le réflecteur en coin [10-12], ni les réflecteurs à topologie complexe [13-15], ne sont convenables à la situation. Nous nous orienterons donc plutôt vers une solution de type réflecteur plan, la surface de ce réflecteur étant constituée par un réseau de motifs élémentaires dimensionnés de façon à contrôler la direction de l'onde réfléchie.

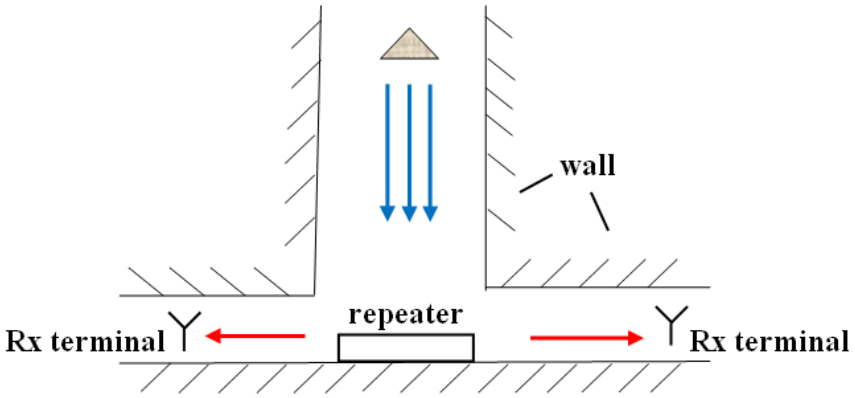

Fig.1 Amélioration de la couverture radio dans un couloir en T par utilisation d'un réflecteur plan

A partir de la théorie des réseaux d'antennes, la topologie générique pour ce répéteur peut être dérivée (Fig.2).

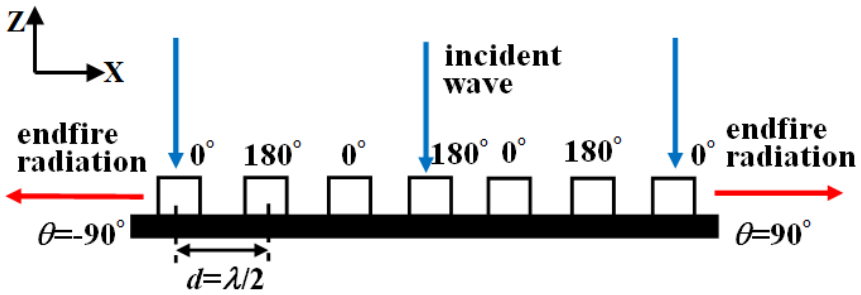

Fig.2 Topologie générique pour le répéteur passif avec rayonnement latéral

Le répéteur est constitué de deux types d'éléments réfléchissants, espacés d'une demi-longueur d'onde ($d=\lambda/2$). Afin d'orienter la réflexion du faisceau vers la direction latérale (correspondant à $\theta=\pm 90^{\circ}$), la différence de phase entre deux éléments voisins doit être $\Delta\varphi=\pm\pi$. En d'autres termes, deux éléments successifs doivent être en opposition de phase. Notre conception visera donc à identifier et étudier différentes topologies et technologies d'antennes adaptées à cette application. Pour ce faire, nous nous inspirerons souvent des travaux sur les réseaux réflecteurs dont le principe est assez similaire.

On notera d'emblée que la technologie microruban, fréquemment utilisée dans les réseaux réflecteurs [22] [26] [38] [41] n'est pas adaptée à notre application. D'abord, les pertes dans une ligne microruban sont potentiellement trop fortes à 60GHz. Pire encore ici, une antenne microruban se comporte comme un dipôle électrique parallèle au plan de masse. Son image est un dipôle électrique de sens opposé, ce qui annule toute possibilité de rayonnement latéral.

Dans cette thèse, trois technologies alternatives sont proposées pour les éléments rayonnants déphaseurs. La première technologie utilise des éléments à base d'antennes à résonateurs diélectriques (DRA). Le DRA se compose d'un matériau diélectrique de relativement forte permittivité et de faible perte [96-98]. Il est un bon candidat pour une application à 60GHz. En plus, le DRA rayonne généralement comme un dipôle magnétique. Son image par rapport au plan de masse est un dipôle magnétique de même sens, ce qui est propice à l'obtention d'un rayonnement latéral.

Le deuxième élément utilise la technologie des guides d'ondes métalliques. Le guide rectangulaire a été utilisé comme un élément réfléchissant dans les premiers réseaux réflecteurs en 1963 [25], mais a été rapidement abandonné compte tenu de son encombrement à basse fréquence. Il redevient concurrentiel à 60 GHz du fait notamment de ses très faibles pertes.

Finalement, une structure dérivée à base de plans métalliques parallèles est choisie [119]. Cette solution bénéficie une grande commodité pour la conception et la fabrication. Ses performances sont analysées à l'aide de la théorie des réseaux et en s'appuyant sur de nombreuses simulations électromagnétiques. Finalement, un réseau est fabriqué et une campagne de mesures est effectuée pour évaluer ses capacités à répondre aux besoins de l'application.

2. La Conception du Réseau Latéral basé sur des Éléments DRA

Les études sur les DRA peuvent être datées des années 1930 [90], mais l'application comme élément réfléchissant de réseau réflecteur a juste commencé cette décennie [106]. Les méthodes classiques du déphasage, comme varier les dimensions [106], utiliser un chargement réactif [107-109], ou graver une fente variable dans le plan de masse [105-106], ne s'avèrent pas adaptées à notre problème, car elles utilisent des éléments avec des fréquences de résonance différentes. Une étude en simulation est d'abord menée afin d'illustrer ce problème. On en rappelle ici simplement le résultat.

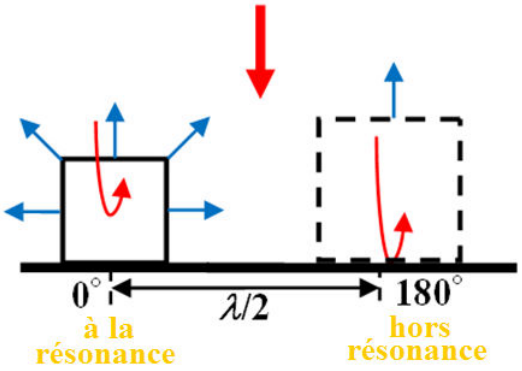

Fig.3 Schéma des DRA éléments à la résonance et hors résonance

Comme présenté précédemment, notre structure demande des DRA successifs produisant des phases réfléchies de 0° et 180° respectivement. Le DRA avec une phase de 0° (à gauche sur la Fig.3) fonctionne à la résonance tandis que l'autre (à droite sur la Fig.3) est hors résonance. Dès lors, les deux éléments rayonnent différemment. Le DRA résonant produit un rayonnement omnidirectionnel dans le plan E et contribue ainsi au rayonnement latéral. Au contraire, le DRA hors résonance est presque transparent à l'onde incidente: la réflexion est essentiellement contrôlée par le plan de masse et s'effectue donc dans la direction spéculaire. Par conséquent, l'effet attendu par deux éléments en opposition de phase n'est pas obtenu de façon satisfaisante. Il est ainsi montré qu'il est indispensable d'utiliser deux éléments identiques et de synthétiser le déphasage autrement qu'en variant la dimension des résonateurs.

2.1 Topologie de DRA à Encoche

La première topologie proposée est le DRA à encoche. Un DRA carré est entaillé avec des encoches sur la diagonale (Fig.4). En ajustant la taille de l'encoche (la longueur *a* sur la Fig.4 (a)), une onde incidente polarisée selon *y* peut être convertie en une onde réfléchie polarisée selon *x*. Pour l'étape suivante, deux DRA avec les encoches sur les diagonales opposées sont combinées ensemble pour former une cellule à 2×1 éléments (Fig.4 (b)). En réponse à une onde incidente polarisée selon *y*, les réfléchis par les DRA consécutifs sont polarisés selon *x* et de sens opposés.

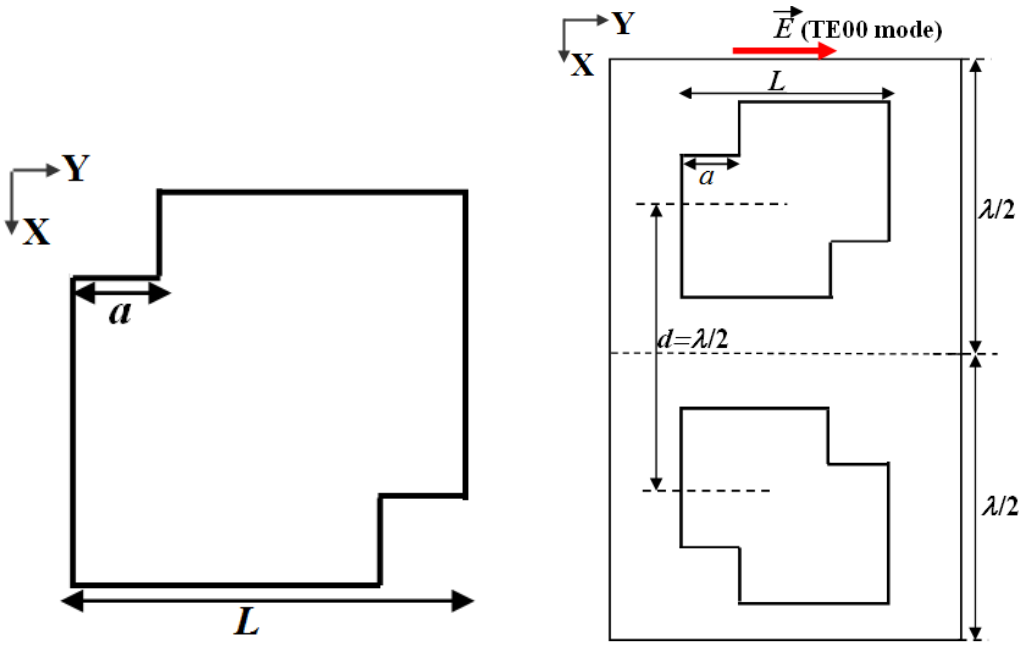

(a) (b)

Fig.4 Schéma du DRA avec encoches diagonales (a) et de la cellule 2×1 (b)

Après analyse et optimisation électromagnétiques, un réseau 6×6 est étudié en simulation. Ses performances sont optimisées en ajustant la dimension *a* des encoches pour les différents éléments du réseau.

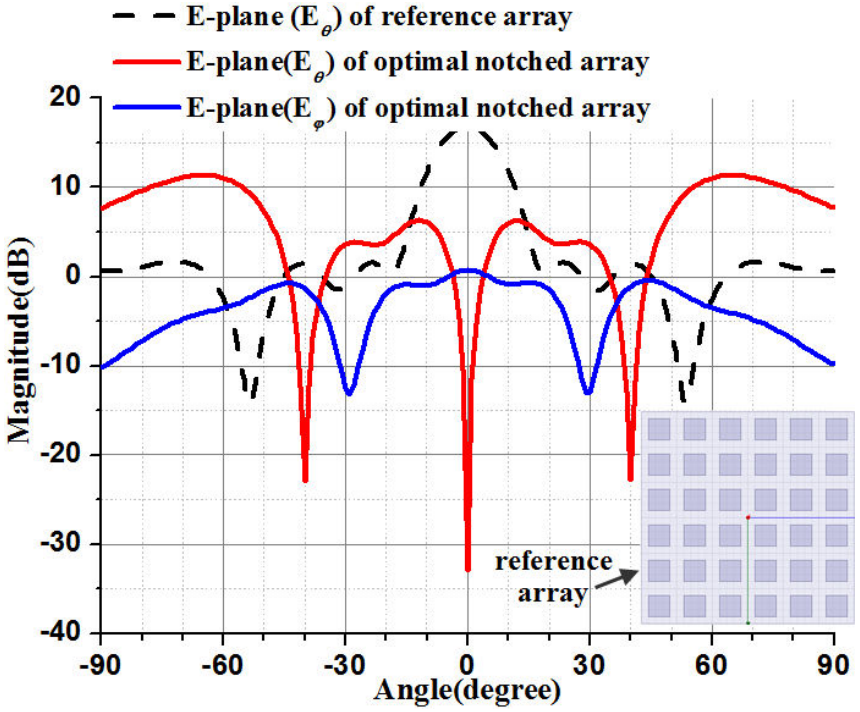

Fig.5 Directivité dans le plan E (E_θ et E_φ). Comparaison entre le réseau optimal et le réseau de référence

La directivité dans le plan E est présentée sur la Fig. 5. Elle est comparée à celle d'un réseau de référence (lorsque toutes les encoches sont supprimées ; a=0 pour tous les DRA). Grâce à l'introduction d'encoches, la réflexion spéculaire est supprimée, et le rayonnement s'effectue latéralement. De plus, la conversion de polarisation est manifeste.

2.2 Topologie de DRA Couplé à une Ligne Déphaseuse

Une deuxième topologie est proposée en Fig.5, mettant en œuvre un DRA carré couplé à une ligne déphaseuse par une fente dans le plan de masse. La puissance incidente est capturée par le DRA et transmise à la ligne microruban en circuit ouvert. Elle est ensuite réfléchie et ré-rayonnée avec un déphasage contrôlé par la longueur L_{stub}.

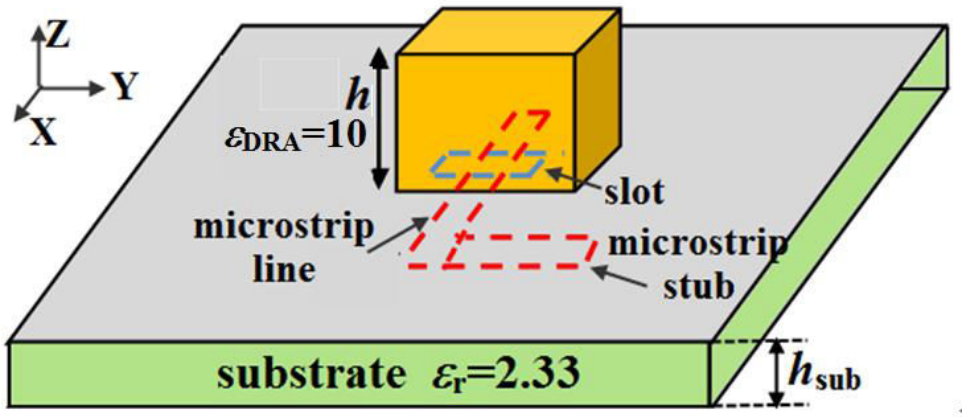

(a)

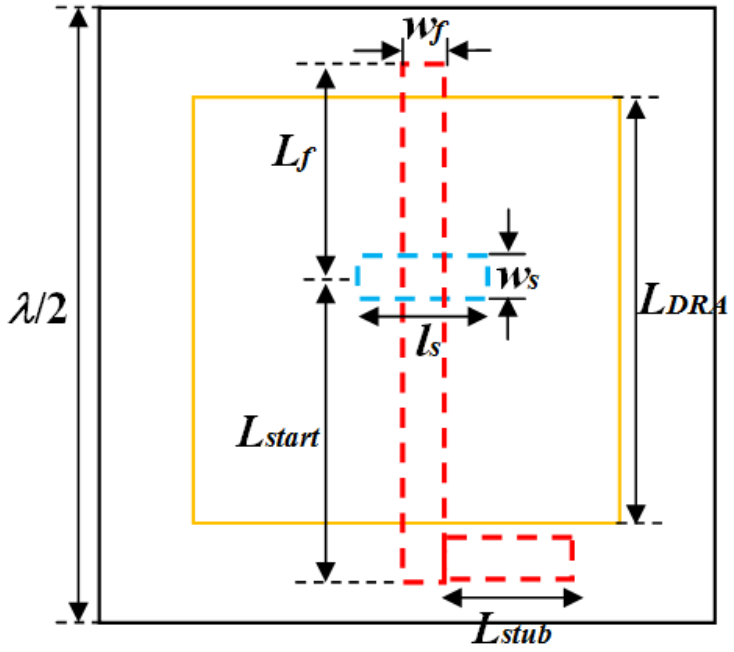

(b)

Fig.6 Schéma du DRA couplé à la ligne déphaseuse: (a) vue 3D et (b) vue de dessus

Premièrement, des études paramétriques ont été menées pour assurer un bon couplage entre DRA et ligne. Ensuite, deux longueurs de ligne L_{stub} différentes (L_1 et L_2) ont été synthétisées pour réaliser les phases de 0° et 180°. Finalement, un réseau 6 ×6 a été conçu en simulation. Des optimisations additionnelles sur L_1 et L_2 ont permis de réduire la réflexion spéculaire et de transférer une partie du rayonnement sur les lobes latéraux. La directivité dans le plan E (E_θ) est présentée sur la Fig.7. L'amélioration par rapport au réseau initial (avant optimisation) est montrée.

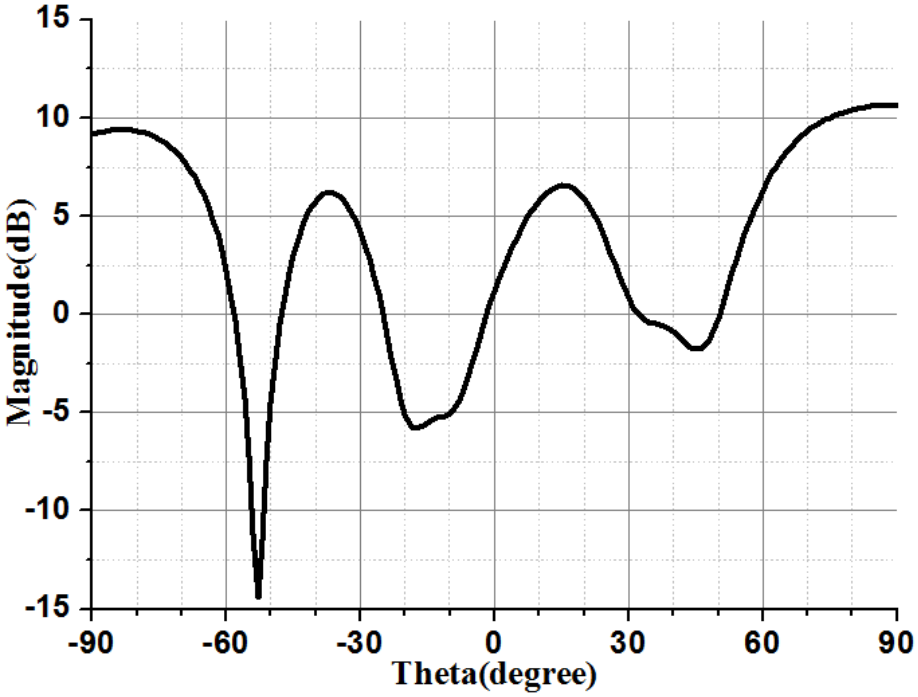

Fig.7 Directivité dans le plan E (E_θ et E_φ) pour le réseau 6× 6

Bien que deux structures à base de DRA présentent des performances intéressantes, la relative complexité du procédé technologique requis n'est pas compatible avec une fabrication à faible coût. D'autres technologies ont donc été investiguées.

3. Topologie à base de Guides d'ondes Métalliques

Les guides métalliques peuvent offrir une solution à faibles pertes en hautes fréquences. Le premier dispositif réfléchissant utilisant des guides d'onde a été proposé en 1960 par Berry [25], qui a conçu un réseau réflecteur à base des 4×26 éléments avec des longueurs variables. Mais la structure était très encombrante pour une application à des fréquences relativement basses. A 60GHz, le guide métallique devient une solution compétitive.

La géométrie du guide d'onde chargé par matériau diélectrique (DFW) est illustrée sur la Fig.8, et le principe de fonctionnement pour notre réseau à rayonnement latéral est illustré sur la Fig.9. Le réseau est constitué d'éléments de guides d'ondes avec deux hauteurs différentes pour produire les phases de 0° et 180°. Ces guides sont terminées par un court-circuit. L'espacement entre les guides est $\lambda_0/2$, avec une dimension de cellule de $\lambda_0/2\times\lambda_0/2$. Pour que la dimension des ouvertures des

guides ($a_1 \times b_1$) soit compatible à la fois avec l'espace disponible dans la cellule et avec la propagation du mode dominant TE10, le guide est chargé par un matériau diélectrique de type RT/Duroid 5870 (ε_r=2,33 et la tanδ=0,0012). Il convient de souligner que les tailles a_1 et b_1 sont importantes, puisqu'elles contrôlent la puissance transmise dans le DFW. En choisissant la dimension de a_1, b_1 et h, un 6×6 réseau est simulé et optimisé pour réaliser un bon rayonnement latéral.

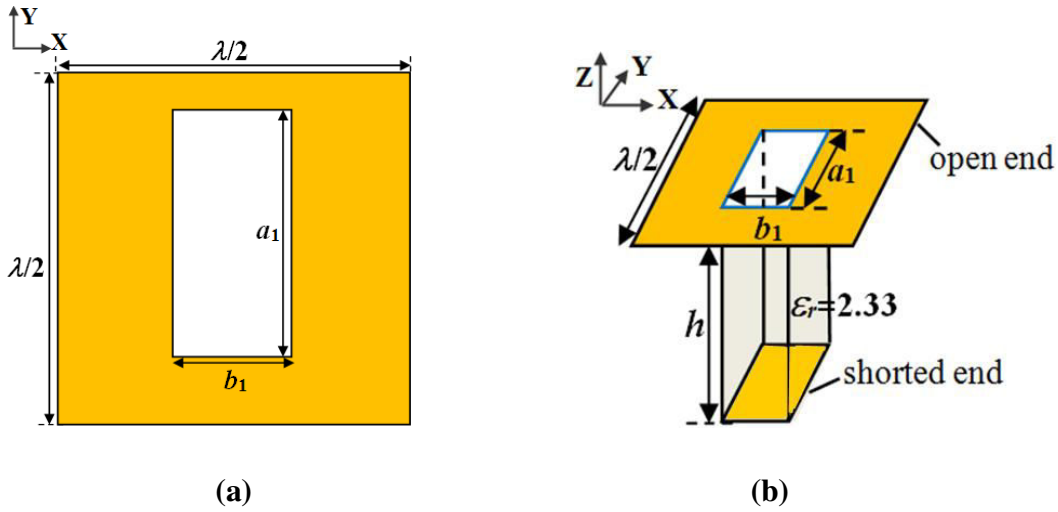

(a) **(b)**

Fig.8 Géométrie de l'élément proposé (a) Vue de dessus et (b) Vue de côté

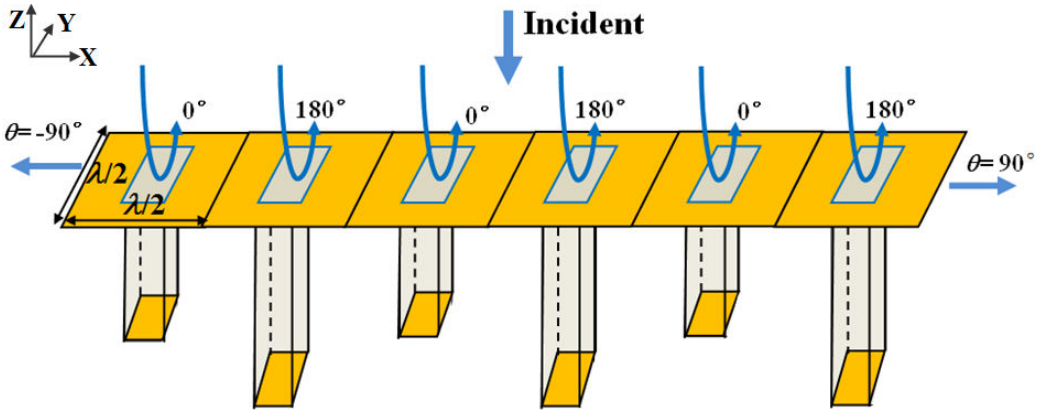

Fig.9 Principe de fonctionnement pour le réseau latéral basé sur le guide d'onde

4. Topologie à base de Guides à Plaques Métalliques Parallèles

Une structure alternative est présentée sur la Fig.10. Les guides rectangulaires sont remplacés par des rainures métalliques de façon à obtenir des plaques métalliques

parallèles supportant un mode TEM. Il n'est dès lors plus nécessaire d'utiliser un chargement diélectrique, ce qui simplifie grandement la fabrication.

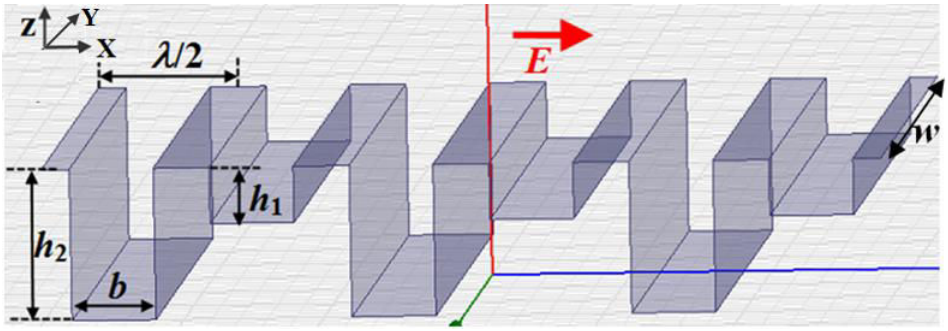

Fig.10 Schéma de réseau à base d'éléments rainuré (ou plaques parallèles)

Un réseau de 24 rainures avec w=60mm (taille totale de 60mm×60mm) est simulé et optimisé. Le diagramme de directivité dans le plan E (E_θ), montre qu'un bon rayonnement latéral est obtenu.

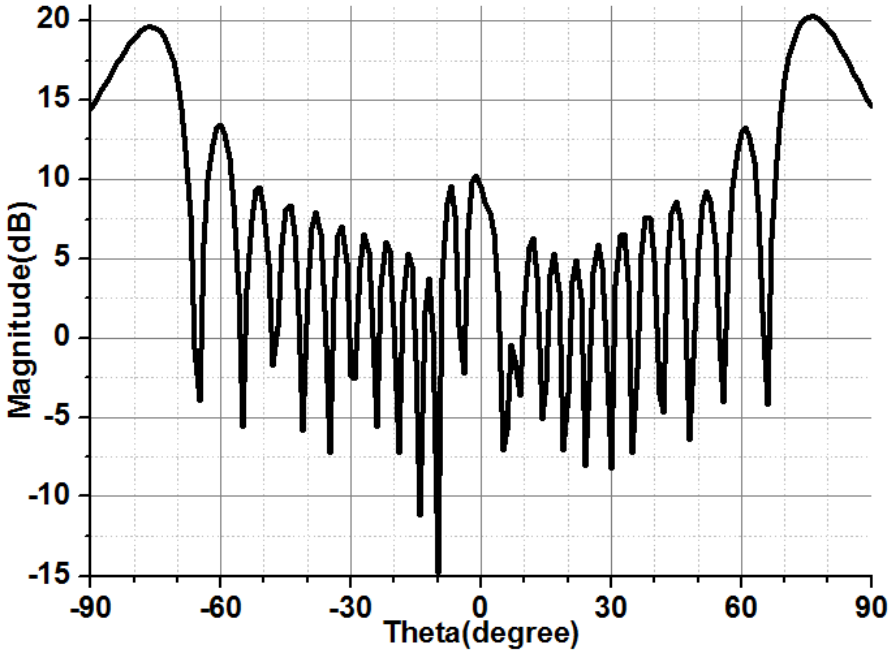

Fig.11 Directivité dans le plan E (E_θ) pour le réseau de 24 rainures avec w= 60mm

Nous pouvons toutefois noter que les lobes principaux ne sont pas situés exactement à ± 90°, mais plutôt à ± 75°. Afin d'expliquer ce problème, une analyse basée sur la théorie des réseaux d'antennes a été menée.

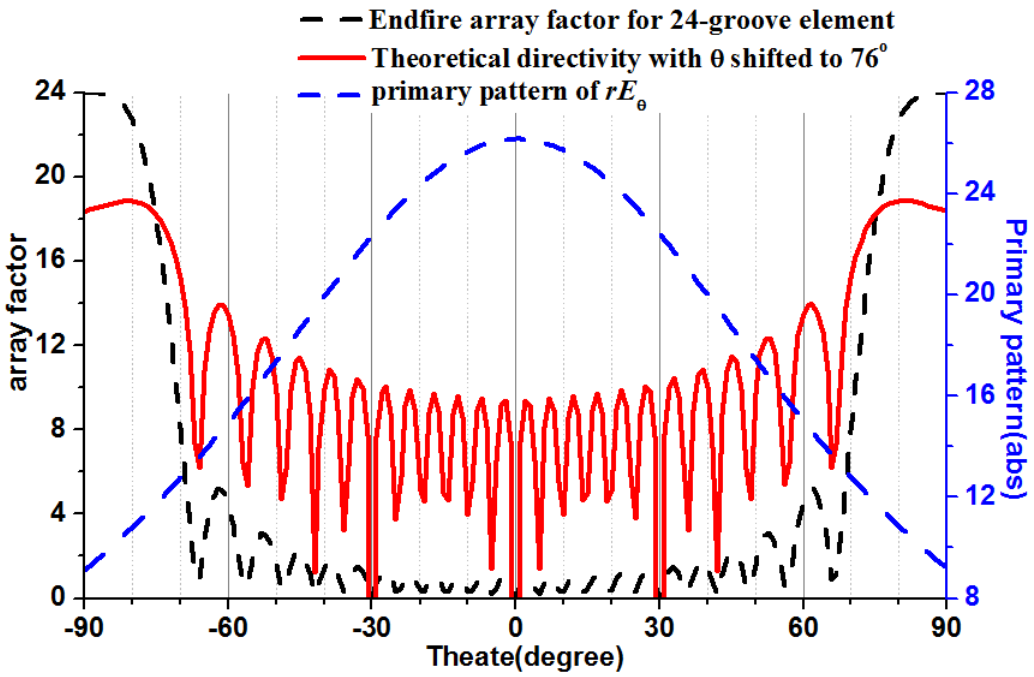

Fig.12 Illustration de la déviation du faisceau principal pour le réseau de 24 rainures

Nous avons ainsi multiplié le diagramme élémentaire d'une seule rainure (ligne pointillée bleue sur la Fig.12) par le facteur de réseau d'un réseau latéral à 24 éléments (ligne noire pointillée dans Fig.12). Le résultat (ligne rouge sur la Fig.12) présente un décalage des faisceaux (θ_{max}=±81°), voisin de celui observé en simulation. Lorsque le nombre d'éléments est réduit, la largeur du faisceau devient plus large et le décalage augmente.

5. Validation de la Mesure

A des fins de validation expérimentale, un réseau rainuré métallique de taille de 200mm×200mm (correspondant à 80 rainures) a été fabriqué (Fig.13). La taille (plus grande qu'en simulation) est choisie pour améliorer le bilan de puissance lors de la campagne de mesure. Ces dimensions sont aussi plus réalistes s'agissant d'un scénario pratique.

(a)

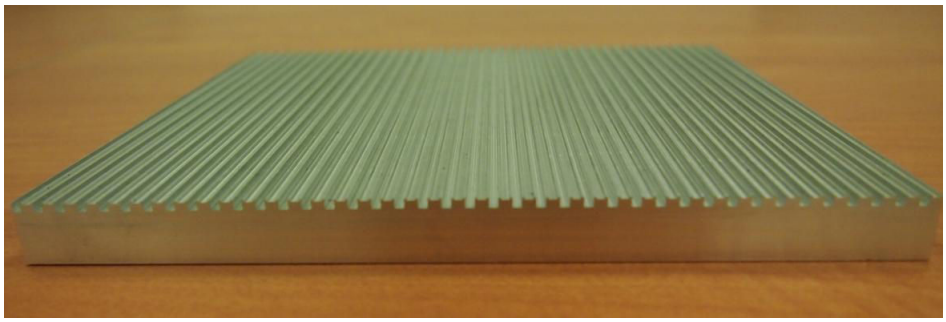

(b)

Fig.13 Le réseau de 200mm×200mm en (a) vue de dessus et (b) vue de côté

La chaîne de mesure à 60 GHz est expliquée sur la Fig.14. Elle a été développée dans une étude précédente pour un sondeur de canal à 60 GHz [159-161].

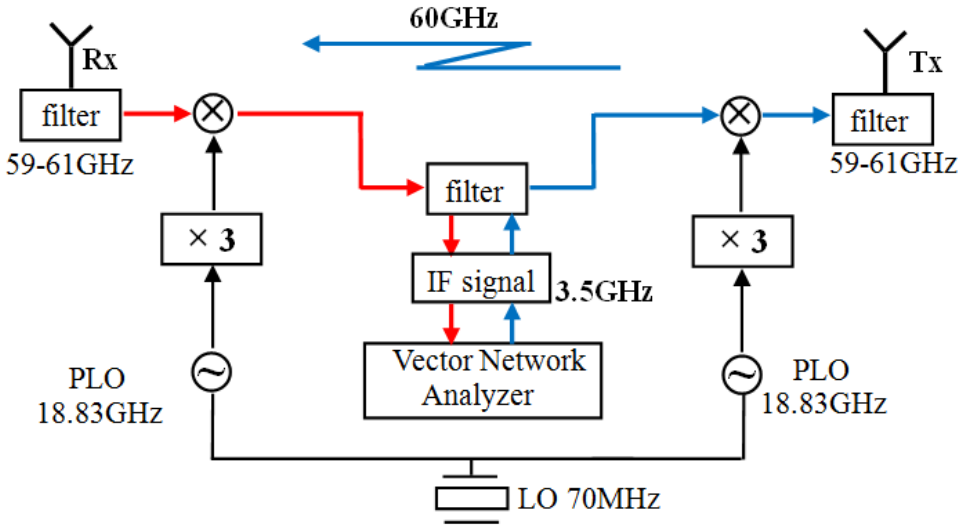

Fig.14 Schéma du système de mesure

Dans une première phase (mesure de référence), aucun réflecteur n'est utilisé. Deux antennes directives (Rx et Tx) sont placées à 90° l'une de l'autre de façon à se rapprocher d'une configuration sans visibilité directe. La distance entre les deux antennes orthogonales est *S* le long de l'axe *x* et *F* le long de l'axe *z*. La puissance reçue par l'antenne Rx est mesurée.

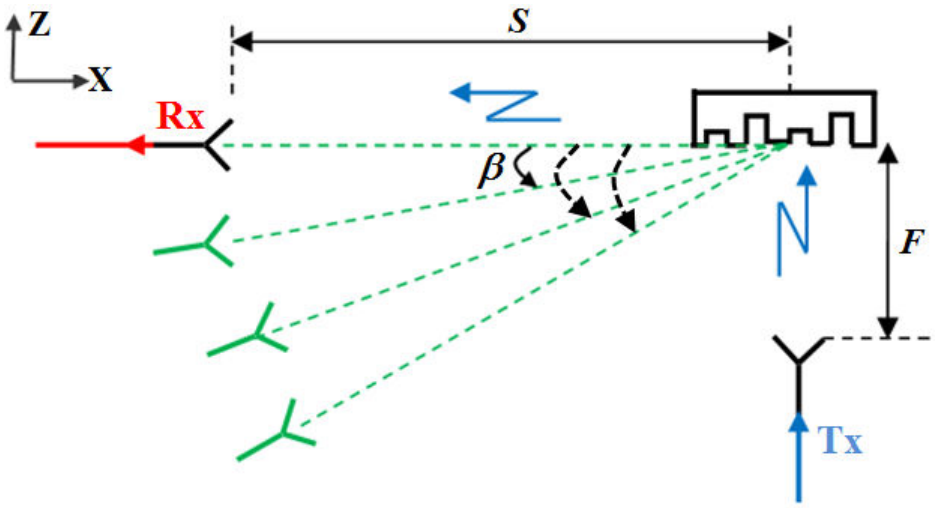

(a)

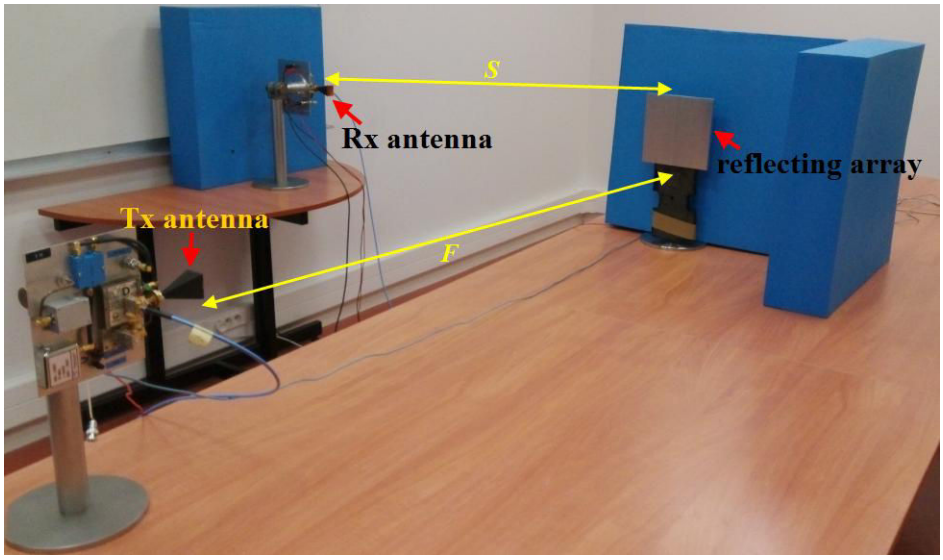

(b)

Fig.15 (a) Schéma et (b) photo de la configuration de mesure

Ensuite, le réseau rainuré est ajouté au point d'intersection (Fig.15). Des mesures de transmission sont réalisées pour différentes valeurs de l'angle β et des distance S et F. Dans tous les cas, l'antenne Rx pointe vers le centre du réseau. La puissance reçue est enregistrée et comparée à la mesure de référence dans la Fig.16

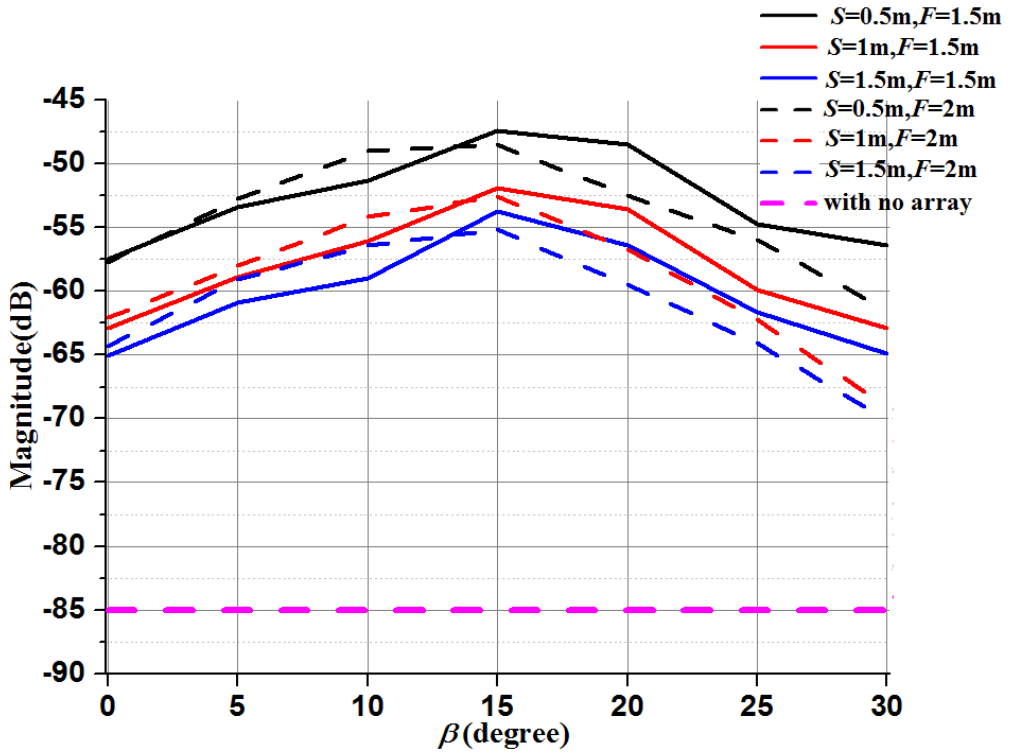

Fig.16 Puissance mesurée P_{Rx} pour β= 15° lorsque S varie entre 0,5 m et 1,5 m et F entre 1,5 m et 2m – Comparaison avec et sans réflecteur

D'après la Fig.16, la puissance initiale reçue dans la configuration de référence est proche de bruit. Grâce à l'utilisation du répéteur passif, la puissance reçue est sensiblement augmentée. La puissance maximale est toujours obtenue pour $10^{\circ}<\beta<20^{\circ}$. Le gain obtenu dépend de S et F. Par exemple, lorsque S=1,5m et F=2m, l'augmentation de la puissance reçue est de 20dB pour $\beta=0^{\circ}$ et 30dB pour $\beta=15^{\circ}$. En conclusion, le niveau du signal est grandement amélioré par l'insertion du réseau.

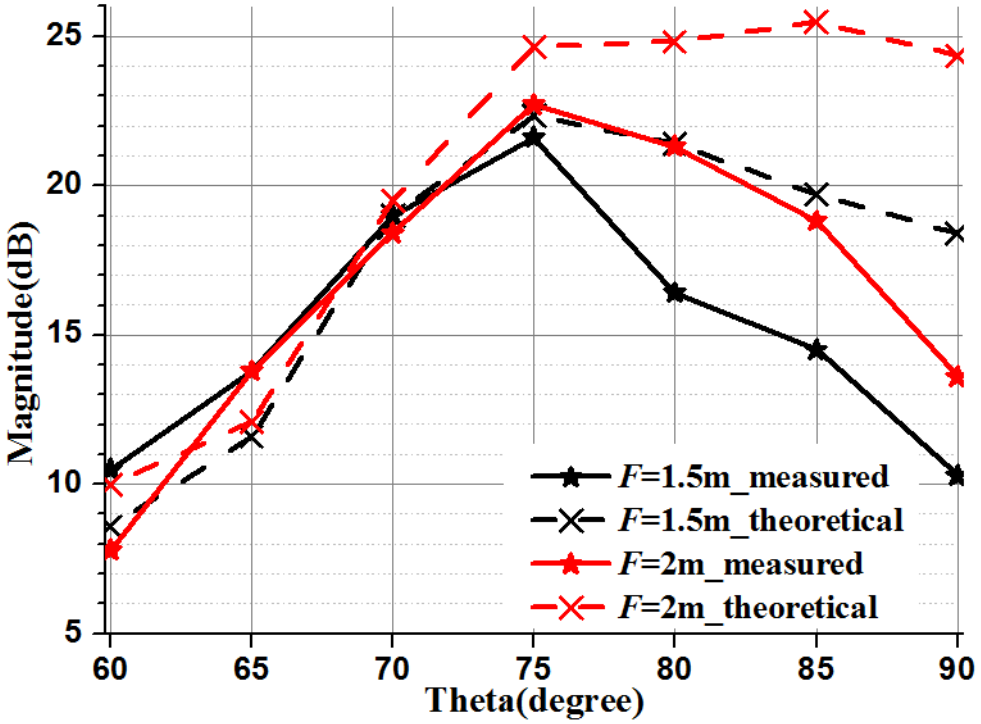

Fig.17 Comparaisons entre « gain » mesuré et directivité théorique lorsque S=1,5 m et F varie entre 1,5m et 2m

Finalement, bien que la distance de mesure soit inférieure à la limite de Fraunhoffer, le «gain» du réseau est évalué à partir de la formule de Friis [163] et comparé à la valeur théorique en Fig.17. L'accord est très bon jusqu'à $\theta=75^{\circ}$. Pour les plus grands angles, les prédictions théoriques sont trop optimistes, ce qui peut être dû à l'estimation approximative du diagramme élémentaire de la rainure.

6. Conclusion

Afin d'améliorer le bilan de liaison associé à une communication à 60GHz en environnement « indoor » sans visibilité directe, un répéteur passif et plat avec rayonnement latéral est étudié. Une architecture générique impliquant des motifs

réfléchissant en opposition de phase et espacés d'une demi-longueur d'onde est proposée. Différentes topologies et technologies sont investiguées pour la mise en œuvre pratique : résonateur diélectrique, guide rectangulaire et plaque rainurée.

Le réseau final à base d'une plaque métallique rainurée a été choisi pour sa simplicité de fabrication et ses bonnes performances en rayonnement latéral. Plus d'analyses sur les performances de la topologie, en particulier sur la déviation du faisceau principal, ont été présentées. Pour la dernière étape, un réseau de taille de 200mm ×200mm a été fabriqué et mesuré dans un environnement sans visibilité directe. Grâce à ce réseau, le niveau du signal reçu a pu être amélioré systématiquement, le gain obtenu atteignant 40 dB dans les configurations les plus favorables. La faisabilité du concept a ainsi été démontré et son intérêt pour l'application visée apparaît prometteur.

Table of contents

General Introduction

Objective and context of the study

During the last couple of years, the information and consumer electronics industries have developed fast beyond our expectation. The pressing demands for high-speed communications are proposed at the same time, especially in the short-and-medium-distance communications. For these specific scenarios, traditional communication protocols (e.g. Wi-Fi and UWB) are incapable to provide a transmission rate higher than 600Mbit/s. On the other hand, we must face the awkward fact that the lower bands are all occupied and there are no more available frequency bandwidths left. As an alternative, investigations on 60GHz radio have sparked great attentions. Thanks to the wide unlicensed spectrum (57GHz to 64GHz), the 60GHz radio [123-124] enables a maximum data transmission rate more than 5Gbit/s. Besides, due to its short wavelength and specific atmosphere attenuation characteristic, the 60GHz communication system is suitable for the desired medium distance (up to 100m) applications for wireless local area network (WLAN) with high security such as ultra-fast file transfer, and short distance (3-10m) wireless personal area network (WPAN) such as indoor communication.

As the most potential applications, the 60GHz indoor communication has been reported by many studies [125-126] until now. In practical situations, the indoor environment is usually complicated (e.g. walls, corridors, stairs, etc.), which results in non-line-of-sight (NLOS) areas [127]. The associated reflected signals exhibit significant attenuation, which is responsible for uncovered regions. Usually, these NLOS areas account for a great proportion of the whole environment. Therefore, specific repeaters are highly required to increase signal coverage for these situations. Ideally, these devices should be passive and flat for an easy deployment. A quite high gain is mandatory to maintain the signals at a high level. Of course, low cost and simple fabrication are essential requirements.

Based on these considerations, this thesis proposes to investigate the capabilities of passive repeaters made of planar reflectors. The challenging configuration of a T-shaped corridor (Fig.0.1) is considered as a relevant test-case all along this manuscript. This leads to radiating structures reflecting the incident wave longitudinally to their surface (endfire radiation), thus expanding the coverage in

NLOS areas.

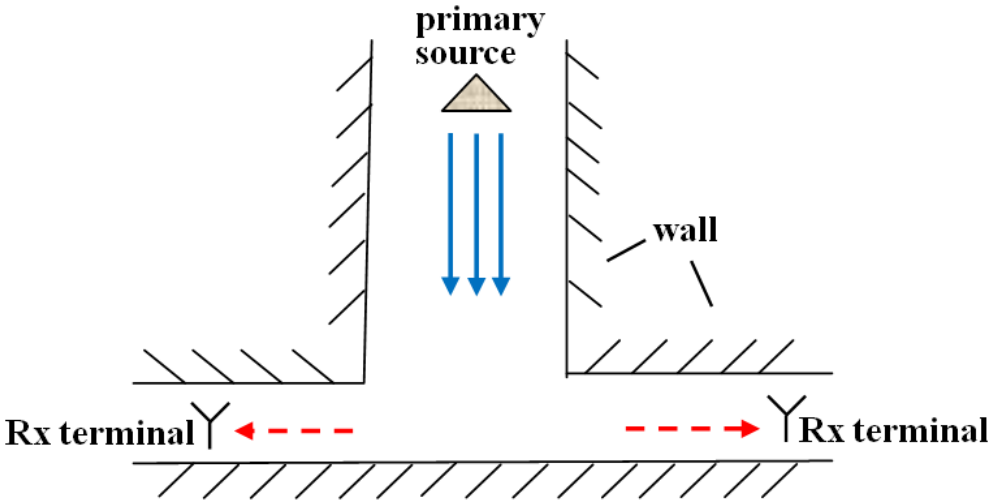

Fig.0.1 Top view of T-shaped corridor

A conventional passive repeater [23] [128] is usually a flat reflecting surface that consists of many reflecting unit-cells. The incident wave illuminates these reflecting unit-cells and gets re-radiated. By elaborately adjusting each unit-cell's parameters, the reflected wave can be controlled to form a beam towards a prescribed direction. Design of such planar reflectors enjoys the advantages of simple structure, easy manufacturing, high gain and low cost. The design configuration is quite comparable to that of a reflectarray antenna [129]. The main difference lies in the role of the illuminating source. In the case of a reflectarray, it is part of the antenna itself. In the case of the passive repeater, this illuminating source is a remote and independent system that generates a plane wave at the location of the reflector. Taking benefit of the similarities between both types of structure, this thesis may also be seen as some continuation of recent researches carried out at IETR in the field of reflectarrays [130-131].

As the key technology, the design of reflecting unit-cells has attracted lots of researchers to explore for better performance. After C. S. Malagisi [30] introduced microstrip into reflectarray, a great number of investigations have been reported taking microstrip patch as the reflecting unit-cell [22] [26] [38] [41]. However, when it comes to 60GHz, the loss suffered by microstrip patches increases. Moreover, this microstrip topology would meet a much trickier problem for the endfire radiation requirement. Due to the existence of a ground plane, traditional microstrip patch performs like an electric dipole and produces an opposite image electric current, which completely cancels out radiation at grazing angles.

In this thesis, three alternative technologies are proposed to address this issue. The first one suggests making the unit-cells with dielectric resonant antennas (DRA). A DRA usually consists of material with high dielectric constant and low loss tangent [96-98]. So it is a quite conducive candidate for the 60GHz operation with high Q-factor and low loss (no conductor loss) performance. Furthermore, a DRA at resonance usually radiates like a magnetic dipole. Hence, if a ground plane is used, the corresponding image magnetic current is in phase with the DRA itself, and the cancellation effect brought by the ground plane is avoided. Researches on DRA can be dated back to 1930s [90], but its application as reflecting unit-cell in reflectarray just started this decade [106], in which Keller controlled the unit-cell's reflection phase by adjusting the DRA length. Different DRA unit-cells will be studied and compared in this thesis.

The second unit-cell comes from rectangular waveguide technology. It appeared as a reflecting unit-cell in 1963 in the first reflectarray in the world [25], but didn't attract many interests as it was too bulky at low frequency. Actually, since the waveguide shares size in proportional to operation wavelength, it is compatible with the 60GHz design. Additionally, rectangular waveguide benefits from a high power capacity, very low loss and low cost, so it has a great potential for the high frequency application. This technology will thus be studied in this application.

Finally, as a last attempt, the rectangular waveguide unit-cell will be further simplified to a groove structure by eliminating one degree of freedom in the dimensions of the cross-section [122]. This final solution with metal groove unit-cell enjoys promising convenience in the design and fabrication, and the cost and complexity can be reduced further. For a better understanding of the proposed endfire array, detailed theoretical analysis of its performance is presented based on array theory. At last, experiments using the fabricated array have been carried out in NLOS areas and recorded in the thesis.

Thesis Organization

This thesis is organized with five chapters and a final conclusion.

Chapter 1 provides detailed presentation of the design's background, and compares the existing solutions. Based on specifications for the desired solution, a foreseen generic array topology with endfire radiation is established for the whole thesis. Potential unit-cell technologies are discussed relying on existing literature.

Chapter 2 focuses on DRA technology as a first solution to design unit-cells. Two different topologies are investigated and compared. Different modelling strategies are also studied using either a single cell, a couple of cells with opposite phases or a small array. For each topology, a preliminary 6×6 array is simulated and optimized.

Chapter 3 investigates a rectangular waveguide unit-cell. Parametric analyses are carried out and possible fabrication technologies are discussed. Once again, a preliminary 6×6 array is designed and optimized to validate the feasibility of such a structure.

Chapter 4 presents an evolution of the structure in chapter 3. The rectangular waveguide unit-cell is simplified into a groove structure. Based on previous investigation procedures, the groove unit-cell is studied, and arrays with different sizes are also designed. Further work is taken to explore the array' performances regarding bandwidth and maximum radiation direction. As an emphasis, detailed theoretical analysis based on the simulation results are demonstrated in the end.

Chapter 5 considers the fabrication and measurement of the arrays based on groove unit-cells. The array in the size of 200mm×200mm is taken into practical 60GHz communication experiments in NLOS environment. Analysis on the experiment results is given.

Chapter 1 State of the Art

Contents

Chapter 1 State of the Art

In this chapter, the general context of 60GHz indoor communications is first briefly introduced. The need of repeaters to improve radio-coverage at a moderate cost is then highlighted. The specific configuration of T-shaped corridors is chosen as a challenging application for this Ph.D. work. Examples from literature are analyzed in order to derive general requirements. Then, printed reflectors are identified as a possible low cost and low profile solution to address this issue. As printed reflectors can be seen as specific case of reflectarrays, a particular attention is paid to this architecture. Based on the analysis of its working principle, a generic topology aiming at endfire radiation is established for the whole thesis. In the following, several possible phase-shifting unit-cells are compared. Dielectric resonator antennas (DRA) and rectangular waveguides are investigated in more details as the most promising technologies for millimeter waves.

1.1 Characteristics of 60GHz Communication

With the development of millimeter wave technologies, almost all the radio spectrum resources in lower frequency band have been allocated to local wireless application. For example, the congested 2.4GHz Industrial-scientific-medical (ISM) band is stuffed with protocols like IEEE 802.15.4 (ZigBee), IEEE 802.11a/b/g/n/ac (Wi-Fi), IEEE 802.15.1 (Bluetooth) [1], etc. Therefore, the un-channelized license-free spectrum around 60GHz gives rise to great interest. Since the bandwidth directly determines the maximum data transfer rate in the communication, its unprecedentedly wide bandwidth in V-band seems so appealing. Though the spectrum definition witnesses a minor difference throughout the world (the authorized bandwidth for 60GHz is 57-64GHz in United States, 57-66GHz in Europe, and 59-66GHz in Japan [2]), the 60GHz communication embraces a potential data throughput of 7Gbit/s. Compared with the conventional Wi-Fi's data rate of 600Mbit/s (IEEE 802.11n) and UWB's 480Mbit/s, the emerging 60GHz communication becomes the most promising technology in the future.

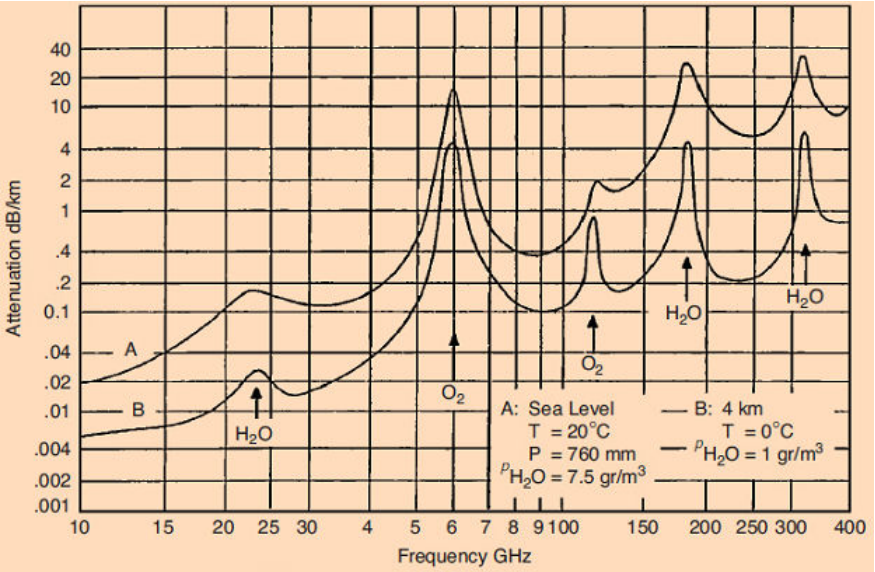

Fig.1.1 Atmospheric absorption of micro-and-millimeter waves [3]

At 60GHz, the special attenuation behavior is another important propagation characteristic, which greatly affects its radio performance. Due to the atmospheric attenuation in free space, the millimeter wave transmission encounters loss. Fig.1.1 [3] compares the atmospheric absorption rate versus frequency ranging from 10 to 400GHz. Curve A stands for the situation at sea level, where the water vapor (H_2O) plays the main role, and curve B represents dry air where oxygen (O_2) is mainly considered. We can clearly observe the peculiar attenuation peak at 60GHz, when the drastic gaseous loss is mainly brought by O_2 as high as 15dB/km. This clarifies the 60GHz communication is preferable for short-distance applications. However, its applications in the indoor communications are still limited. Due to the short wavelength (around 5mm), the 60GHz radio is very keen to be blocked by obstacles (e.g., it is barely able to scatter through a wall). So current investigations only assume the light-of-sight (LOS) scenario, and the implementations in NLOS environments are full of challenges.

Over the last couple of years, many commercial applications at 60GHz have already marched into real life. The WirelessHD team [4] supported by electronics giants is working on a new digital network interface for indoor uncompressed high-definition video transmission. Its first technology standard was issued in 2010, and the related chips, transmitters and adapters have been released in market in 2013 [5]. Another team of WiGig is endeavoring on indoor wireless large file transfer and smart home network connection solution [6]. Its first technology standard was proposed in 2009, and related chips and computer processors have been issued in

2014 [7]. Undoubtedly, they all aim at LOS environment.

Therefore, targeting signal relay and recovery in NLOS environment, a solution of reflecting device with high-directivity and high-gain would be a great advance for the 60GHz indoor communication.

1.2 Topology Establishment for Passive Repeater Array

In this section, we explore a promising reflecting device for the 60GHz indoor communication in NLOS environment. Before taking discussions on detailed structures, we outline the general specifications of the design:

1). since our design goal is to establish indoor signal relay linkage for the indirect paths, we assume the desired device is air-fed, and the primary source is an independent system which is located remotely to produce a normally-incident plane wave. More precisely, the expected device is a reflector or repeater, and we do not address the design of the illuminating feed.

2). as one typical example of the NLOS environment, the challenging configuration of a T-shaped corridor (Fig. 1.2) is chosen as the test-case and will be used through the whole thesis. The T-shaped corridor is a very common indoor scenario. Due to the obstruction of walls, the 60GHz signal (shown in blue line) cannot reach the Rx terminals following direct radio paths. So in our solution, the desired repeater structure (the black module) should perform as a linkage junction and scatter the signals towards the Rx terminals in the horizontal direction. In other words, the repeater should be designed to provide endfire radiation (as shown in red line).

3). as the repeater is mounted on the surface of the wall, its design must consider the convenience for fabrication and deployment. For example, traditional reflectors with bulky size, like parabolic reflector [8-9] and corner reflector [10-12], or synthesized reflectors with complicated topology [13-15], are not suitable for the situation. As an alternative, planar repeaters with low profile and low mass are our preferred solution.

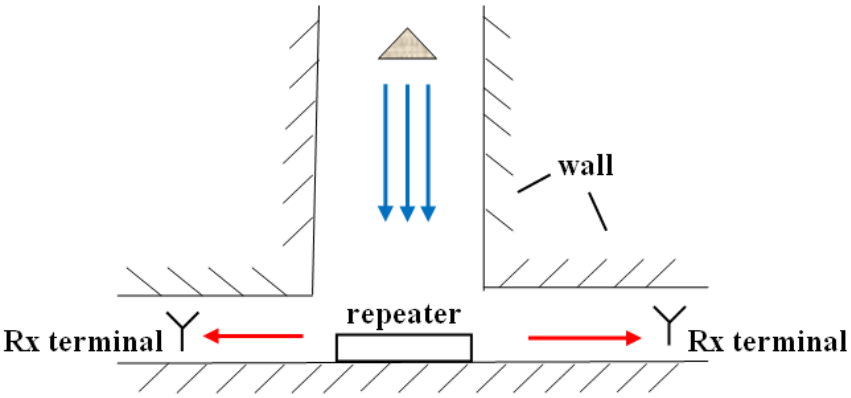

Fig.1.2 Scenario depicting endfire-radiation repeater in T-shaped corridor

Based on these considerations, a general design perspective for the repeater has been outlined. Subsequently, a background discussion about repeaters will be given in the next section, to further clarify the repeater topology.

1.2.1 Introduction to Repeaters

Repeaters have been widely used as electromagnetic devices for a long time. Their main feature is to increase the coverage range of the transmitted radio signals, or to improve the communication interconnection between the transmitting and receiving points. For example, in [16], a wideband passive repeater operating at 4GHz has been designed to improve the wireless link reliability.

Depending on the existence of power supply, repeater architecture can be categorized into two types: active repeater and passive repeater. An active repeater [17-19], which owns independent power supply, is actually a complicated circuit integrating both power amplifier and radio front. It amplifies the incoming signal before broadcasting it. Then, the design and fabrication are quite complex and the whole cost is high. In addition, the amplified signals may boost significant interferences in areas that are already covered by a direct signal of the same frequency channel (even interfere with the mobile network), or cause oscillation in the repeater itself. This also causes regulations on the utilization of the active repeaters.

On the other hand, the passive repeater [20-24], with no power supply, provides a trade-off solution for far simpler structures. Although it cannot increase the power level of the incoming signal, it gives the option to efficiently establish the linkage relay with affordable cost, as expected in our situation.

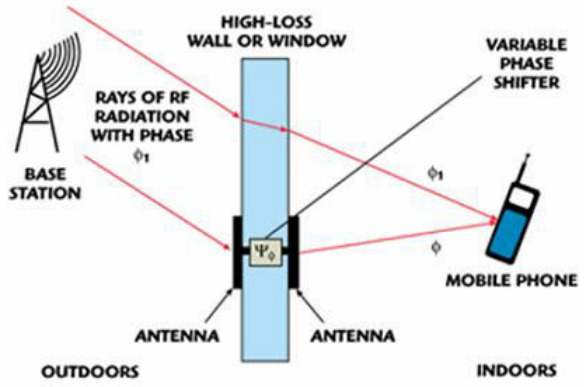

Fig.1.3 Scheme of a through-wall passive repeater

Fig.1.3 gives an example of a through-wall passive repeater [20], which realizes the communication relay between a base station (outdoor) and mobiles (indoor) over an obstacle (here a wall). This passive repeater is constituted of a receiving antenna, a transmitting antenna, a phase-shifter and a cable. The two antennas, connected by the cable and phase-shifter, are locating at the two sides of the wall, respectively. Signals from base station are captured by the receiving antenna, and transferred across the wall through the cable. The phase is then adjusted and the signal is re-radiated by the transmitting antenna, towards the target mobile.

The architecture in Fig.1.3 is not always the same for all the passive repeaters. It may vary depending on application requirements. For example, a passive repeater with MIMO performance for indoor multipath environment at 2GHz is presented in [21]. As shown in Fig.1.4 (a), the repeater is composed of four folded-patch antennas (FPA), one Yagi-Uda antenna and power combiners. The FPAs are combined to perform as the repeater's receiving antenna, the Yagi-Uda antenna is chosen as the transmitting antenna for its high-directivity, and the two parts are connected through the microstrip power combiner. When the repeater is illuminated, the FPAs collect the incident power and deliver it to the Yagi-Uda antenna for re-radiation. By adjusting the boresight of the Yagi-Uda antenna, this passive repeater can reflect the normal incident wave towards any desired angles, thus obtaining a broad-angle scattering, including endfire direction. In Fig.1.4 (b), the bistatic radar cross section (BRCS) of the repeater demonstrates an endfire scattering (along *y*-axis) under the *z*-axis incidence. As a matter of fact, this repeater structure provides one possible implementation for an endfire array at 2GHz. However, this solution is not applicable in our case. At 60GHz, the FPA parts (together with the corresponding feeding networks and power combiners) would be challenging for fabrication due to the small

size and complicated geometry. What's worse, the microstrip combiners would contribute greatly to high insertion loss.

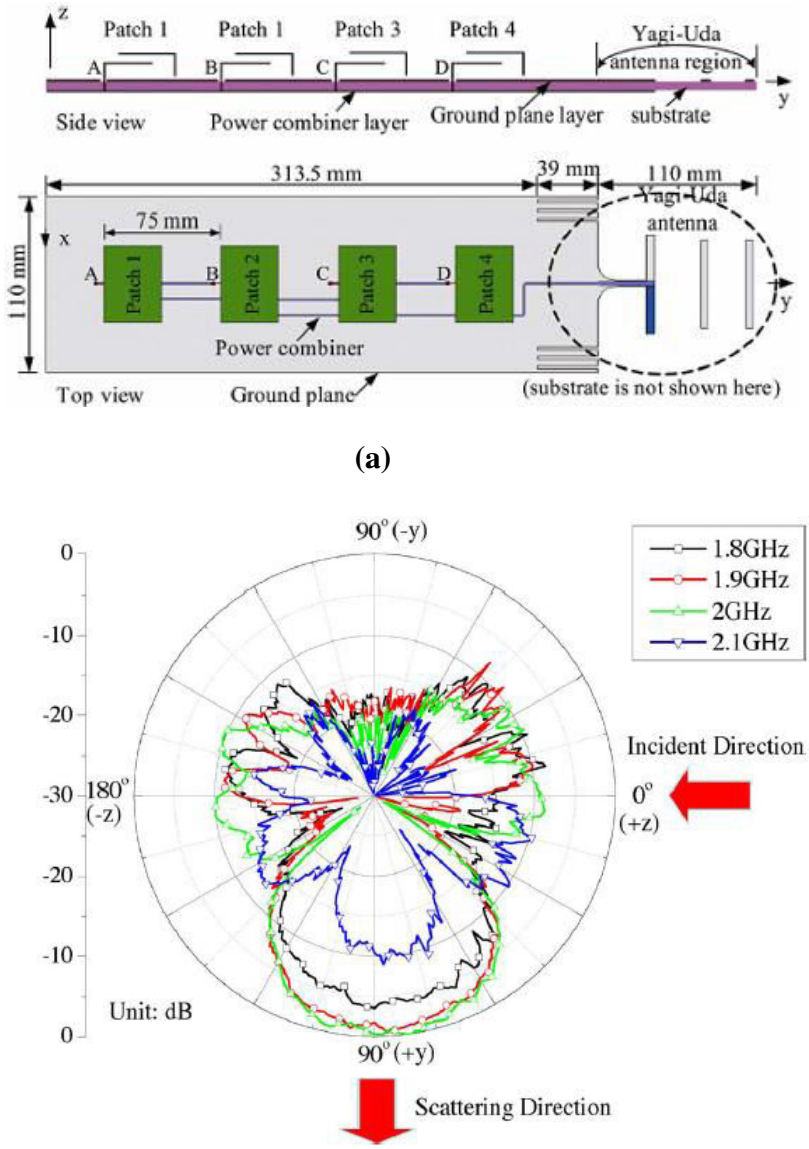

(a)

(b)

Fig.1.4 One MIMO passive repeater at 2GHz [21] with (a) geometrical configuration and (b) Normalized BRCS pattern

Another passive repeater structure involving a broadband reflectarray [22] is presented in Fig.1.5. It aims at eliminating blind spots in wireless communication between a base station and mobile users. The typical application is shown in Fig. 1.5b where the base station is on top of building 3 while the mobile user is supposed to be located between buildings 1 and 2. In that case, the introduction of the repeater on top of building 1 enables the communication. The used unit-cell (Fig.1.5a) consists of one

main dipole and two parasitic dipoles to extend the bandwidth with a central frequency at 2050MHz for WCDMA system.

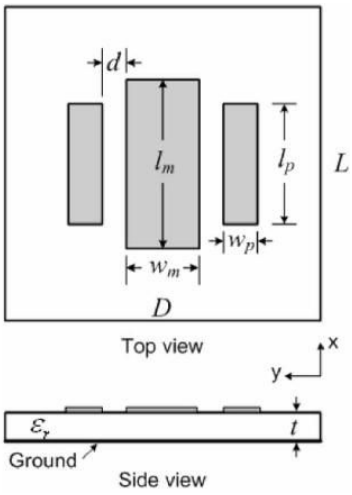

(a)

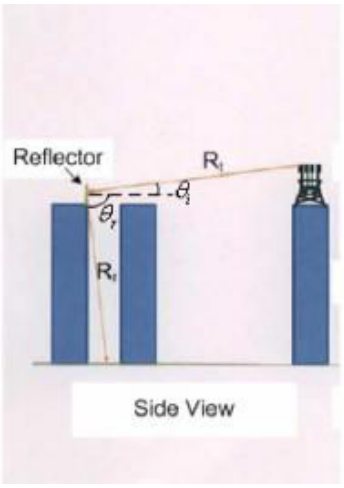

(b)

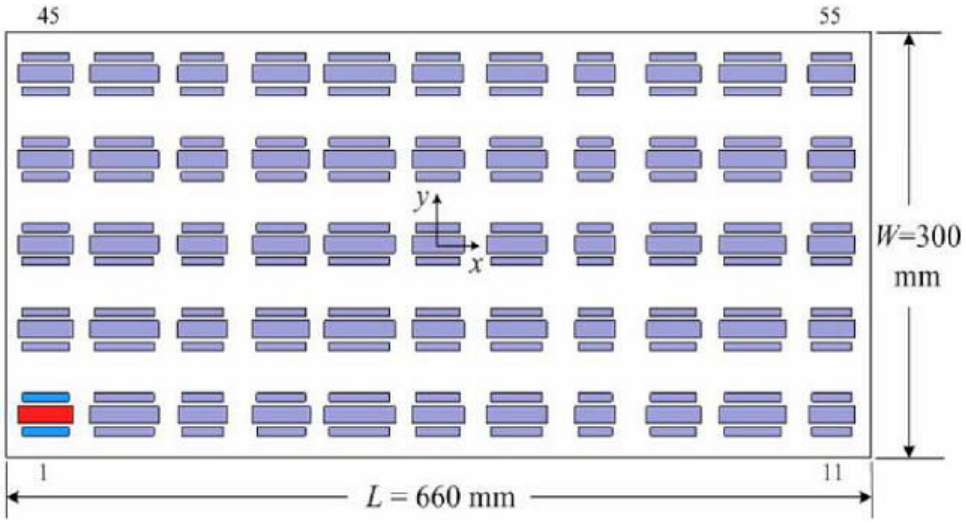

(c)

Fig.1.5 Schematic of (a) geometry of single element based on parasitic dipoles, (b) working principle of the array in the scenario with three buildings, and (c) a parasitic dipole reflectarray of 11×5 elements

Back to our case, the critical point lies in the fact that the passive repeater has to radiate orthogonally to the direction of arrival of the incoming signal. Using a classical reflector, this can be achieved with a dihedral structure [13]. However, these solutions involve bulky 3D structures, which is not convenient for our purpose.

Therefore, the most likely passive repeater topology for our situation should rather derive from the one in Fig.1.5, which is only made of reflecting surfaces.

Furthermore, in order to better fulfill the constraint of low profile, the qualified passive repeater should preferably be determined as one single reflecting surface made of compact reflecting unit-cells (and will be called a printed reflector in the following).

1.2.2 Introduction of Reflectarray Antenna

Based on such considerations, possible structure for the repeater introduced in Fig.1.2 is given in Fig.1.6. The low profile passive repeater is made of reflecting unit-cells (typically microstrip cells) and it is very similar to a reflectarray antenna.

Fig.1.6 Geometry of compact passive repeater

Researches on reflectarray antenna can be dated back to 1962, when Malech firstly proposed the conception of reflectarray, and Berry [25] confirmed its feasibility by constructing the first reflectarray antenna in the world. A reflectarray consists of a feeding horn antenna and a planar reflecting surface, which is composed with a large numbers of reflecting unit-cells. A typical reflectarray [26] is depicted in Fig.1.7. If we compare it with Fig.1.6, the only difference lies in the primary source. Since it is also part of the reflectarray antenna, extra design is required for the horn antenna. In our case, on the contrary, the excitation is supposed to be distant and only the printed surface has to be designed. As already said, we assume it is illuminated by a simple plane wave under normal incidence (produced by the remote hot point). In the following section, the discussion for the repeater design will thus be led by using reflectarray antenna as a guiding starting point.

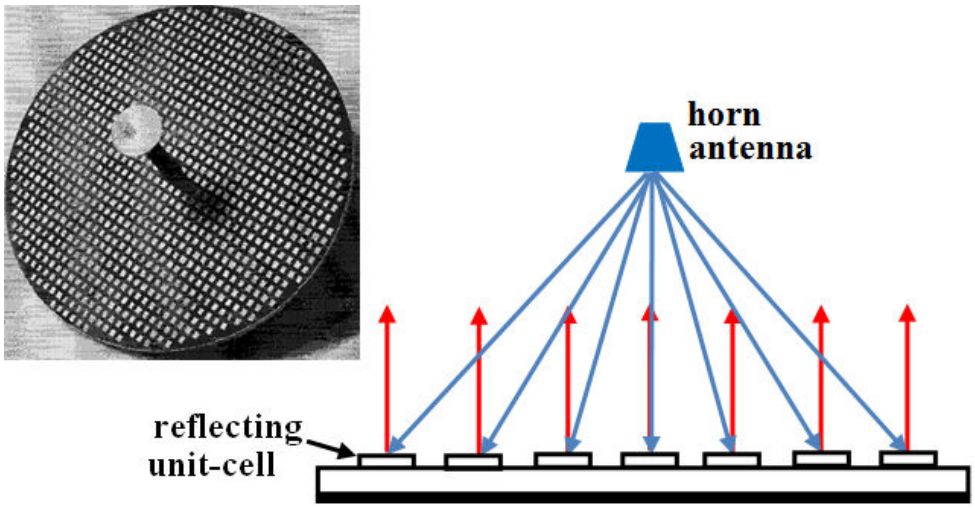

Fig.1.7 Illustration of a reflectarray antenna (upper left is a 28GHz reflectarray using 996 linearly polarized patches [26])

As can be guessed from Fig.1.7, a typical reflectarray antenna combines the principles of both a parabolic reflector [8-9] and an array antenna [26-29]. It gets rid of parabolic reflector's bulky volume and array antenna's complicated feeding network with power loss, and enjoys the advantages of low profile, low cost and simple fabrication using printed circuit technology.

1.2.3 Topology Derivation based on Reflectarray Working Principle

In this section, the objective is to derive the principle of the foreseen printed reflector using simple antenna array theory.

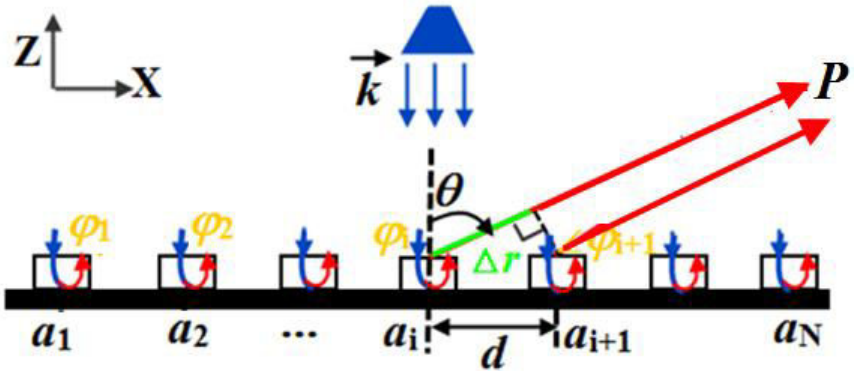

Fig.1.8 Working principle of the reflector

As depicted in Fig.1.8, a linear *N*-element printed reflector deployed along *x*-axis

is considered. The spacing between unit-cells is uniformly set as d. A normal incident wave (as the blue lines indicate) is illuminating the planar reflector. The unit-cells reflect the incident power with a prescribed phase φ. This results in a radiated beam (as the red lines indicate) towards point P (θ angle with z-axis) in far field.

An initial uniform phase difference $\varphi_i=(i\text{-}1)\,\Delta\varphi$ for ith unit-cell is introduced. For the whole array, the total electric field superposed at angle θ can be expressed as:

$$E=\sum_{i=1}^{N}E_i=E_1\sum_{i=1}^{N}e^{j(i-1)\psi} \tag{1-1}$$

In (1-1), E_1 stands for the electric field from the first element a_1. The term $e^{j\psi}$ indicates the extra phases introduced by the initial phase differences and the wave path differences, which could be further written as:

$$\psi=\Delta\varphi+k_0 d\sin\theta \tag{1-2}$$

with $k_0=2\pi/\lambda$ is the wave number in free space.

If we define the variable term $\sum_{i=1}^{N}e^{j(i-1)\psi}$ in (1-1) as the array factor, it can be expressed as:

$$F(\theta)=\sum_{i=1}^{N}e^{j(i-1)\psi}=\frac{\sin\left(\frac{N\psi}{2}\right)}{\sin\left(\frac{\psi}{2}\right)}e^{j\frac{N-1}{2}\psi} \tag{1-3}$$

When $\psi=0$, the maximum value for the array factor can be obtained as:

$$\left|F(\theta)\right|_{\max}=\left|\frac{\sin\left(\frac{N\psi}{2}\right)}{\sin\left(\frac{\psi}{2}\right)}\right|_{\psi=0}=N \tag{1-4}$$

For a main beam at θ, the initial phase difference $\Delta\varphi$ between two neighboring unit-cells and the spacing d must meet the relationship:

$$\Delta\varphi+k_0 d\sin\theta=0 \tag{1-5}$$

In our case, the endfire radiation corresponds to beam towards $\theta=\pm 90^{\circ}$. The spacing is set to half wavelength ($d=\lambda/2$). As will be seen, this permits to have the main lobe at $\theta=90°$ and a grating lobe at $\theta=-90°$ simultaneously. What's more important, the $\lambda/2$ spacing is the most favorable choice that facilitates the design as only two different phase-states are required for our application. Applying these conditions into (1-5), the initial phase difference between two neighboring unit-cells can be calculated out as $\Delta\varphi=\pm\pi$. Therefore, we choose the equivalent phase for the successive elements as 0, π, 0, π.... In other words, in order to steer the reflection beam towards endfire radiation as expected, two successive elements should only be out of phase.

This conclusion can be directly applied for our passive repeater. Fig.1.9 depicts the generic topology for the repeater array. It will be utilized throughout the whole thesis.

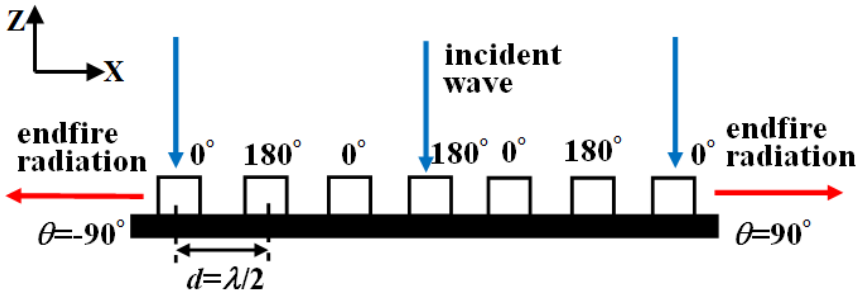

Fig.1.9 Generic topology for the endfire passive repeater array

The topology in Fig.1.9 thus specifies the design target. Right now, the priority becomes constructing appropriate phase-shifting unit-cells to produce the prescribed out-of-phase reflection. Therefore, the existing technologies for phase-shifting unit-cells are to be discussed in the following.

1.3 Investigations on Phase-shifting Unit-cells of Microstrip Reflectarrays

In this section, the reflectarray antenna background is referred again. Several conventional phase-shifting unit-cell technologies in reflectarray design are compared and analyzed.

Though the first reflectarray was made of short-ended rectangular waveguides, it won great popularity only when printed microstrip patches were used as array elements. Investigations on microstrip reflectarray were initialized in 1978, when

Malagisi [30] firstly proposed the conception of microstrip reflectarray, and then Montgomery [31] introduced infinite array approximations to examine the microstrip array. Thereafter, the microstrip reflectarray was widely developed with a great number of publications [32]. Compared with waveguide elements, the printed microstrip patch elements enjoy the advantages of low profile, low mass, low cost, easy fabrication and deployment.

1.3.1 Existing Solutions for Microstrip Reflectarrays

Theoretically, critical mechanism of phase-shifting technology is to control the reflection phases by varying the unit-cell's geometry parameters. For microstrip reflectarrays, there are several typical phase-shifting techniques. Here we will focus on the ones relevant to our design:

1. The first solution is to use a transmission line [33]. More precisely, identical microstrip patches are loaded with transmission lines of different lengths. The adjusted length is regarded as the geometry variable to produce expected phase delay.

2. The second solution is to adjust the patch size itself [38]. Patches with different dimensions are directly deployed as unit-cells. As the geometry variable, the patch size is responsible for the expected phase-shifting.

3. Another solution is to introduce a variation of rotation angle [40-41]. Identical microstrip patches are deployed but rotated with different angles. Phase-shifting is realized relying on the rotation. This solution is only applicable for circular polarization.

4. The last considered solution is to etch a slot aperture in the ground plane [42]. By varying the aperture size, the unit-cell's reflection phase is controlled.

These four models are described in detail in the following section.

1.3.1.1 Model based on Loaded Transmission Line

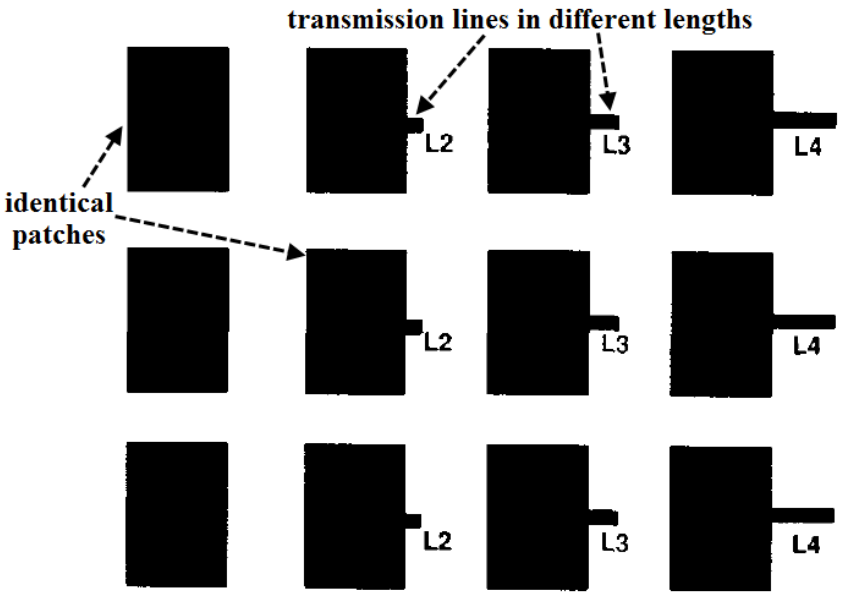

Fig.1.10 A 3×4 microstrip reflectarray based on loaded transmission lines model. It realized a 20° main beam at 10GHz [33].

The design of loaded transmission line model originated in the early 1990s [33] [45]. As depicted in Fig.1.10, the open-circuit transmission lines with different lengths are attached at the side of identical patches. The patch size is resonant at the frequency of the incident wave. Then, all the incident power will be captured by the patches and transferred to the transmission lines. At the open end of the transmission lines, the power gets totally reflected and finally re-radiated back from the patches. In conclusion, the loaded transmission lines play the role of phase-shifters, and the phase delays are produced by their different electric lengths.

However, this structure demonstrates a low efficiency. In such configuration, large space has to be provided in order to accommodate the lines. Therefore, the overall aperture efficiency is reduced. In order to solve this problem, the structure was improved by moving the transmission line downwards below the ground [35-37]. By etching a slot in the ground plane, the transmission line is now coupled to the patch through the slot, thus saving space for the patches.

1.3.1.2 Model based on Variable Size Patch

The design of variable size microstrip patch unit-cell was firstly proposed in 1993 by Pozar [38-39]. In 1997, he further gave thorough analyses on the applications of such reflectarray in millimeter waves [40]. As shown in Fig.1.11, such configuration utilizes printed microstrip patches as the array elements. By directly adjusting these

patches' dimensions, their resonant frequencies get altered accordingly, together with the reflection phases.

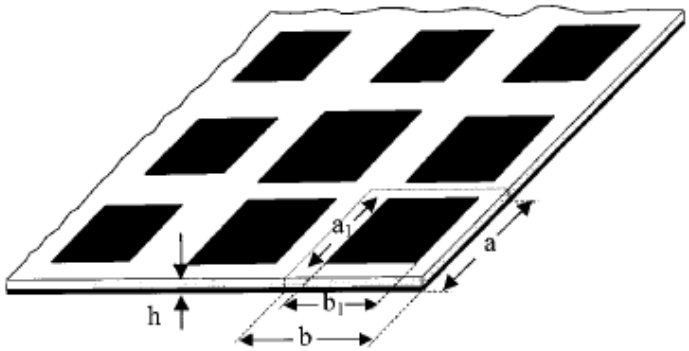

Fig.1.11 Schematic of reflectarray based on variable size patches model [47]

Compared with the loaded transmission line model, this structure witnesses improved performance i.e. easier design, higher radiation efficiency and lower cross polarization level (no more parasitic radiation from the lines). So it has become the most popular model to construct phase-shifting unit-cells. On the other hand, as this model is greatly sensitive to the patch size, it requires a precise fabrication technique. Moreover, this model usually produces insufficient phase-shifting range, less than the required full 360° one. As one improvement, the multilayer structure was proposed [48-50] for broad phase-shifting range and improved bandwidth. Meanwhile, many other derivations have also been proposed for dual polarization dual band (e.g. square loop [51], annular ring [52] and crossed dipole [53]). However, as we will see later, this principle is not suitable for our application since the elementary pattern for radiating elements differing in size is not identical anymore.

1.3.1.3 Model based on Variable Rotation Angle

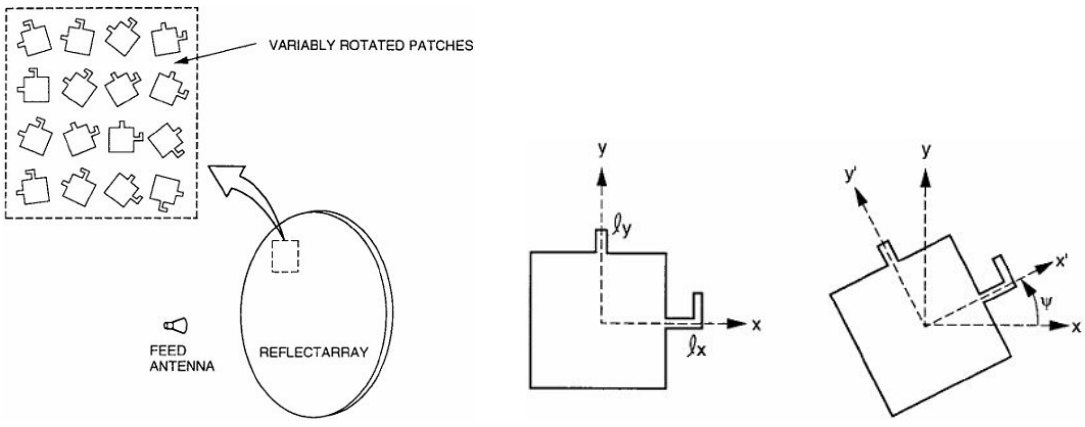

(a) **(b)**

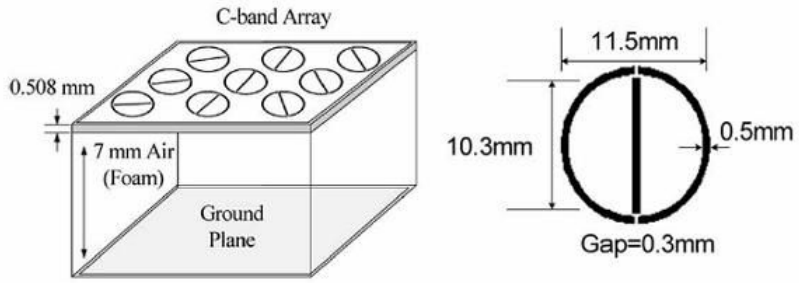

(c)

Fig.1.12 Schematics of (a) a CP reflectarray with elements having variable rotation angle, (b) detailed patch element topology [54] and (c) a CP reflectarray at 7.1GHz with split ring elements having variable rotation angles [56]

Previous two models are more related to linear polarization, the rotation angle model in this section is dealing with circular polarization (CP). The idea to adjust reflection phase by rotating the unit-cell was first proposed and realized by J. Huang and Pogonelski in 1998 [41]. As drawn in Fig.1.12 (a) and (b), transmission lines were loaded on the two orthogonal sides of the patch to establish a circular polarization. The length difference between the two transmission lines was properly chosen so that the reflected waves in the two orthogonal directions are out of phase. Therefore, when the patch is rotated by an angle ψ, the total reflection phase by the unit-cell is 2ψ. This model has been updated by C. Han (from the same team as J. Huang) in 2004 [54-57], when he proposed a novel rotation unit-cell, as presented in Fig.1.12 (b). The structure uses a split ring to realize the polarization separation in the orthogonal directions along x and y-axis, and also achieves a 2ψ phase-shifting when the unit is rotated by the angle ψ.

In summary, this model uses CP elements to produce a full 360° phase range. Though the design is more complicated than that of variable size patch, it lowers the demand for precise fabrication processing. The proposed elements (e.g. the split ring) with symmetrical structure demonstrate frequency selective characteristic, so they are promising for the design of multi-layer structure [58].

1.3.1.4 Model based on Patch with Slot Loaded Ground

In 2003, Chahamir [42] proposed a reflectarray design using slot apertures in the ground plane. The model consists of identical microstrip patches and a ground plane with many slot apertures of different lengths. The unit-cell prototype is depicted in

Fig.1.13. For each element, the etched slot behaves as an inductance loading the patch. The length of the slot controls the loaded inductance, thereafter defining the patch's reflection phase. Such structure has been improved by Cadoret [59] in 2005, when he etched the slot directly into the patch itself. This prevents from any back radiation.

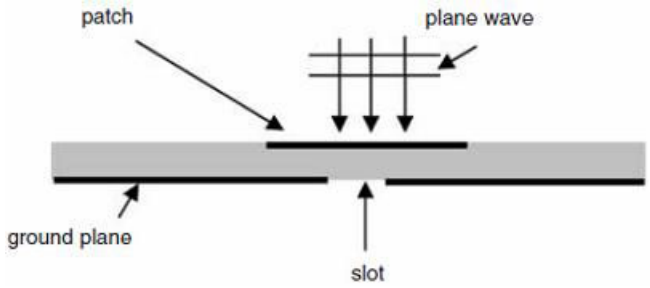

Fig.1.13 Reflectarray unit-cell with slot loaded on the ground [42]

1.3.1.5 Recent Advancements in Reflectarrays

In recent years, new topologies have been studied to enhance the capabilities of reflectarrays. For example, the phoenix cell [60-61] was proposed as a novel reflectarray element to realize a broad bandwidth. Avoiding the complicated design of multilayer structure, the cell integrates multi-resonators on a single-layer substrate. As shown in Fig.1.14, this concept provides a smooth evolution of the geometry corresponding to a whole 360° reflection phase cycle. It also leads to reflection phase curves with a good linearity.

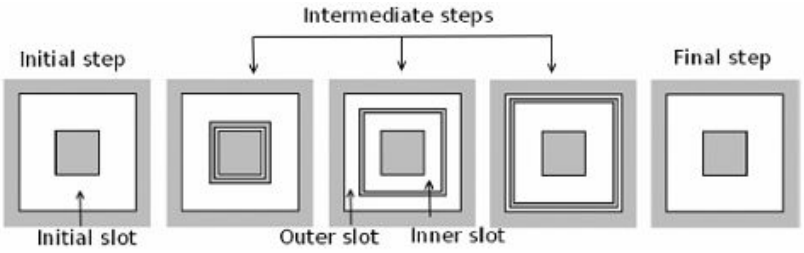

Fig.1.14 Cycle evolution of phoenix cells [60]

The concept of miniaturized-element frequency selective surfaces (MEFSS) [62-65] was also introduced into reflectarray. These elements (such as loop-wire structures [64], Fig.1.15) have sub-wavelength dimensions. They can achieve low sensitivity to the incidence angle and minimal dependency to neighboring elements.

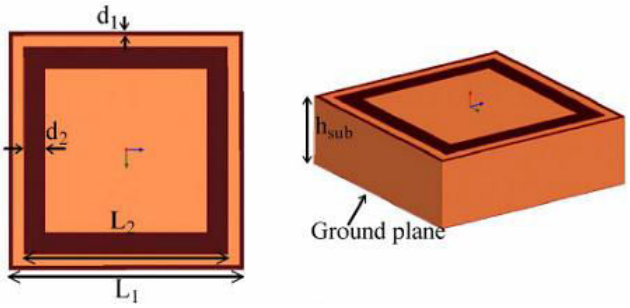

(a)

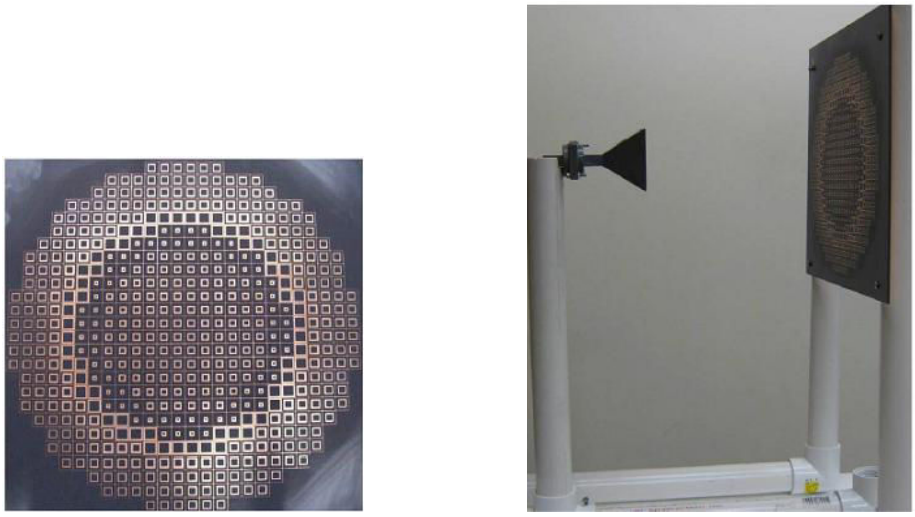

(b)

Fig.1.15 Schematic of a 260mm×260mm reflectarray [64] at 10.5GHz with (a) unit cell of the single-sided loop-wire grounded FSS and (b) the fabricated array

1.3.1.6 Reflectarrays at Millimeter Waves

In this section, we focus on specific achievements at millimeter-waves.

One of the first reported structures is the folded reflectarray (FRA) that was developed for compact radar systems [66-70]. As depicted in Fig.1.16 (a), a classic FRA consists of a primary source, a polarizer plate and a main reflecting plate. The signal transmitted from the source is reflected back by the polarizer grid, which only permits the pass of electromagnetic wave with orthogonal polarization. The main reflecting plate then phase-shifts the reflected wave and twists its polarization by 90°. The re-radiated wave then passes through the polarizer and focuses towards prescribed direction. Further explorations on FRA have pushed its applications into higher frequency band, e.g. a FRA with cosecant squared beam pattern in elevation and a pencil-beam in azimuth is proposed for the foreign object detection on airport

runways at 77GHz [69], and a folded Fresnel reflector using C-patch elements with high gain is measured in helicopter collision avoidance radar at 94GHz [70].

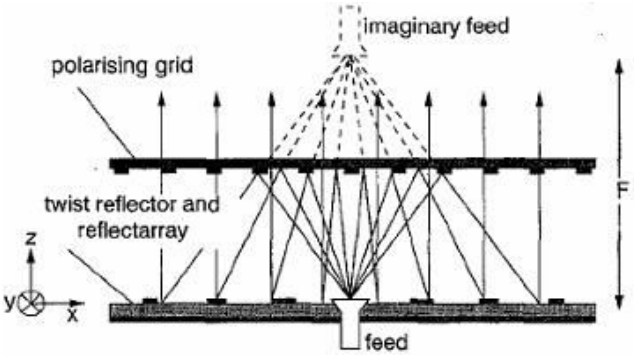

(a)

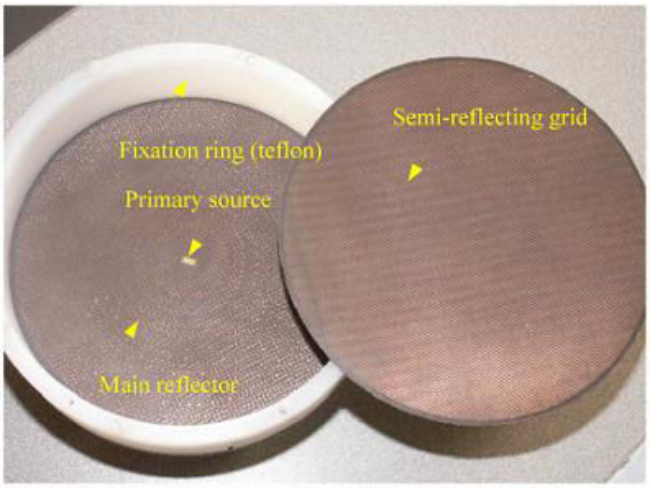

(b)

Fig.1.16 Schematic of (a) working principle of FRA and (b) a 130mm-diameter folded Fresnel reflector at 94GHz for helicopter collision avoidances system [70]

The conception of ultra-low side lobes reflectarray [71-74] is proposed with improved primary feed technique. Based on the relation of the radiated field by the reflectarray and the primary feed radiation pattern [72], a specific primary source with a radiation pattern corresponding to a prolate function is designed to greatly depress side lobes at the expense of widening main lobe. Meanwhile, in order to overcome the aperture blockage effect, the prolate-pattern primary source is illuminating with offset feeding. As one example, Fig.1.17 shows a 94 GHz reflectarray using an offset prolate feed.

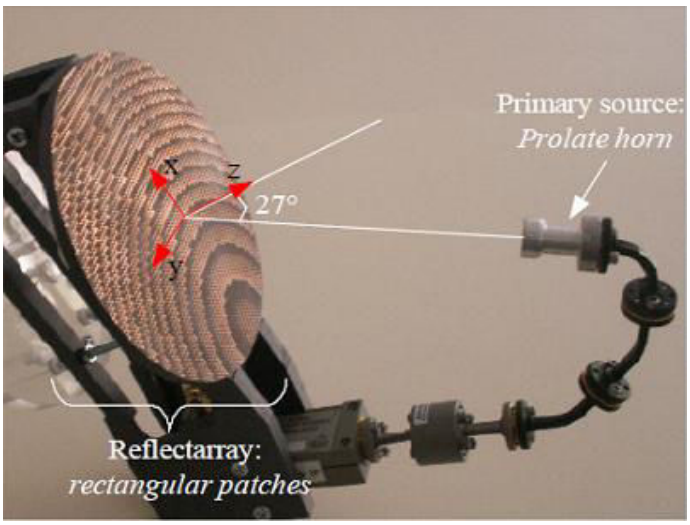

Fig.1.17 A 94GHz reflectarray using prolate horn with 27° offset feeding [73]

1.3.2 Limitation of Microstrip Reflectarray

As reviewed in previous section, there have been a couple of mature solutions to design phase-shifting unit-cells for microstrip reflectarrays. These models could provide inspiring guidance for our study. In this section, however, we investigate the possible associated limitations, particularly considering the specific requirements for our application.

The first limitation is the high loss [76-77]. At the working frequency of 60GHz, the dielectric loss from the substrate would be high, and the increased conductor loss would be the main loss in this situation, due to the skin-effect [78].

The second limitation is the possible cancellation of endfire radiation due to image theory, which is the main problem. Indeed, endfire radiation is the emphasis of our design, while traditional microstrip structures usually produce no radiation at endfire. Fig.1.18 gives a brief illustration. Being similar to an electric dipole, the microstrip element parallel to the ground plane produces an image current with equivalent magnitude but opposite phase. Therefore, the associated radiation may be seen as resulting from two dipole elements fed with equivalent magnitude and opposite phase. Clearly, the endfire radiation totally cancels out.

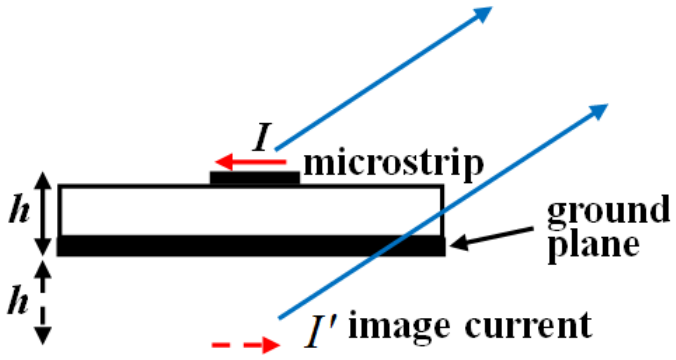

Fig.1.18 Endfire radiation cancellation effect of the microstrip element

The cancellation happens due to the simultaneous existence of the microstrip element and the ground plane. A totally reflecting plane is needed anyhow to insure that the incident wave is fully reflected and no power flows through the structure. The only solution is then to replace the ground plane with high impedance surface (HIS). A HIS [79] is composed of a great number of periodic subwavelength elements. In a specific frequency range, a HIS can behave as an ideal magnetic wall and provide an in-phase reflection [80-82]. Therefore, the combination of microstrip and HIS would eliminate the opposite image current. Many configurations have been carried out recently [83-85] in this specific field which is tightly connected to metamaterials. However, the HIS solution is still not easy for implementation. In this study, we decided not to entangle in HIS due to the very high frequency of the foreseen application. Definitely, it would have made the design of HIS quite tricky. The periodic sub-wavelength elements at 60GHz should have been in the range of [λ/5, λ/10] (i.e. [0.5-1] mm range, which is a usual dimension for such structures [86-87]), thus greatly increasing sensitivity to fabrication tolerances and cost. Meanwhile, we will see latter on that bandwidth is an actual issue for our application. It is believed the use of HIS would certainly have reduced the bandwidth further as such structures are usually narrow band [88-89].

Conclusions

In this section, we focused on the possible topologies for the phase-shifting unit-cell. Based on the reflectarray background, four typical microstrip unit-cell models being relevant to our design have been reviewed. Though microstrip elements appear not completely compatible with our design specifications, these models provide inspiring guidance for the work. In next section, other options will be

explored relying on 3D technologies.

1.4 Solution based on DRA Elements to the Passive Repeater Array

Two candidates are now proposed: dielectric resonator antenna (DRA) and rectangular waveguide. They both demonstrate a low loss and high radiation efficiency compared to microstrip, thus appearing relevant for the design requirement. In this section, the DRA structure will be investigated first.

1.4.1 Background Introduction of DRA

Dielectric resonator (DR) entered into researchers' vision as early in 1939 [90], and got applied as microwave filter and oscillators [91-92] since 1960s. Consisting of materials with high permittivity and low loss tangent, DR demonstrates the advantages of high Q-factor, low loss (there is no conductor loss), relative wide bandwidth (usually more than 10%), ease of excitation, low profile and numerous degrees of freedom in the geometry, which is quite convenient for antenna optimization. Therefore, after Long firstly reported the theoretical and experimental exploration of DRA performance [93] in 1983, investigations on this technology were put into spotlight and quickly gained wide attention [94-100].

Another important factor leading to the choice of DRA in our application is its distinctive radiation characteristic. Contrary to a microstrip element, a DRA at fundamental mode usually radiates like a magnetic dipole (as one example, Fig.1.19 (d) depicts the E-field and H-field distribution of DRA at TE^{x}_{111} mode. Detailed discussions about the mode will be given in next chapter). Therefore, the corresponding image current in the presence of a ground plane is now exactly in phase, and the endfire radiation cancellation effect is completely avoided.

Fig.1.19 draws several typical shapes of the DRA (i.e. hemispherical, rectangular and cylindrical). Their operation mechanisms are quite similar. However, only rectangular DRA owns three degrees of freedom (length D, width L and height $2h$), which offers more flexibility for performance control in design. Moreover, the rectangular DRA is easier for fabrication, especially if the whole reflecting surface is fabricated from a single dielectric block [108]. So for the next discussion, we will concentrate on rectangular DRA.

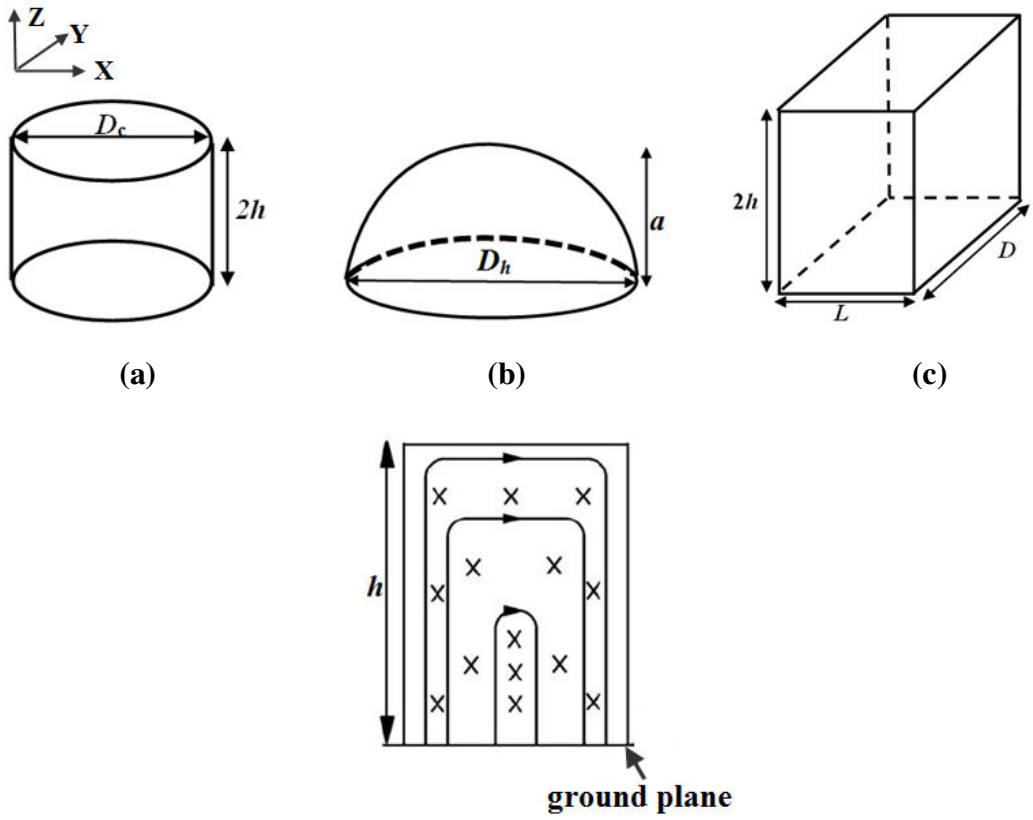

(a) **(b)** **(c)**

(d)

Fig.1.19 Geometries of one isolated (a) cylindrical DRA, (b) hemispherical DRA, (c) rectangular DRA; and (d) the E-field (lines) and H-field (crosses) distribution on rectangular DRA cell with ground at TE^{x}_{111} mode [96].

1.4. 2 State of the Art of DRA-based Reflectarray

In last section, a brief introduction was presented to explain why DRA is a viable alternative for the endfire array. Subsequently, we will try to further seek for feasible topologies to construct the phase-shifting unit-cell with DRA element.

The development history of DRA-based reflectarray just started in this decade. In 2000, the first DRA-based reflectarray was proposed by Keller [106]. Fig.1.20 gives a schematic of this structure. He constructed a 529-element array in Ka-band, and realized a 360° phase-shifting range by varying the lengths of the DRA elements. This technique, as a matter of fact, is quite similar to the one using variable size microstrip patches. As introduced before, this method is not easy for fabrication with so many elements to adjust individually. In addition, the deployment of DRA is not as easy as for microstrip elements, so a residual substrate was used in this array.

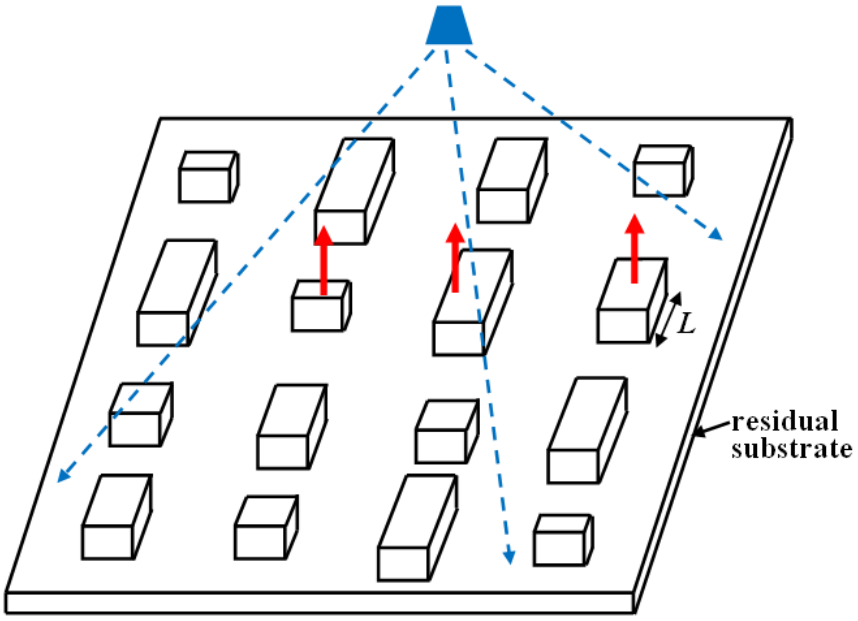

Fig.1.20 Schematic of reflectarray based on variable length DRA

A second idea, which uses reactive loading of the DRA elements, was proposed in [107-109]. Non-resonant parasitic metallic strips were printed on the top surface of the DRA elements, as depicted in Fig.1.21 (a), in order to change their resonant frequency. In [104], a 24×24 reflectarray at Ka-band was fabricated. This technique is indeed quite similar to that using slot-loading of patch elements in microstrip reflectarrays.

Indeed, a topology with variable slot in the ground plane was also used in [119-121]. One example is shown in Fig.1.21 (b), which realizes a 360° phase-shifting range for a 23×23 reflectarray working at 10GHz.

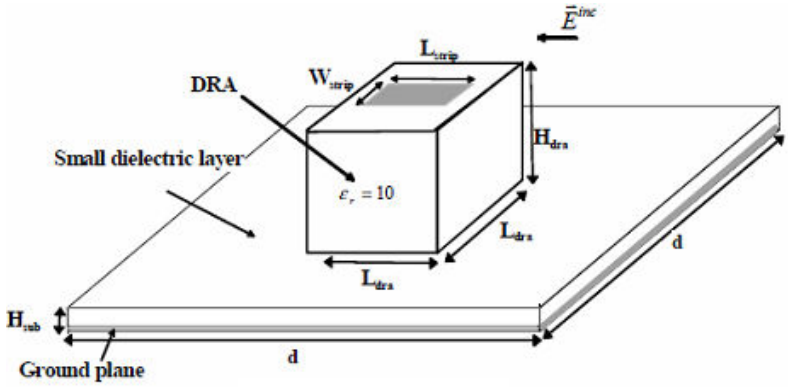

(a)

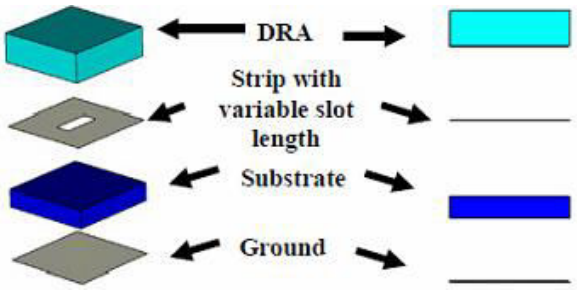

(b)

Fig.1.21 Schematic of reflectarray based on DRA elements with (a) loaded metallic strip of variable size [107] and (b) loaded slots with variable size [119]

To summarize, in the previous technique, the critical mechanism used to tune the reflected phase is to alter the DRA elements' resonant frequency. As we will see in a future chapter, other topologies could be used directly deriving from microstrip designs. For instance, identical DRA could be slot-coupled to microstrip lines of variable length.

Finally, it should be noticed than another approach using pure dielectric structures has been proposed recently at 100GHz [75]. As for fabrication technique, the 3D printing technology has been used to achieve a rapid manufacturing of a 400-element dielectric reflectarray. Instead of conventional DRA reflectarray using high dielectric constant, the array takes low dielectric constant material (polymer with ε_r=2.78 and loss tangent=0.0039 at 100GHz). As shown in Fig.1.22, the array consists of dielectric slabs covering the entire ground, and phase is controlled for each element by adjusting the dielectric slab's height.

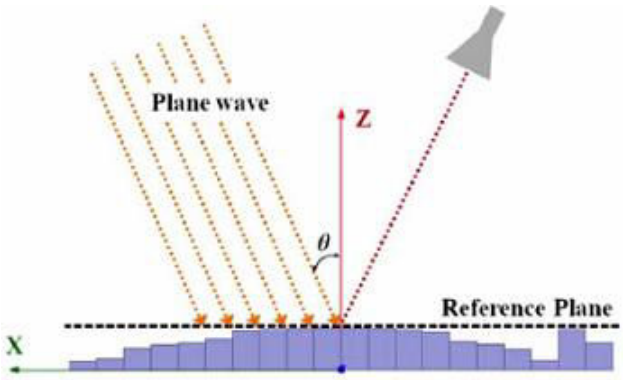

Fig.1.22 Schematic of the dielectric slab reflectarray [75]

1.5 Solution based on Rectangular Waveguide to the Passive Repeater Array

In last section, DRA element has been introduced as one possible solution to the design. Right now, another solution based on rectangular waveguide is discussed.

Waveguide is not new for reflectarray design, since it appeared in 1963 when Berry [25] constructed the first reflectarray in the world. As we already mentioned, this array used short-ended waveguides of variable lengths, and the phase-shifting was controlled by adjusting these lengths. Actually, waveguide element did not attract much attention in the early times of reflectarray history due to its bulky dimensions. However, when we turn our eyes to millimeter waves, like 60GHz in this thesis, the waveguide element becomes quite promising. Since the waveguide dimension is directly related to working frequency, its size is no longer a problem at millimeter waves. Meanwhile, its advantages of low loss and high power capacity make it quite conducive for the high frequency applications, and the quite simple structure can be compatible with a low fabrication cost using modern CNC (Computer Numerical Control) machining.

Investigations on waveguide-based reflectarray just started again a couple of years ago. As shown in Fig.1.23, a reflectarray based on short-ended rectangular waveguide at 75GHz was reported in 2011 [122]. Full wave analysis was used to calculate the required compensation phase for 5961 elements.

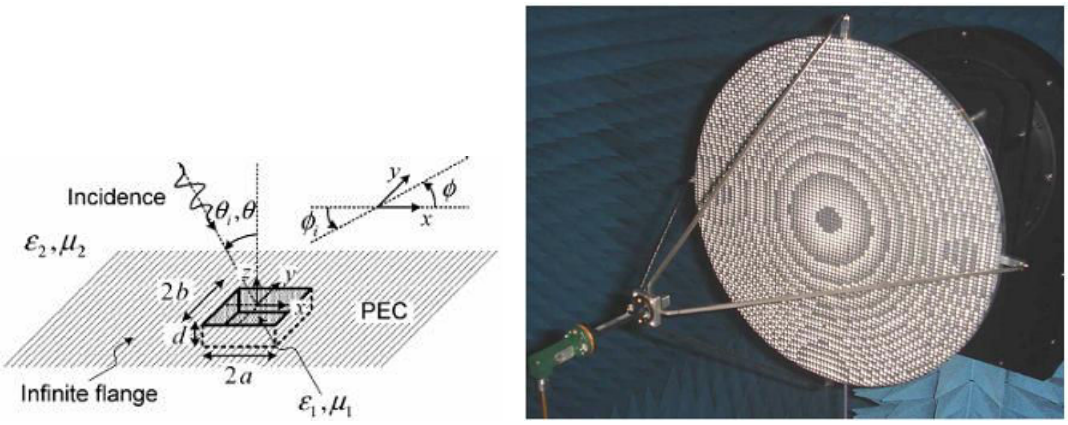

(a) **(b)**

Fig.1.23 Schematic of one reflectarray based on rectangular elements with (a) geometry of waveguide element and (b) photo of the circular-plate reflectarray with 5961 elements [122]

1.6 Conclusion

The development of 60GHz communications was introduced at first, and the general design requirement for a passive repeater array with endfire radiation was established, considering the challenging configuration of a T-shaped corridor. Based on existing microstrip reflectarray models, possible solutions for the phase-shifting unit-cells were categorized and analyzed. Due to the limitations of microstrip elements, DRA and rectangular waveguide are proposed as two potential candidates. By reviewing the development history, promising topologies of DRA and waveguide-based reflectarrays were discussed.

Chapter2 Investigations on Endfire Array Designs based on DRA Elements

Contents

Chapter 2 Investigations on Endfire Array Designs based on DRA Elements

As introduced in chapter 1, the DRA element is a potentially suitable candidate for our design. Therefore, this solution is investigated in this chapter. In the beginning, the fundamental theoretical background of the rectangular DRA will be discussed. Then, an important issue when designing reflectarrays will be discussed: what is the impact of using unit-elements with different resonant frequencies? Based on the provided answer, two topologies for the foreseen application will be proposed. The first one involves notched DRAs while the second uses aperture-coupled DRAs. This chapter only relies on simulations. Both unit-cells and canonical subarrays are analyzed.

2.1 Design of Basic Rectangular DRA Cell

2.1.1 Theoretical Background of Rectangular DRA Cell

Many papers discuss the analysis of cylindrical and spherical DRA [90-97], much less investigations on rectangular DRA can be found [98-100]. Compared with cylindrical or spherical DRA, rectangular DRA owns more degrees of freedom (i.e. the length, width and height), which offers more flexibility to control the radiation performance (but also makes the modal analysis trickier). Other advantages can be mentioned. For example, spherical DRA [91] and cylindrical DRA [92] may experience the problem of modes degeneracy and associated cross-polarization. On the contrary, this can be avoided in rectangular DRA.

There are several ways to analyze rectangular DRA [99-101]. For example, Okaya and Barash provided an approximate modal analysis and divided the possible modes into TE and TM modes. However, all the predicted modes, including the lowest-order TM modes, cannot be observed experimentally [102]. Therefore, only TE modes are discussed in this thesis. Considering the rectangular DRA depicted in Fig.2.1, TE lowest-order modes are TE^{x}_{111}, TE^{Y}_{111} and TE^{Z}_{111}, which can radiate like a magnetic dipole oriented along *x*-axis, *y*-axis and *z*-axis direction respectively. Considering the

similarity of these three modes, we will only analyze TE^{x}_{111} mode in the following.

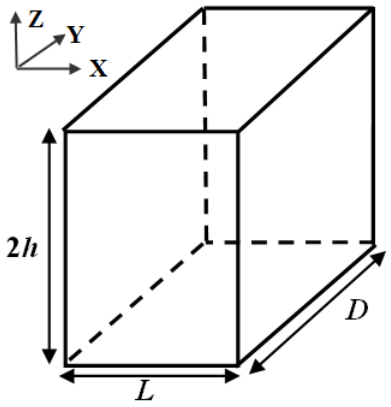

Fig.2.1 Schematic of typical rectangular DRA

In Fig.2.1, an isolated rectangular DRA element (without any ground plane) in the size of $L \times D \times 2h$ is considered. As $D>2h>L$, its fundamental mode is defined as TE^{x}_{111}. According to [100], all the surfaces of the rectangular DRA satisfy the magnetic wall boundary of a non-confined mode, so its corresponding H-field and E-field components along x-axis can be expressed as:

$$H_x = A\cos(k_x x)\cos(k_y y)\cos(k_z z)$$

$$E_x = 0 \tag{2-1}$$

In these equations, k_x, k_y and k_z denote the wavenumbers along x-axis, y-axis and z-axis direction, respectively. They comply with the dispersion equation:

$$k_x^2 + k_y^2 + k_z^2 = \varepsilon_r k_0^2$$

$$k_0 = \frac{2\pi f_0}{c} \tag{2-2}$$

Here ε_r is the dielectric constant of the DRA, and k_0 stands for the wavenumber in free space. Meanwhile, for the DRA cell, k_x, k_y and k_z can be determined as

$$k_y = \frac{\pi}{D},\ k_z = \frac{\pi}{2h}$$

$$k_x tan\left(\frac{k_x L}{2}\right) = k_{x0},\ k_{x0}^2 = \left(\varepsilon_r - 1\right)k_0^2 - k_x^2 \tag{2-3}$$

So we can solve out L:

$$k_x tan\left(\frac{k_x L}{2}\right) = k_{x0} \Rightarrow L = \frac{2}{k_x}\tan^{-1}\frac{k_{x0}}{k_x} \tag{2-4}$$

Based on (2-4), a rectangular DRA element can be easily designed, if we set its resonant frequency f_0 and the other two dimensions: $2h$ and D. Accordingly, we will consider constructing one single rectangular DRA element working at 60GHz, which will be used in the following array design.

2.1.2 Description of Simulation Settings for Infinite Periodic Structure

The anticipated array will be a quasi-periodic structure composed of almost identical elements, called the radiating cells. In the following, we discuss the simulation approach to analyze such cells. The main assumption relies on the use of an infinite periodic model. This model, based on Floquet Theorem, considers the cell is extracted from a 2D infinite and periodic array of identical cells. By forcing periodic boundary conditions on each unit-cell, the electromagnetic analysis can then be limited to a single element. In the simulation, the cell is illuminated by a plane wave and the reflection coefficient is calculated. All reported simulations in this document use Ansys HFSS solver. Note that mutual coupling is accounted for by the model but it considers all cells are identical.

Two different implementations of the model will be introduced in the following, which are utilized through the whole thesis. The first one is the Waveguide Approach (WGA) [103]. It constructs an equivalent waveguide made of two pairs of perfect electrical conductor (PEC) and perfect magnetic conductor (PMC) boundaries to accommodate the simulated cell. The incident wave is supposed to have normal incidence and is realized via a waveport. As shown in Fig.2.2 (a), the polarization of the incident field (here along x-axis) is normal to the PEC boundaries, and the simulated phase-shifting information can be obtained by collecting the reflection coefficient S11 at the waveport. This method is quite simple and time-saving, but it only works for normal incidence and symmetrical structures.

The second method is Master-Slave Boundary Approach (MSBA). As demonstrated in Fig.2.2 (b), it utilizes two pairs of master and slave boundaries. The E-field on the slave boundary is forced to be matched with the master boundary with a

certain phase difference, thus the periodic structure repetition is obtained. Floquet port is used for the excitation, which allows accounting for different modes, in which the fundamental modes (TE mode or TM mode) will determine the excitation polarization. In conclusion, this method is qualified for complicated problems (e.g. oblique incidence, asymmetrical structure, and higher-order mode analysis), while it is relatively time-consuming.

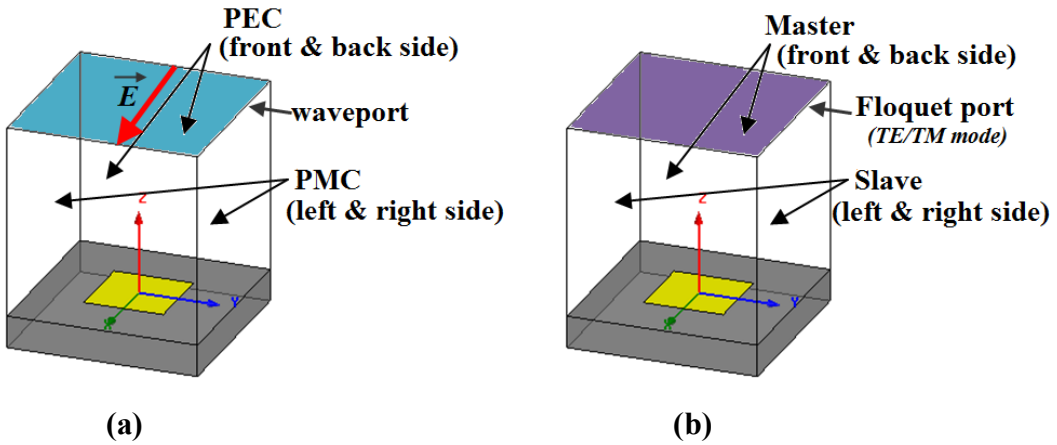

Fig.2.2 Two implementations for infinite periodic simulation in HFSS: (a) Waveguide Approach and (b) Master-Slave Boundary Approach

2.1.3 Preliminary DRA Cell Design at 60GHz

In this section, as a preliminary step, a rectangular DRA working at 60GHz is designed. The Master-Slave Boundary Approach is chosen for the sake of generality. The simulation setting is drawn in Fig.2.3 (a). Based on the general guidelines established in chapter 1, the spacing between the neighboring unit-cells is $\lambda_0/2$ (as λ_0=5mm, the spacing equals 2.5mm). Then, the dimensions of the studied unit-cell are $\lambda_0/2\times\lambda_0/2$. In Fig. 2.3 (b) and (c), the two fundamental modes (mode 1: TE_{00} and mode 2: TM_{00}) are displayed, which correspond to the *y*-axis and *x*-axis polarized wave respectively. In the following simulations, TE_{00} mode is chosen as the excited mode, which stands for a *y*-axis polarized incident wave. It should be mentioned that, contrary to the isolated DRA in Fig.2.2, the investigated DRA here is mounted on a ground plane with only half height (the resonant frequency is not changed).

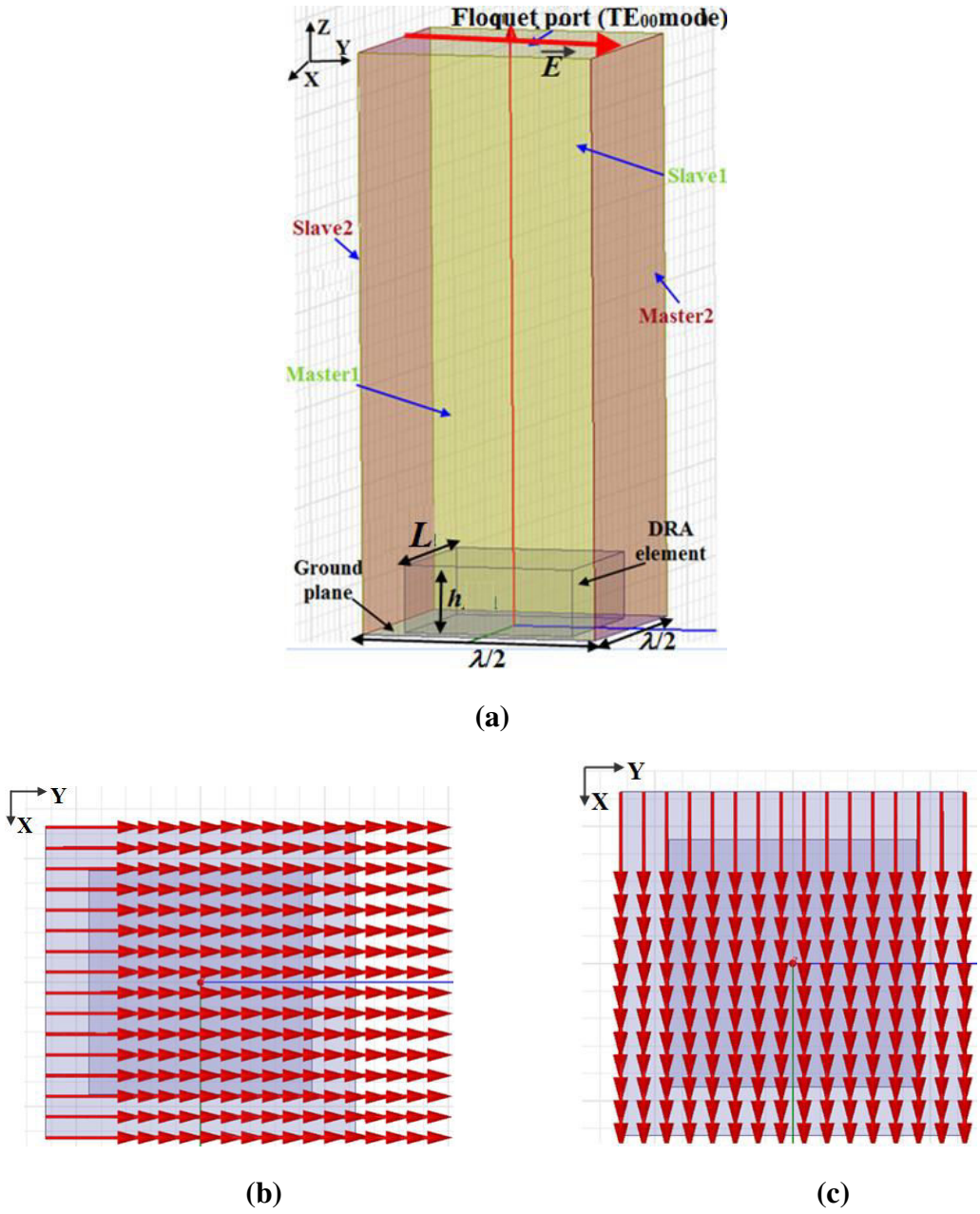

Fig.2.3 (a) simulation setting for the DRA cell, (b) TE_{00} mode and (c) TM_{00} mode (E-field distributions).

The height of the studied DRA is h, the width and length are identical as L. The dielectric material is set as HiK (ε_{DRA}=10 and loss tangent=0.002). L is defined using (2.4) for a theoretical resonance at 60 GHz. When L=1.8mm and h=0.52mm, Fig.2.4 (a) shows the DRA's reflection phase, and Fig.2.4 (b) compares the simulated S11 and S12 (here S11 quantifies the reflection on TE_{00} mode for TE_{00} mode excitation, and S12 quantifies the reflection on TM_{00} mode for TE_{00} mode excitation).

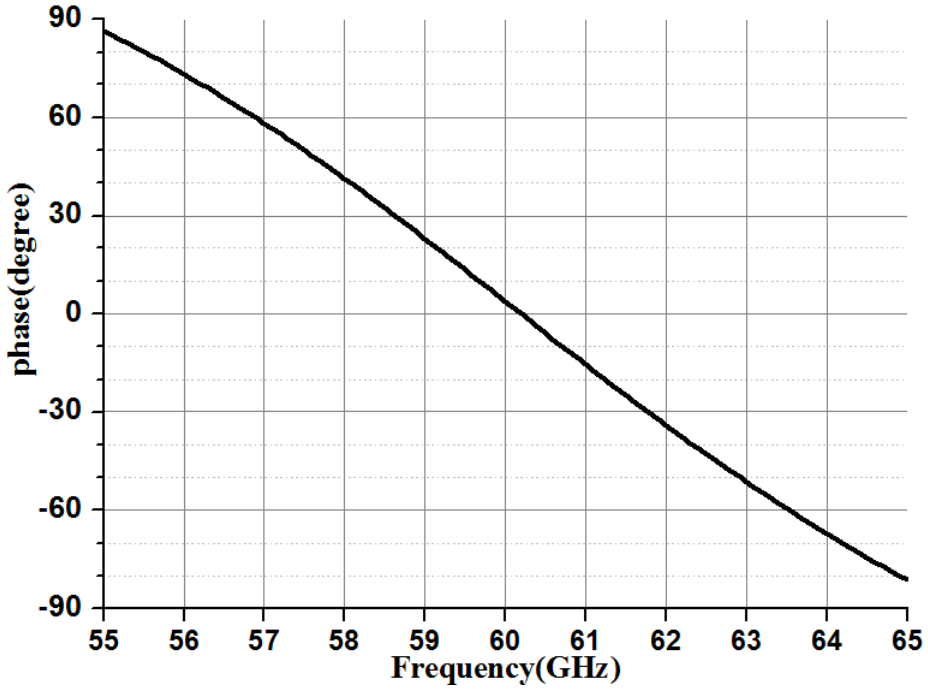

(a)

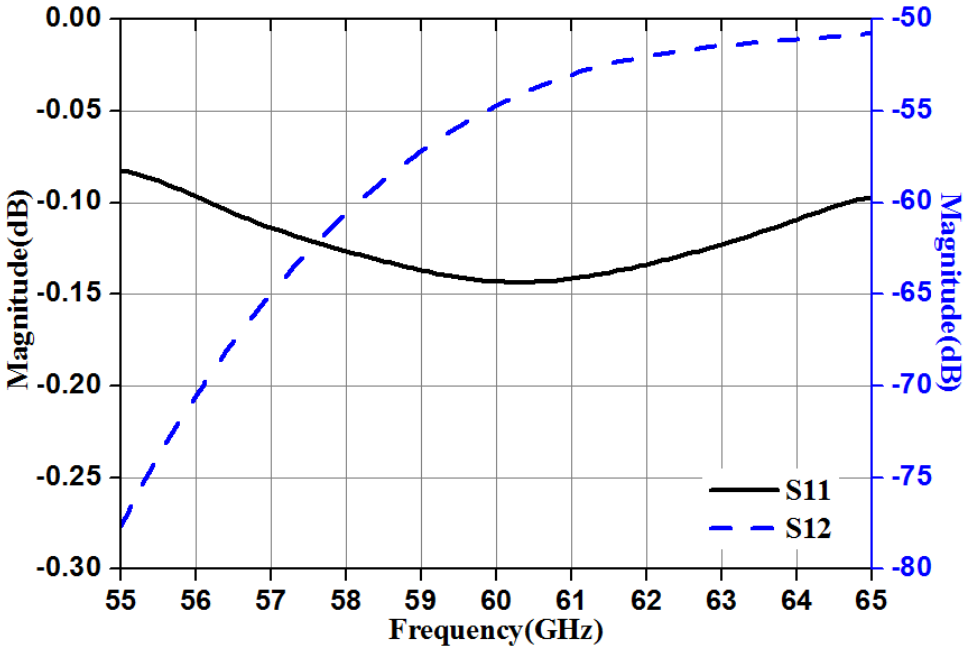

(b)

Fig.2.4 (a) reflection phase and (b) comparison of S11 and S12 (*L*=1.8mm and *h*=0.52mm)

The reflection phase is 0° at 60.1GHz, which corresponds to the resonant frequency for such a shunt-resonant circuit. Note that the minimum value of S11 is also observed for this frequency, which also confirms this statement. The minimum

value is close to -0.15dB due to the low loss in the HiK material. Meanwhile, the S12 in Fig.2.4 (b) is quite low (-55dB at 60GHz and smaller than -50dB for the whole simulation range), showing no polarization conversion is obtained. Note that the non-symmetrical mesh may be responsible for the residual observed cross-polarization. Furthermore, the E-field distribution on the DRA at 60GHz is depicted in Fig.2.5 at ωt=0° and ωt=90°, respectively. The fundamental TE^{x}_{111} mode can clearly been recognized.

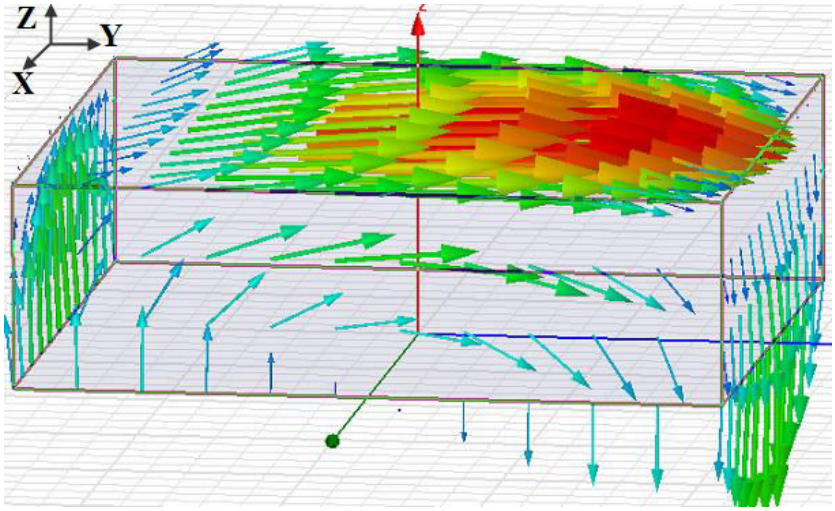

(a)

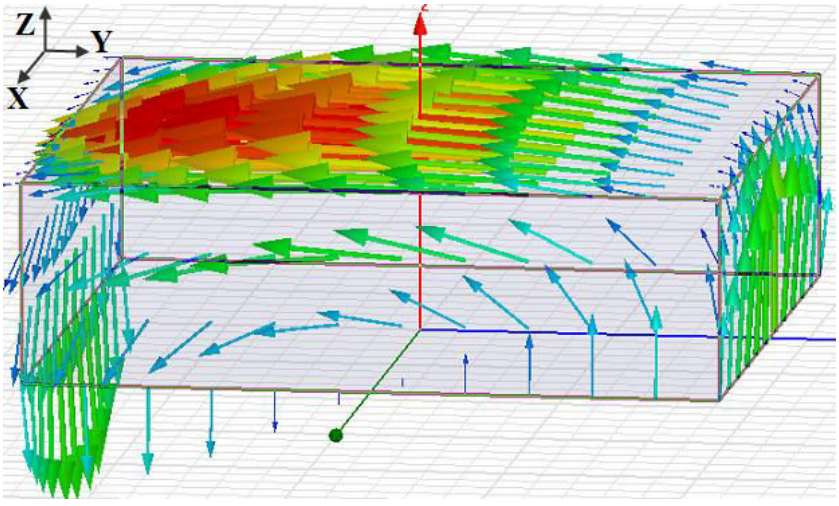

(b)

Fig.2.5 E-field distribution at 60GHz on DRA at (a) 0° and (b) 90°

Now, this preliminary design will be used for further simulations.

2.2 Investigations on DRA Unit-Cells with Variable Size

In chapter 1, different cell topologies for reflectarrays have been discussed. Usually, phase variation is obtained by varying the size of the radiating element. By doing so, the resonant frequency of the element is also modified. In this section, we investigate the potentialities of this simple phase-shifting technique in the case of DRA and for our specific application.

Fig.2.6 shows two consecutive cells made of DRA with variable size. As required for our application, the first one is designed for 0° phase-shift and the second one for 180°. As seen before from Fig. 2.4, the DRA cell with 0° reflection (denoted in solid line) works at resonance, while the other with 180° reflection (denoted in dashed line) is out of resonance. Therefore, the two cells radiates differently.

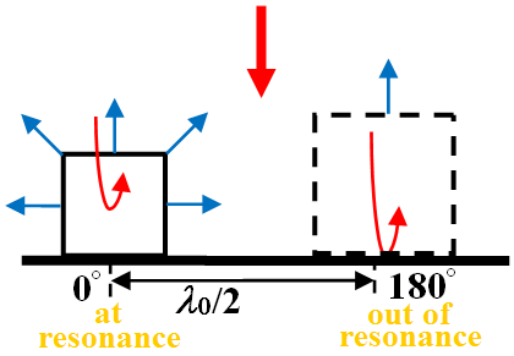

Fig.2.6 Schematic of DRA cells at and out of resonance

The DRA at resonance performs like a magnetic dipole and produces a quite omnidirectional radiation in E-plane; then, a part of the incident power is reflected in the horizontal direction (at endfire and backfire). On the other hand, the one out of resonance is almost transparent to the incident wave and most of the reflected power is controlled by the ground plane itself, resulting in a simple specular reflection at broadside. Clearly, the contributions of the two unit-cells in a given direction are different: for instance, the second cell produces a much higher field at broadside than the first one. We remind that our application requires the cancellation of the overall reflected wave at broadside. Definitively, this can only be achieved if the contribution of consecutive out-of-phase cells is well balanced there. As discussed above, this is not the case in the described configuration.

For a better illustration of this issue, a quite canonical simulation is raised as below. We analyze a 6×1 array (Fig.2.7a) composed of 6 DRAs at the spacing of $\lambda_0/2$.

The array is excited by an *x*-polarized incident wave under normal incidence.

At first, all DRAs have identical dimensions (h=0.52mm and L=1.8mm from Fig.2.4), which means they are resonant at 60GHz and produce a 0° reflection phase. The corresponding pattern (black solid curve in Fig.2.8) is that of a uniform array with maximum at broadside and decreasing side lobes when moving towards $\pm 90^{\circ}$. For the next step, the height h_2 of half the DRAs (named as DRA2 in Fig.2.7) is gradually reduced. When h_2 is 0, DRA2 are actually suppressed and the structure reduces to a 3×1 array, as shown in Fig. 2.7 (b). The corresponding directivity patterns in E-plane (E_{θ}) for several different h_2 are included in Fig.2.8.

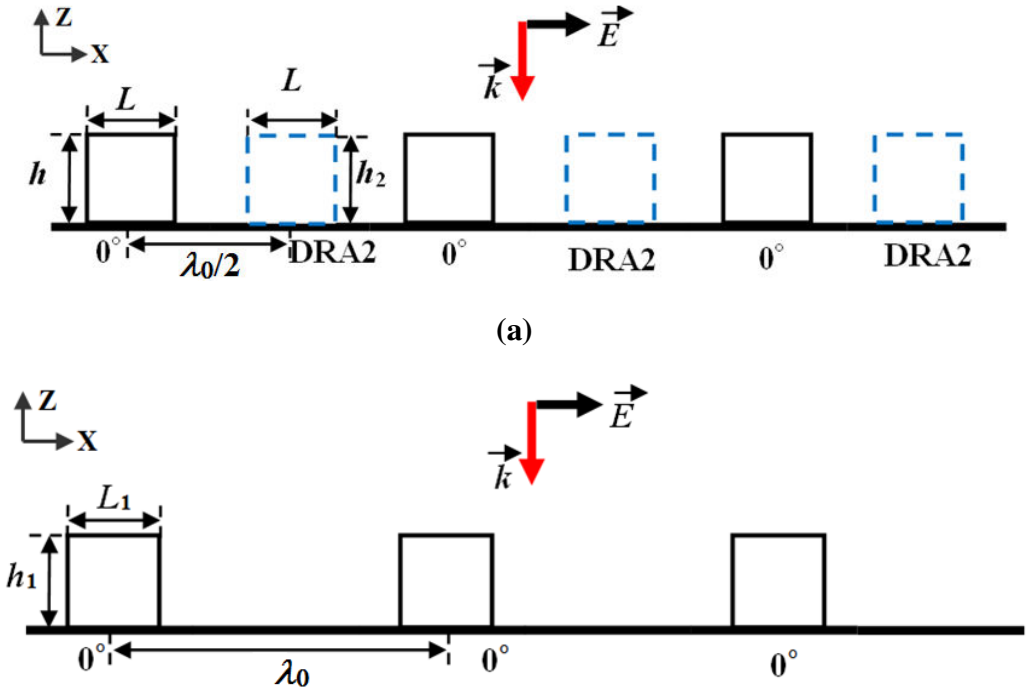

Fig.2.7 Schematic of two arrays: (a) 6×1 array of DRAs and (b) 3×1 array of DRAs

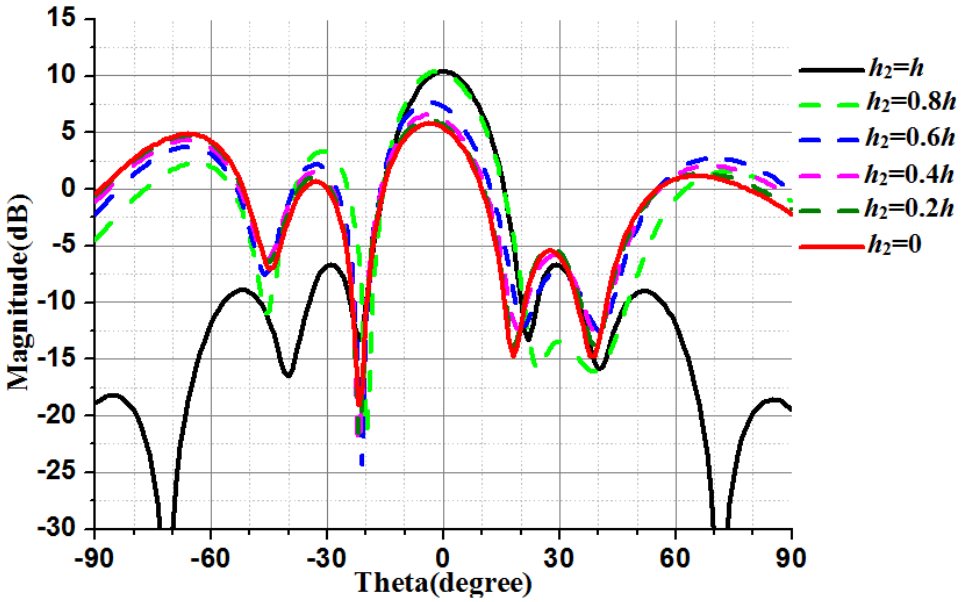

Fig.2.8 Directivity patterns comparison in E-plane (E_θ) for the 6×1 versus h_2

It appears that all arrays with reduced h_2 almost radiate similarly to the 3×1 array (red solid curve in Fig.2.8). This means DRA with reduced height become "transparent" and do not contribute anymore to the overall radiation. Then, only the reflection from the ground plane takes place in the corresponding cells. This is consistent with the fact these DRA are not resonant anymore and thus do not intercept any incident power.

It should be highlighted that when h_2 approaches 0, the reflected phase from DRA2 converges to 180° (this is the phase produced by the ground plane alone). Then, if the design process only considered the value of the reflected phase under normal incidence, the 3×1 array would be the optimal solution for our application! It is definitively not. It is interesting anyhow to analyze a bit further the radiation of this array. Clearly, the radiation close to ±90° has been raised significantly. A classical explanation for array designers would be the apparition of grating lobes as the inter-element spacing is now λ. Another (equivalent) interpretation may be given that better fits our problem: this array (with non-identical cells successively providing 0° and 180° reflected phases) succeeds in raising the field level close to endfire because the radiations from the 3 DRAs sum up there. However, it does not succeed in providing field cancellation at broadside because the contribution from 0° cells (the 3 DRAs) does not balance the out-of-phase contribution from the 180° cells (the ones with only ground).

This problem is quite general. However, it is prominent in our application

because we want to control the radiation for two directions simultaneously (cancellation at broadside and constructive combination at endfire). One could object that the configuration we considered is an extreme case (the 0° DRA is at resonance and the 180° DRA is not resonating at all). A better choice might be to have both DRAs' reflected phases shifted symmetrically apart 0° (for instance one DRA producing -90° phase-shift and the second one 90°). However, although this would certainly produce the required constructive combination of reflected fields at endfire, this would not improve the situation at broadside. Indeed, in that case, as none of the DRA is resonant, the contribution of the ground plane in the overall reflection would be quite high and the specular reflection at broadside would be even worse.

Finally, we can conclude that the use of DRA with different sizes (i.e. different resonant frequencies) is not suitable for our application. Then, in the following, we will concentrate on phase-shifting techniques that do not modify the geometry of the resonant element itself, and the consecutive DRAs have to be identical to maximize the desired endfire radiation and properly cancel broadside reflection.

2.3 Array Design based on Notched DRA Cell

In this section, we propose a DRA unit-cell capable of providing out-of-phase reflection while preserving the same size for consecutive elements. It consists of a square DRA with notches on two diagonally-opposite corners. By properly adjusting the notches sizes, an *x*-polarized incident wave can be converted into a *y*-polarized reflected wave (and the reverse). Then, we will show how the association of two such DRA cells with notches on opposite diagonals can produce out-of-phase fields.

2.3.1 Analysis of Notched DRA

The implementation of notched DRA was reported for improved bandwidth in [97], since a partial removal of the DRA decreases its radiation factor Q. Here, we will focus on the capability of this structure to provide polarization conversion. Fig.2.9 depicts the top view of a square DRA cell with square notches on opposite corners.

By adjusting the notch size (which corresponds to length *a* in Fig.2.9), a *y*-polarized incident wave can be converted into an *x*-polarized reflected wave (as explained in Fig.2.3). Consequently, the *y*-polarized reflected wave can be reduced significantly. A quite similar conception was reported for a 1-bit digital phase shifter

in [104-105].

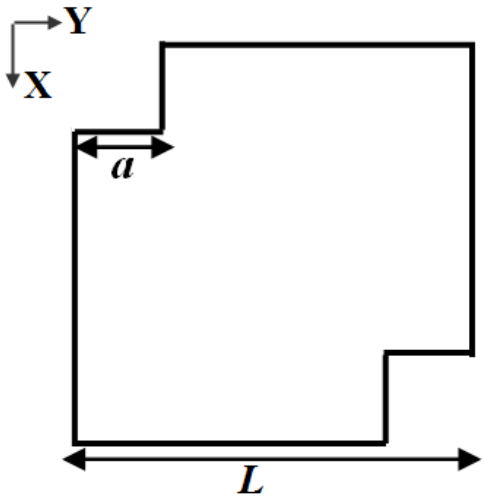

Fig.2.9 Diagonal-notched DRA cell

Before studying polarization conversion, we must be aware of the frequency-shift brought by the introduction of the notches. As seen in previous sections, the designed DRA made of HiK (L=1.8mm and h=0.52mm) works at 60GHz. However, the introduction of notches affects its resonant frequency. Fig.2.10 shows S11 versus a.

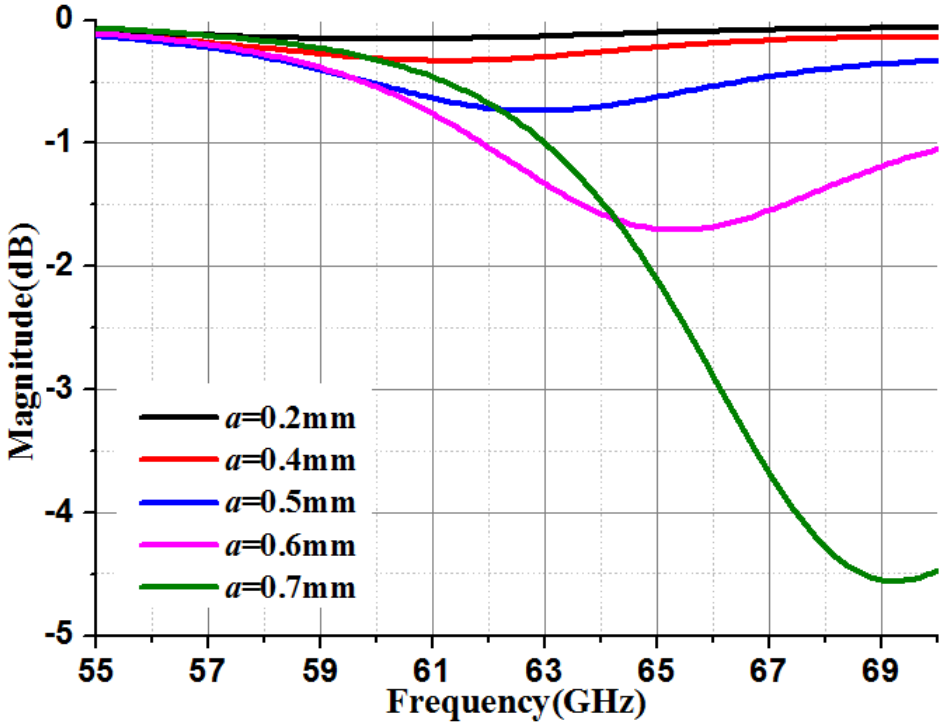

Fig.2.10 S11 of the notched DRA cell when L=1.8mm, h=0.52mm and a varies in [0.2, 0.7] mm

Table 2.1 Three DRAs resonating around 55GHz

		Dimensions (mm)		f_0 (GHz)
		L	*h*	
DRA	**1**	1.5	0.73	54.8
	2	1.8	0.61	54.8
	3	2	0.57	55

When *a* increases, the resonant frequency is shifted upward (we remind that the resonant frequency corresponds to the minimum of the magnitude – we will see later that here, this minimum is related to polar conversion). Therefore, the initial dimensions for the basic DRA cell from last section cannot be directly used, and we have to update the design for a lower initial resonant frequency, thus leaving enough margin for the increase brought by the notches.

Considering the typical frequency shift in Fig.2.10 is 5GHz (f_0=65GHz when *a*=0.6mm), a 5GHz margin is used. Then, by adjusting *L* and *h*, three DRAs with different dimensions are obtained in Table 2.1, with a resonant frequency f_0 around 55GHz. The corresponding S11 for the three DRAs are depicted in Fig.2.11.

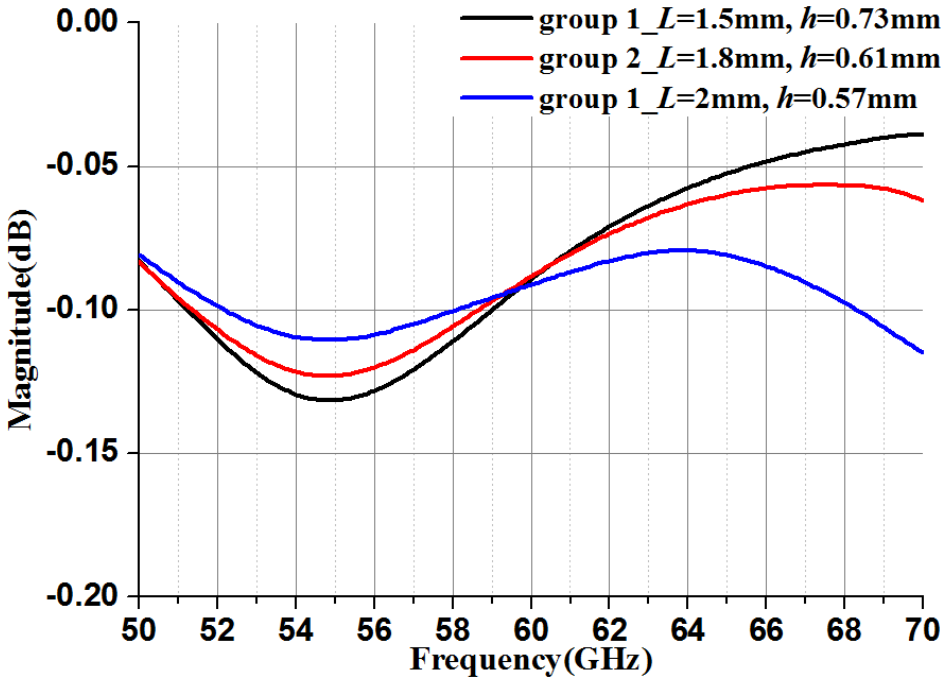

Fig.2.11 S11 for three DRAs resonating around 55GHz

Then, notches with size *a* are introduced in these DRAs. Fig.2.12-14 present the

scattering parameters for the notched DRA versus *a,* for the 3 considered configurations. We remind that the excited mode (TE_{00}) is *y*-polarized, S11 and S12 measure the *y*- and *x*-polarized reflected waves, respectively.

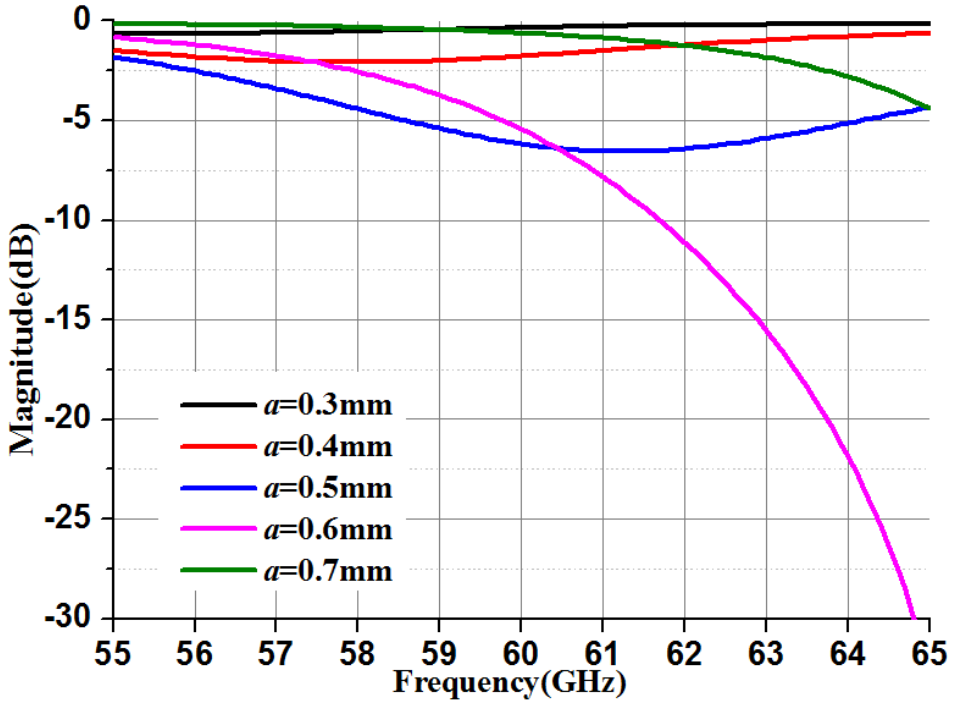

(a)

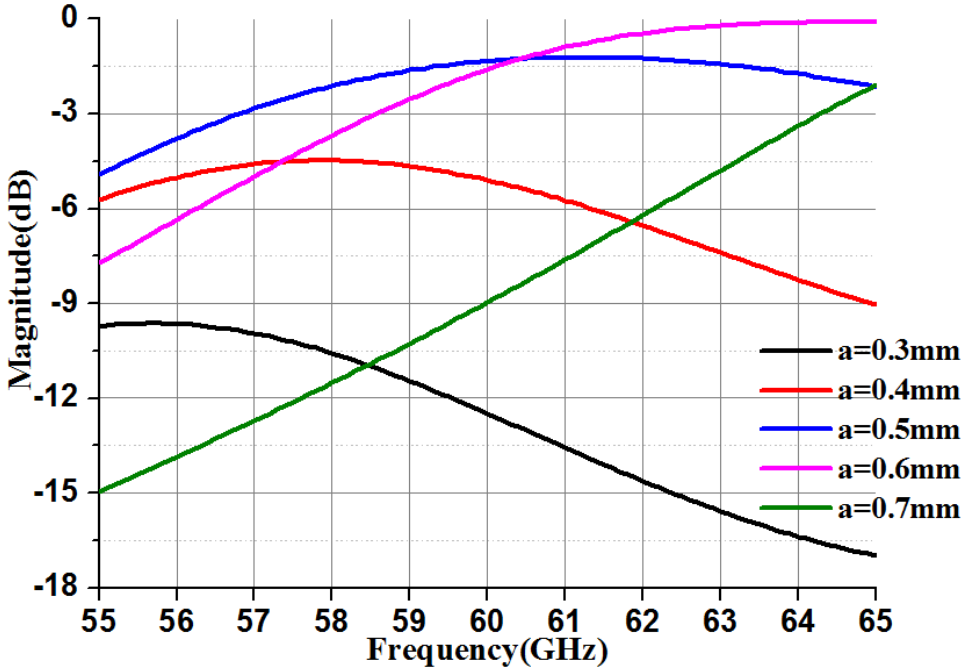

(b)

Fig.2.12 When *a* varies in [0.3, 0.7] mm, (a) S11 and (b) S21 of notched DRA 1 (*L*=1.5mm, *h*=0.73mm)

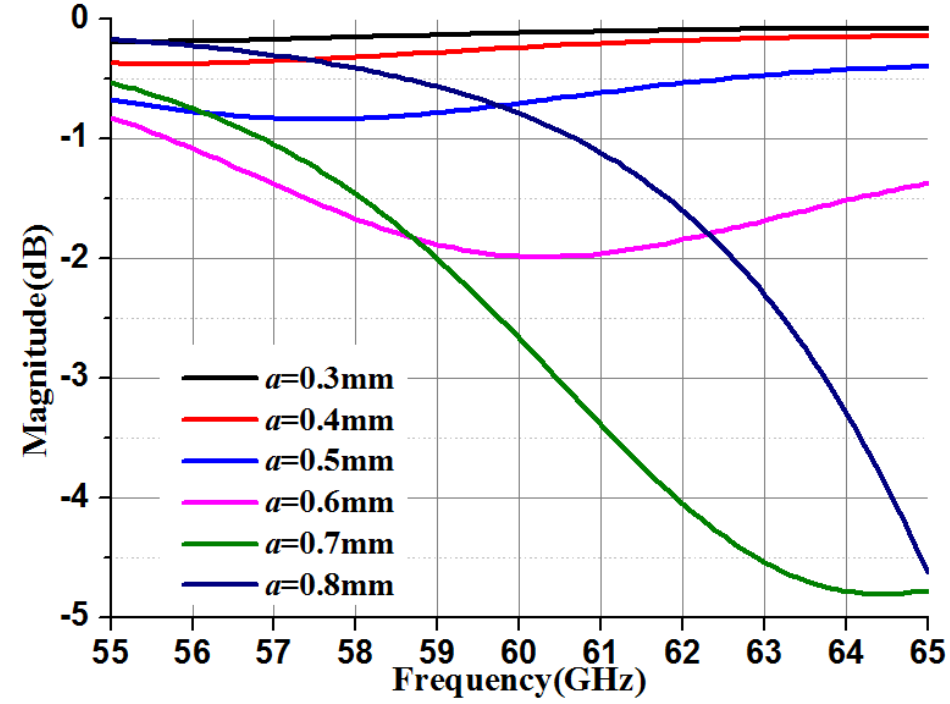

(a)

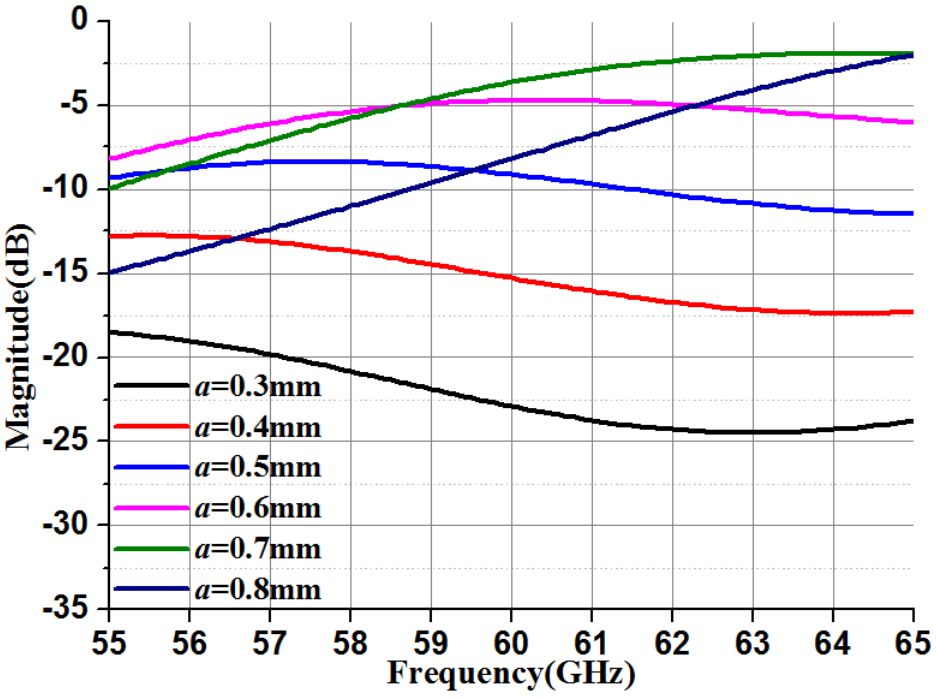

(b)

Fig.2.13 When *a* varies in [0.3, 0.8] mm, (a) S11 and (b) S21 of notched DRA 2 (*L*=1.8mm, *h*=0.61mm)

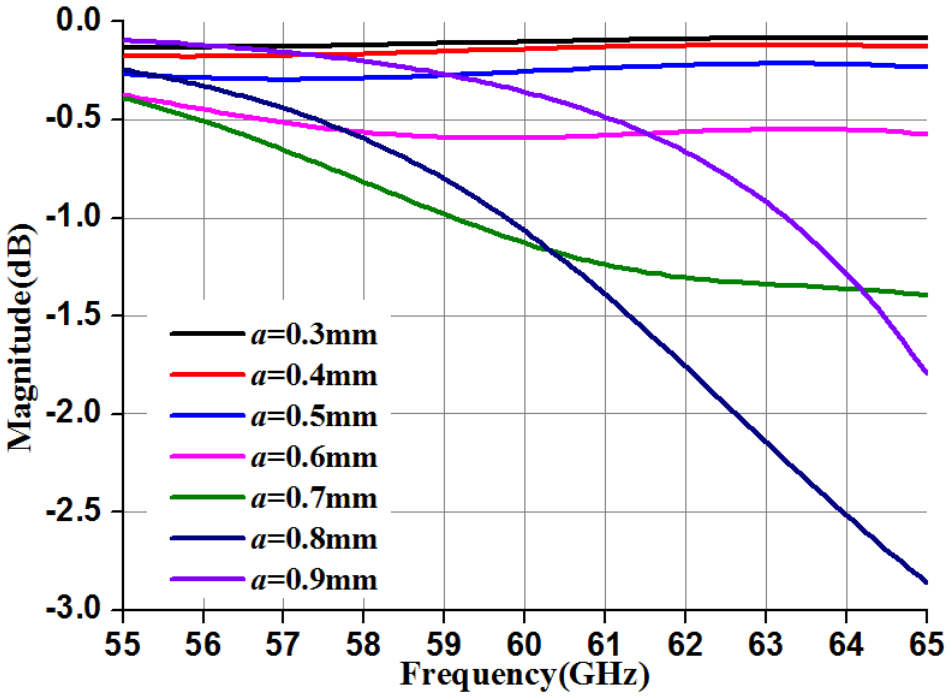

(a)

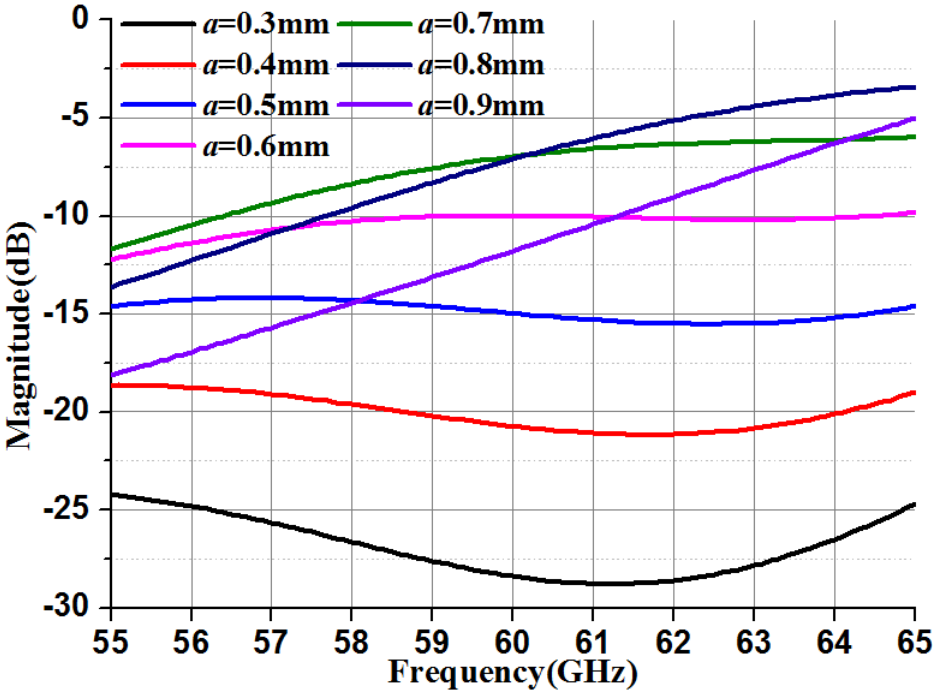

(b)

Fig.2.14 When *a* varies between [0.3, 0.9] mm, (a) S11 and (b) S21 of notched DRA 3 (*L*=2mm, *h*=0.57mm)

Clearly, as the square notch size increases, the desired polarization conversion is improved. For example, in Fig.2.12, when *a*=0.5mm, S11 is -6.2dB and S21 is -1.3dB at 60GHz. This indicates that 86% of the incident power is converted to TM_{00} mode.

For comparison, DRA 2 and 3 produce weaker S21 at 60GHz, whatever *a*. Therefore, DRA 1 is selected for further investigations.

Fig.2.15 presents more details about the scattering parameters of the best notched DRA (*L*=1.5mm, *h*=10.73mm and *a*=0.5mm), including magnitude (Fig.2.15 (a)) and phase (Fig.2.15 (b)). Actually, we can notice the configuration achieves resonance at 61GHz instead of 60GHz, but this is not a problem since there will be further optimization.

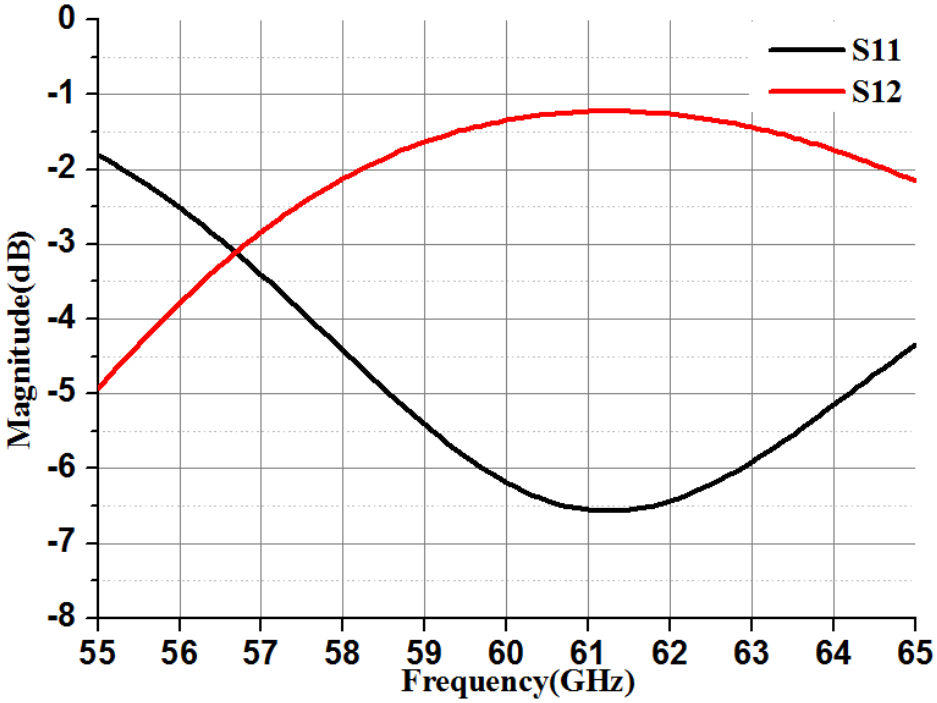

(a)

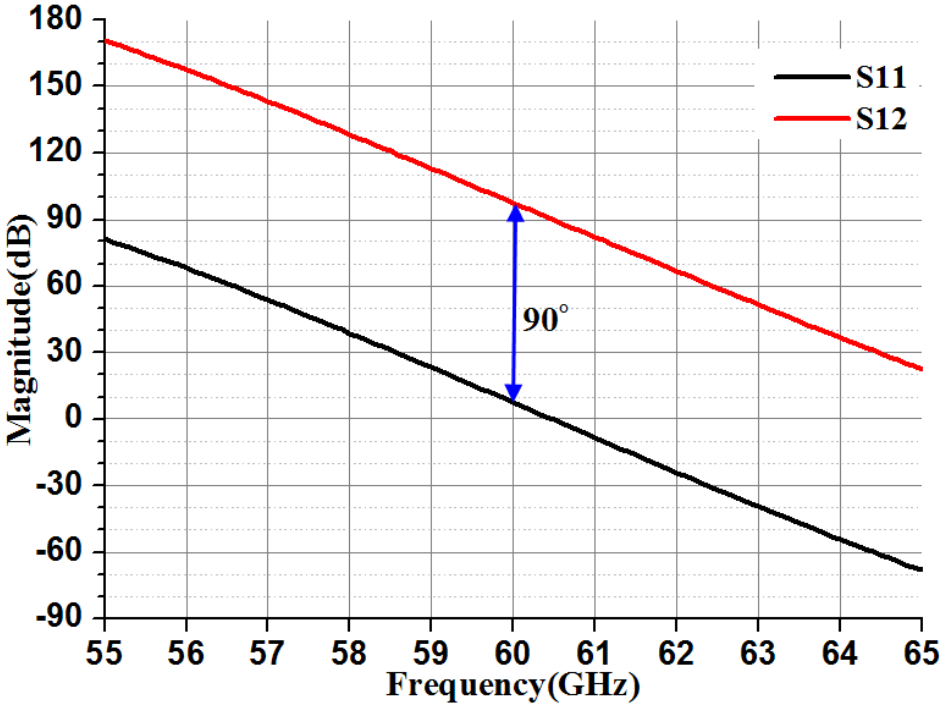

(b)

Fig.2.15 Scattering parameters of the best notched DRA (*L*= 1.5mm, *h*=0.73mm and *a*=0.5mm): (a) magnitude and (b) phase

If we compare the scattering parameters of the notched DRA (in Fig.2.15 (a)) with the basic DRA cell (in Fig.2.4 (b)), we can clearly observe polar-conversion thanks to the introduction of notches. We can also note that S11 and S21 exhibit a 90° phase-difference in the whole simulation frequency range, as shown in Fig.2.15 (b). This is classical for the S-parameters of a lossless 2-port (we have almost a lossless circuit here). This does not mean however that the reflected wave is circularly polarized as the magnitudes are different (except at *f*=56.6GHz).

In this section, preliminary investigations on the diagonally-notched DRA cell have been carried out. With the properly chosen parameter *a*, good polarization conversion was achieved as expected. For the next step, two DRA cells with opposite notches will be combined into a 2×1 unit to achieve out-of-phase reflection.

2.3.2 Analysis of Two Consecutive DRAs

2.3.2.1 Design of a 2×1 DRA Unit

Based on the notched DRA from previous section (*L*=1.5mm, *h*=0.73mm and *a*=0.5mm), two DRAs with notches on opposite diagonals are now studied as a 2×1

unit-cell. As depicted in Fig.2.16, the two elements are placed along x-axis, with spacing $d=\lambda_0/2=2.5$mm and the excitation mode is still TE_{00} (y-polarized).

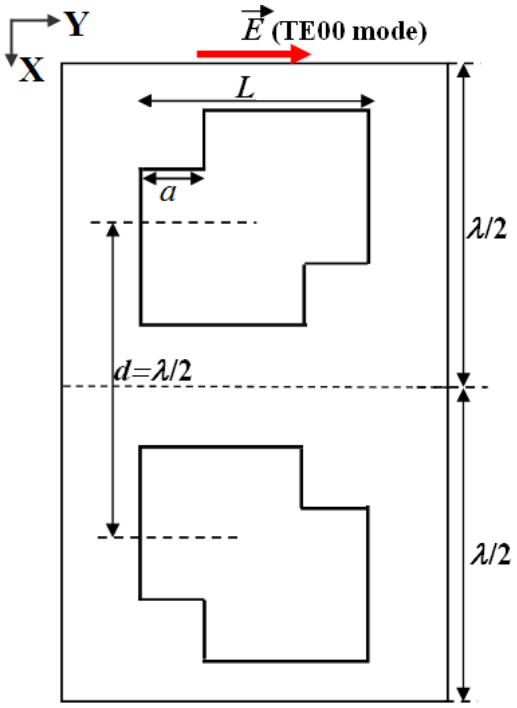

Fig.2.16 Schematic of 2×1 unit with oppositely-notched DRA cells

For this structure, we expect opposite reflected E-fields with x-polarization on the consecutive DRAs. In the simulation, such a field configuration will be associated to a higher-order Floquet mode. The snapshots of several higher-order modes are given in Fig.2.17. For comparison, the two fundamental modes (TE_{00} and TM_{00}) are also included.

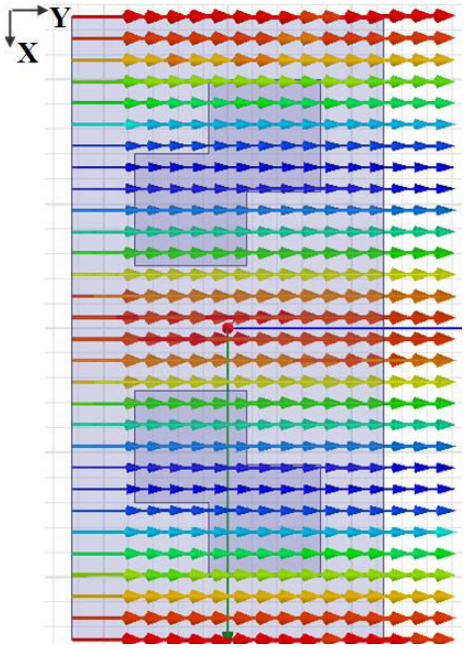

(a)

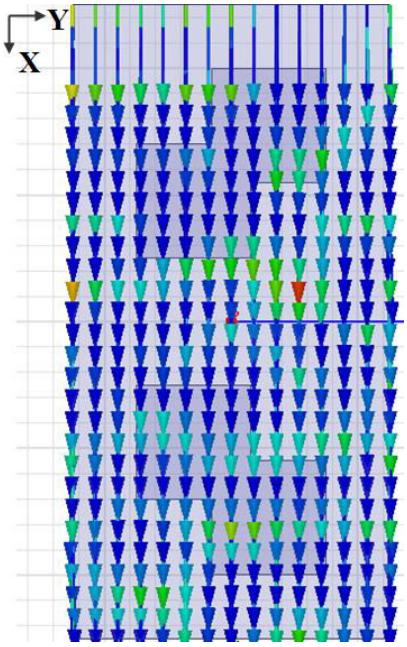

(b)

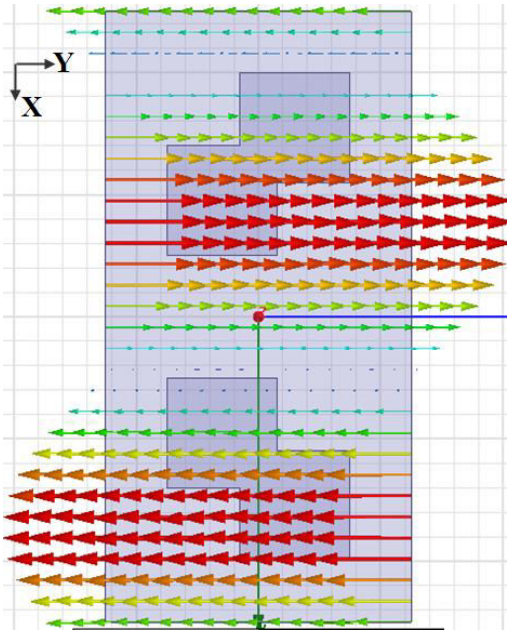

(c)

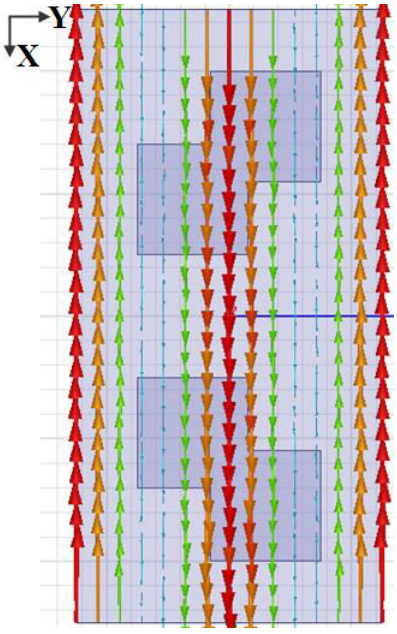

(d)

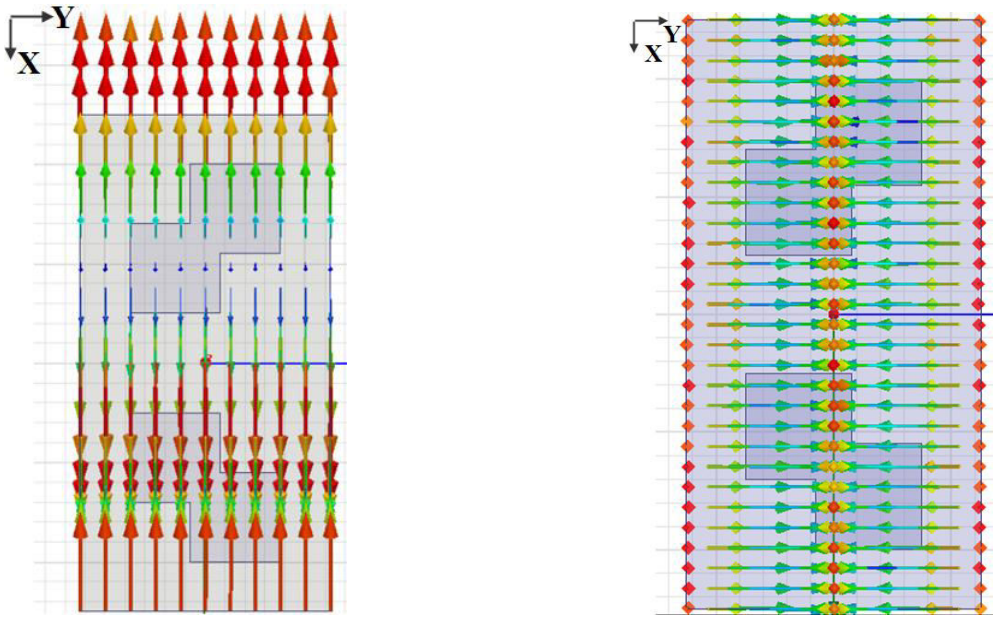

(e) **(f)**

Fig.2.17 E-field distribution in the 2×1 unit for several modes: (a) TE_{00}, (b) TM_{00}, (c) TE_{10}, (d) TE_{01}, (e) TM_{10} and (f) TM_{01}

From this inspection, it appears that only the TM_{10} mode is appropriate to describe the expected E-field distribution, with both *x*-polarization and direction-reversal along *x*-axis. Therefore, for the following simulations, a special attention will be paid to the amount of power reflected on the TM_{10} mode. It is supposed to be representative of polarization conversion. Note that the fact we now have to take higher-order modes into account is consistent with the increase of the size of the studied structure (from $\lambda/2\times\lambda/2$ to $\lambda\times\lambda/2$). The scattering parameters are presented in Fig.2.18.

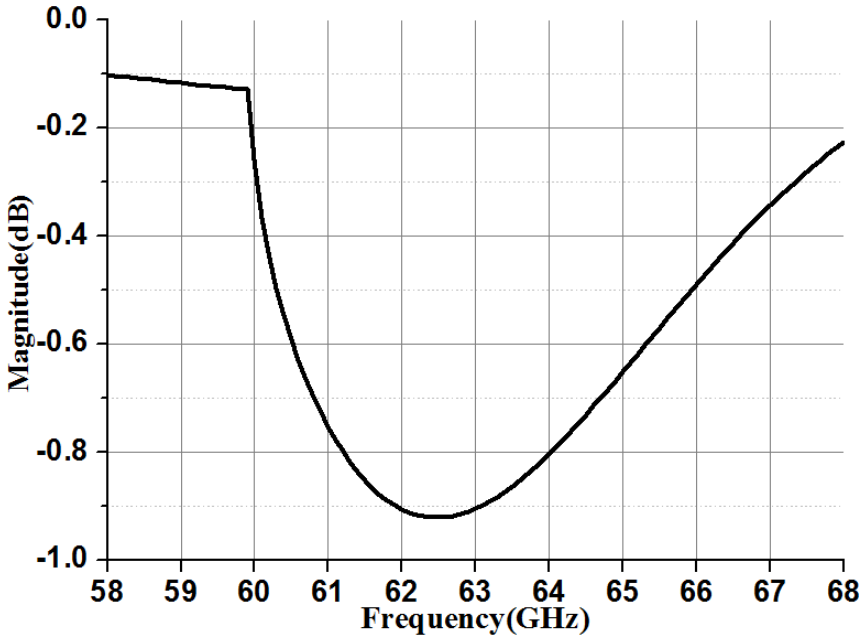

(a)

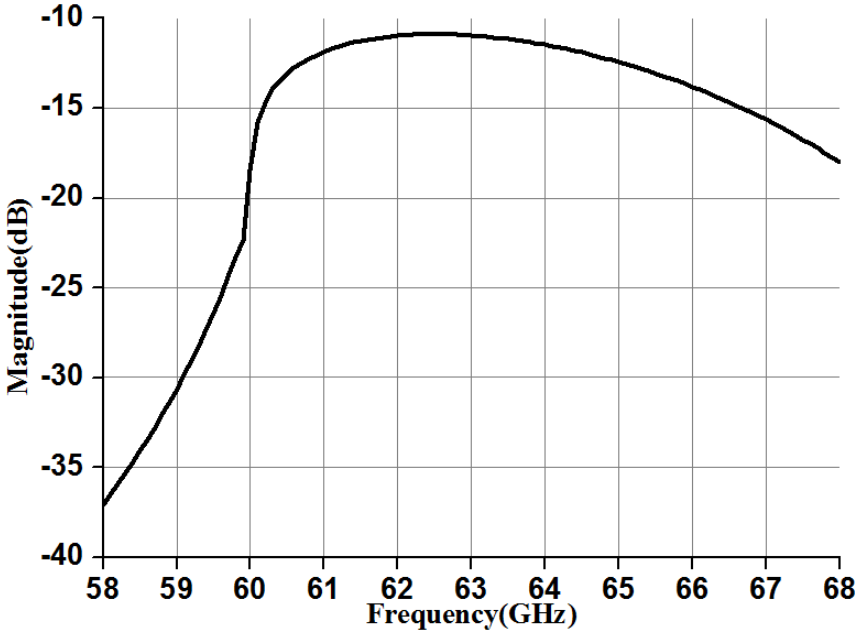

(b)

Fig.2.18 When *L*=1.5mm, *h*=0.73mm and *a*=0.5mm, (a) S11 and (b) S15 for the 2×1 unit

S11 still quantifies the reflection on TE_{00} mode for TE_{00} mode excitation, and S15 quantifies the reflection on TM_{10} mode for TE_{00} mode excitation. It should be explained at first, the discontinuous points appear in S11 and S15 around 60GHz, because it corresponds to the TM_{10} mode's cut-off frequency in this 2×1 unit.

Based on Fig.2.18, two conclusions can be made:

1). The resonant frequency is now f_0=62.5GHz, which means it shifted again (about 1.5GHz increase), due to the combination of the two DRAs together.

2). At 62.5GHz, we have S11=-0.9dB and S15=-11.1dB. This means, 90% of the incident wave in TE_{00} mode is directly reflected back on the same mode. In other words, the expected polarization conversion from TE_{00} mode to TM_{10} mode is weak (it is even worse at 60 GHz).

Table 2.2 Full-modes reflection parameters at 62.5GHz (Unit: dB)

	TE_{00}	**TM_{00}**	**TE_{10}**	**TM_{10}**	**TE_{01}**	**TM_{01}**
reflection parameter (TE_{00} excitation)	-0.9 **(S11)**	-61	-53.6	-11.1 **(S15)**	-93	-69.9

In order to get a complete view of the excited high-order modes, the full-mode reflection parameters at f=62.5GHz are given in Table 2.2. It is clear that only the TM_{10} contributes significantly to the reflection (in addition to the excited TE_{00} mode). This is consistent with the analysis of the mode configuration proposed in Fig.2.17. In the following, we will then only focus on the TE_{00} (S11) and TM_{10} (S15) reflections.

Furthermore, the E-field distribution at 62.5GHz is given in Fig.2.19.

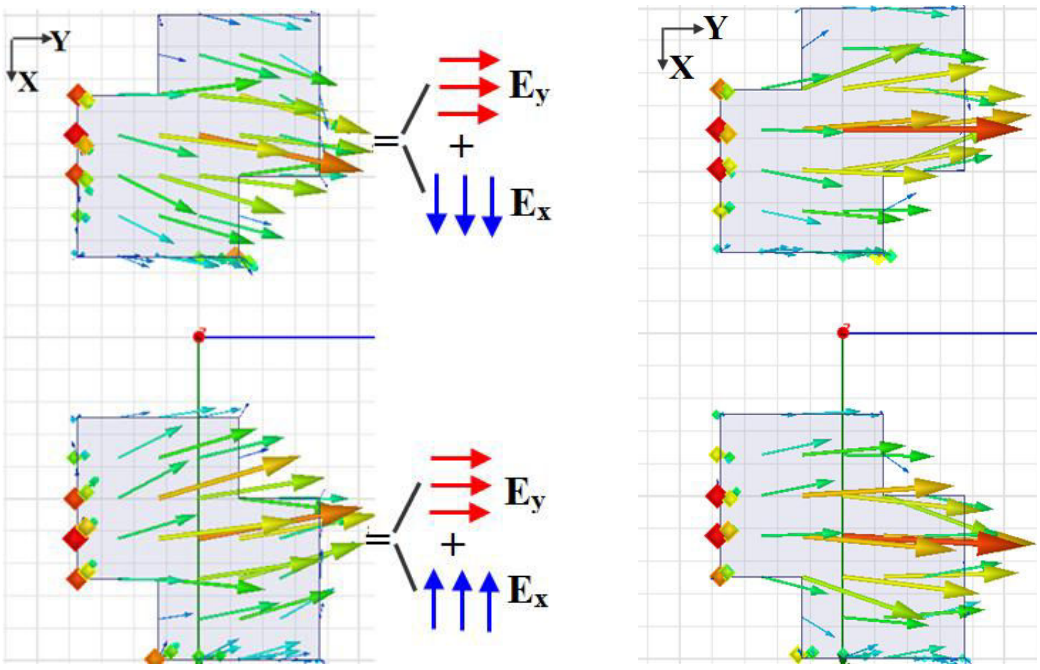

(a) **(b)**

Fig.2.19 When L=1.5mm, h=0.73mm and a=0.5mm, E-field distribution in 2×1 unit at 62.5GHz for (a) ωt=0° and (b) ωt =90°

The two snapshots presented in Fig.2.19 are the total E-field, which includes the incident and reflected electrical fields together. As Fig.2.19 (a) depicts, the overall E-field is divided into E_x component along x-axis, and E_y component along y-axis. The E_y component comes from two sources: the incident wave, and the residual (undesired) reflection on TE_{00}. The E_x components on the two successive DRA elements, which are out-of-phase, represent the (desired) reflected TM_{10} mode. Clearly, in the overall E-field in Fig.2.19, E_y is prominent and E_x seems weak. This is highly consistent with the obtained S11 and S15. Based on this conclusion, optimization for this 2×1 unit will be carried out, trying to reach a high S15 and a low S11 at 60GHz.

2.3.2.2 Optimization of 2×1 DRA Unit

The structure from last section (L=1.5mm, h=0.73mm and a=0.5mm) fails to achieve a strong polarization conversion at 60GHz. So optimizations of the notched DRA in the 2×1 unit have to be carried out. This optimization is necessary because the environment of DRA in the 2×1 configuration does not match the one that was used to determine the dimensions of the notches.

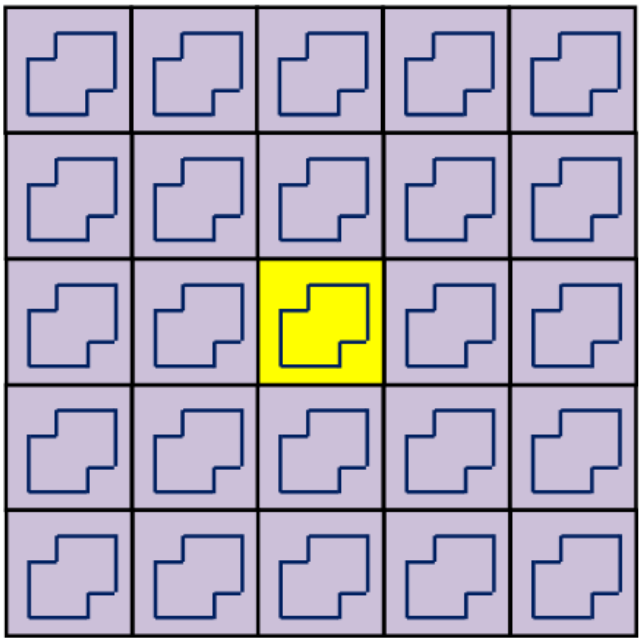

(a)

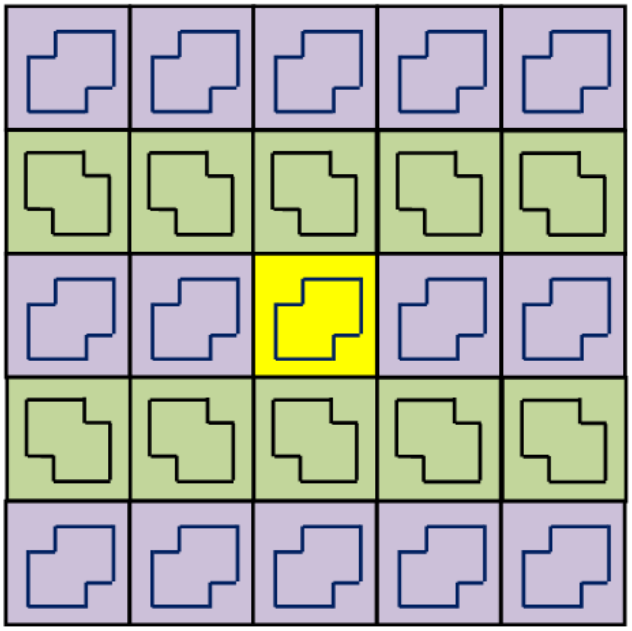

(b)

Fig.2.20 Importance of optimization due to the changed local periodicity when simulated for (a) single cell and (b) two types of cells combined together

Indeed, the design of the initial notched DRA has been carried out using the infinite periodic simulation method. This means a single cell extracted from an infinite periodic array with identical elements has been simulated (as Fig.2.20 (a) depicts). However, when it comes to the 2×1 array, two types of DRAs are combined together, which makes the environment quite different (as shown in Fig.2.20 (b)). Therefore, in order to better approximate the actual mutual coupling between consecutive elements, the parameter *a* has to be re-optimized considering this actual environment.

Firstly, simulations varying *a* in the range [0.4, 0.7] mm are achieved and the corresponding scattering parameters are shown in Fig.2.21.

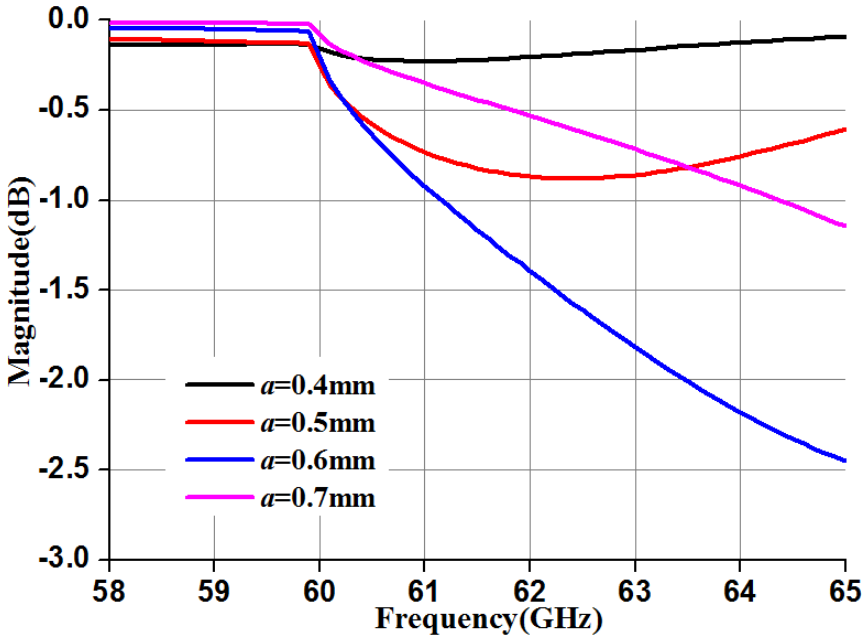

(a)

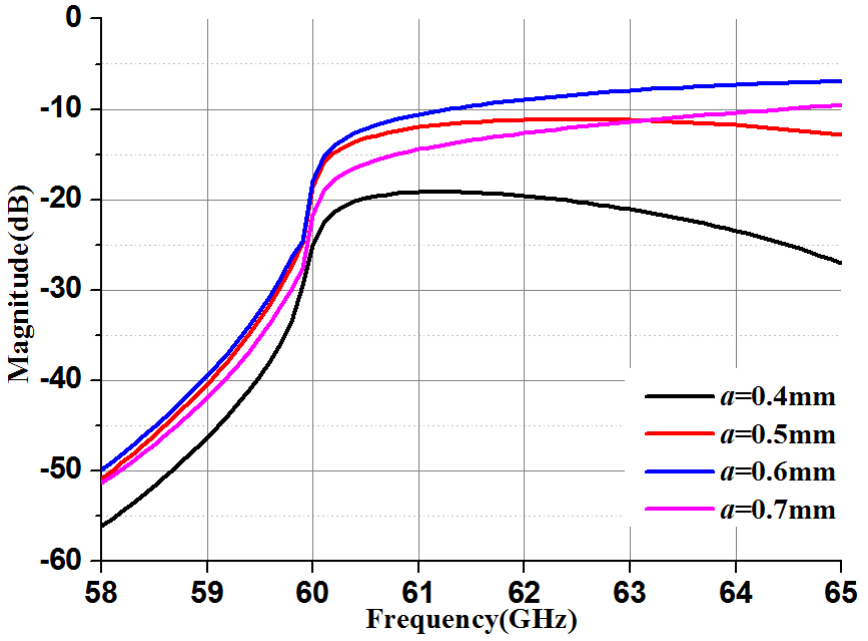

(b)

Fig.2.21 When *L*=1.5mm and *h*=0.73m, *a* changes in [0.4, 0.7] mm in the 2×1 unit, scattering parameters of (a) S11 and (b) S15

When *a* increases, S11 is reduced and S15 gets improved. However, the resonant frequency is increased at the same time, shifting away from 60GHz. In conclusion, Fig.2.21 demonstrates the same tendency as for the single notched DRA. Therefore, the simple variation of *a* is not sufficient and the optimization will now turn to *L* and

h.

Here *h* is chosen first, because it is simpler (if we vary *L*, we have to consider different *a*/*L* ratios). When *L*=1.5mm and *a*=0.5mm, *h* is varied in [0.73, 1.4] mm, and the obtained S11 and S15 are recorded in Fig.2.22.

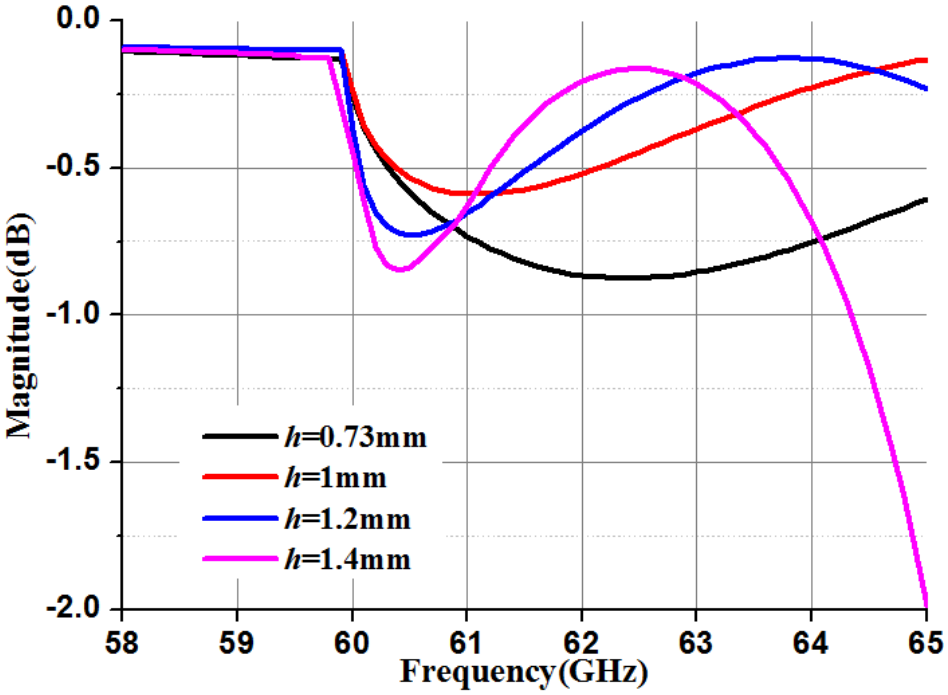

(a)

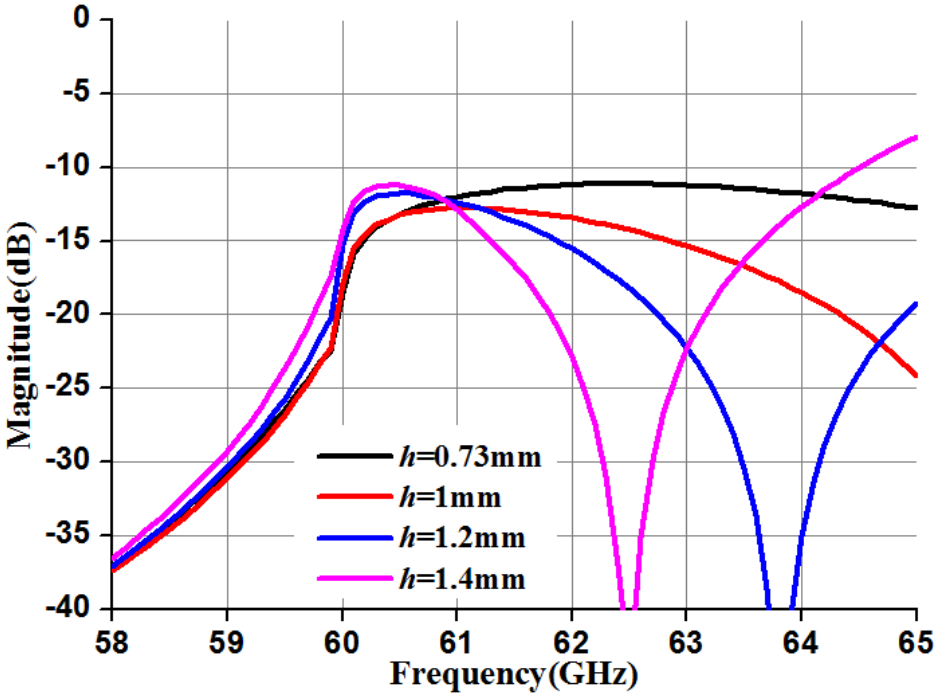

(b)

Fig.2.22 When *h* changes between [0.73, 1.4] mm, scattering parameters of (a) S11 and (b) S15

It should be noted that the optimization range stops at h=1.4mm because the simulation does not converge anymore, which may be caused by the complicated modes distribution at the critical points. Anyway, based on current results, the obtained mode conversion is still quite low for S15 (<-10dB). This means we cannot obtain satisfactory results when a=0.5mm. So for the next step, the size a has to be increased to 0.6 mm, aiming for stronger mode conversion.

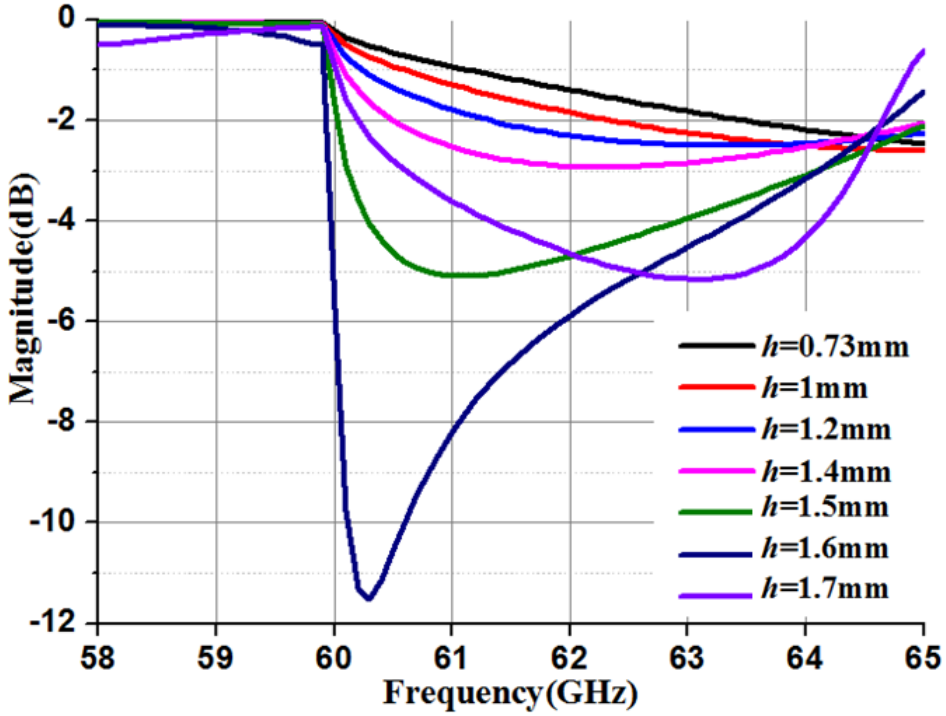

(a)

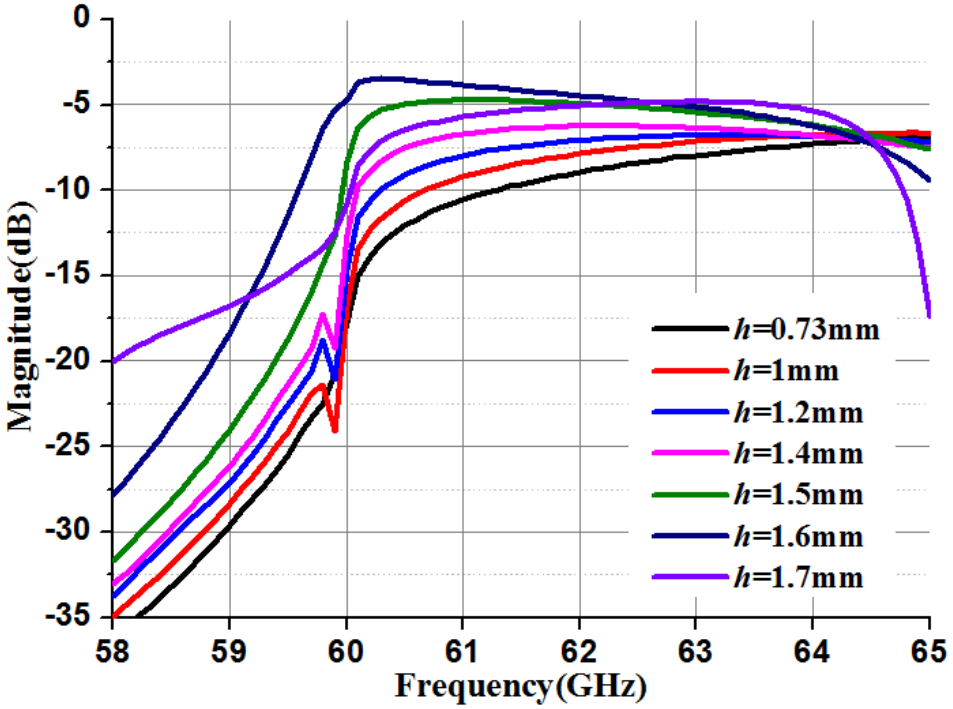

(b)

Fig.2.23 When *h* changes between [0.73, 1.7] mm, *L*=1.5mm and *a*=0.6mm, scattering parameters of (a) S11 and (b) S15

Fig.2.23 presents S11 and S15 when *h* changes in the [0.73, 1.7] mm range. When *L*=1.5mm, *a*=0.6mm and *h*=1.6mm, S11 is -11.5dB and S15 is -3.5dB at f_0=60.3GHz (at 60GHz, S11=-5.8dB and S15=-4.7dB). This result witnesses a significant improvement from the initial geometry (*h*=0.73mm, *L*=1.5mm and *a*=0.5mm), but the results at 60GHz are not as good as for the single notched DRA in last section (S21 close to -1dB). Actually, based on Floquet theorem, the cut-off frequency for TM_{10} mode in this 2×1 unit is at 60GHz (the cut-off phenomenon can clearly be seen in all figures), which means it can only propagate when *f*>60GHz theoretically. So at the critical point *f*=60GHz, it is not easy to realize a high S15. Meanwhile, the involvement of other high-order modes makes the cell's radiation tricky and the simulation itself is greatly time-consuming or even non-convergent.

Nevertheless, E-field distributions for the 2×1 unit when *L*=1.5mm, *a*=0.6mm and *h*=1.6mm are depicted in Fig.2.24 at *f*=60.3GHz and 60GHz.

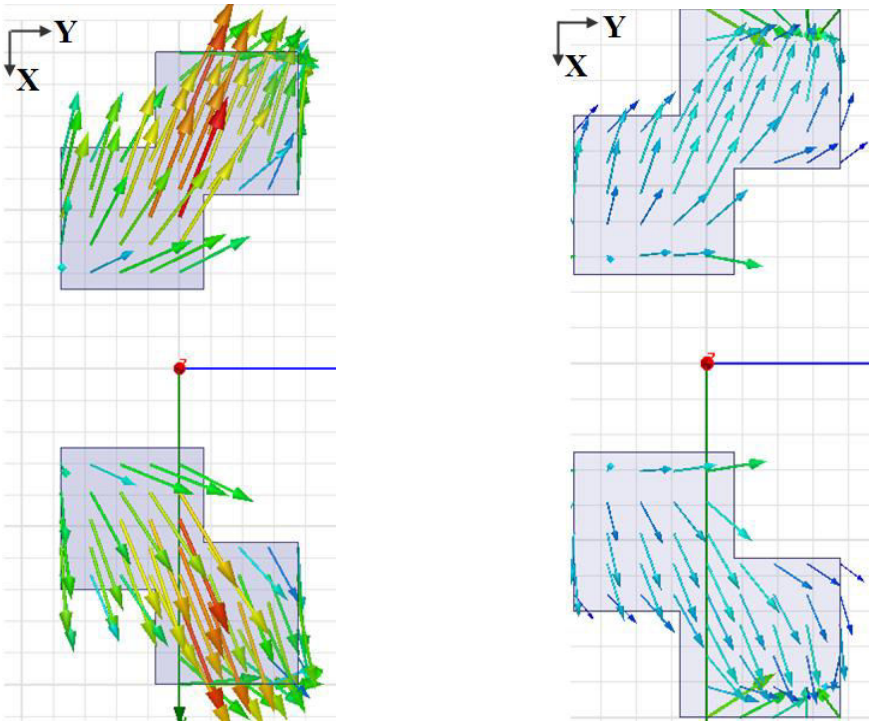

(a) (b)

Fig.2.24 When *L*=1.5mm, *h*=1.6mm and *a*=0.6mm, E-field distributions at (a) *f*=60.3GHz and (b) *f*=60GHz

The E_y component in Fig.2.24 is obviously weakened, compared with the initial situation in Fig.2.19. Meanwhile, the E-field is now dominated by the Ex component, which shows desired opposite distributions on the two notched DRAs. Then for the next step, a 6×1 array and a 6×6 array will be simulated based on this 2×1 unit, and their endfire radiation will be assessed.

2.3.3 Validations at Array Level

2.3.3.1 Implementation and Optimization of a 6×1 Array

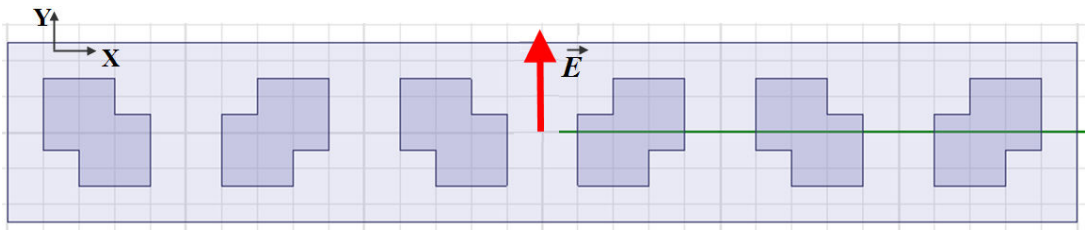

Fig.2.25 Simulation settings for 6×1 array

In this section, the 2×1 unit from last section is expanded to a 6×1 finite array.

Investigations are taken on the array's endfire radiation, and additional optimization is implemented.

As shown in Fig.2.25, the array is expanded along *x*-axis, while the excitation is still *y*-polarized. The 6×1 array involves DRAs whose dimensions derive from previous optimization (L=1.5mm, h=1.6mm and a=0.6mm). Note that the array is now finite, and the ground plane is 15mm×2.5mm. The array is illuminated by a plane wave under normal incidence (neither Floquet ports nor modes are considered anymore). The directivity patterns in E-plane (XOZ plane) are given in Fig.2.26.

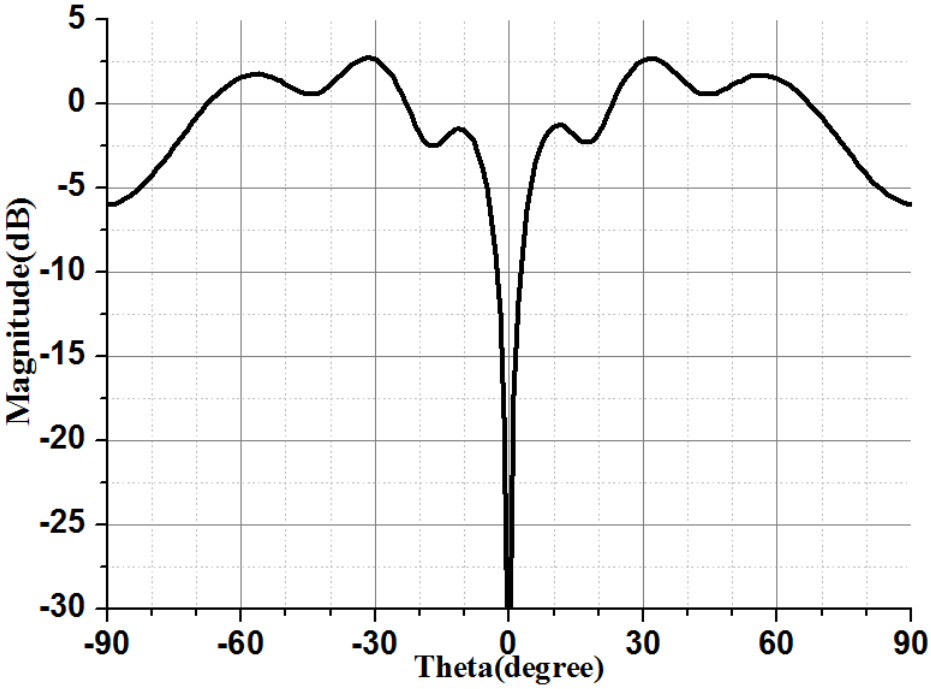

(a)

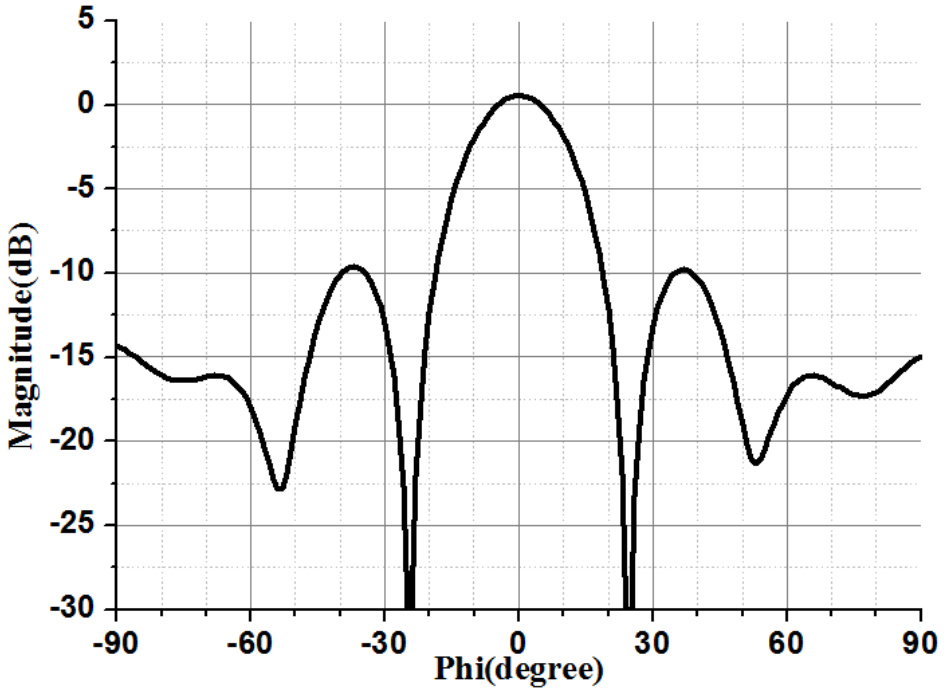

(b)

Fig.2.26 When *L*=1.5mm, *h*=1.6mm and *a*=0.6mm, directivity for the 6×1 array in (a) E-plane (E_θ) and (b) E-plane (E_φ)

Considering the excitation polarization, the E_θ component (Fig.2.26 (a)) stands for the desired *x*-polarized reflected wave while the E_φ component (Fig.2.26 (b)) corresponds to the parasitic residual *y*-polarized reflected wave.

A few observations can be made:

1).The maximum of the E_θ does not occur at endfire (-6dB at $\theta=\pm90^\circ$) but at $\theta=\pm32^\circ$ (2.7dB), with a high second lobe lying at $\theta=\pm60^\circ$. The main beam shift may be due to ground plane finiteness. It is also influenced by the elementary pattern of the notched DRA. This second issue will be addressed in detail in chapter 4 for the case of the metallic groove array and won't be discussed here.

2). The E_φ component does not cancel at broadside ($\theta=0^\circ$); it is 0.6dB, which is 6.6dB bigger than endfire radiation.

Globally, although polar conversion can be observed and the E_θ component is directed off broadside, the obtained performance is quite poor. So we need to further optimize the notch size by adjusting *a* independently for each of the six DRA, to better address the problem of array finiteness.

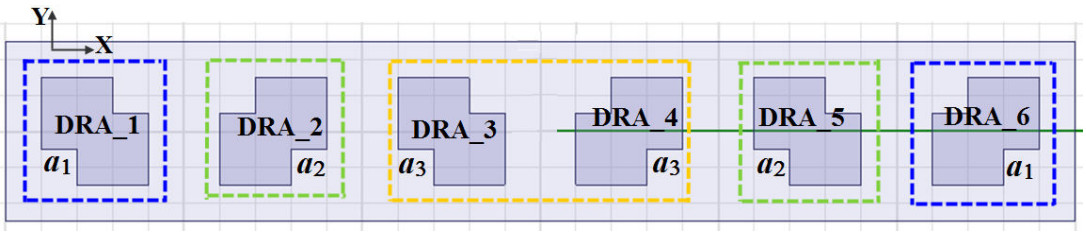

Fig.2.27 Optimizations of a_1, a_2 and a_3 for the 6×1 array

As shown in Fig.2.27, the six DRAs are named from DRA_1 to DRA_6. Considering the symmetry in the array, two DRAs in symmetrical positions (marked in the same color) share the same notch size and only 3 notch sizes (a_1, a_2 and a_3) have to be tuned. In order to get clear comparison, we defined one parameter Ψ to measure the amount of reflection at broadside relatively to the amount of reflection at endfire. It is given as:

$$\Psi = \frac{\left|E_\theta\left(\text{endfire}\right)\right|}{\left|E_\varphi\left(\text{broadside}\right)\right|} = \frac{\left|E_\theta\left(\varphi=0,\theta=\pm 90^\circ\right)\right|}{\left|E_\varphi\left(\varphi=\theta=0\right)\right|} \tag{2-5}$$

Logically, as the minimum broadside radiation and maximum endfire radiation is our target, the biggest Ψ is the final goal.

The optimization is divided into three steps. We start with a_3: when a_1 =a_2=0.6mm, a_3 is adjusted in the range of [0.5, 0.7] mm to localize the optimal Ψ; after a_3 is fixed, a_1 is still kept as 0.6mm and the procedure is repeated for a_2. Finally, a_1 is optimized. The results of Ψ at each step are presented in Fig.2.28, together with the optimal a (remarked in yellow lines).

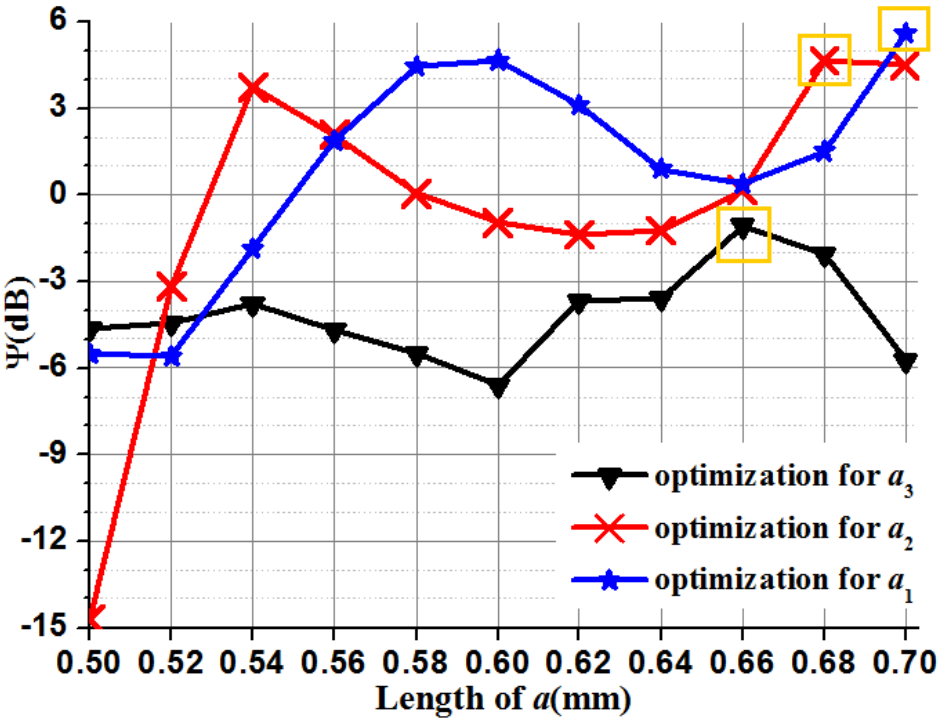

Fig.2.28 Parameter Ψ for the optimizations of a_1, a_2 and a_3 at 60GHz

Finally, a_1=0.7mm, a_2=0.68mm and a_3=0.66mm, and the optimized Ψ 5.6dB. Compared with the initial geometry, it witnesses a 12.2dB improvement. In Fig.2.29, the corresponding directivity patterns in E-plane (E_θ and E_φ) are given and compared with those of the initial structure (when a_1=a_2=a_3=0.6mm).

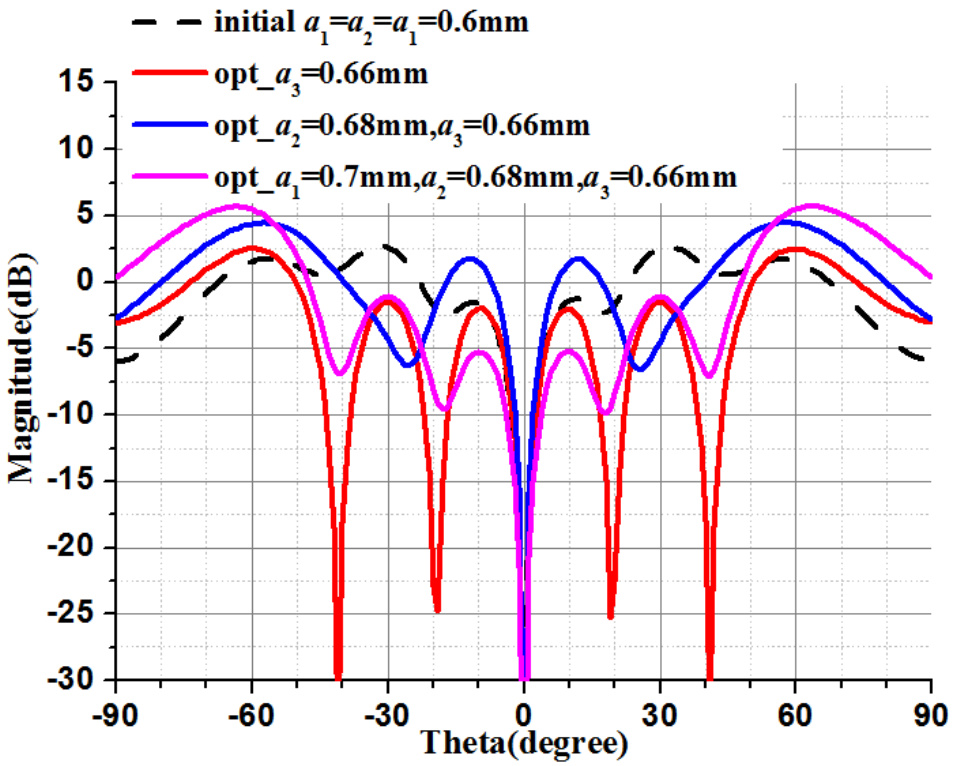

(a)

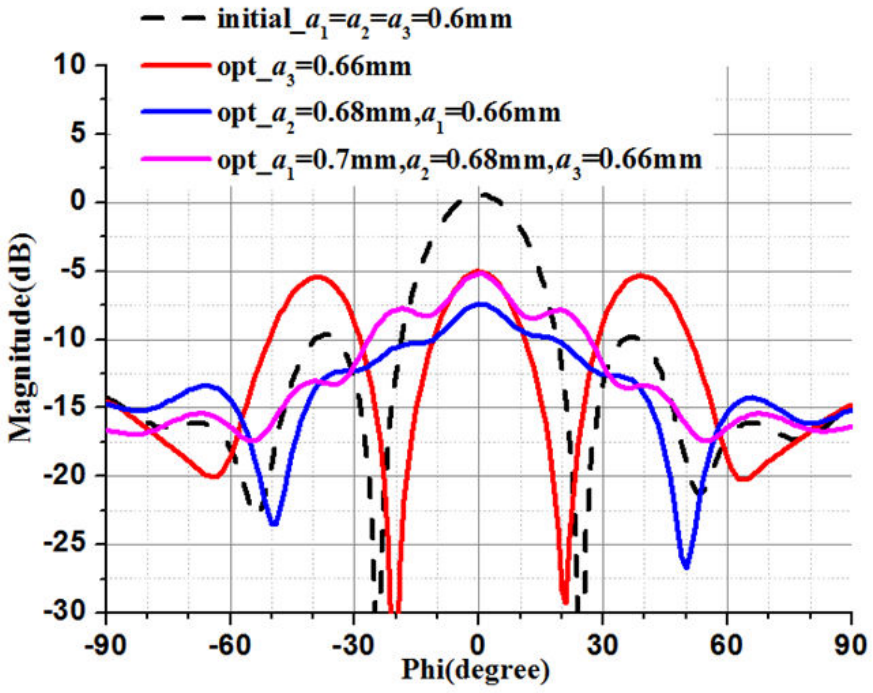

(b)

Fig.2.29 Directivity patterns comparisons of (a) E-plane (E_θ) and (b) E-plane (E_φ) to show the optimization procedure of a_1, a_2 and a_3

The main beam of the optimized structure (pink line) is shifted steadily to

θ=±65°. The polar conversion is significantly increased and, consequently, both the reflection cancellation at broadside and the power enhancement close to endfire are improved.

The E-field distribution at 60GHz is shown in Fig.2.30.

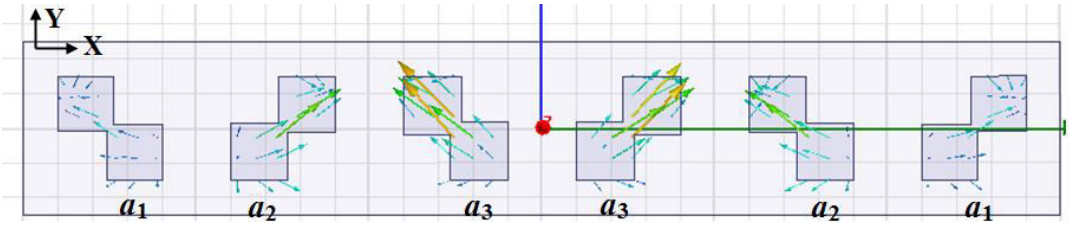

Fig.2.30 Top view of the E-field distribution when a_1=0.7mm, a_2=0.68mm and a_3=0.66mm

The E-field distribution in Fig.2.30 is total electrical field and the observed E_y component is mainly attributed to the incident field. Meanwhile, the E_x components on consecutive DRAs are out-of-phase, this confirms the polarization has been twisted. We can observe the magnitude of the field is not uniform on all DRAs. This is unavoidable due to the very small size of the array and subsequently the difference in mutual coupling for each DRA.

2.3.3.2 Validation in 6×6 Array

Finally, a 6×6 array is studied. The array is obtained by repeating the 6×1 array along *y*-axis, as shown in Fig.2.31. All the simulation settings are kept the same. Note that a larger array would not be easilly simulated with the available computer (Processor: Intel Xeon E5645 CPU, RAM: 48G). For the simulation of such structures (6×6 DRA arrays) , the total CPU is less than 1 hour, which is still compatible with some optimization steps, as has been done here.

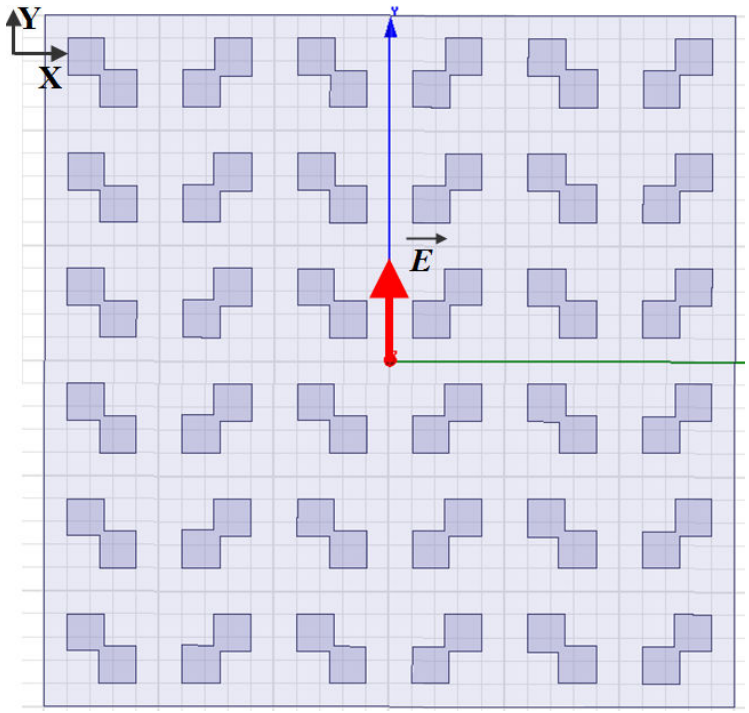

Fig.2.31 Simulation settings for 6×6 array

At the end of the optimization (the optimization is carried out as previously and assumes all rows in the array are identical), we obtain a_1=0.7mm, a_2=0.68mm and a_3=0.7mm with Ψ=7dB. The corresponding directivity patterns in E-plane (E_θ and E_φ) are given in Fig.2.32.

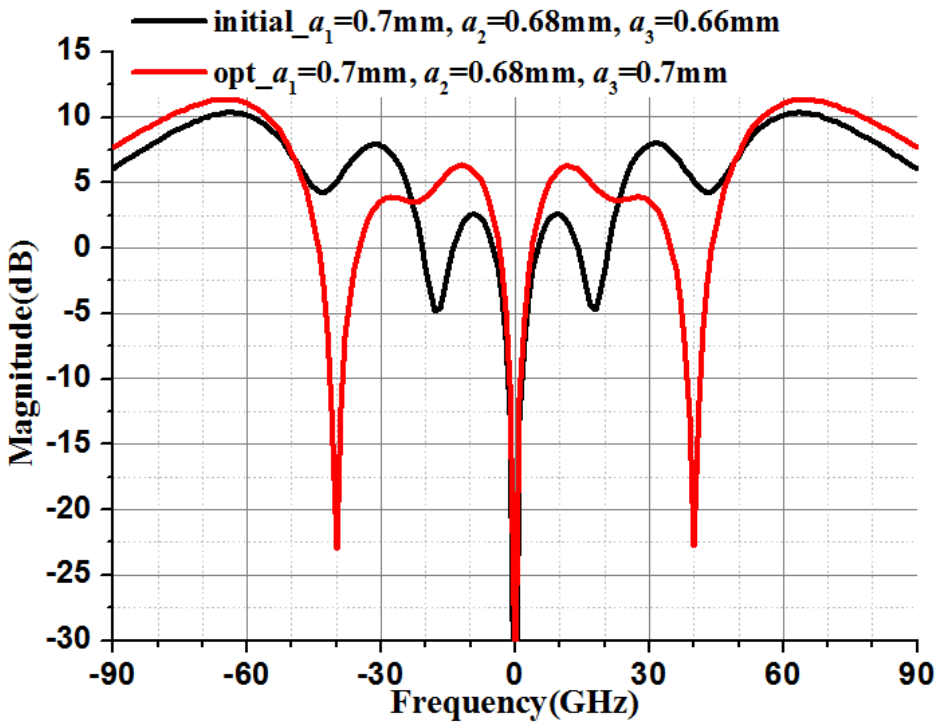

(a)

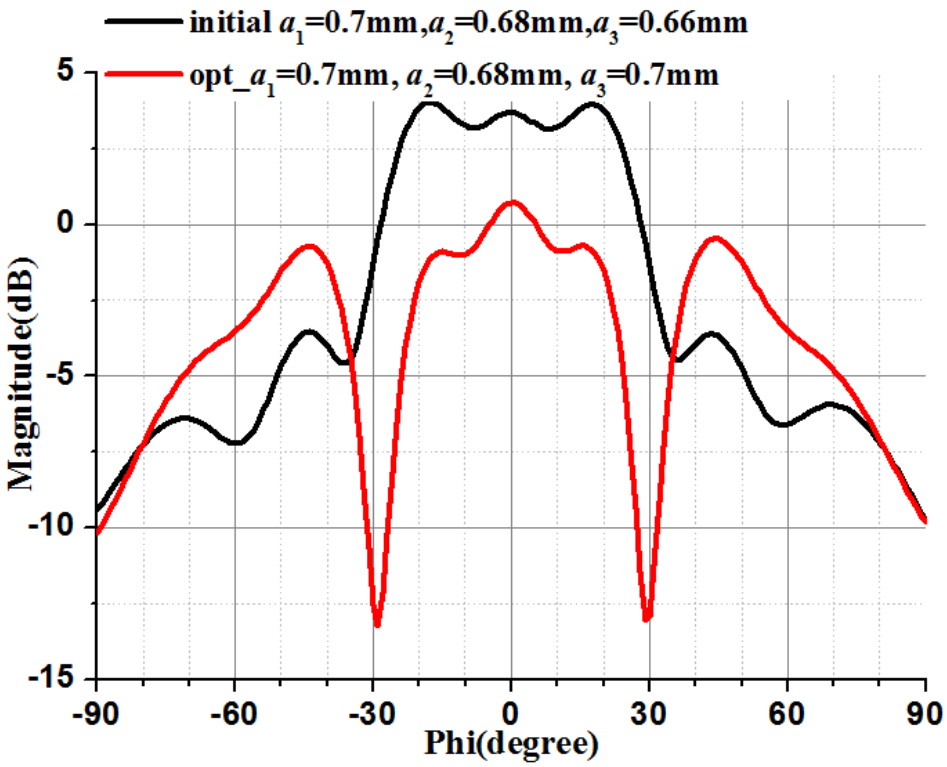

(b)

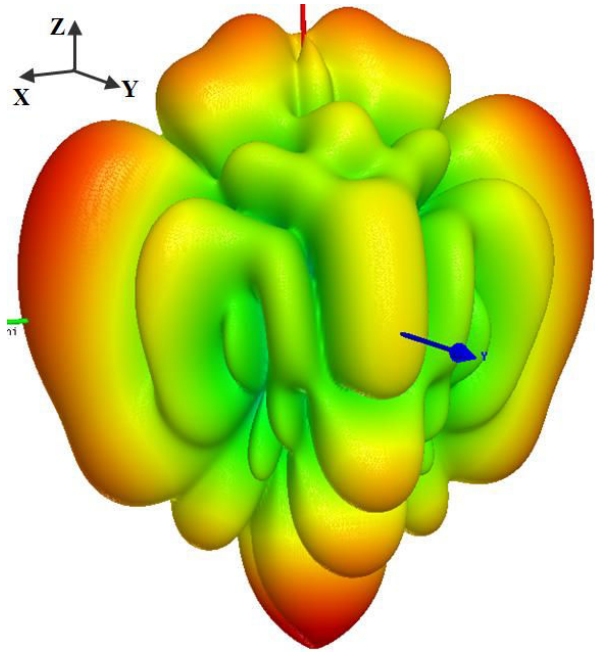

(c)

Fig.2.32 Directivity patterns (a) E-plane (E_θ) and (b) E-plane (E_φ), for initial and final optimal dimensions; (c) 3D plot E-plane (E_θ) for final optimal dimension.

The 3D pattern in Fig.2.32 (c) gives a more global overview of the obtained

radiation in the desired polarization. First, it is important to point out that the strong observed back radiation (bottom lobe) is meaningless. Indeed, it results from the simulation conditions: what we plot is the total field (incident and reflected field). Then, as we excite the reflector with an ideal plane wave, a large incident field exists behind the reflector. Apart from this artefact, we clearly see that most power is reflected back close to endfire and backfire.

Finally, in order to better assess the contributions of the notches, the same array is simulated when all notches are suppressed (a=0 for all DRAs). For this reference array, there is no polar conversion and, consequently, the E-plane is the YOZ plane. Fig.2.33 compares the radiation for both arrays in their respective E-planes.

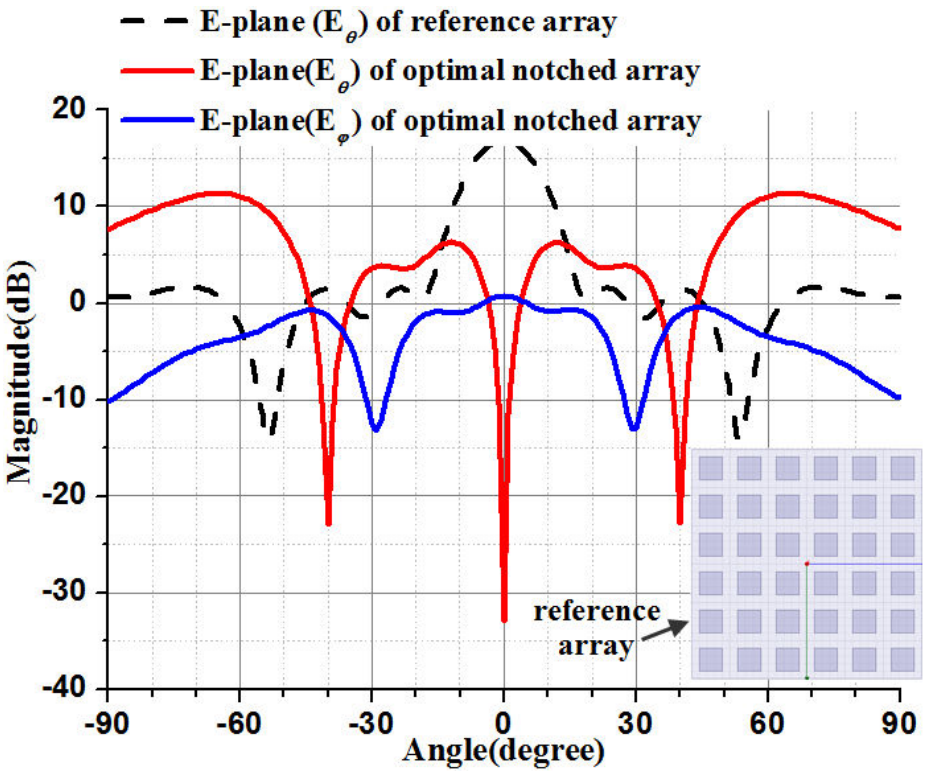

Fig.2.33 Comparison of directivity in E-plane between the optimal notched DRA array and the reference array

As could be expected, the reference array is characterized by a strong reflection at broadside (16.8dB in the black dashed line), and barely no endfire radiation. Thanks to the introduction of notches, the notched array greatly suppresses the broadside reflection (blue solid line), and converts it to endfire radiation on the orthogonal polarization (red solid line). Therefore, a large part of incident power has been successfully radiated towards horizontal direction.

Conclusion

In this section, an original notched DRA structure has been proposed and investigated. By introducing notches into the diagonally-opposite corners of a square DRA, we first tried to twist the incident polarization. Then, by combining two such DRAs with inverted geometries, we produced out-of-phase reflection between consecutive cells with $\lambda/2$ spacing. This structure demonstrated promising capabilities to cancel the broadside reflection and enhance the radiation along horizontal direction. Different simulation configurations (single DRA and 2×1 DRA unit-cell) have been assessed and discussed. Preliminary arrays (6×1 and 6×6 elements) have also been simulated. Finally, it appears this structure could be eligible for the foreseen application although it requires a quite complex optimization process.

2.4 Array Design based on DRA Coupled to Phase-Delay Stub

In last section, an array based on diagonally-notched DRA cells has been investigated. We now consider a second solution where no polarization twisting is required. Once again, the proposed solution aims at guaranteeing a unique DRA size all over the array in order to avoid issues highlighted in section 1.2. Here, this is accomplished by using simple square DRAs that are coupled to phase-delay stubs through apertures in the ground plane. All DRA elements are identical and only the stubs differ from one cell to another one.

Parametrical studies will be carried out firstly on the single cell, in order to tune the stubs for the expected 0° and 180° reflection phases. Finally, simulations and optimizations will be accomplished at the level of a 6×6 array to validate the concept.

2.4.1 Parametric Investigations on the Aperture-Coupled Network

2.4.1.1 Initial Design

The principle of aperture-coupled antenna comes from microstrip technology and was proposed in 1985 by Pozar [110]. Since 1993 [111], it has often been applied to DRA design [112-117]. A typical aperture-coupled DRA is depicted in Fig.2.34. Its working principle is quite similar to the microstrip structure introduced in chapter 1. In a

reflectarray configuration, the incident power is captured by the DRA and coupled to the open-circuit microstrip stub, through the aperture etched in the ground plane. It is then reflected back and re-radiated with a phase-shift controlled by the length of the stub.

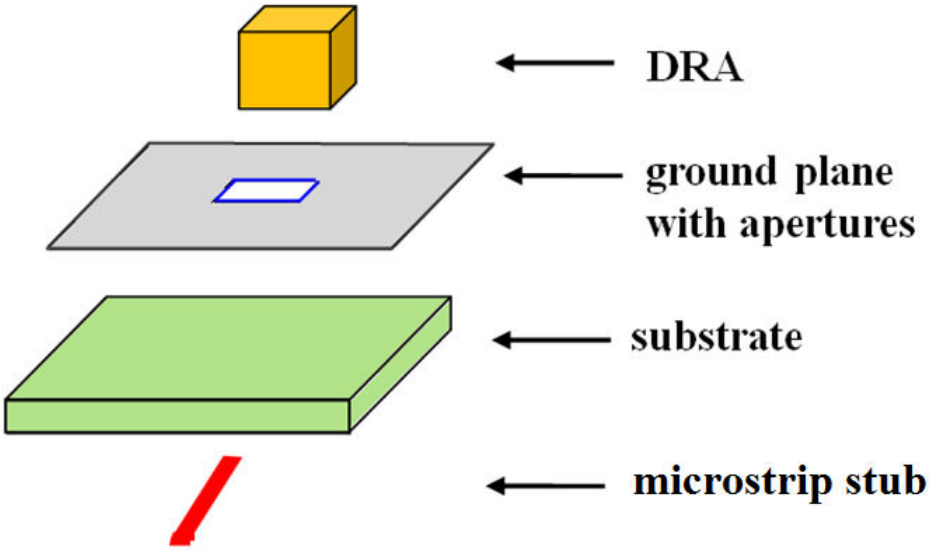

Fig.2.34 A typical aperture-coupled DRA

This topology is perfectly suitable for our design. In the structure, the radiation component and the phase-shifting network are separated apart by the ground plane, thus undesirable parasitic interference and spurious radiation can be avoided. Moreover, the two parts can be designed quasi-independently. This means, we can easily construct the array with identical DRA cells (as explained in section 2.2) on the top half, and select out the desired 0° and 180° reflection phases by tuning the open-circuit terminated phase-delay stub, under the substrate.

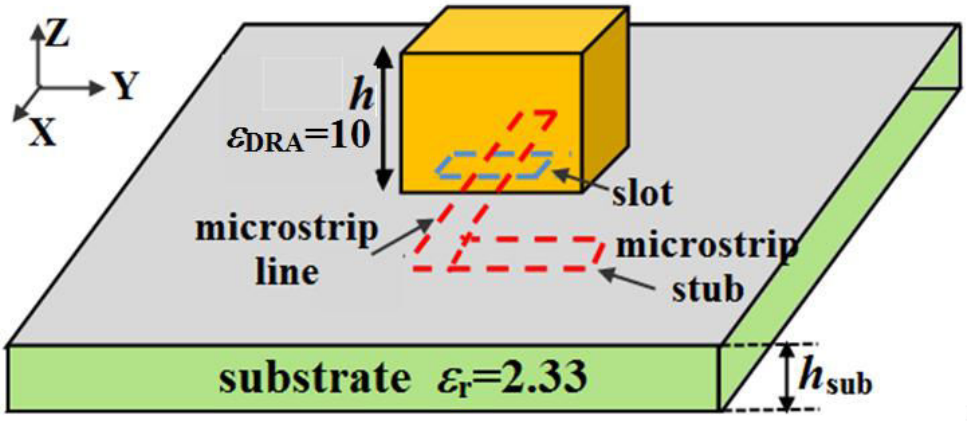

(a)

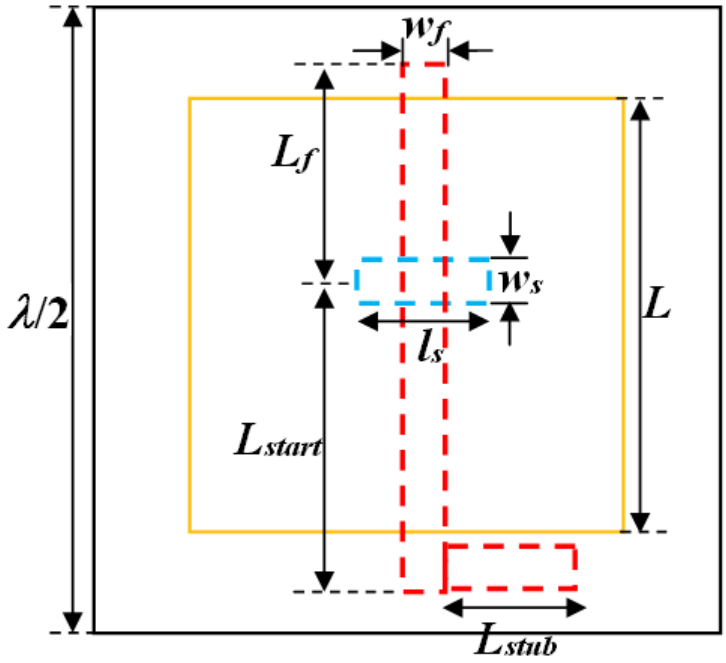

(b)

Fig.2.35 Schematic of the DRA coupled to phase-delay stub: (a) 3D view and (b) top view

A schematic of the proposed DRA cell with detailed geometry is presented in Fig.2.35. The whole cell dimension is still set to $\lambda/2\times\lambda/2$ (λ=5mm), the DRA and the slot are centered with respect to the cell. The DRA dimensions are h=0.52mm and L=1.8mm (material is HiK with ε_{DRA}=10, loss tangent=0.002), which is the basic cell resonant at 60GHz (its resonance performance was given in Fig.2.4). The microstrip substrate is chosen with ε_r=2.33 (loss tangent=0.0012) and h_{sub}=0.08mm. This value does not correspond to any practical material and only the concept will be studied here. The width of the microstrip line (along x-axis) is set to w_f=0.24mm for Z_0=50Ω and its total length is L_f+L_{start}. A microstrip stub (along y-axis) with the length of L_{stub} is added at the end of the microstrip line, performing as the phase-delay stub. In order to maximize coupling, the microstrip line should extend out $\lambda_g/4$ over the slot. As a starting point, L_f is set to 0.85mm and will be optimized later. The length of L_{start} is not important in controlling the coupling, it is set as $L_{start}=\lambda_g/2$=0.88mm.

The etched slot is the most critical part in controlling the coupling level. If the slot dimensions ($w_s\times l_s$) are too small, the coupling would be quite weak and the incident power would hardly be transmitted to the stub. On the other hand, if the slot is too large, it may resonate within the operation band, thus causing significant back radiation. Meanwhile, since the DRA will be significantly overloaded, its resonant

frequency will be shifted away 60GHz, making the design difficult.

Usually, the length l_s is much more important than the width w_s. Based on experience [118], a good starting value for l_s could be:

$$l_s = \frac{0.4\lambda_0}{\sqrt{\varepsilon_e}}$$

$$\varepsilon_e = \frac{\varepsilon_{DRA} + \varepsilon_r}{2} \tag{2-4}$$

Therefore, we can obtain l_s=0.8mm. As for the width w_s, it is usually in the range of [0.1, 0.2] time l_s, so here we set it as w_s=0.1mm initially.

2.4.1.2 Optimization of Aperture-Coupled Network

The initial values for the geometry in Fig.2.36 are summarized in Table 2.3.

Table 2.3 Initial dimensions for the DRA cell (Unit: mm)

L_{DRA}	1.8
h_{DRA}	0.52
h_{sub}	0.08
L_f	0.85
w_f	0.24
L_{start}	0.88
l_s	0.8
w_s	0.1

Optimization is then carried out to improve the coupling between the aperture-coupled circuit and the DRA at 60GHz. Simulation settings are shown in Fig.2.36. A periodic cell is used, in which the upper waveport excites the cell along x-axis. Another waveport at the bottom is used to assess the back radiation. At this

stage, the microstrip stub is replaced by a matched load. The optimization goal is then to transmit all the incident power to the load. To do so, S11 should be made as small as possible.

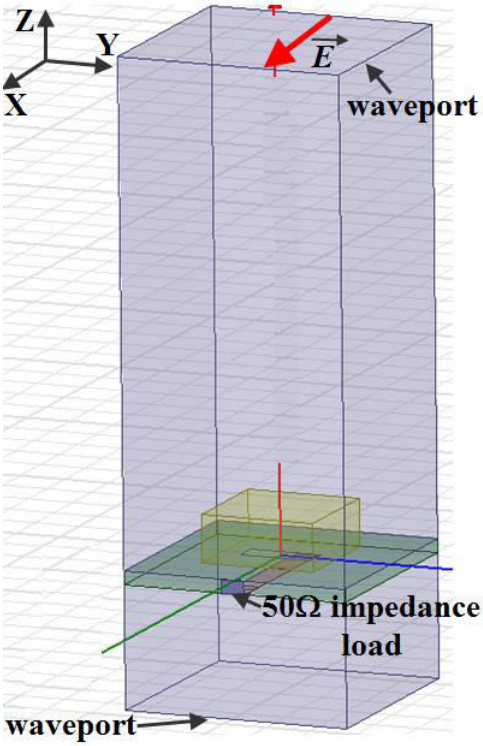

Fig.2.36 Simulation settings for aperture-coupled DRA

With the initial dimensions listed in Table 2.3, the obtained S11 is presented in Fig.2.37.

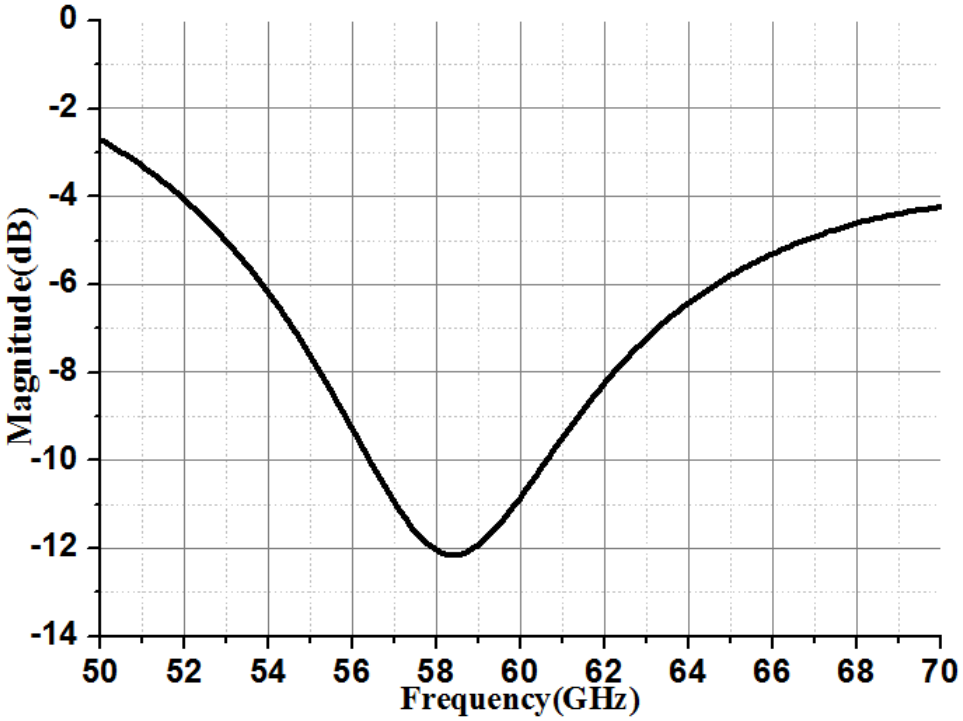

Fig.2.37 S11 for the initial dimensions of the DRA cell

At 60GHz, S11 is -11dB and the resonant frequency is shifted to 58.4GHz. Therefore, optimizations of the aperture-coupled network (mainly l_s, L_f and w_s) are required.

Firstly, l_s is adjusted from 0.6mm to 1.4mm when L_f=0.85mm, w_s=0.1mm, and the corresponding S11 is shown in Fig.2.38.

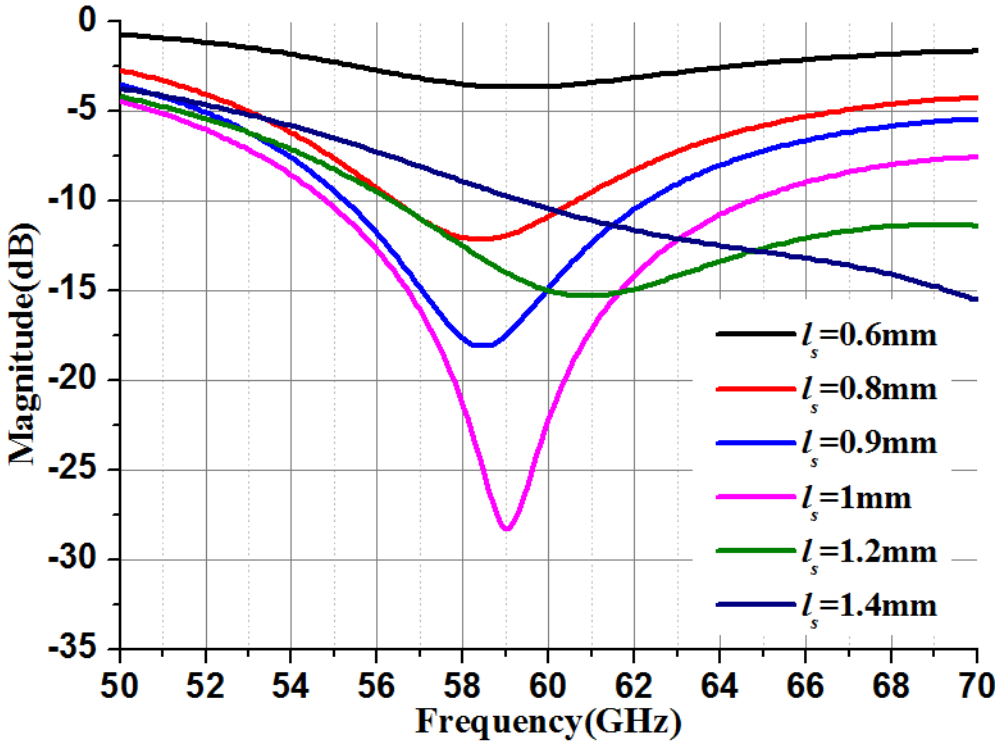

Fig.2.38 S11 when L_f=0.85mm, w_s=0.1mm and l_s varies in [0.6, 1.4] mm

According to Fig.2.38, when l_s=1mm, the resonant frequency is at 59GHz with S11=-28dB. Therefore, l_s=1mm is chosen and l_f is now optimized in the range [0.6, 1.1] mm. The corresponding S11 is recorded in Fig.2.39.

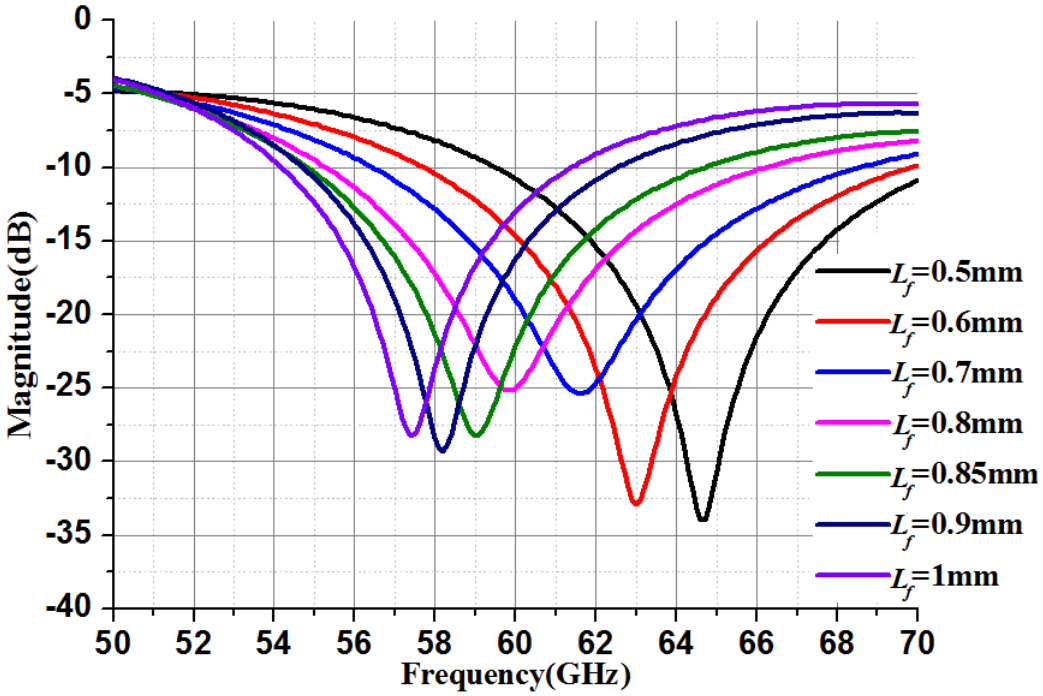

Fig.2.39 S11 when l_s=1mm, w_s=0.1mm and L_f varies in [0.6, 1] mm

When l_f =0.8mm, the corresponding resonant frequency is located at 59.8GHz

with S11=-25dB, and we are quite close to the optimization objective. Based on Fig.2.39, a minor adjustment of w_s and L_{start} is then taken to make sure we reach the best coupling at 60GHz. The final scattering parameters are demonstrated in Fig.2.40.

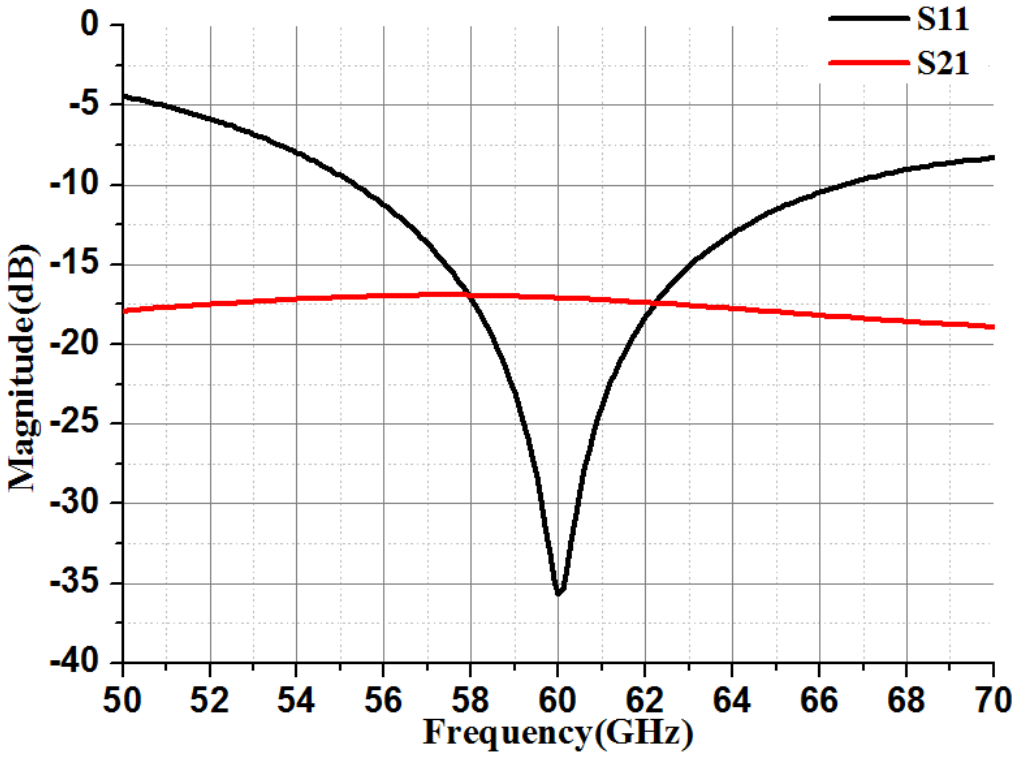

Fig.2.40 Scattering coefficients at 60GHz when L_f =0.8mm, l_s=1mm and w_s=0.06mm

The final optimized dimensions are: L_f =0.8mm, l_s=1mm, w_s=0.06mm and L_{start}=0.7mm. At 60GHz, S11=-35.7dB, which indicates the reflection is only 1.6%; S21=-17.3dB, which means the back radiation is 13.6%. Therefore, 85% of the incident wave is coupled to the load, and this result is acceptable for further array design.

Furthermore, the E-field distribution on the DRA at 60GHz is provided in Fig.2.41, which proves the excitation of the fundamental mode TE^{Y}_{111} at 60GHz.

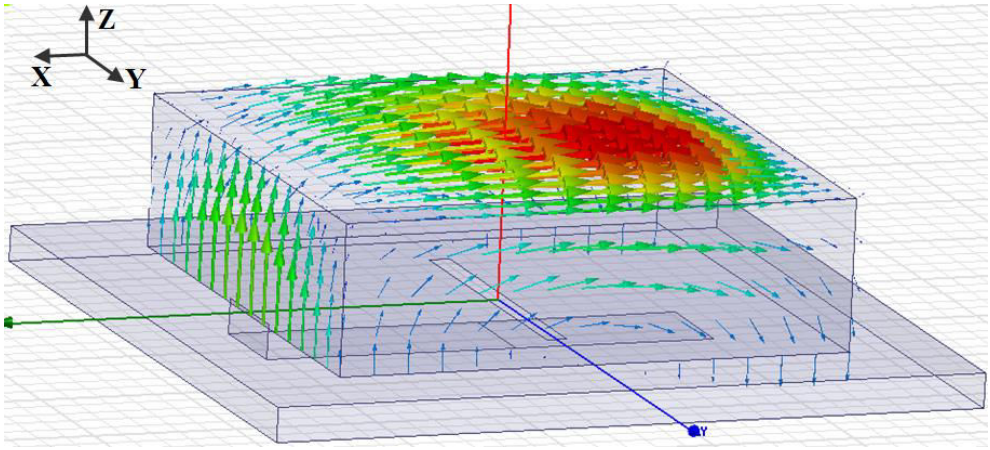

Fig.2.41 E-field distribution on the DRA at 60GHz

Finally, the final optimal dimensions for the DRA cell based on the aperture-coupled network are updated in Table 2.4.

Table 2.4 Optimal dimensions for the aperture-coupled DRA (Unit: mm)

L_{DRA}	1.8
h_{DRA}	0.52
h_{sub}	0.08
L_f	0.8
w_f	0.24
L_{start}	0.7
l_s	1
w_s	0.06

Until now, the DRA cell coupled to the microstrip stub through slot has been optimized at 60GHz, and a good coupling has been achieved between the network and the DRA. For the next step, investigations will be conducted concerning the DRA cell's phase-shifting characteristic.

2.4.2 Investigations on the Phase-Shifting Characteristic of the DRA Cell

In this section, the microstrip stub replaces the 50Ω load, as the phase-delay stub. When its length L_{stub} is varied, the DRA cell's reflection will be controlled.

Fig.2.42 shows the simulation settings. In case any unexpected back radiation is produced, the simulation cell is terminated with PML boundary at the bottom.

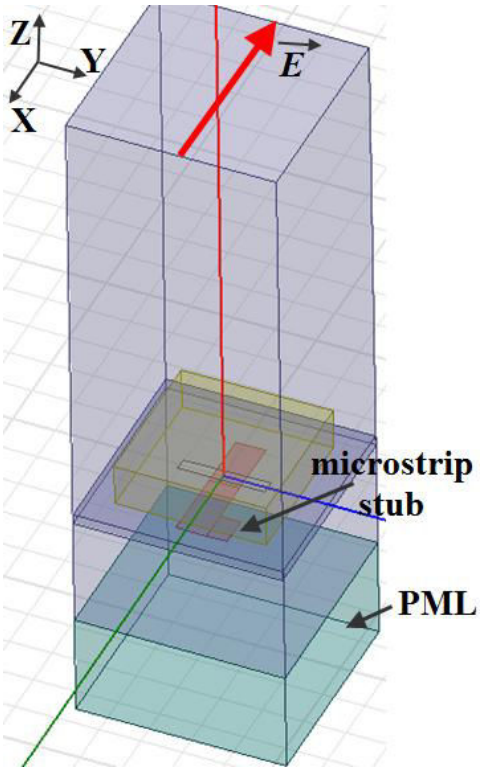

Fig.2.42 Simulation settings for investigations on the phase-shifting performance of the DRA cell

When L_{stub} varies in the range [0, 1.1] mm (note that L_{stub} is limited by the size of the cell, L_{stub}≤1.13mm), the reflection phases and magnitudes of S11 are plotted in Fig.2.43.

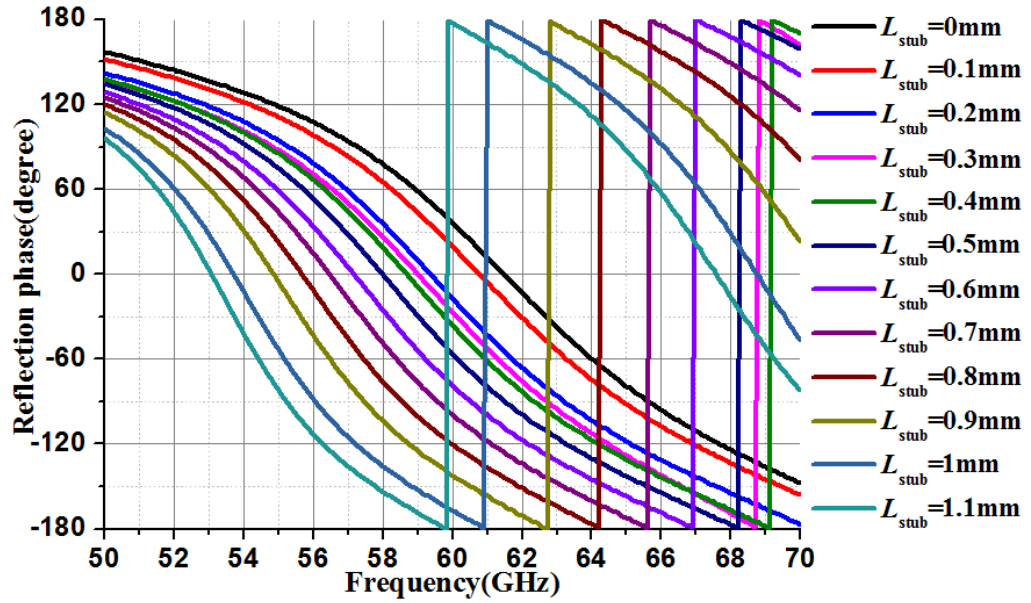

(a)

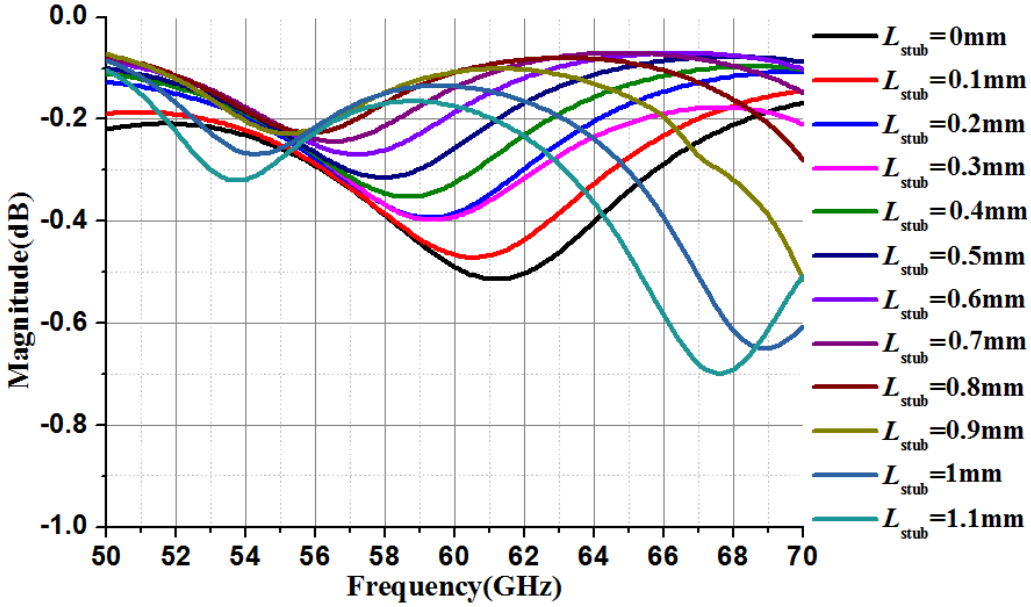

(b)

Fig.2.43 Phase-shifting performance of the DRA cell when L_{stub} varies in the range [0, 1.1] mm: (a) reflection phase and (b) reflection magnitude of S11

The phase-shifting performances at 60GHz are summarized in Fig.2.44.

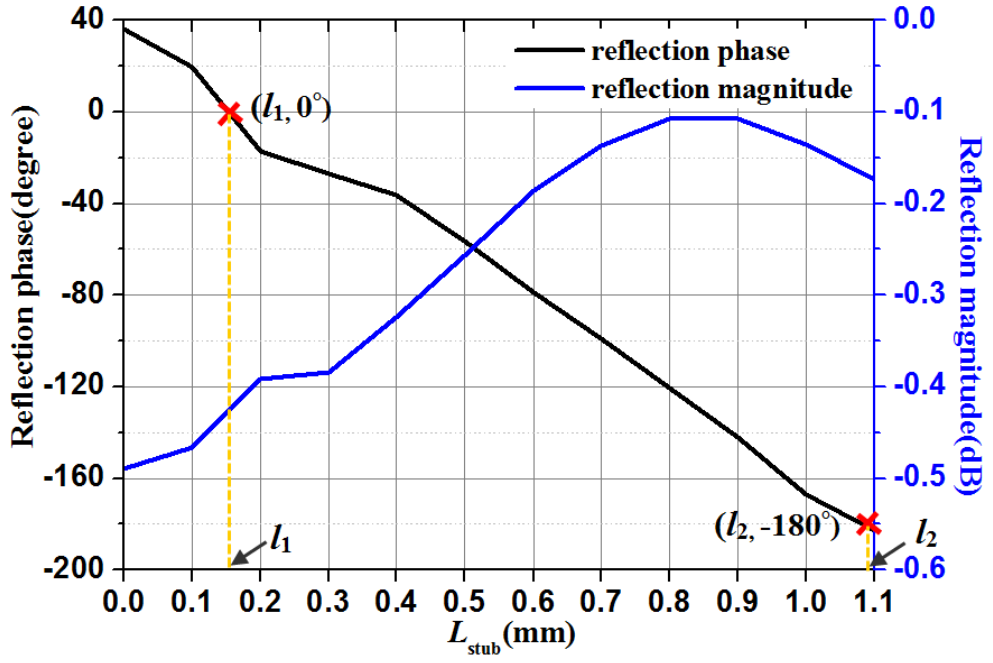

Fig.2.44 Phase-shifting curve versus L_{stub} at 60GHz

When L_{stub}=0.15mm, the reflection phase is 0°, and when L_{stub}=1.08mm, the reflection phase reaches 180°. Meanwhile, the reflection magnitude is -0.44dB and -0.18dB respectively. Therefore, these two lengths, named L_1 and L_2, will be used for further investigations.

2.4.3 Implementation and Optimization of 6×1 Array

In this section, a 6×1 array based on the dimensions obtained in previous sections is simulated. Furthermore, optimizations of L_1 and L_2 are conducted for maximum endfire radiation.

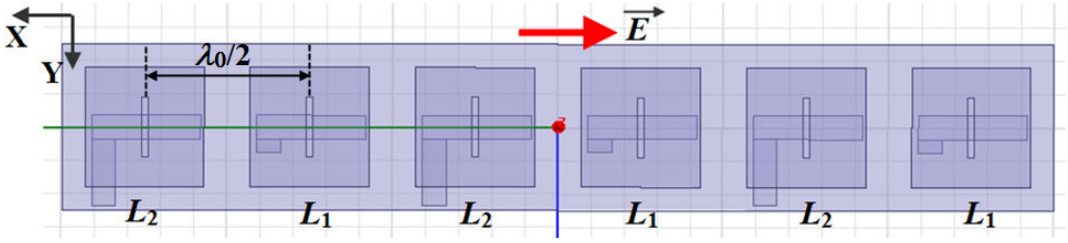

Fig.2.45 Simulation settings for the 6×1 array

As shown in Fig.2.45, the 6×1 array is obtained by alternating L_1 and L_2 along x-axis. The incident wave is illuminating the array normally with polarization along x-axis. The E-plane is XOZ plane. The directivity pattern in E-plane (E_θ) is recorded in Fig.2.46.

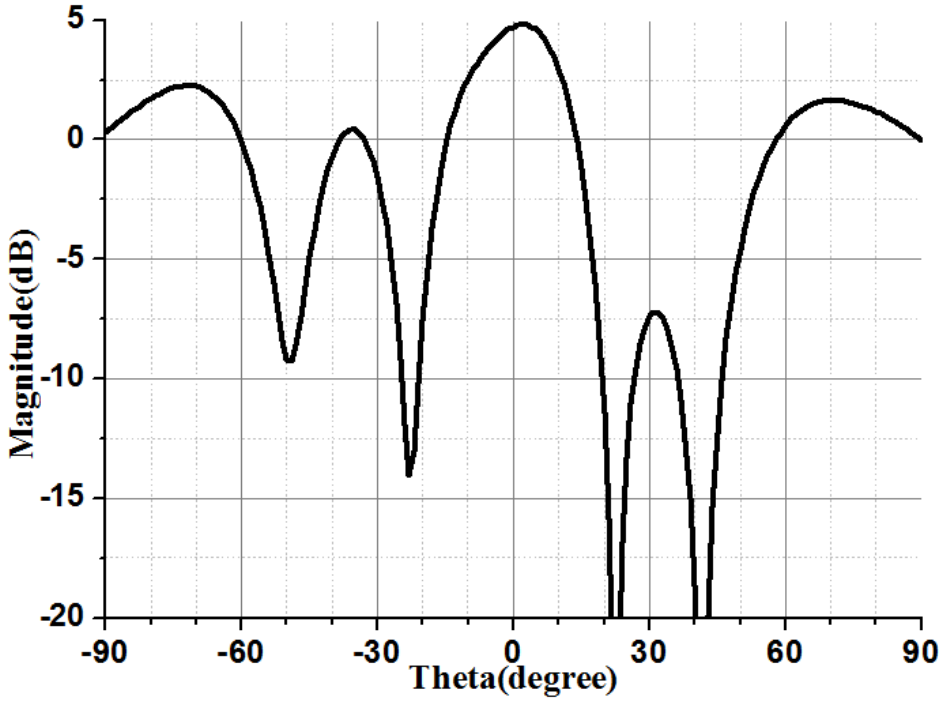

Fig.2.46 Directivity pattern in E-plane (E_θ) at 60GHz when L_1=0.15mm and L_2=1.08mm

The following observations can be made:

1). At 0°, the broadside reflection is up to 4.7dB, which is 4.5dB bigger than the endfire radiation.

2) As for previous arrays (section 2.3.3), the expected beam at θ=±90° is shifted off endfire. Here, it is maximum at θ=±72° with a magnitude equal to 2dB.

Definitively, the results are not those expected. As what have been done for the notched DRA, optimizations are required to account for the effect of the actual DRA environment. Again, parameter Ψ is used to maximize endfire radiation.

For optimization, L_1 is adjusted in the range [0, 0.3] mm and L_2 in the range [0.8, 1.1] mm. The corresponding directivity patterns in E-plane (E_θ) are recorded in Fig.2.47-50.

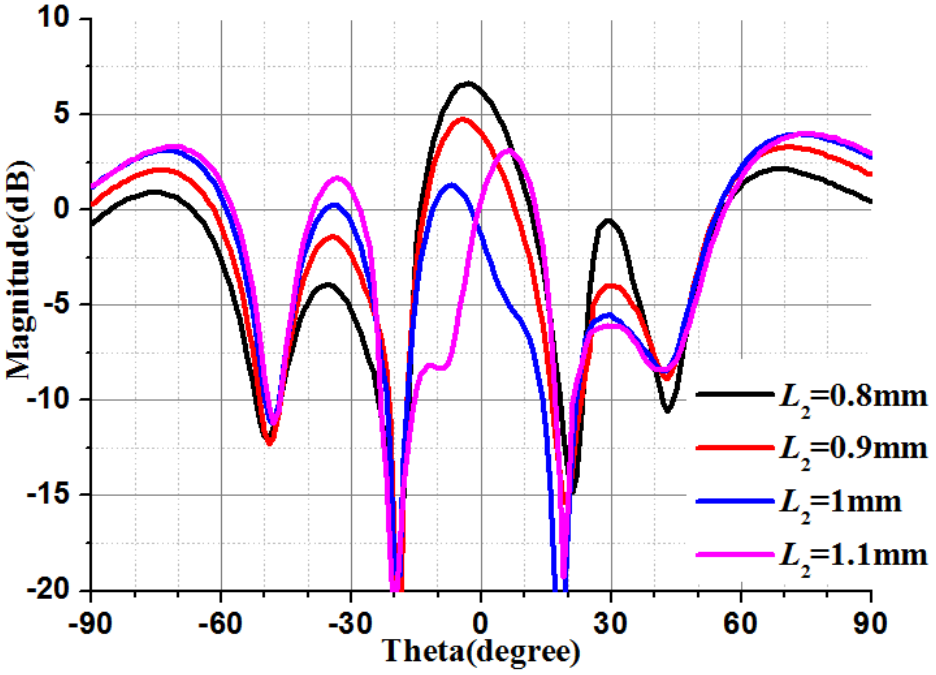

Fig.2.47 Directivity pattern in E-plane (E_θ) at 60GHz when L_1=0mm and L_2= [0.8, 1.1] mm

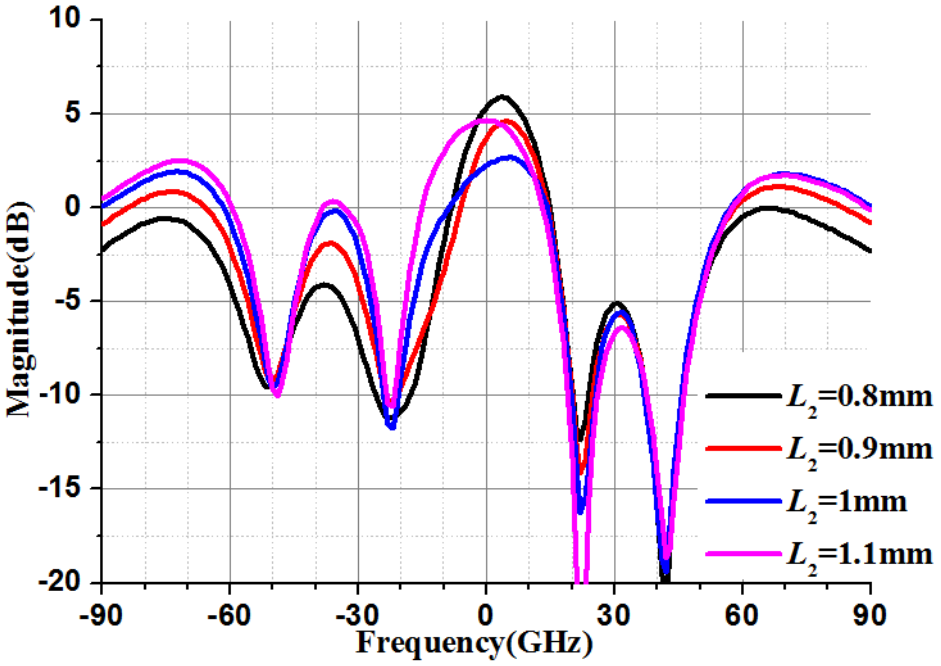

Fig.2.48 Directivity pattern in E-plane (E_θ) at 60GHz when L_1=0.1mm and L_2= [0.8, 1.1] mm

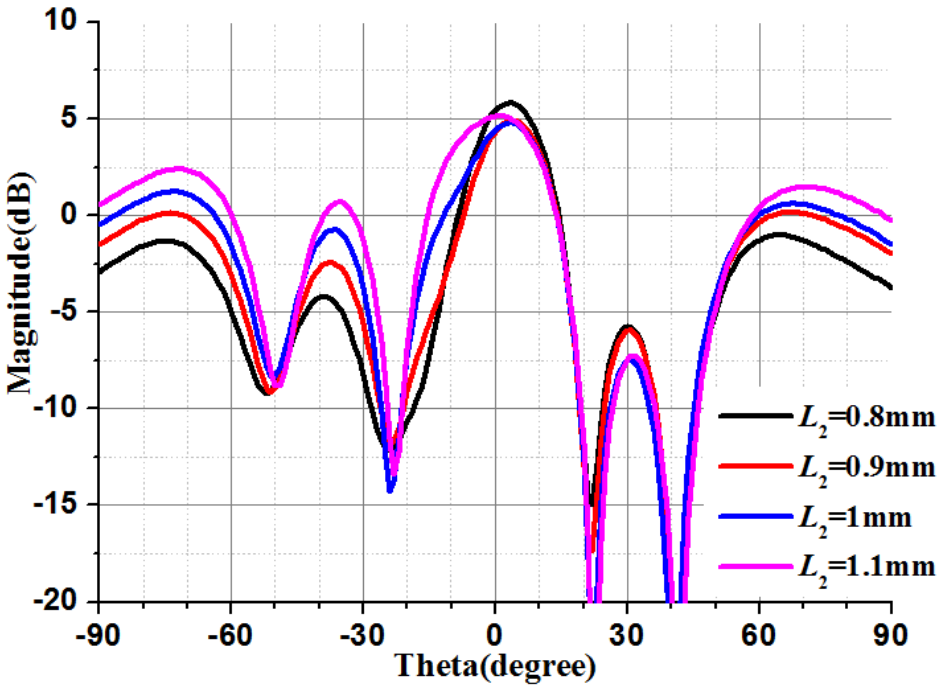

Fig.2.49 Directivity pattern in E-plane (E_θ) at 60GHz when L_1=0.2mm and L_2= [0.8, 1.1] mm

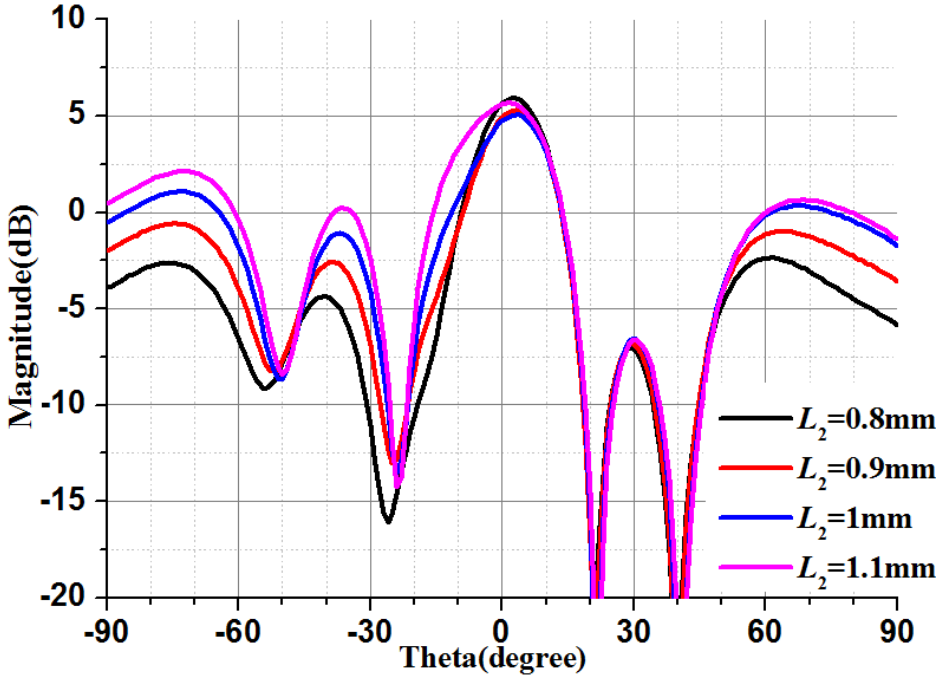

Fig.2.50 Directivity pattern in E-plane (E_θ) at 60GHz when L_1=0.3mm and L_2= [0.8, 1.1] mm

For the convenience of optimization, 2D contour plots of Ψ are given in Fig.2.51.

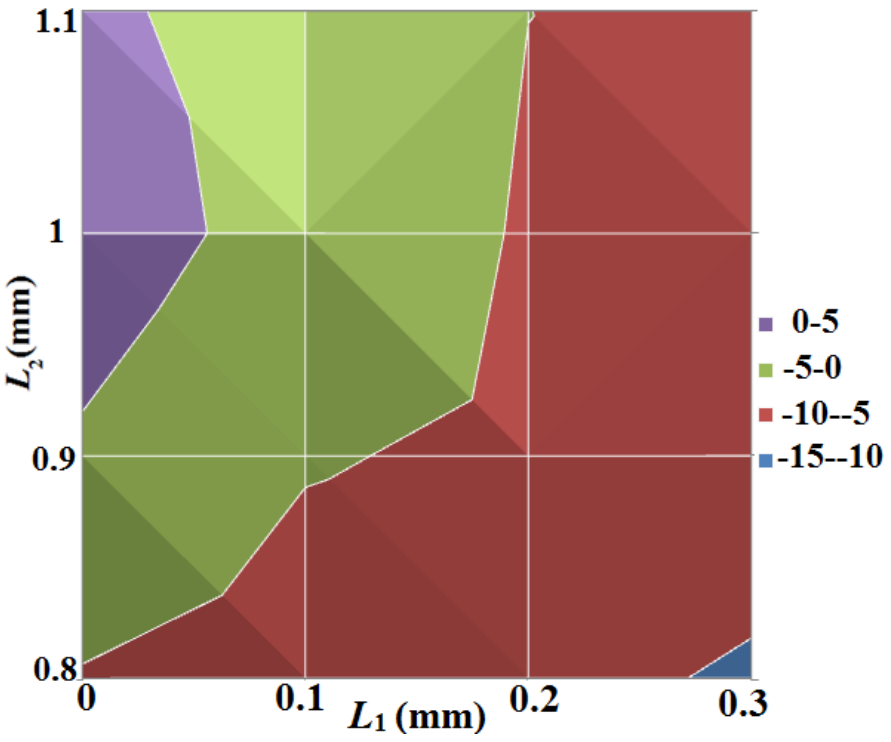

Fig.2.51 Ψ comparison in 2D contour when L_1= [0, 0.3] mm and L_2= [0.8, 1.1] mm

Ψ records the biggest values when L_1 varies in the range [0, 0.1] mm and L_2 in [1, 1.1] mm. However, this situation is not optimal since it is obvious L_1 has reached is minimum value (L_1=0mm) and should be reduced further. In order to do so, the phase-delay stub is now totally suppressed, and the length L_{start} is reduced as Fig.2.52 shows. In this way, L_1 is counted now as a negative value (e.g. L_1 =-0.1mm actually corresponds to L_{start} =0.7mm-0.1mm=0.6mm).

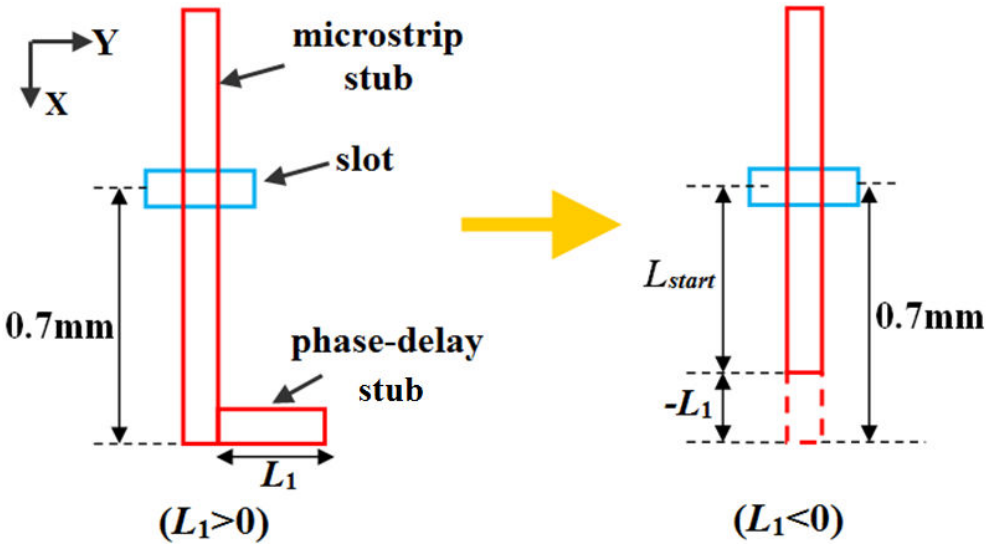

Fig.2.52 New topology to further reduce the stub length (L_1<0)

When L_1 is changed in [-0.4, -0.1] mm and L_2 remains in the range [0.8, 1.1] mm, corresponding directivity patterns in E-plane (E_θ) are depicted in Fig.2.53-56.

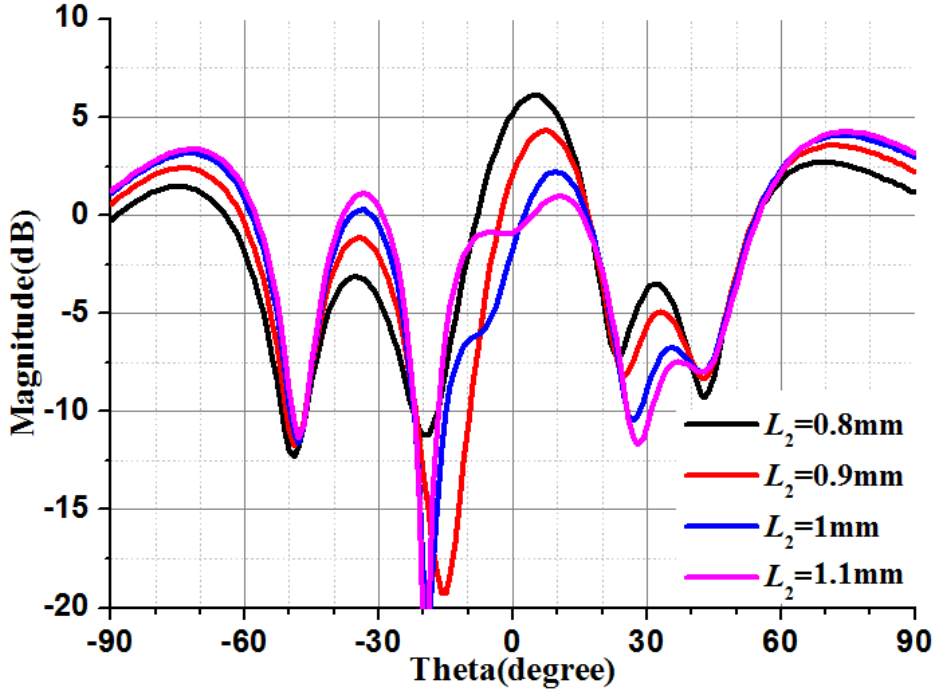

Fig.2.53 Directivity pattern in E-plane (E_θ) at 60GHz when L_1=-0.1mm and L_2= [0.8, 1.1] mm

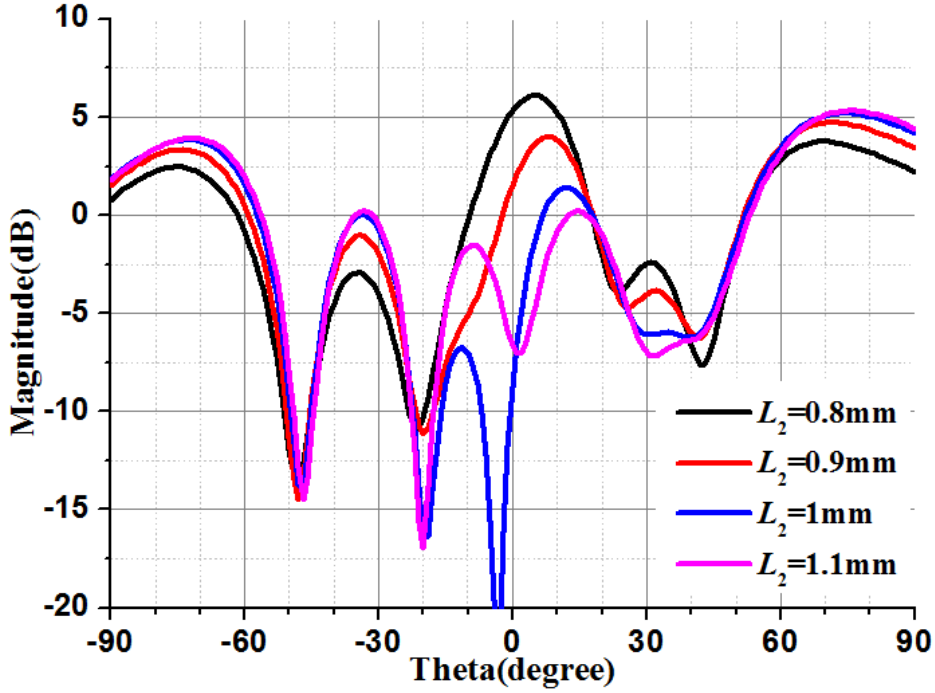

Fig.2.54 Directivity pattern in E-plane (E_θ) at 60GHz when L_1=-0.2mm and L_2= [0.8, 1.1] mm

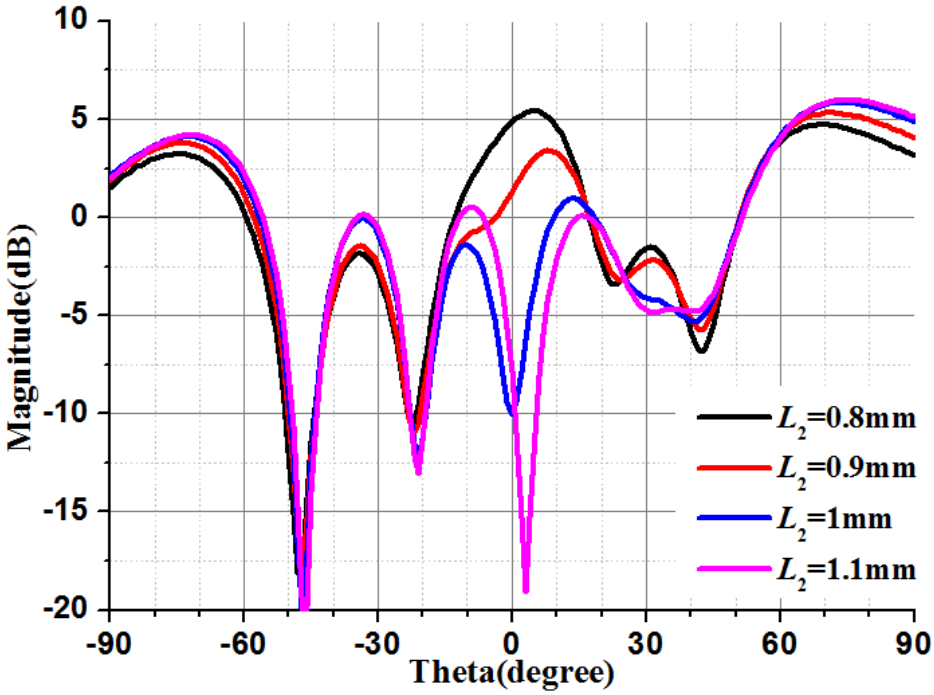

Fig.2.55 Directivity pattern in E-plane (E_θ) at 60GHz when L_1=-0.3mm and L_2= [0.8, 1.1] mm

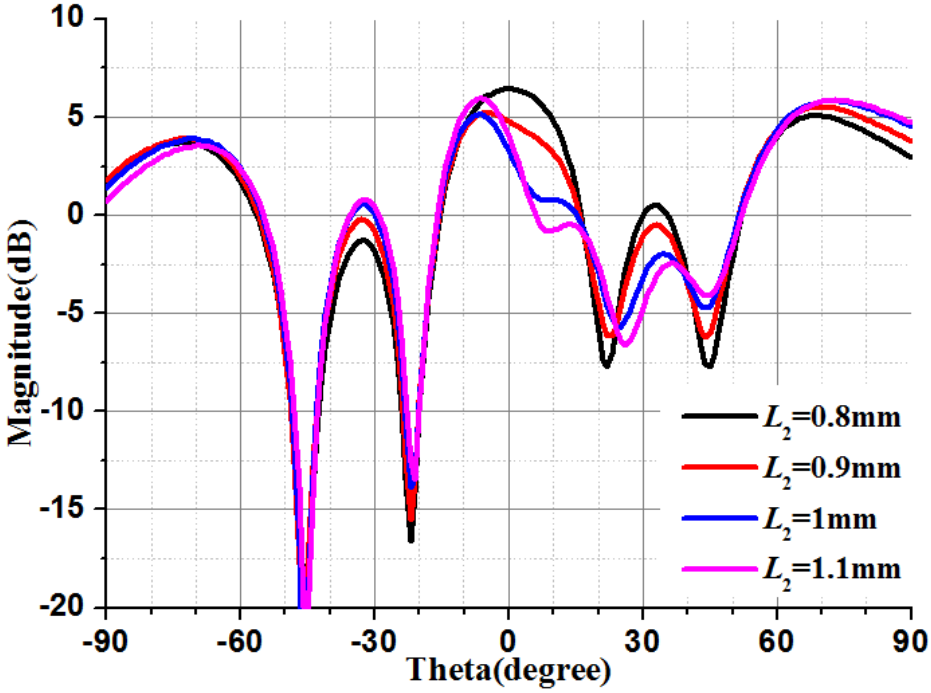

Fig.2.56 Directivity pattern in E-plane (E_θ) at 60GHz when L_1=-0.4mm and L_2= [0.8, 1.1] mm

The 2D plot of Ψ is updated in Fig.2.57 using a fine scanning around the vicinity of the maximum.

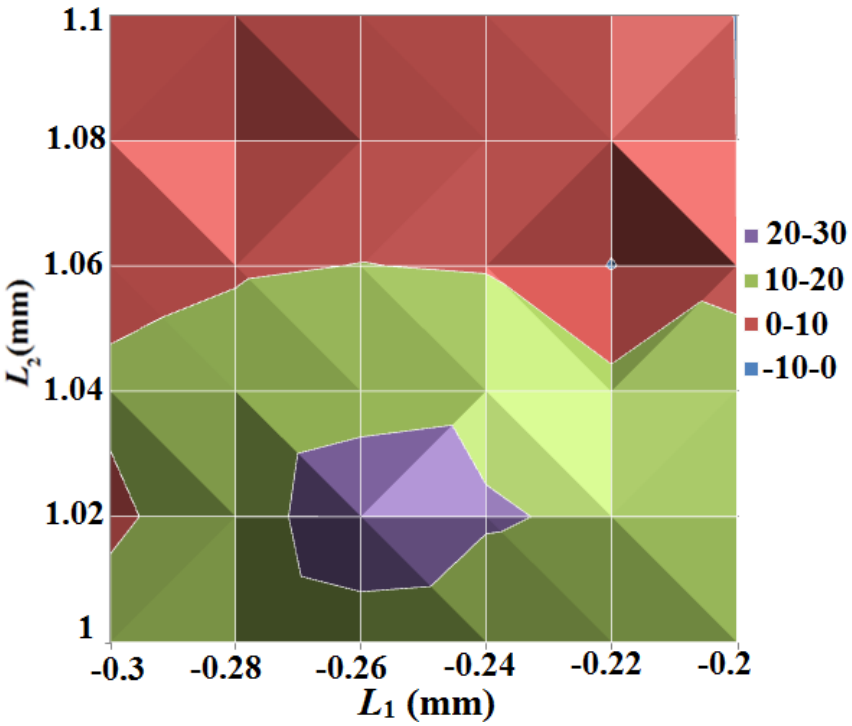

Fig.2.57 2D contour plots of Ψ when L_1= [-0.3, -0.2] mm and L_2= [1, 1.1] mm

The optimal result is obtained when L_1=-0.26mm, and L_2=1.02mm, with Ψ=26.9dB. Its directivity pattern is compared with that of the initial dimensions in Fig.2.46.

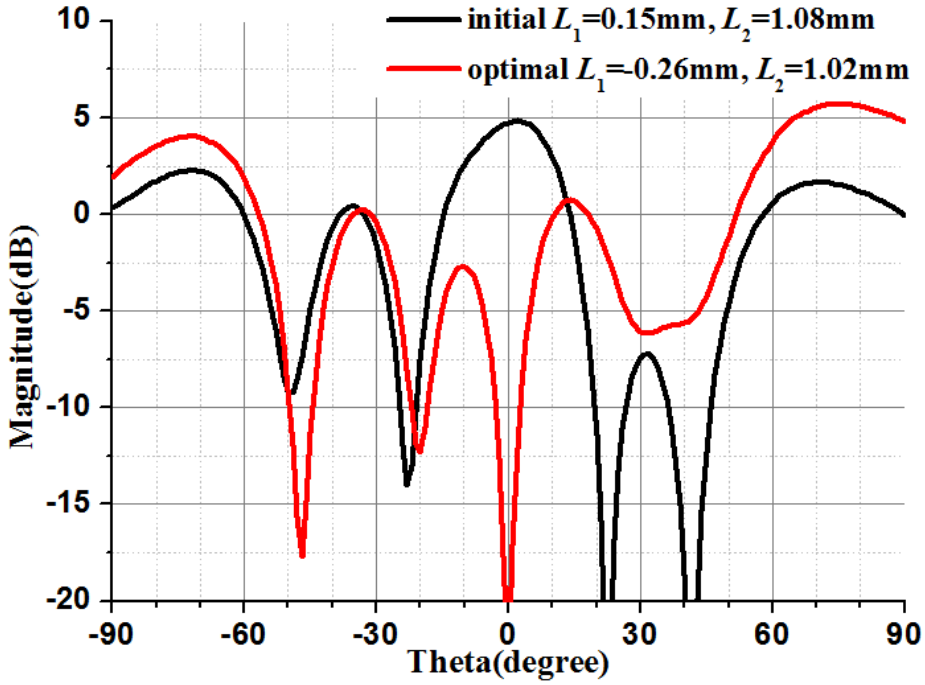

Fig.2.58 Comparison of directivity patterns in E-plane (E_θ) between the initial and optimized dimensions for 6×1 array

According to Fig.2.58, the main beam of the optimized structure (red line) is shifted to $\theta=\pm 75^{\circ}$. The broadside reflection is significantly reduced, and the power at endfire radiation and main beams get obviously improved.

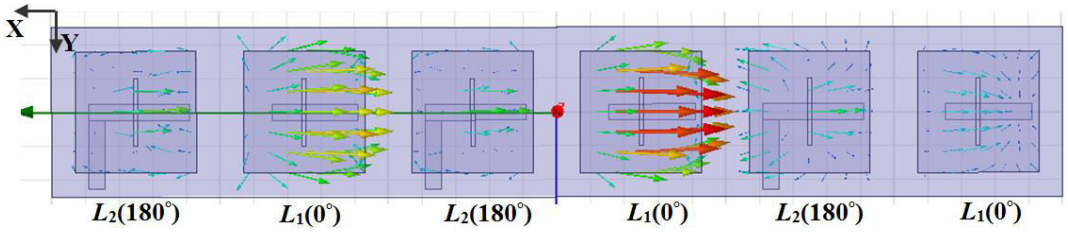

Fig.2.59 E-field distribution on 6×1 array at 60GHz with optimal dimension

Finally, the total E-field distribution on the 6×1 array is presented in Fig.2.59. The second, fourth and sixth DRAs provide 0° reflection phase. Then, the reflected field is in phase with the incident field and the resulting total E-field is large. On the other hand, the first, third and fifth DRAs provide 180° reflection phase. Then, the reflected field is out of phase with the incident field and the resulting total field is weak. It is interesting to note that the field magnitude is not identical when the DRA is located in the middle of the array or close to its ends. This can clearly be seen when comparing the second DRA with the fourth or the sixth. We can thus conclude that the effect of array finiteness is not negligible.

2.4.4 Implementation and Optimization of 6×6 Array

A bigger 6×6 array (15mm×15mm) is finally studied as for the notched DRA. It is shown in Fig.2.60.

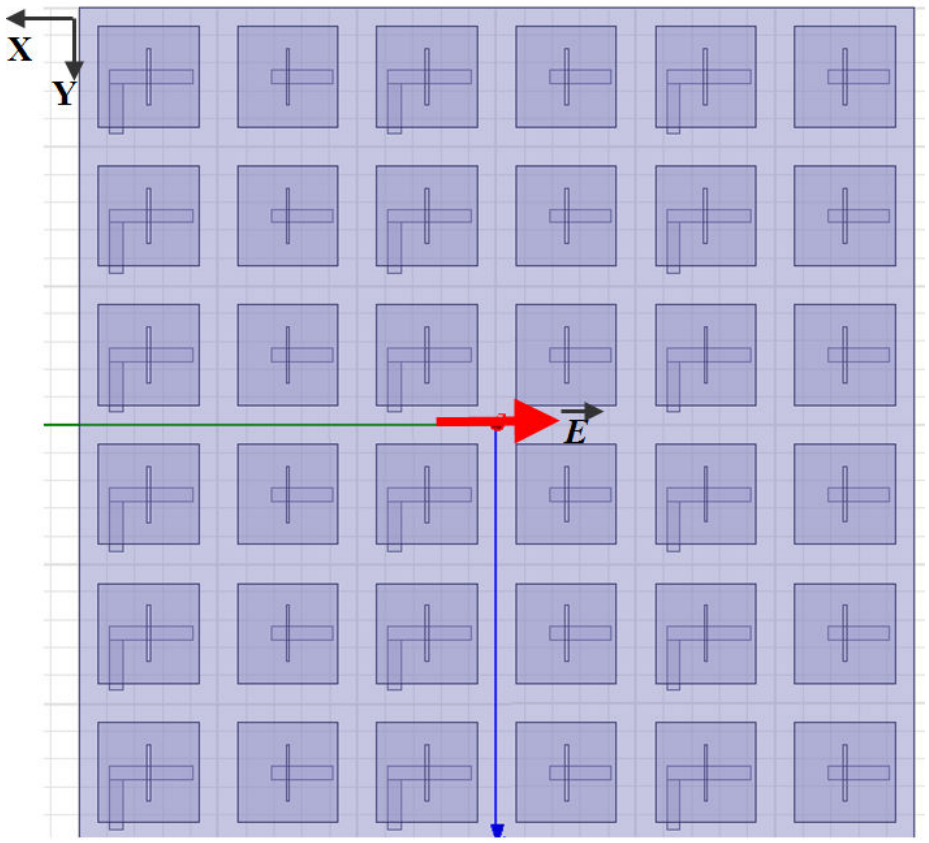

Fig.2.60 Simulation settings for 6×6 array

The stub lengths are re-optimized to L_1=-0.38mm and L_2=1mm (yielding Ψ=**9**dB). Fig.2.61 compares the performance obtained with these optimal dimensions and that obtained with the dimensions from previous section.

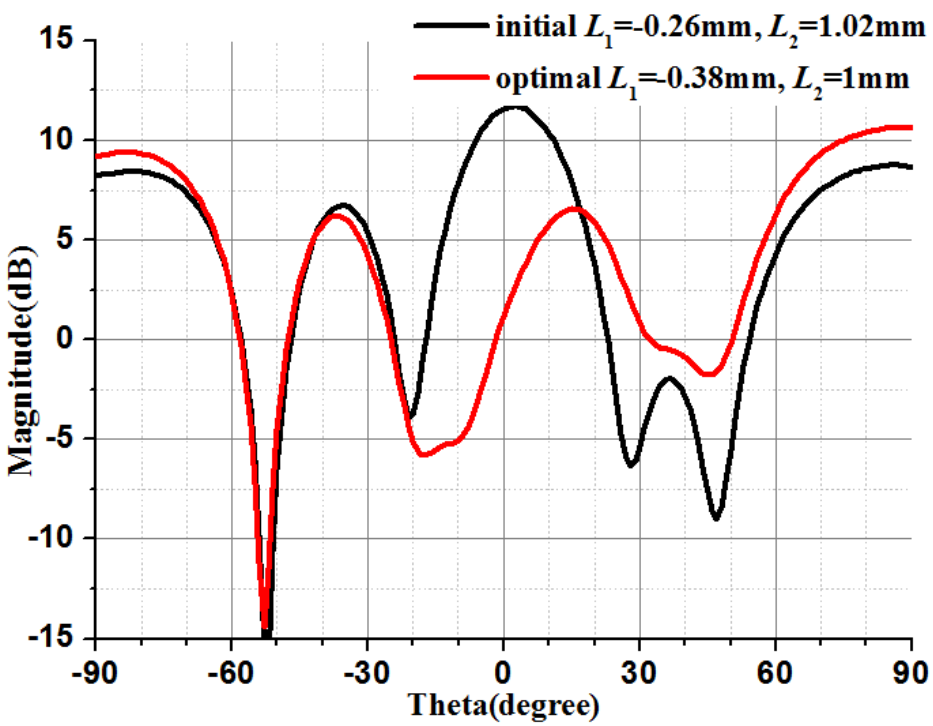

Fig.2.61 Comparison of directivity patterns in E-plane (E_θ) between the initial and optimized dimensions for 6×6 array

After optimization, the endfire level of the array pattern is improved to 9.2dB (average value of directivities at ±90°), and the main beams at θ=±83° is up to 10dB (also average value of the two main beams). The broadside reflection is also largely reduced.

In Fig.2.62, we further compare this optimal result with the one of the notched DRA array (in Fig.2.32), we can find the aperture-coupled DRA array is better: it produces a stronger endfire radiation, and the main beams are closer to ±90°.

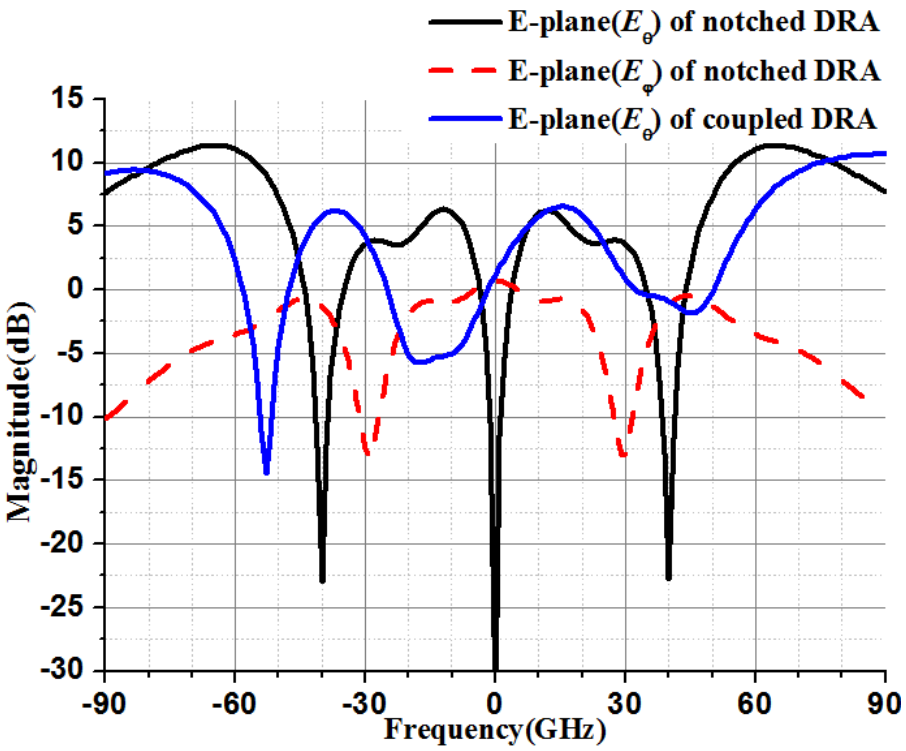

Fig.2.62 Comparison of directivity patterns of the 6×6 array based on notched DRA and on aperture-coupled DRA

Finally, the 3D pattern for the optimal dimensions is given in Fig.2.63. The back radiation, as explained before, comes from the simulation setting and is meaningless. Most of the power is now radiated towards horizontal direction, which confirms the feasibility of endfire array using DRA coupled to phase-delay stub.

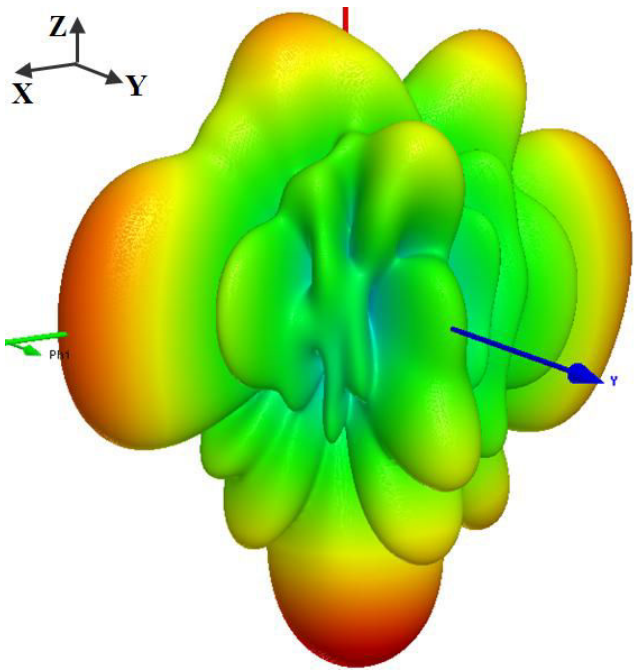

Fig.2.63 3D directivity pattern of the 6×6 array at 60GHz

Conclusion

In this chapter, two topologies based on DRA elements with identical dimensions have been proposed for quasi-endfire arrays. These arrays appear as possible candidates for the foreseen application where a passive repeater aims at illuminating the orthogonal branches of a T-shaped corridor.

The first topology introduces two notches on the diagonally-opposite corners of a square DRA to twist the incident polarization. Out-of-phase reflection from two consecutive DRAs is then produced by rotating the second DRA by 180°. In this topology, the desired reflected wave is polarized orthogonally to the incident one, which could certainly be used to prevent from multiple path fading (for instance if any unexpected scattering is responsible for leakage of the incident power in the orthogonal branches of the corridor).

The second structure uses the same square DRA cell and couples it to a phase-delay microstrip stub through a rectangular slot etched in the ground plane. By properly adjusting the stub lengths, out-of-phase reflections can be obtained on successive DRA, thus approaching the desired endfire radiation.

Different simulations strategies have been used (relying on the analysis of a periodic motive made of one or two DRA). However, only the optimization of the structure at the array level is capable to account for the actual coupling phenomena, especially where the structure is finite.

In the end, simulations of canonical 6×6 arrays have shown the applicability of the proposed concepts. For example, in the second structure, the radiation at endfire is 9dB more than the radiation at broadside.

However, at this stage, no practical breadboard has been manufactured. The reason is the relative complexity of the induced fabrication process. The second structure, the more promising one regarding radiation, would for instance require a multiple-layer process with quite challenging alignment issues at 60GHz.

In the following chapters, we will investigate simpler topologies for which breadboards will be designed and fabricated. We will also address in more detail some highlighted issues (such as the shifting of the reflected beam off endfire).

Chapter 3 Investigations on Endfire Array Based on Rectangular Waveguide

Contents

Chapter 3 Investigations on Endfire Array Based on Rectangular Waveguide

3.1 Introduction

3.1.1 Background of Waveguide Theory

The conception of waveguide was first proposed by J.J. Thomson in 1893 [134], and then promoted by Lord Rayleigh who performed the first mathematical analysis of electromagnetic waves in a metal cylinder [135-136], and Sommerfeld who established theoretical analysis on different modes [137-138]. In 1920-1960, due to its application on optical fibers and radars, researches on the theoretical and experimental investigation about waveguide were rekindled [139-145]. Due to its distinctive structure, waveguide enjoys remarkable advantages in microwave application: 1) the waveguide is designed as a closed system, thus it is shielded from outer interference and radiation loss; 2) Waveguide is usually made of high conductivity material (e.g. copper or aluminum) and doesn't require inner conductor. So its conductor loss is reduced to very low level, and the power capacity is quite high. These characteristics make waveguide greatly potentials for high-frequency and high-power applications.

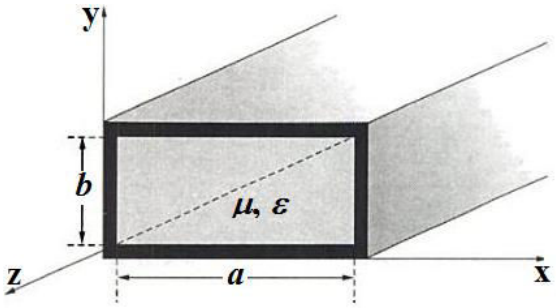

Fig.3.1 Schematic of rectangular waveguide

On the other hand, waveguide also sees limit in its vast volume, especially at low-frequency band. Here we take a standard rectangular waveguide (as depicted in Fig.3.1) as an example. For arbitrary mode (TE_{mn} or TM_{mn}) transmitted in the waveguide, its operating frequency f must exceed the corresponding cutoff frequency f_c ($f > f_c$), or the wavelength must be smaller than cutoff wavelength λ_c ($\lambda < \lambda_c$). In detailed, this can be expressed as:

$$f > f_c = \frac{1}{2\pi\sqrt{\mu\varepsilon}}\sqrt{\left(\frac{m\pi}{a}\right)^2+\left(\frac{n\pi}{b}\right)^2} \tag{3-1}$$

$$\lambda < \lambda_c = \frac{\sqrt{\mu\varepsilon}}{f_c} = \frac{2}{\sqrt{\left(\frac{m}{a}\right)^2+\left(\frac{n}{b}\right)^2}} \tag{3-2}$$

In (3-1) and (3-2), a and b are the waveguide port's length and width respectively. This means, at low-frequency band (which corresponds to large wavelength λ), the waveguide dimension has to be huge to accommodate the transmitted waves.

Table 3.1 Recommended waveguide dimensions of different frequency (ε_r=1)

Band	Recommended Frequency range (GHz)	TE_{10} cutoff Frequency (GHz)	Inside dimension (cm)	Outside dimension (cm)
L	1.12–1.70	0.908	16.51×8.255	16.916×8.661
R	1.70–2.60	1.372	10.922×5.461	11.328×5.867
S	2.60–3.95	2.078	7.214×3.404	7.620×3.810
C	5.85–8.20	4.301	3.485×1.580	3.810×1.905
X	8.20–12.4	6.557	2.286×1.016	2.540×1.270
Ku	12.4–18.0	9.486	1.580×0.790	1.783×0.993
K	18.0–26.5	14.047	1.07×0.43	1.27×0.635
Ka	26.5–40.0	21.081	0.711×0.356	0.914×0.559
Q	33.0–50.5	26.342	0.57×0.28	0.772×0.488
U	40.0–60.0	31.357	0.48×0.24	0.681×0.442
E	60.0–90.0	48.350	0.31×0.15	0.513×0.356

Usually, the rectangular waveguide uses TE_{10} as main mode. Based on (3-2), its corresponding cutoff wavelength is λ_c=2a. Further, the recommended dimensions in industrial standard rectangular waveguide under different frequency of TE_{10} mode [146],

are selected and listed in Table 3.1.

Table 3.1 confirms the above conclusion: compared with conventional patch antennas, the waveguide geometry is too bulky at low-frequency. This problem would be soothed when the operating frequency increases.

3.1.2 Background of Reflectarray Design Based on Waveguide

Reflectarrays evolve from parabolic reflectors. It aroused overwhelming interests from the 1990s with the development of low-profile printed reflectarrays relying on microstrip technology [26] [38] [41] [65] [85] [147-150]. Actually, the conception of reflectarray was first initiated far early in the 1960s by Berry, Malech and Kennedy, and the first reflectarray was realized in 1963 based on 4×26 waveguide elements [25].

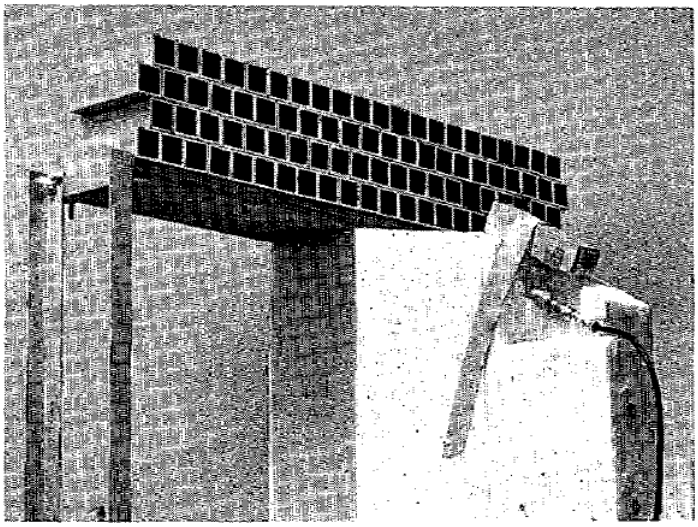

Fig.3.2 4×26 waveguide reflectarray by Berry et al

As depicted in Fig.3.2, the array consisted of short-ended waveguides with variable length. Electromagnetic wave radiated from the feeding horn is transmitted to the waveguides and reflected back from the shorted ends with a phase depending on the travelled distances within the waveguides. Then, the phase law on the radiating aperture can be controlled by appropriately adjusting the lengths of the waveguides.

This reflectarray, though being quite efficient, was very bulky especially because the application was carried out at relatively low microwave frequencies. Now, as the operating frequency moves to *E*-band, it could be a competitive solution. In addition, the structure separates the feeding and the radiation unit is suitable for endfire radiation design [133].

Therefore, in this chapter we will try to design one endfire array based on

rectangular waveguide elements.

3.1.3 Rectangular Waveguide Application in Endfire Array

The working principle of the foreseen endfire array based on waveguides is shown in Fig.3.3. The array consists of waveguide elements with two different heights. These waveguide elements are terminated with short circuit. Here we use the 2-element primary model again, so the spacing between the neighboring unit-cells is $\lambda_0/2$ and each unit-cell's dimension is $\lambda_0/2\times\lambda_0/2$.

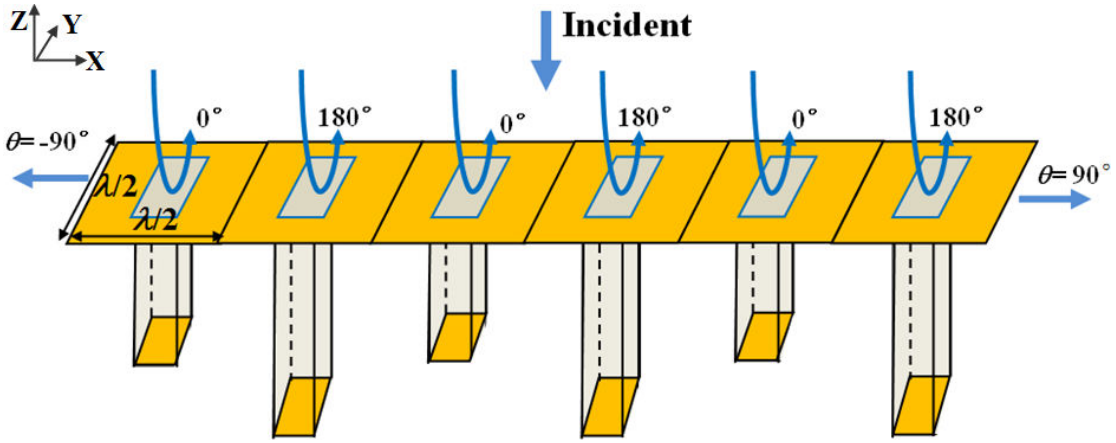

Fig.3.3 working principle for endfire array based on waveguides

3.2 Unit-cell Design Based on Dielectric Filled Waveguide Element

In practical waveguide design, the dominant TE_{10} mode has to be excited. For a standard air-filled rectangular waveguide, the suggested dimensions at *E* band (60-90GHz) in Table are a_0=3.1mm and b_0=1.5mm. In order to accommodate the waveguide element in a $\lambda_o/2\times\lambda_o/2$ cell (as explained before), the waveguide cross-section has to be reduced. This can be accomplished by using a dielectric filled waveguide (DFW) element as the unit-cell. Here, we load the waveguide with RT/Duroid 5870 dielectric material (ε_r=2.33 and loss tangent=0.0012). Then, the initial cross-section is defined by $a_1\times b_1$ with $a_1=\frac{a_0}{\sqrt{\varepsilon_r}}$=2.03mm and $b_1=\frac{b_0}{\sqrt{\varepsilon_r}}$ =1.01mm (see Fig.3.4).

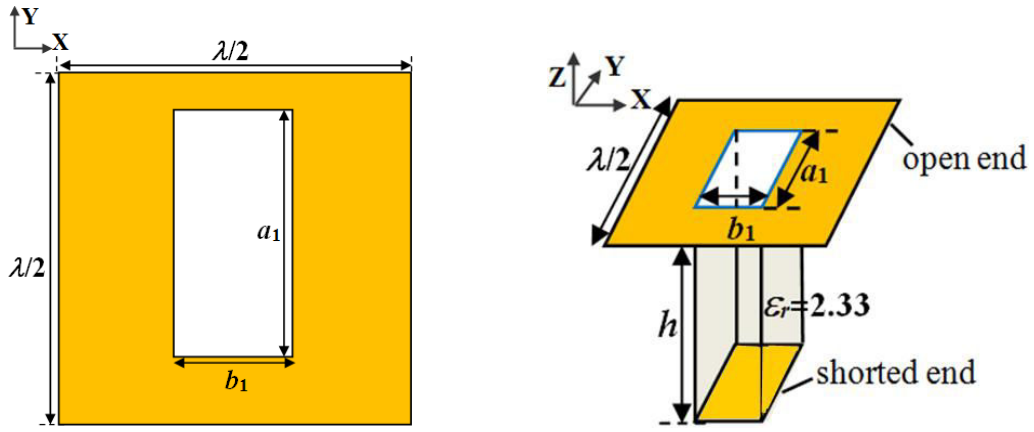

(a) **(b)**

Fig.3.4 Geometry of the proposed DFW element in (a) top view and (b) side view

Based on (3-2), the cutoff wavelength for dominant TE_{10} mode is $\lambda_c=2a_1=4.06$mm. Meanwhile, its guided wavelength can be calculated out with the formula:

$$\lambda_g=\frac{2\pi}{\beta}=\frac{\lambda}{\sqrt{1-\left(\frac{\lambda}{\lambda_c}\right)^2}} \tag{3-3}$$

So at f_0=60GHz, TE_{10} mode corresponds to λ_g=5.54mm.

It should be emphasized that the dimensions of the waveguide cross-section (a_1 and b_1) controls the incident power into the waveguide. If the dimensions are too small, most of the incident power will be reflected by the flange itself and the cell will not operate as expected. Therefore, it's of great importance to perform an optimization for appropriate a_1 and b_1, and make sure almost all the power is captured into the waveguide. This is theoretically similar to the task done before in the DRA structure coupled to phase-delay line. However, we should pay attention to the optimization procedure. As a_1 is determinative for the prescribed dominant mode TE_{10} ($\lambda_c=2a_1$), it can't be varied easily. So the optimization will only be focused on b_1.

3.2.1 Optimization for b_1

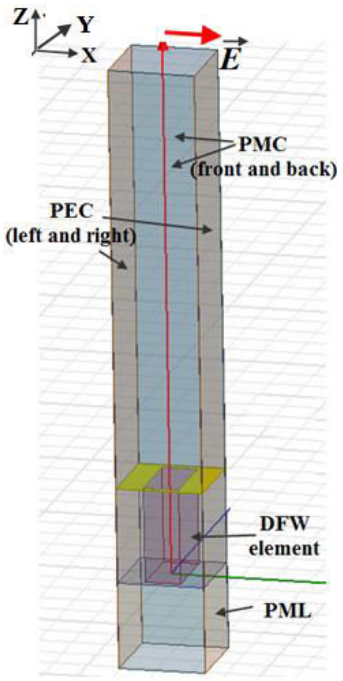

Fig.3.5 simulation setting for b_1 optimization

Fig.3.5 depicts the simulation setting for optimization of b_1. One DFW element is placed in the simulation cell (in the size of $\lambda_o/2\times\lambda_o/2$), which is surrounded with periodic boundaries. Since this structure is quite simple and symmetric, here the waveguide approach is used with PEC and PMC. The DFW element is terminated with PML at the bottom in this simulation, instead of short-end, and its height is set as $\lambda_g/4$=1.385mm. Reference plane is set at the entrance, and excitation is along x-axis. Here we vary b_1 and record reflection coefficient.

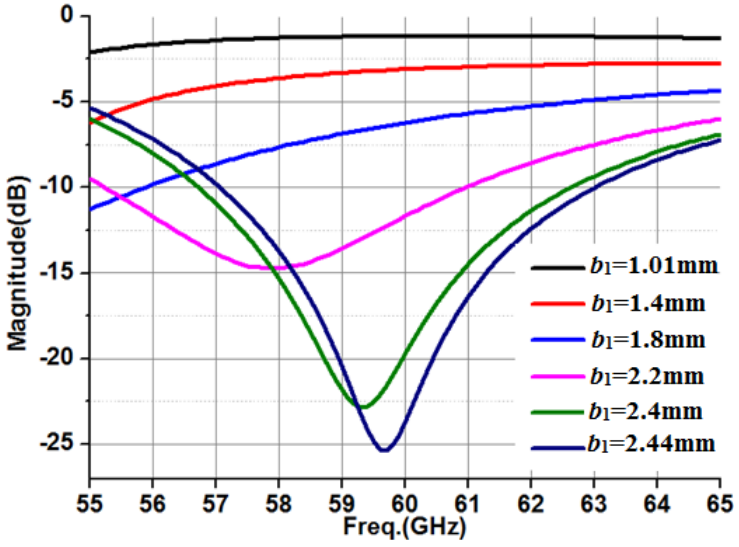

Fig.3.6 optimization for b_1

Fig.3.6 shows the magnitude of the reflection coefficient for different values of b_1 versus frequency. Reflection at 60GHz for initial b_1=1.01mm is as high as -1dB, this means most of the incident power is directly reflected back. As b_1 increases, the cross-section of the DFW element gets larger, so the reflection accordingly witnesses a reduction. When b_1 grows to 2.44 mm (due to the limit of the unit-cell size, $b_1 \leq \lambda_0/2$=2.5mm), the reflection at 60GHz is less than -25dB, which means nearly 95% of the incident power is transmitted into the waveguide. Therefore, the optimization dimension for the DFW element is set as a_1=2.03mm and b_1=2.44mm. However, it should be pointed out, based on this dimension, current dominant mode becomes TE_{01} instead of TE_{10}. Further investigations would find out whether this would cause problems in the array performance. The DFW element's parameters are listed in Table 3.2.

Table 3.2 Parameters for the proposed DFW element

Parameters	**Value**
ε_r	2.33
loss tangent	0.0012
length a_1 (mm)	2.03
width b_1 (mm)	2.44
cutoff wavelength λ_c (mm)	4.06
guided wavelength λ_g (mm)	5.54

With such a configuration, we can proceed with the investigation on the last parameter of the unit-cell which is the height h of the waveguide. As explained in section 1.3, this parameter will be used to tune the reflected phase.

3.2.2 Determination of *h*

For the next step, we will choose two different heights h to produce expected out-phase reflection for the neighboring unit-cells. To realize this, a single unit-cell is simulated now by scanning variable h. It should be noted that, though the cell is surrounded with the same simulation settings, it's no longer terminated by the PML boundary, but by a short circuit. When h is scanned in the range of [0, 2.8] mm, the element's reflection phase at 60GHz is depicted in Fig.3.7.

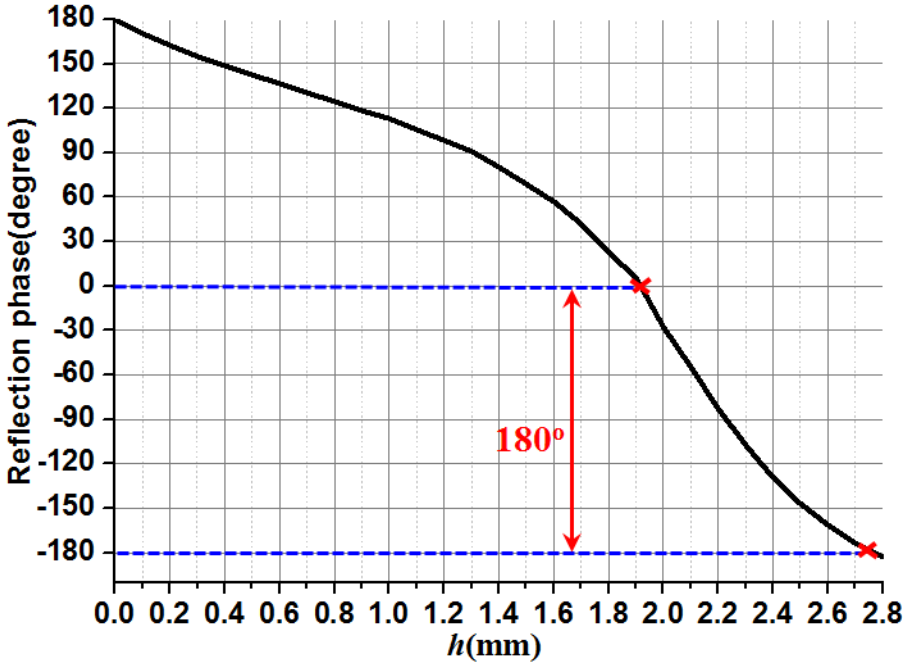

Fig.3.7 DFW element's phase-shifting curve versus *h*

The phase-shifting curve covers a 360° range when h_1 increases from 0 to around 2.8mm. This is logical since this larger height is very close to a half-wavelength ($\lambda_g/2$=2.77mm). Meanwhile, we can notice the 0° reflection appears around h=1.9mm. For the purpose of simplification, we choose 0° and 180° as the successive phases to produce the desired out-phase reflection.

Using a scanning step equals to 0.01mm, we can find the 0° reflection phase corresponds to h_1=1.89mm(it's bigger than a quarter wavelength $\lambda_g/4$=1.385mm, since the reflection phase curve sees a small nonlinearity). Similarly, the -180° phase corresponds to h_2=2.76mm. The reflection magnitudes for h_1 and h_2 are compared in Fig.3.8. Since the dielectric has a low loss, the magnitudes at 60GHz are quite close to -0.1dB.

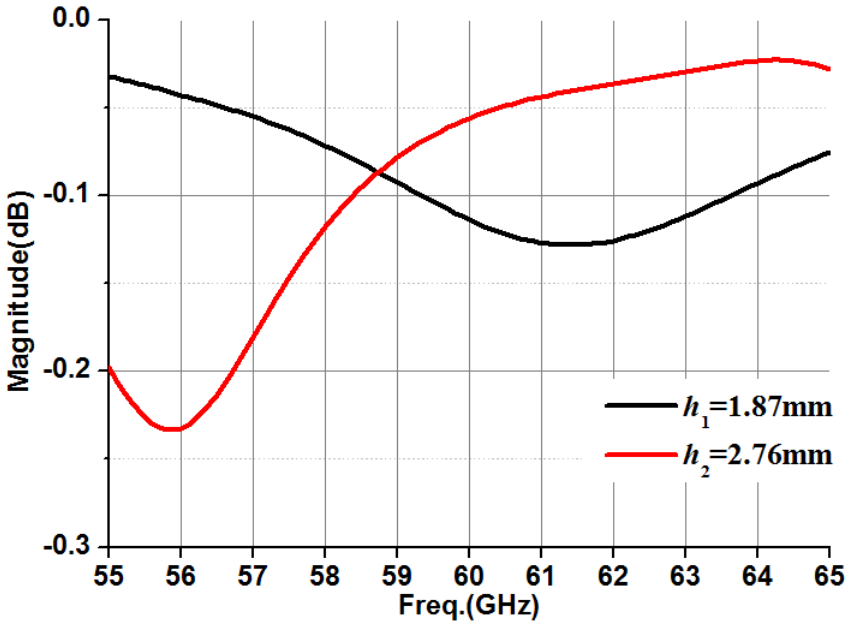

Fig.3.8 Reflection magnitudes for h_1 and h_2

Until now, all the parameters (a_1, b_1, h_1 and h_2) for the single DFW element have been determined. For the next step, we will construct a preliminary array based on the DFW elements, and study its performance.

3.3 Validation and Optimization at Array Level

Based on the DFW elements obtained in last section, a preliminary linear array is studied as shown in Fig.3.9. The simulation boundary is using air box with radiation boundary now. The unit-cells with height h_1 and h_2 are deployed alternatively. Excitation is added with its electric field along x-axis, in the same direction as the array. Consequently, the E-plane locates in XOZ plane. Several configuration will be considered in in the following section with different numbers of the array elements.

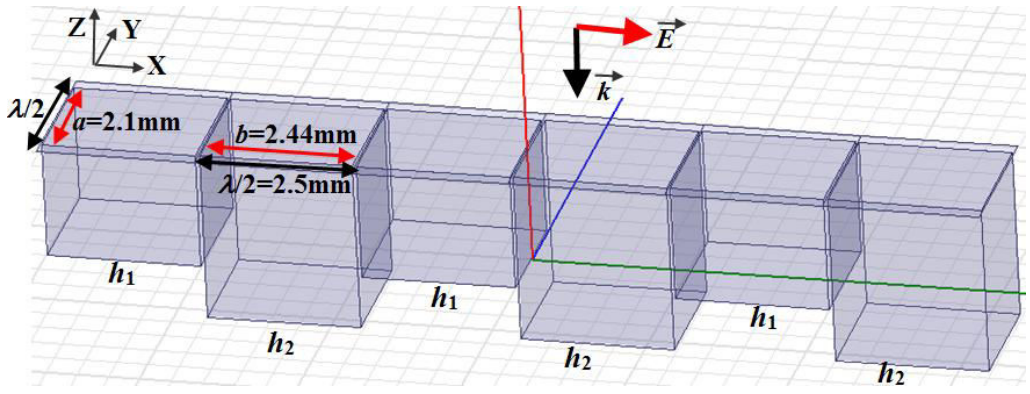

Fig.3.9 Schematic of linear arrays based on DFW elements

3.3.1 Investigation on 6×1 array

We first investigate a 6×1 array (which contains 6 elements along *x*-axis), since this is easier for simulation at the beginning. In order to evaluate the array's endfire radiation performance, the factor of merit $\Psi=\left|\frac{E_\theta\left(\text{endfire}\left(90^\circ\right)\right)}{E_\theta\left(\text{broadside}\left(0^\circ\right)\right)}\right|$ is introduced again.

The 6×1 array is first simulated with h_1=1.89mm and h_2=2.76mm, as deduced from the previous section. Its directivity pattern in E-plane (E_θ) at 60GHz is recorded in Fig.3.10.

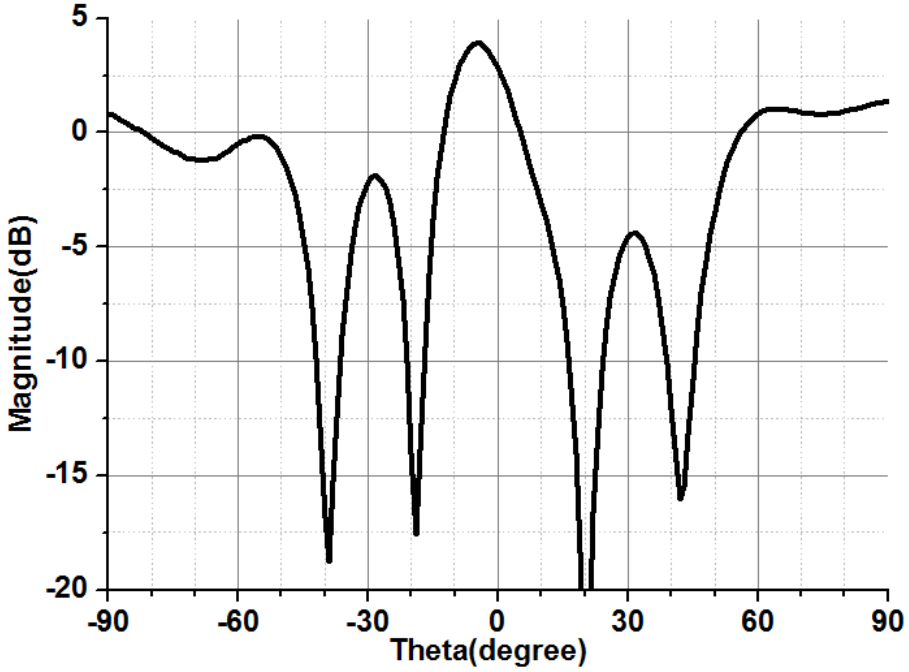

Fig.3.10 Directivity pattern in E-plane (E_θ) at 60GHz for 6×1 array when h_1=1.89mm and h_2=2.76mm

From Fig.3.10, several observations can be made:

1) In horizontal direction ($\theta=\pm90^\circ$), the expected endfire radiation appears, but the magnitude is quite low (around 0 dB).

2) The broadside reflection is high around $\theta=0^\circ$, even much stronger than the endfire radiation. Actually, the referred Ψ is only -1.9dB.

Consequently, this initial design achieves a weak endfire radiation. Similarly, this can be explained by the elements' differed reflection phases due to the varied mutual couplings in different simulation environments. Therefore, the optimizations have to be taken again, in order to maximally improve the array's endfire radiation.

For this optimization, h_1 varies within [1.4, 2] mm and h_2 within [2.5, 2.9] mm, with a 0.1mm step. The corresponding results are presented in Fig.3.11-15.

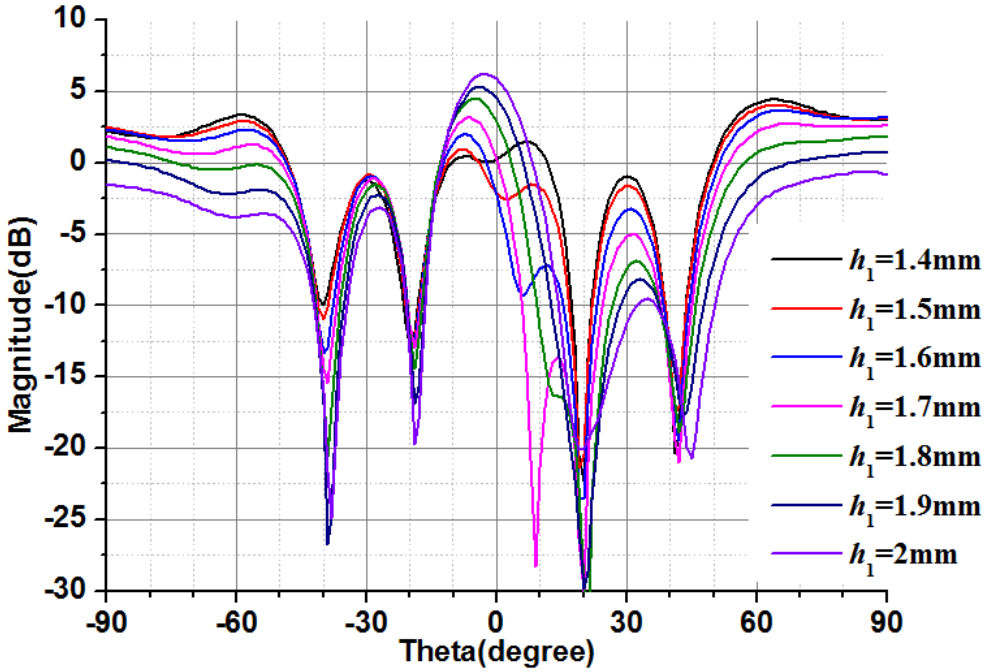

Fig.3.11 Directivity in E-plane (E_θ) when h_1=1.4-2mm and h_2=2.5mm

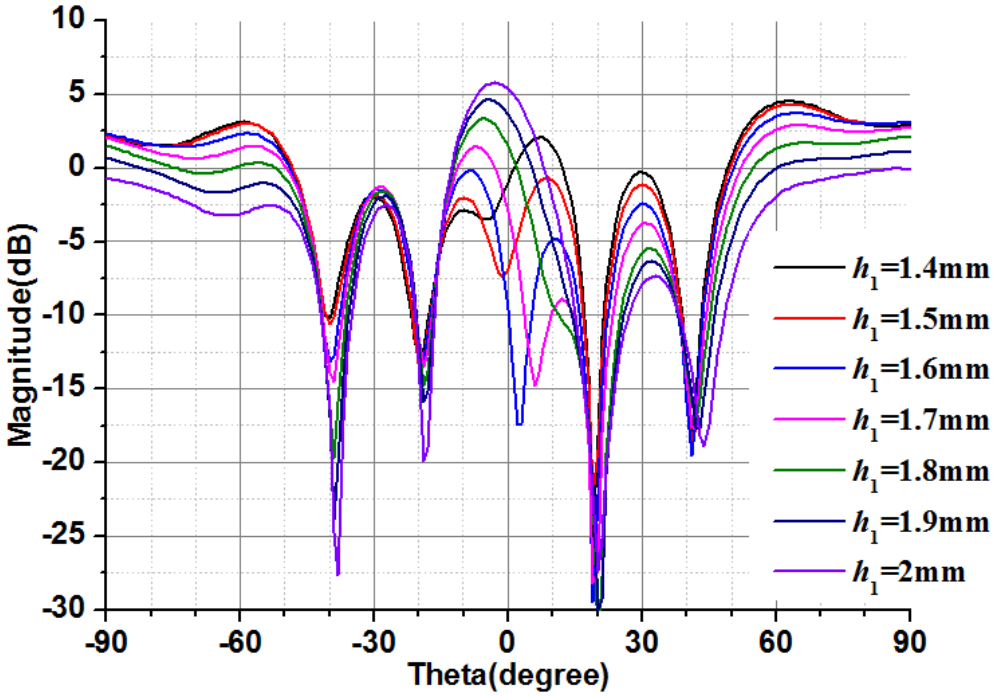

Fig.3.12 Directivity in E-plane (E_θ) when h_1=1.4-2mm and h_2=2.6mm

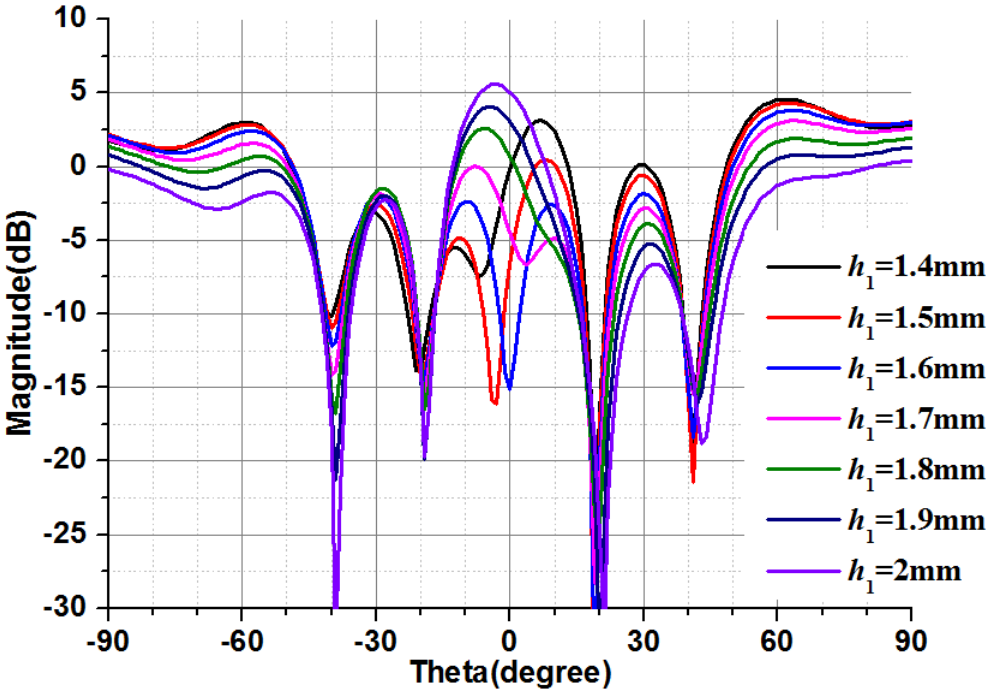

Fig.3.13 Directivity in E-plane (E_θ) when h_1=1.4-2mm and h_2=2.7mm

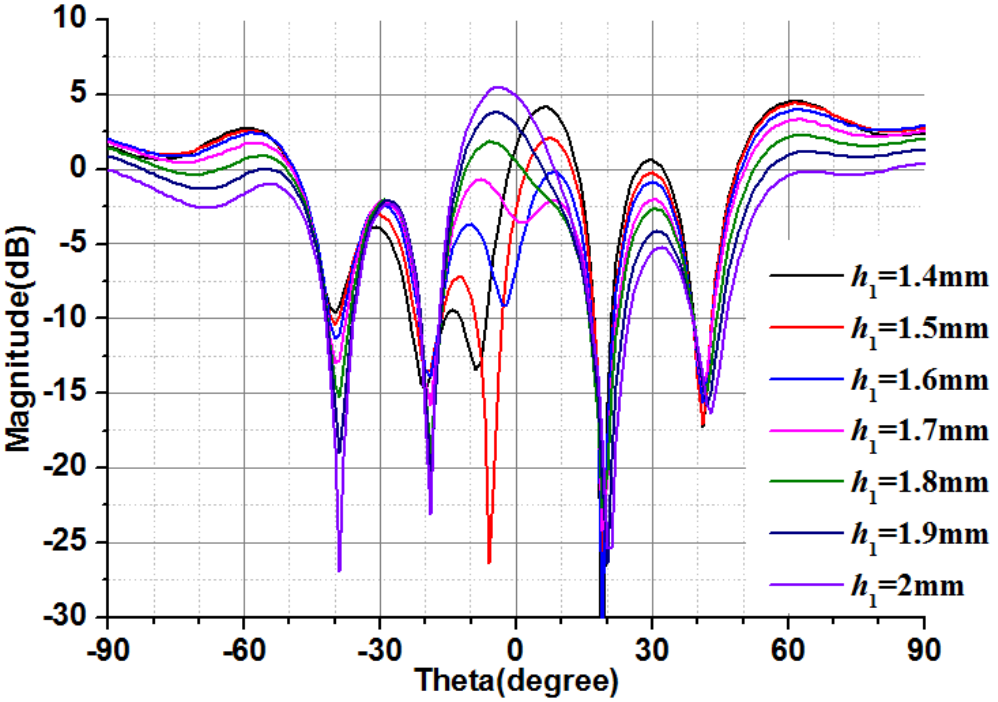

Fig.3.14 Directivity in E-plane (E_θ) when h_1=1.4-2mm and h_2=2.8mm

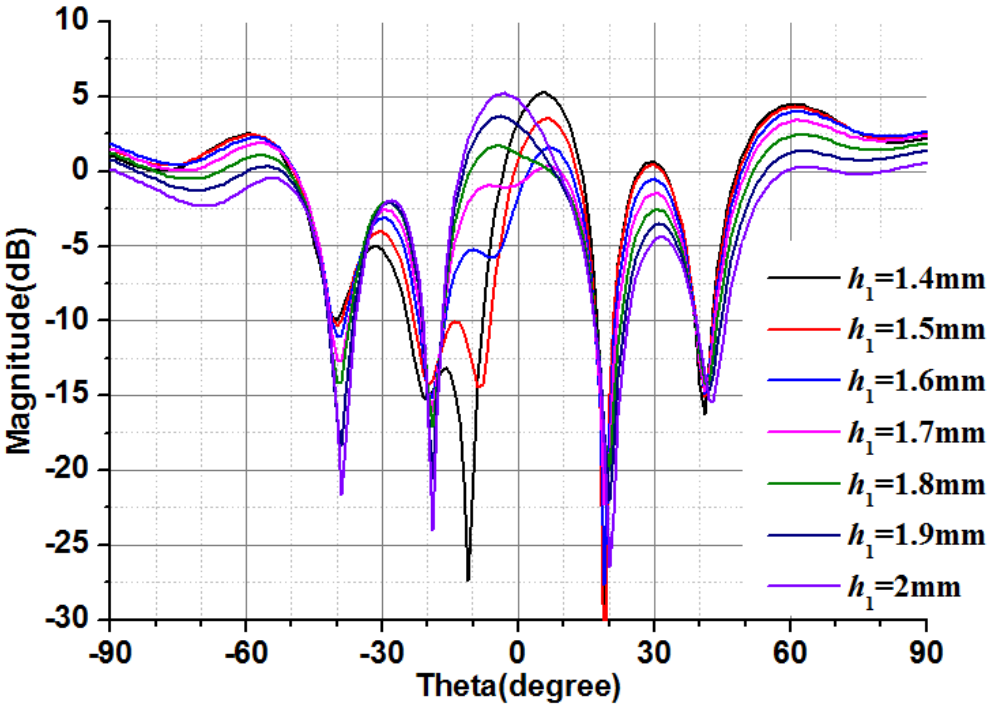

Fig.3.15 Directivity in E-plane (E_θ) when h_1=1.4-2mm and h_2=2.9mm

Based on Fig.3.12-15, Ψ for different h_1 and h_2 are extracted and ploted in Fig.3.16

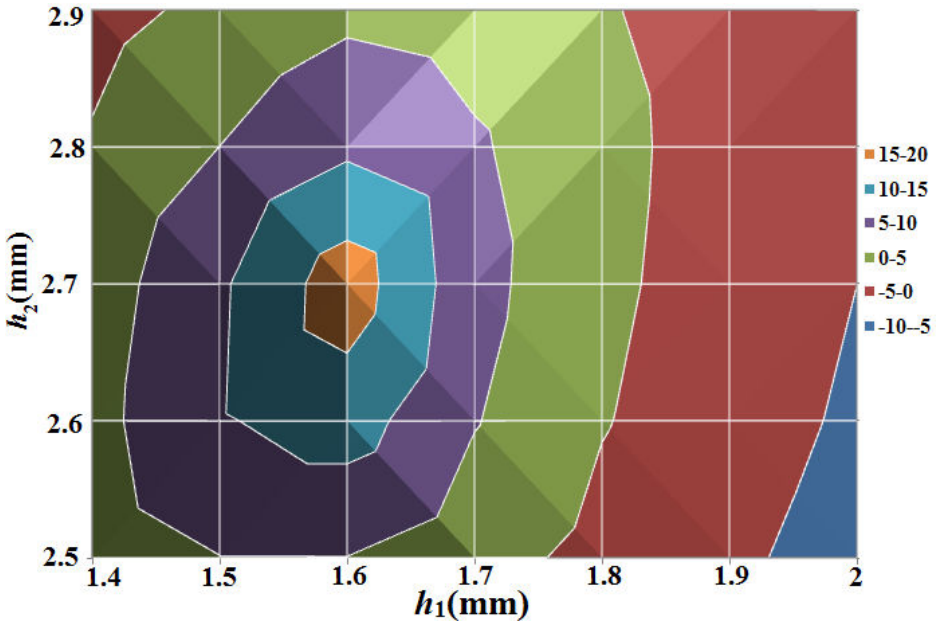

(a)

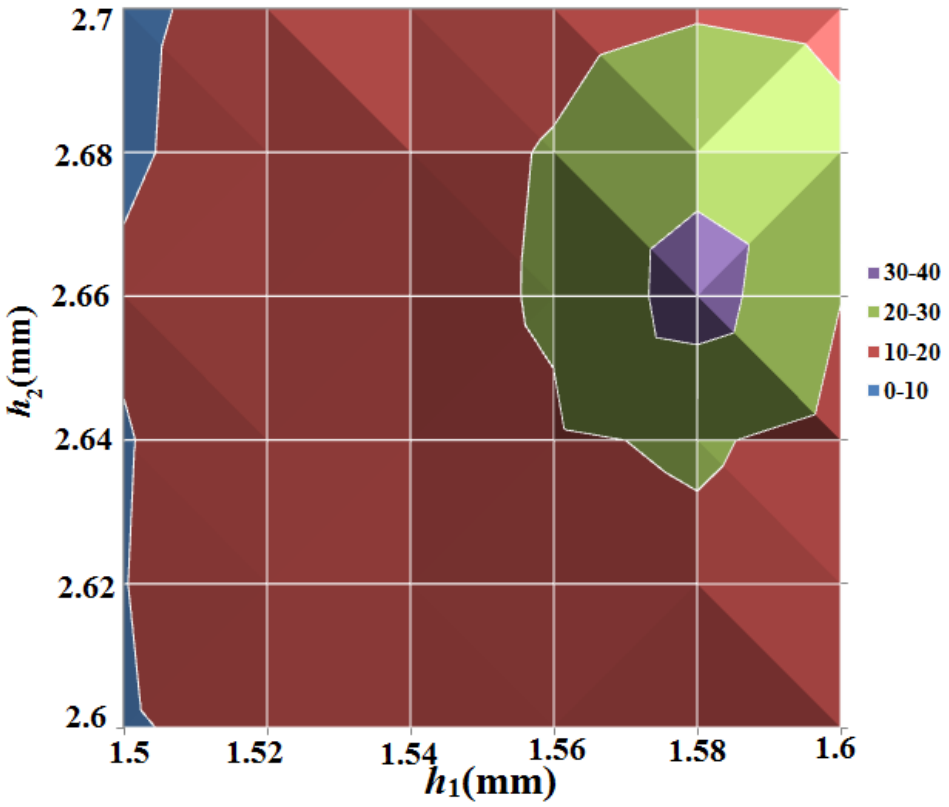

(b)

Fig.3.16 2D contour plots of Ψ when (a) h_1= [1.4, 2] mm and h_2= [2.5, 2.9] mm, and (b) h_1=1.5-1.6mm and h_2=2.6-2.7mm

Clearly, the biggest Ψ is reached when h_1 is in the [1.5, 1.6] mm range and h_2 in the [2.6, 2.7] mm range. Therefore, a further scanning is taken in this range with a smaller step (which is 0.02mm rather than 0.1mm), trying to localize the optimal geometry as precisely as possible (Fig.3.16 (b)). Finally, the optimal dimension is localized as h_1=1.58mm and h_2=2.66mm, with Ψ up to 34.5dB. The corresponding directivity pattern is displayed in Fig.3.17 and compared with the initial result. As can be seen, the radiation at broadside has now perfectly been cancelled and the endfire radiation is increased by 1.7dB.

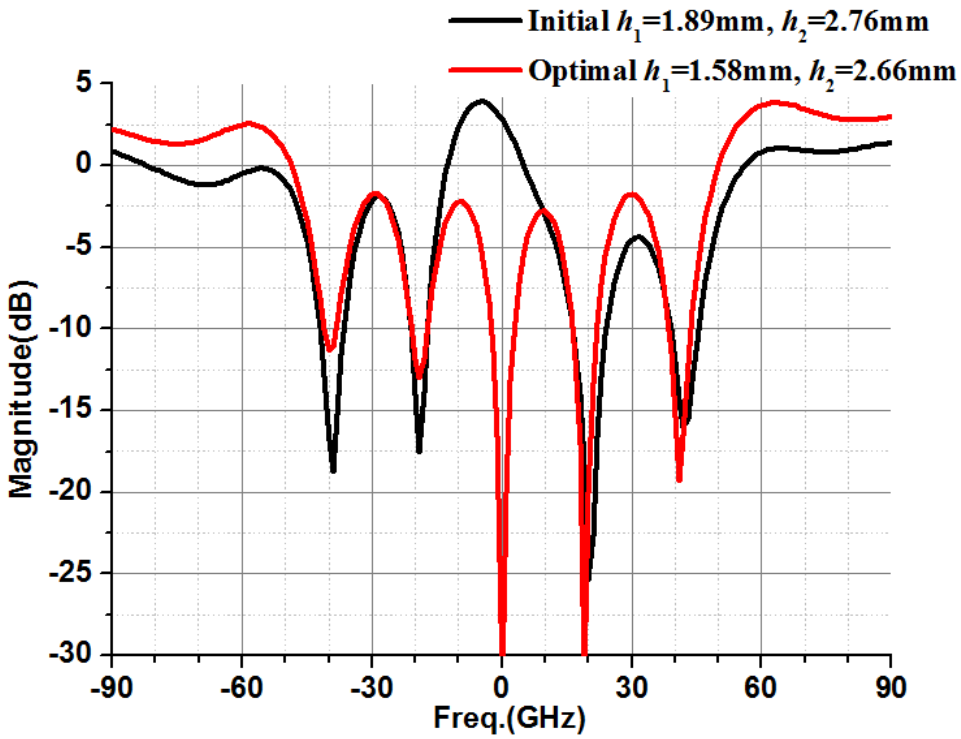

Fig.3.17 Comparison of initial and optimized result for 6×1 array

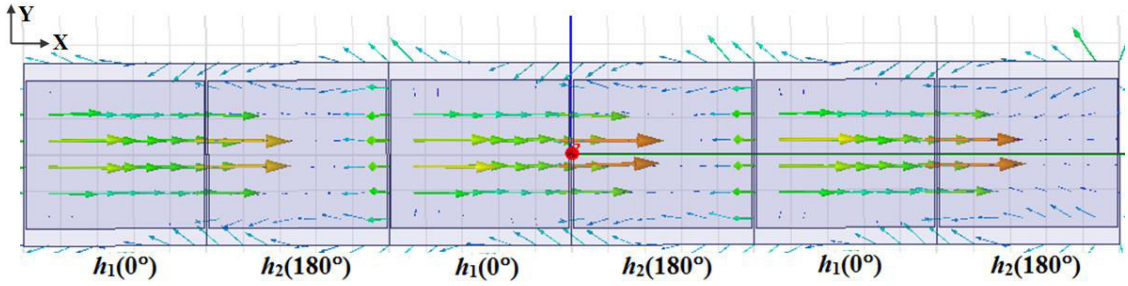

Fig.3.18 Top view of E-field distribution on the array at 60GHz when h_1=1.32mm and h_2=2.66mm

Fig.3.18 presents a top view of the E-field distribution on the array at 60GHz, at the entrance of the waveguides, with the optimized dimension (h_1=1.58mm and h_2=2.66mm). For the first, third and fifth cells (height h_1), the reflected phases are expected to be 0°. Similarly, since the total field (which is observed here) is the sum of the incident and reflected waves, its magnitude is thus high at the entrance of the DFW elements. On the contrary, for the second, fourth and sixth cells, the reflected phases are expected to be 180°. So the total field is almost zero since incident and reflected waves cancel out. The magnitudes of the total field at the entrance of these DFW elements are thus very low. Actually, based on the E-field distribution, we could find out the main mode contributing for the endfire radiation is still TE_{10} mode, which

means the TE_{10} mode leaves no effect on the array performance.

Moreover, a preliminary study of the 6×1 array's bandwidth is carried out. When the incident frequency f varies from 57GHz to 63GHz, the 6×1 array (with optimal geometry) is simulated.

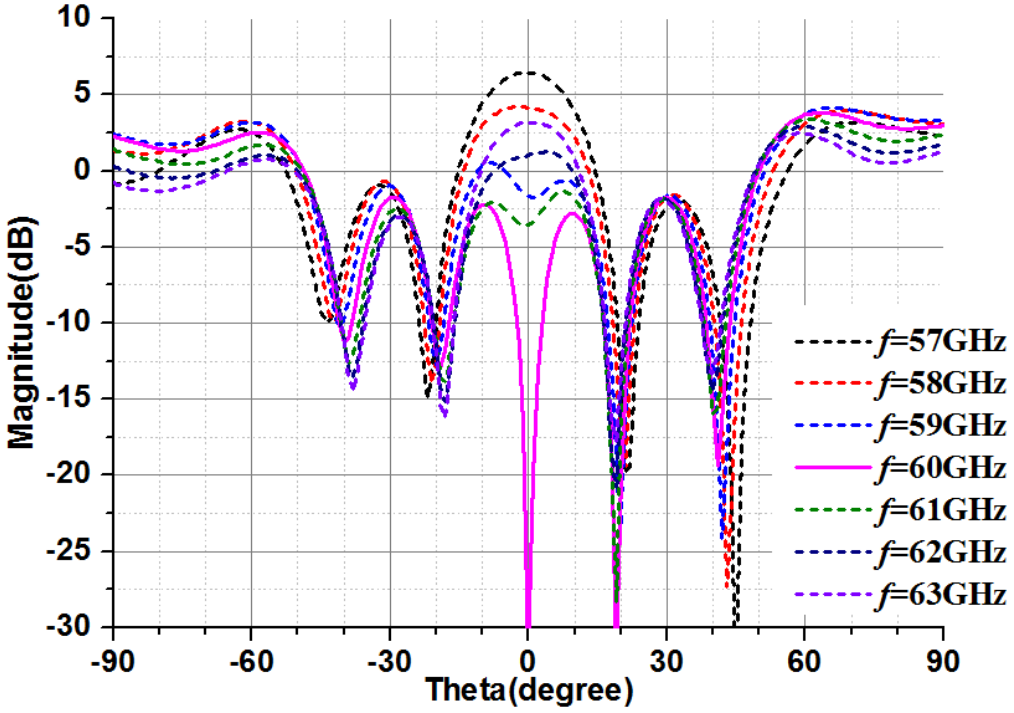

Fig.3.19 Comparison of directivity patterns in E-plane (E_θ) versus variable f when h_1=1.58mm and h_2=2.66mm

Fig.3.19 compares the directivity patterns of the 6×1 array versus frequency f. When f=60GHz (indicated by the solid line in rose color), the array shows good endfire radiation with low broadside reflection. Then, when f changes a little bit (no more than 5%), the broadside reflection around 0° rebounds quickly, and the endfire radiation around ±90° gets weakened. This reveals the array's performance is quite sensitive to f, and its bandwidth around 60GHz is narrow (1-dB bandwidth is 2.5%). A deeper insight on frequency variation will be proposed in the next chapter.

Conclusion

An initial 6×1 array based on the DFW elements has been explored and optimized. The good radiation performances confirm the feasibility of constructing endfire arrays with DFW elements. However, narrow bandwidth appears as a clear limiting factor. For the next step, the array will be expanded along y-axis in order to address a more realistic 2D configuration.

3.3.2 Investigation on 6×6 array

In this section, the linear 6×1 array is expanded along *y*-axis to obtain a 6×6 array, as Fig.3.20 shows. Investigations are taken to see the effects brought by the increased array size.

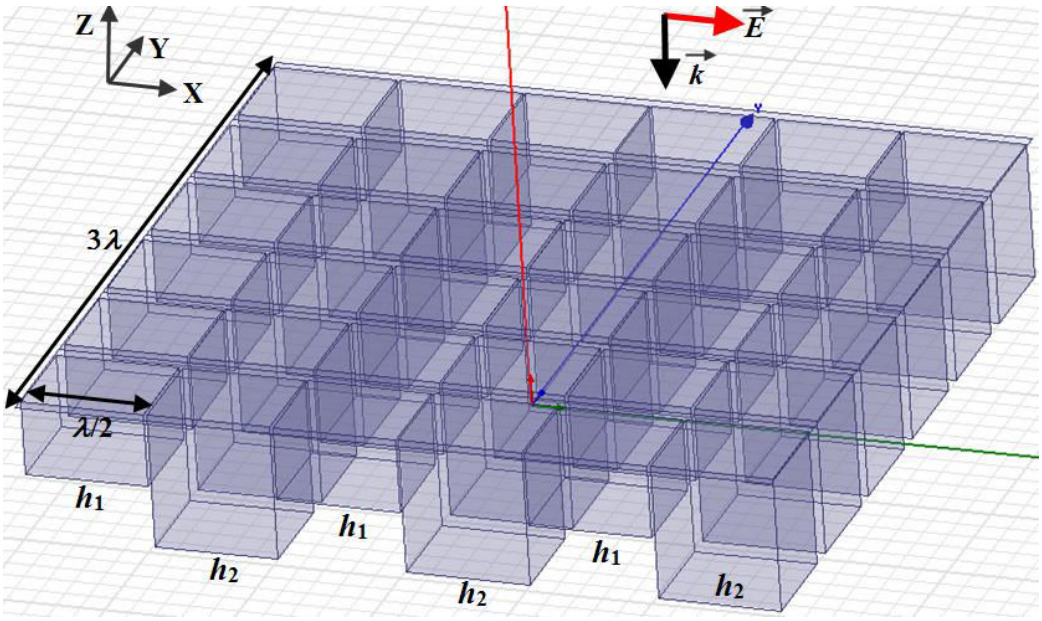

Fig.3.20 Schematic of 6×6 array based on DFW elements

At first, we apply the optimal geometry obtained for 6×1 array in last section (h_1=1.58mm and h_2=2.66mm) as the initial dimension. The directivity pattern in E-plane (E_θ) at 60 GHz is depicted in Fig.3.21.

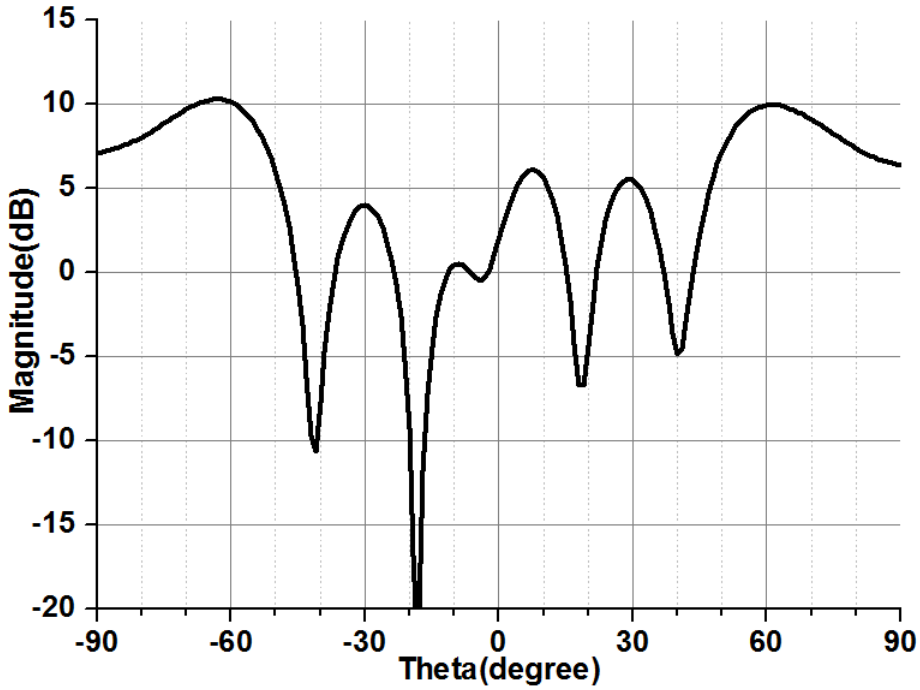

Fig.3.21 Directivity in E-plane (E_θ) at 60GHz for 6×6 array for initial dimension

If we compare with the performance of the 6×1 array (the red curve in Fig.20), the following observations can be made:

1) The maximum direction is shifted from $\theta=\pm 90^\circ$ to $\theta=\pm 61^\circ$.

2) The directivity level at endfire has been increased from 2.4dB to 7.4dB (ΔD =5dB).

2) The broadside reflection around $\theta=0^\circ$ is not as good as for the 6×1 array. As a reference, current Ψ is 4.8dB (for the 6×1 array, it was Ψ=34dB).

The first observation refers to the problem of maximum beam shift, it will be discussed in next chapter in details. For the second observation, the increase of directivity is reasonable, given the expanded array size. But it should be reminded that the magnitude is below expectation. As the array size increases 6 times, the theoretical increase should be ΔD =10log6=7.78dB. Meanwhile, the low Ψ suggests the radiated power is scattered in different directions, that's certainly why the directivity at endfire is weaker than expected.

In conclusion, the element geometries optimized from the 6×1 array can be applied to the 6×6 array to produce endfire radiation, but the performance is far from ideal. Therefore, the element heights have to be re-optimized again for the next step.

To perform this optimization, the scanning range for h_1 is [1.2, 1.7] mm, and for h_2 it is [2.5, 2.8] mm with a 0.1mm step, and the corresponding Ψ is depicted as a 2D

plot in Fig.3.22.

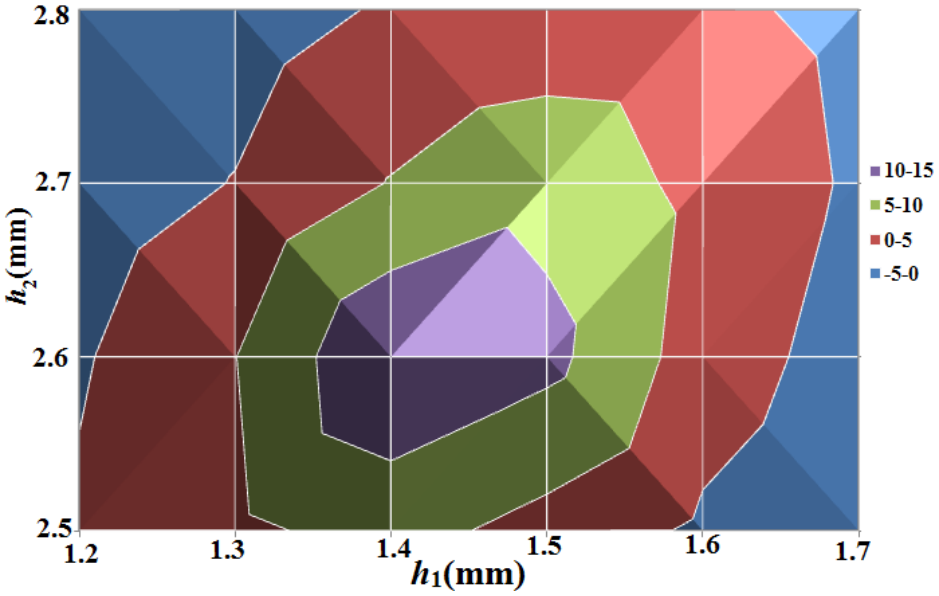

(a)

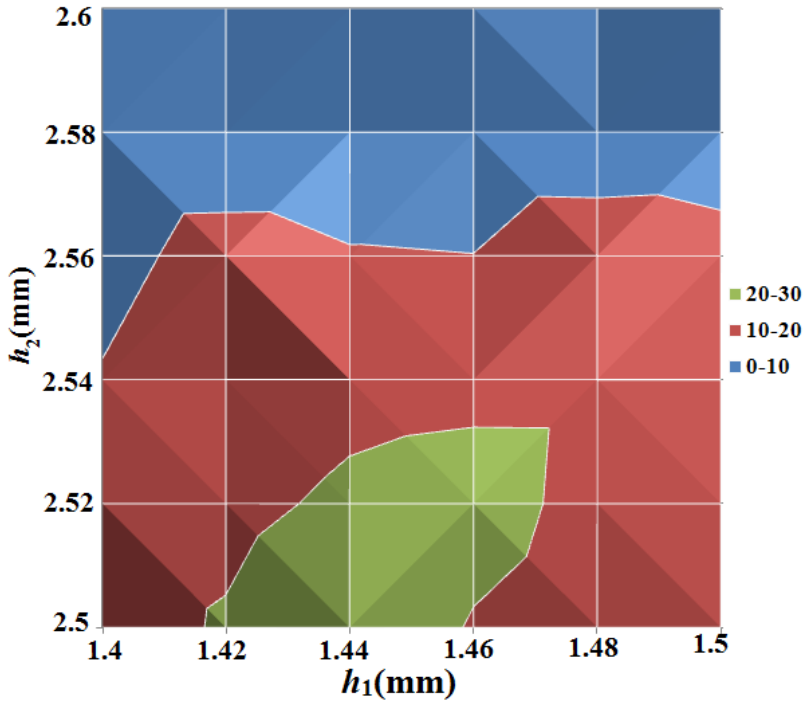

(b)

Fig.3.22 2D contour plots of Ψ when (a) [1.2, 1.7] mm and h_2= [2.5, 2.8] mm, and (b) h_1= [1.4, 1.5] mm and h_2= [2.6, 2.7] mm

The biggest Ψ is reached when h_1 is in the [1.5, 1.6] mm range and h_2 in the [2.6, 2.7] mm range. Similarly, a finer scanning is achieved with a 0.02mm step (Fig.3.22 (b)). Finally, the optimal dimension is localized as h_1=1.46mm and h_2=2.62mm, with

Ψ up to 24.1dB. Its directivity pattern is displayed in Fig.3.23.

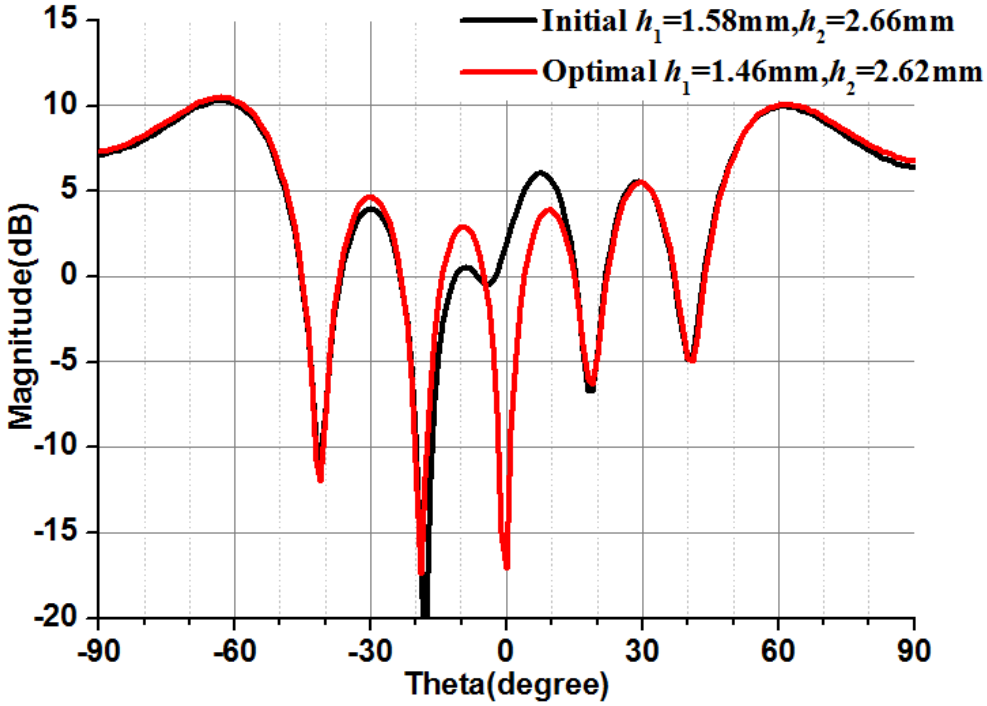

Fig.3.23 Comparison of initial and optimized result for 6×6 array

Fig.3.23 compares the optimal result with the initial one. We can find the broadside reflection has been greatly suppressed and the endfire radiation almost remains the same as the initial one. More important, we should notice the final optimal geometry is close to the initial one. Therefore, it can be concluded that the performance at broadside is quite sensitive to the precise dimensions of the waveguide but it is not the case for the performance at endfire.

This property can be advantageously used in applications where the parasitic reflection at broadside is not a main concern. In that case, the optimization process can be conducted with a small 1D linear array. Then the optimized waveguide heights can be applied to a larger 2D array. This would permit to reduce largely the optimization time since it is conducted with a quite small structure.

Finally, the bandwidth performance for the 6×6 array is also considered. When frequency f varies from 57GHz to 63GHz, the 6×6 array is simulated. The corresponding results are shown in Fig.3.24. The narrow bandwidth problem that has been highlighted previously also appears for the 6×6 array: the broadside rebounds quickly and endfire radiation is reduced (the 1-dB bandwidth is 4.1%). This will be analyzed in details in next chapter.

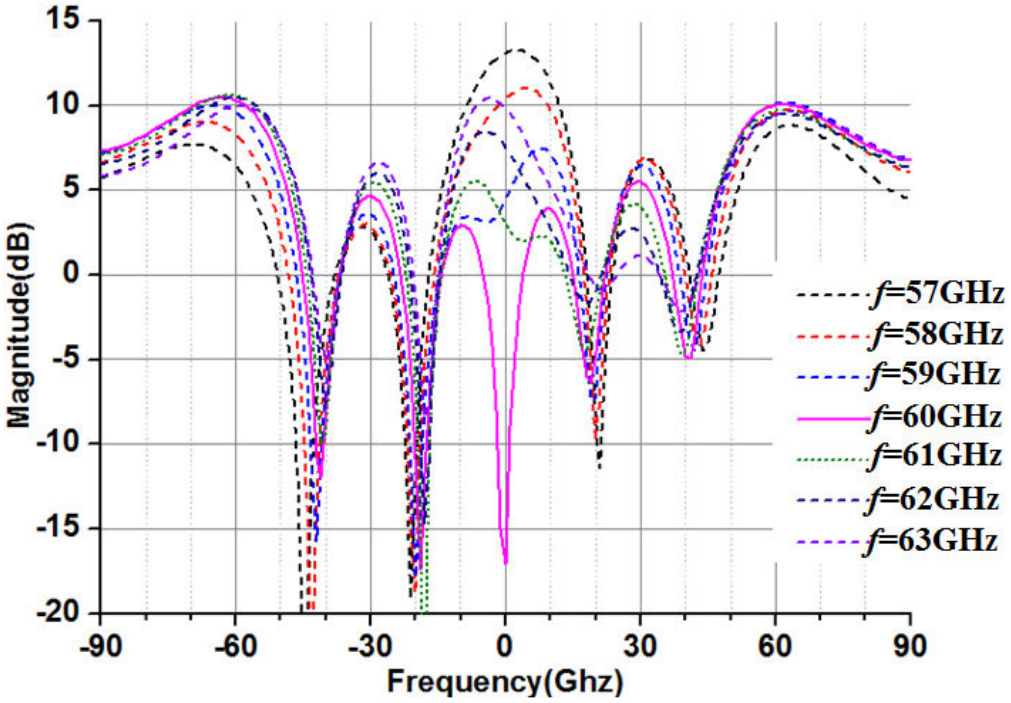

Fig.3.24 Comparison of initial and optimized result for 6×6 array

3.4 Conclusion

In this chapter, a reflectarray for endfire radiation based on rectangular dielectric filled waveguide elements has been investigated. We started from the waveguide element's parameters optimization, produced two unit-cells for out-phase reflection by adjusting height *h*, and simulated one 6×1 array and 6×6 array. With further simulations and optimization, ideal endfire radiation performances are obtained from the two arrays. This result confirms the feasibility of endfire array design based on the DFW element at 60GHz.

Chapter 4 Investigations on Endfire Array Based on Parallel Plate Grooves

Contents

Chapter 4 Investigations on Endfire Array Based on Parallel Plate Grooves

4.1 Introduction

Last chapter investigated endfire array design based on rectangular waveguide [25-26] [144-146]. As demonstrated, the rectangular waveguide element with short-circuit termination can provide a tunable reflection phase in a reasonable range, by simply adjusting the length h between the flange and the shorted-end. Consequently, the rectangular waveguide element can be likewise used as a reflectarray unit-cell, like what has been done before with the DRA.

Actually, this structure benefits from a quite simple design and low loss, so it could be suitable for the foreseen 60GHz application. However, the required fabrication process would not be so simple in practice. As a consequence, in this chapter, we will investigate a simpler solution that can be seen as an evolution of the rectangular waveguide unit-cell [151-152].

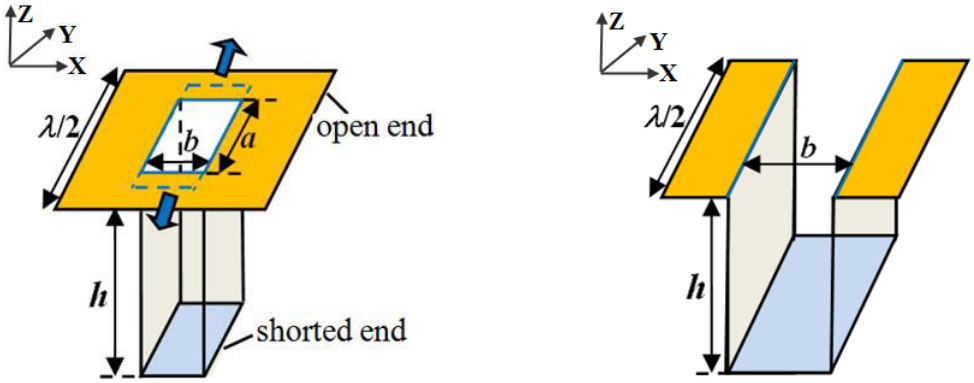

(a) **(b)**

Fig.4.1 Schematic demonstrates the evolution from (a) a rectangular waveguide element to (b) a groove element

As shown in Fig.4.1(a), the transverse dimensions of the rectangular waveguide element are $a \times b$. Now, we propose to replace the rectangular waveguide by a parallel plate waveguide. Considering our $\lambda/2 \times \lambda/2$ unit-cell, this is accomplished by expanding a along y-axis until the rectangular cavity merges with those of the adjacent cells. We thus obtain a metal groove element as depicted in Fig.4.1 (b).

Compared with the rectangular waveguide unit-cell, the fabrication process will be much simpler:

1).Firstly, it is easier to manufacture a single groove than to drill several individual rectangular cavities.

2).Secondly, as we will see later, no dielectric loading will be required anymore.

For the rectangular waveguide element, the main mode is TE_{10} mode; and for the groove element, with the same excitation (here *x*-polarized electric field), the main mode becomes TEM mode. Nevertheless, the groove element has the same working principle: an impinging incident wave is transmitted towards the bottom of the groove and reflected back. The reflection phase is then controlled by the groove height *h*. Therefore, the groove element could also be used in the endfire array design. In Fig.4.2, a brief schematic is depicted to give a global view of such endfire array based on groove element.

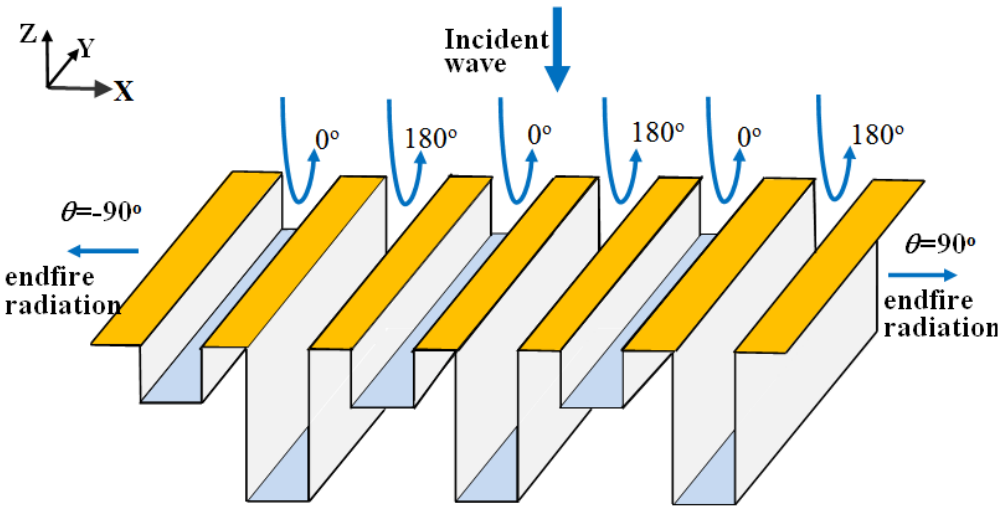

Fig.4.2 Global view of endfire array based on parallel plate groove elements

In this chapter, we will firstly determine the basic geometry of a single groove element working at 60GHz. Then, we will analyze the performance at the array level, considering successively a 6-groove array and a 24-groove array based on the targeted NLOS [155-158] scenario of indoor T-shaped corridor. Specific studies about bandwidth and oblique incidence will also be carried out.

4.2 Design of Single Groove Element

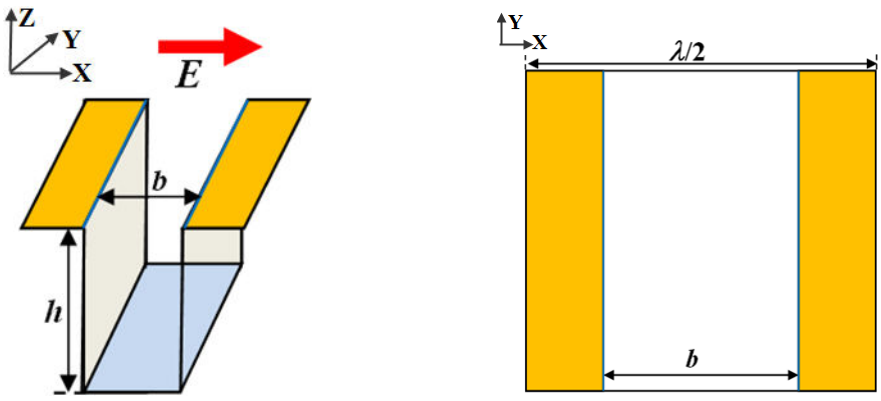

(a) (b)

Fig.4.3 Geometry of single groove element in (a) side view and (b) top view

Fig.4.3 illustrates the geometry of the groove element in details. The excitation polarization goes along *x*-axis. Compared with previous rectangular waveguide, the groove element shares less degree of freedom. The width *b* controls the part of incident wave which is transmitted into the groove, and the height *h* is responsible for reflection phase. So the priority is to determine an appropriate *b* to guarantee that the field is not reflected back before it penetrates into the groove.

4.2.1 Optimization of *b*

In the following, we will try to optimize *b* for the single groove element, like what was done before for the rectangular waveguide. As we have seen, the goal of the optimization is to tune *b* in such a way that the incident wave is not directly reflected back at the entrance of the groove. This will guarantee the incident power is coupled into the metallic groove as expected.

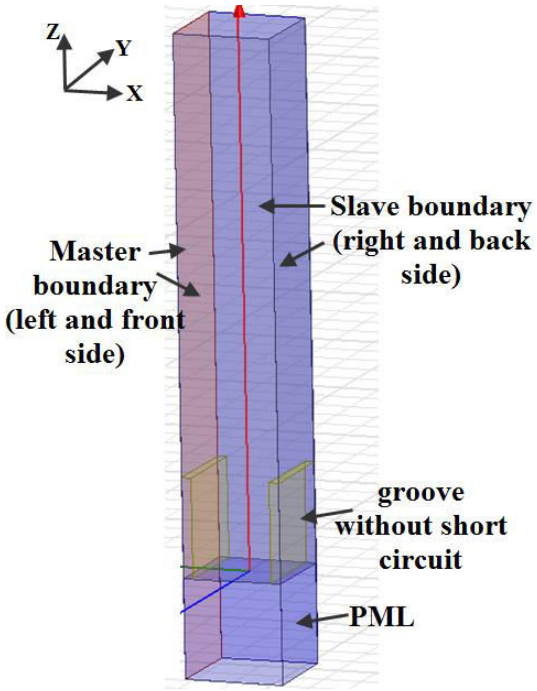

Fig.4.4 Parameter scanning for width *b*

Theoretically, the groove is infinite in the *y*–axis direction. However, for the sake of simplicity, we continue the simulation with $\lambda/2\times\lambda/2$ unit-cell. As presented in Fig.4.4, one single groove element is placed in a $\lambda/2\times\lambda/2$ (2.5mm×2.5mm at 60GHz) simulation cell. As before, the cell utilizes periodic boundaries (Master/Slave) and Floquet excitation. Note that we consider ideal materials (perfect conductors with zero thickness). More realistic conditions will be used later on. For this specific simulation, PML boundaries are used to terminate the parallel plate waveguide (it is not short-circuited anymore) and the reference plane is defined at its entrance. *h* is set to 1.5λ in order to have a well-established TEM mode along the parallel plate waveguide. *b* is scanned between 1.2mm and 2.4mm (2.5mm being the maximum room available for one groove along *x*-axis). The corresponding reflection coefficient S11 is recorded in Fig.4.5.

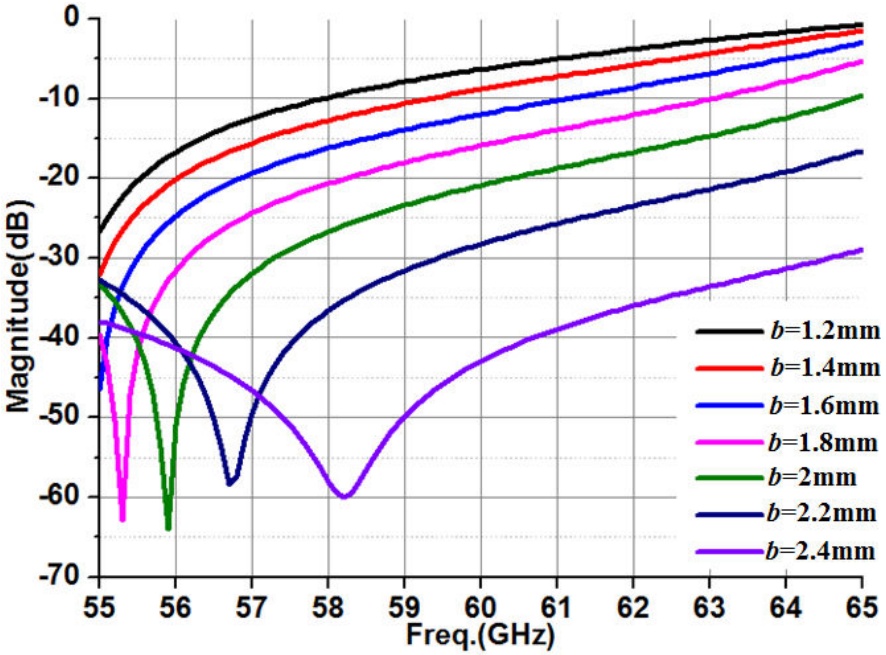

Fig.4.5 S11 parameter for different *b*

Logically, S11 at 60GHz drops quickly as b increases. When b=2mm, S11 is lower than -20dB at 60GHz. This magnitude is already small enough to guarantee almost all the power is transmitted into the groove. If we continue to increase b, the reflection is still lower but the groove becomes so large that the distance between two successive ones would be very small (<0.5mm), which would make the fabrication tricky. So, as a trade-off between fabrication simplicity and performance, b will be set to 2mm in the following.

4.2.2 Determination of *h*

For the next step, we have to choose two different heights h to produce expected out-phase reflection. The simulation now assumes the parallel plate waveguide is terminated by a short circuit. Here we assume the successive phases to be produced are 0˚ and 180˚ for convenience. Fig.4.6 (a) depicts the reflected phase at 60GHz for h varying between 0 and 2.5mm. The searched reflection phases correspond to h_1=1.19mm and h_2=2.5mm respectively. Note that h_2 is equal to $\lambda/2$ and h_1 is quite close to $\lambda/4$. As the metallic groove element has no loss, the reflection magnitude in Fig.4.6 (b) is almost 0 dB for the whole range of h. Subsequently, h_1 and h_2 share the same reflection magnitude, which is of course also required for radiation cancellation at broadside.

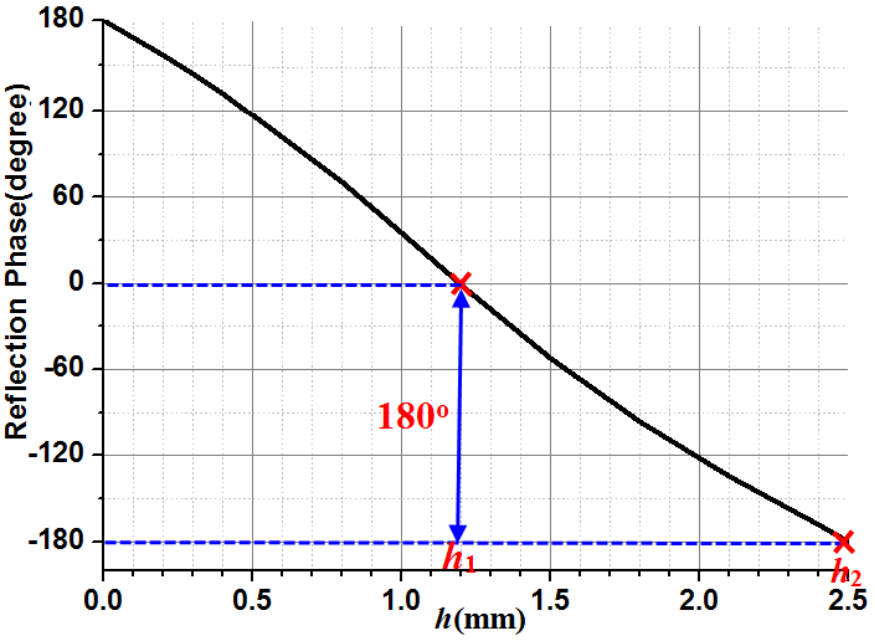

(a)

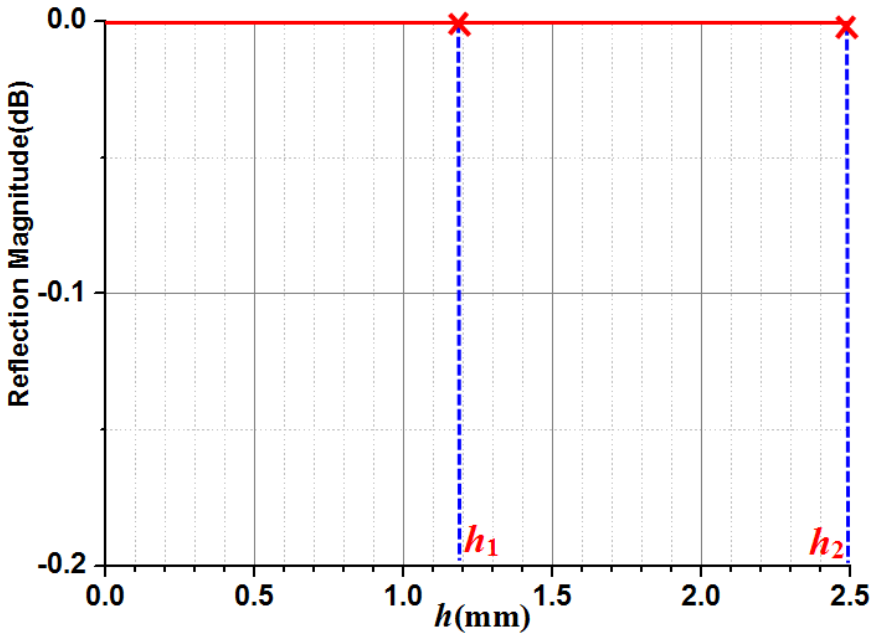

(b)

Fig.4.6 Reflection performance of (a) curve of reflection phase versus *h*, and (b) Reflection magnitude

Until now, the two parameters for a single groove element have been determined. The performance of a preliminary array based on the groove elements will be studied in the next section.

4.3 Validation and Optimization at Array Level

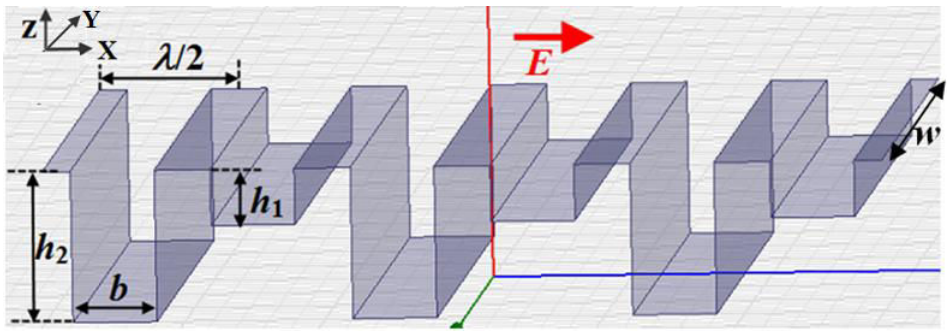

Fig.4.7 Array based on groove elements

As depicted in Fig.4.7, the general array configuration is built by alternating groove elements with h_1 and h_2 heights. Radiation boundary is used now. The excitation electric field is polarized along x-axis, so the E-plane corresponds to XOZ plane. Several arrays with different width w will be investigated in the following.

4.3.1 Preliminary Array Validation (w=2.5mm)

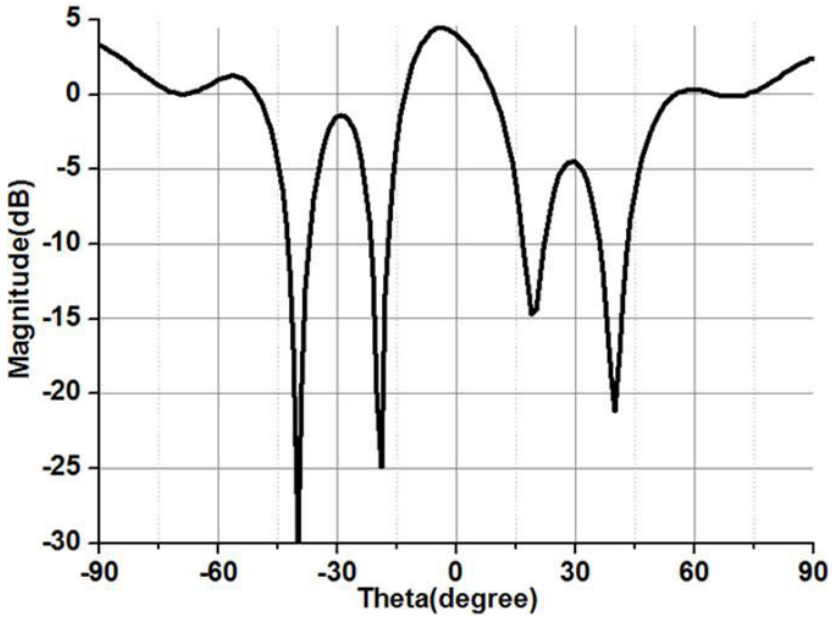

Fig.4.8 Directivity pattern in E-plane (E_θ) (h_1=1.19mm and h_2=2.5mm, f=60GHz)

In order to validate the previous groove design, a preliminary array with 6 grooves and w=2.5mm (total size of 15mm×2.5mm) is first studied. This initial small width was chosen to make simulation faster. The successive groove heights are h_1=1.19mm and h_2=2.5mm as optimized from previous section. The array's far-field

directivity pattern in E-plane (E_θ) at 60 GHz is drawn out in Fig.4.8. The result is not ideal with a strong broadside reflection. This may be due to the fact that the reflected phase has been optimized for a periodic array made of identical grooves, which is not the case here. So, further optimizations are necessary to improve this initial result.

For the optimization, h_1 varies within the [0.6, 1.3] mm range and h_2 within the [2.2, 2.6] mm range, with a 0.1mm step. The corresponding results are presented in Fig.4.9-13. In addition, the parameter Ψ is used again in Fig.4.14 as a global figure of merit, providing a more synthetic view.

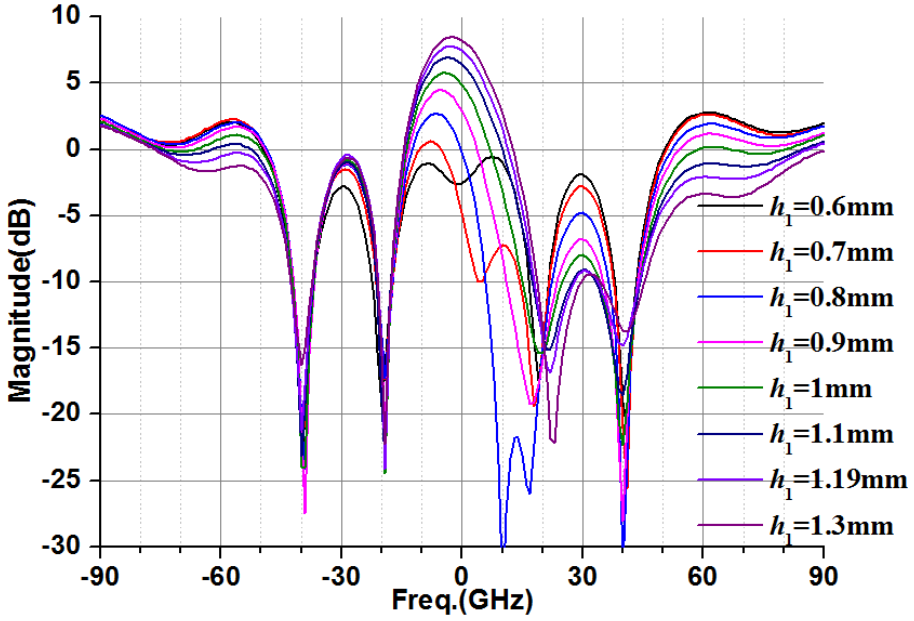

Fig.4.9 Directivity pattern in E-plane (E_θ) for h_1=0.6mm-1.3mm and h_2=2.2mm

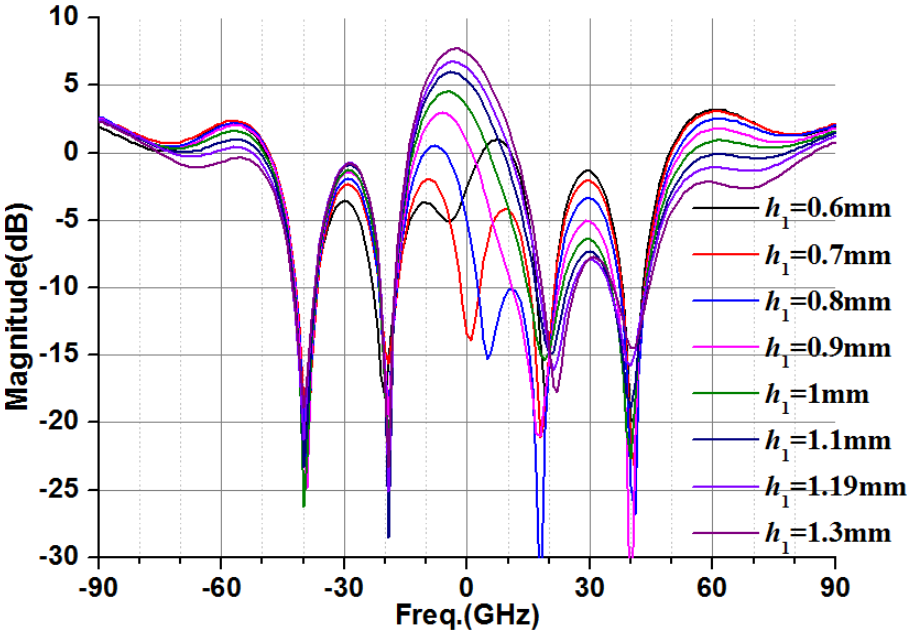

Fig.4.10. Directivity pattern in E-plane (E_θ) for h_1=0.6mm-1.3mm and h_2=2.3mm

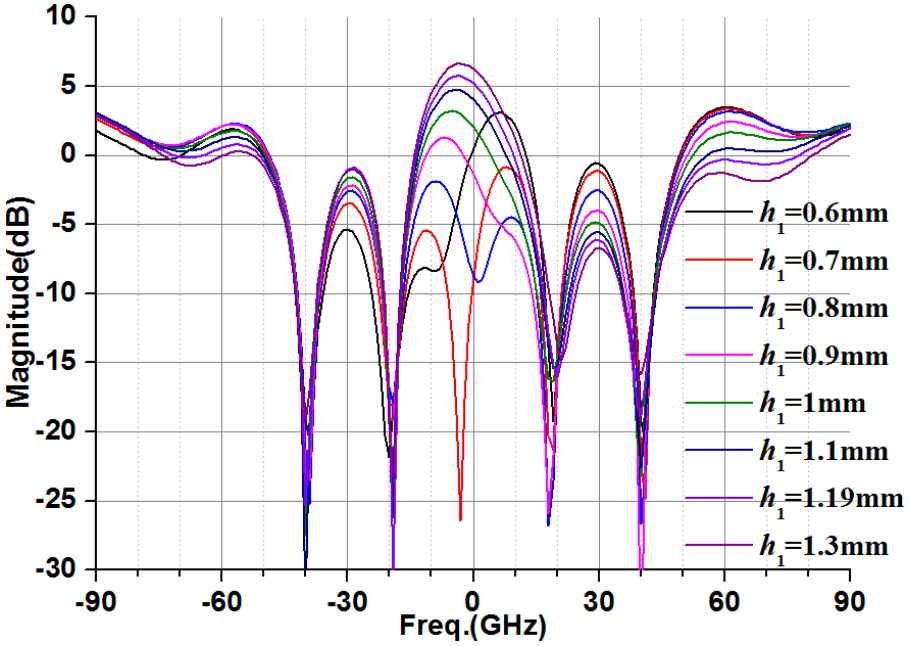

Fig.4.11 Directivity pattern in E-plane (E_θ) for h_1=0.6mm-1.3mm and h_2=2.4mm

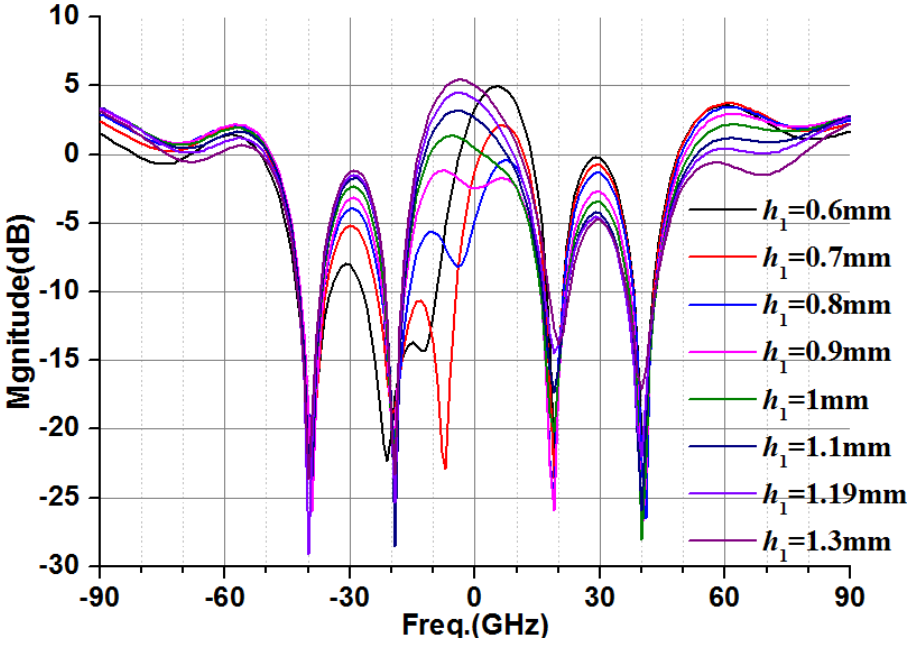

Fig.4.12 Directivity pattern in E-plane (E_θ) for h_1=0.6mm-1.3mm and h_2=2.5mm

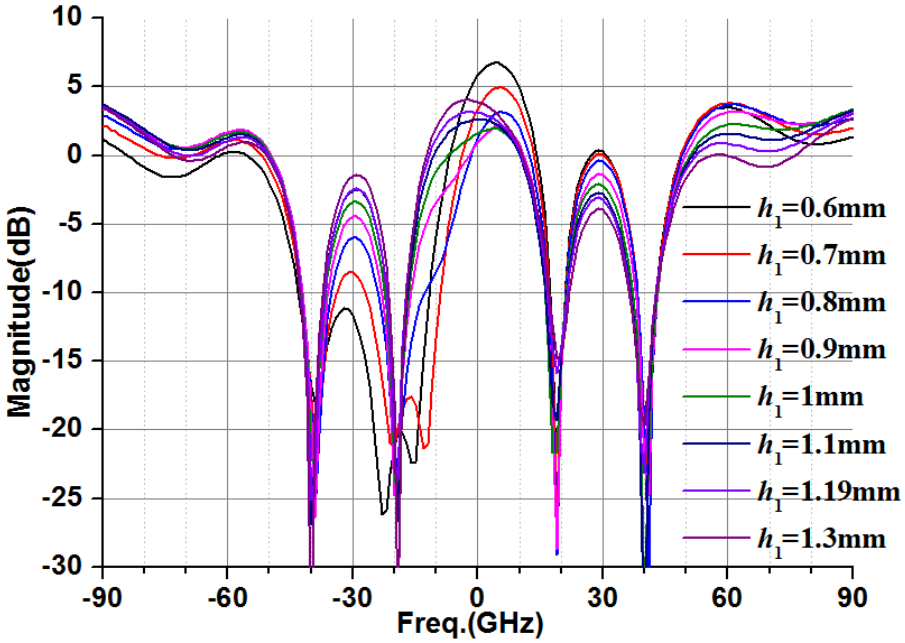

Fig.4.13 Directivity pattern in E-plane (E_θ) for h_1=0.6mm-1.3mm and h_2=2.6mm

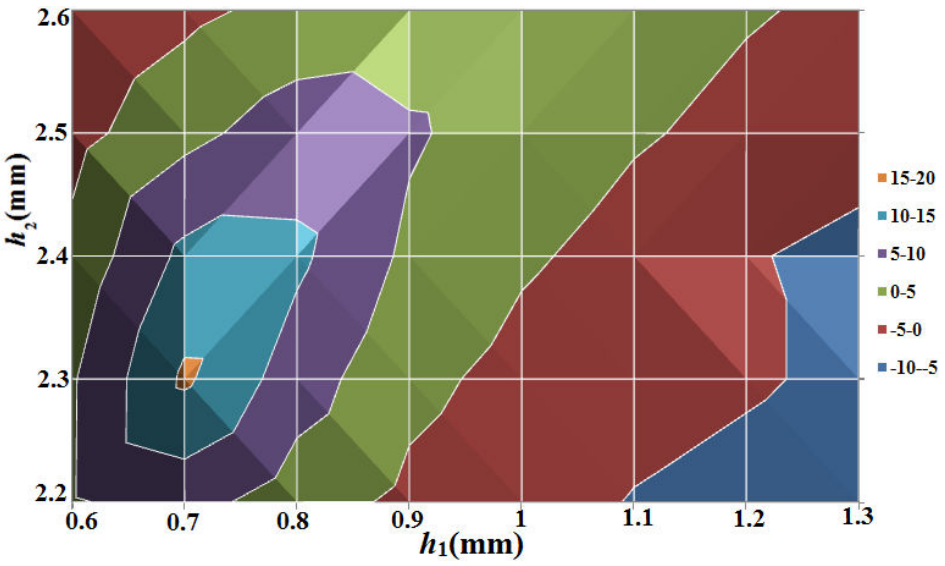

(a)

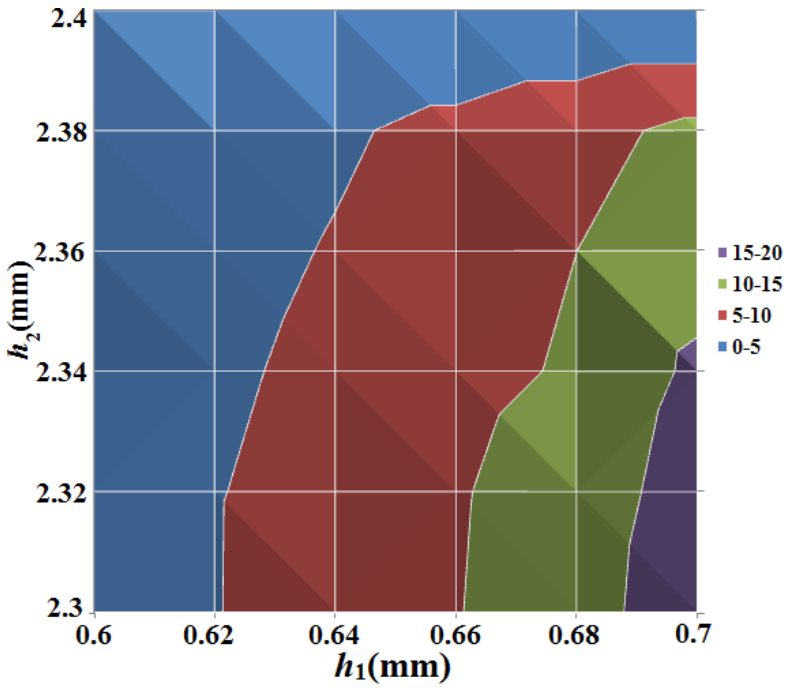

(b)

Fig.4.14 2D contour plots of Ψ when (a) h_1 in [0.6, 1.3] mm and h_2 in [2.2, 2.6] mm and (b) h_1 in [0.6, 0.7] mm and h_2 in [2.3, 2.4] mm

From Fig. 4.14 (a), the best value of Ψ is reached for h_1 in [0.6, 0.7] mm and h_2 in [2.3, 2.4] mm. Within this range, a further optimization with a smaller step (which is 0.02mm) is then carried out (Fig.4.14 (b)). Finally, the optimal dimension is localized as h_1=0.7mm and h_2=2.32mm, which is shown in Fig.4.15. As can be seen, the radiation at broadside has now perfectly been cancelled and the maximum reflection occurs close to endfire.

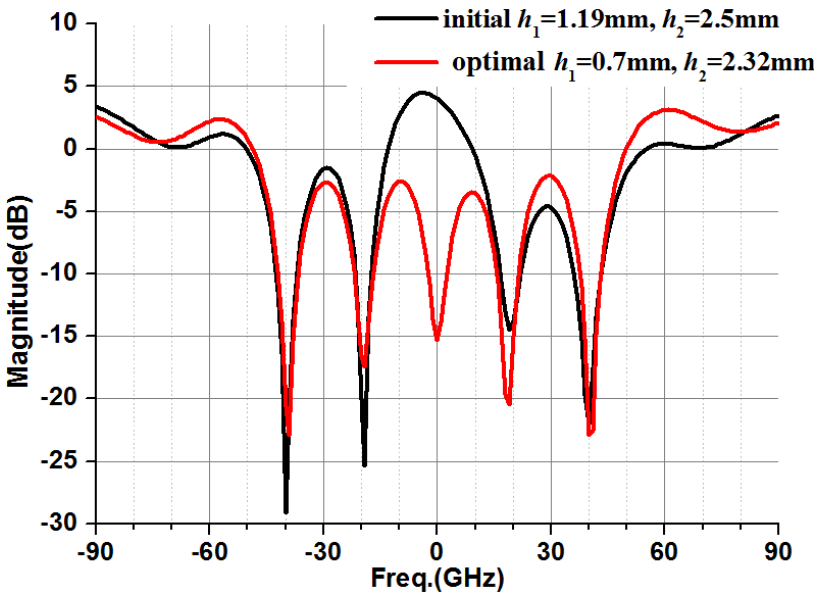

Fig.4.15 Comparison of initial and optimized result for 6-groove array with w=2.5mm

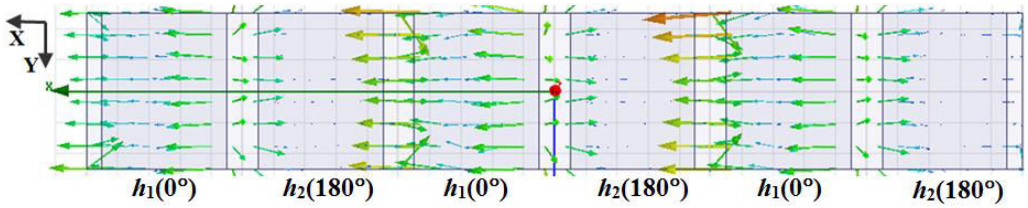

Fig.4.16 Top view of E-field distribution on the array at 60GHz when h_1=0.7mm and h_2=2.32mm

Fig.4.16 presents a top view of the E-field distribution on the array at 60GHz, at the entrance of the grooves, with the optimized dimension (h_1=0.7mm and h_2=2.32mm). This E-field distribution is similar to the one we observed with the dielectric filled rectangular waveguide. For the first, third and fifth grooves, the expected reflected phases are 0°. Then, the total field is the sum of the incident and reflected waves. The magnitude of the total field is thus high at the entrance of these grooves. On the contrary, for the second, fourth and sixth grooves, the expected reflected phases are 180°. Then, the total field is almost zero since incident and reflected waves cancel out. The magnitude of the total field at the entrance of these grooves is thus very low. Similarly, the effect of the array finiteness can be observed when the magnitudes are not the same on the grooves in the middle of close to the ends.

Conclusion

The initial array based on metal groove elements has been explored and optimized. It confirms the feasibility of constructing endfire arrays with groove elements. For the next step, the width *w* will be expanded to 15mm.

4.3.2 Studies on the Effect of *w*

In this section, we investigate the benefit that may be brought by an increase of *w*. We also study whether the previous optimized heights still apply for a larger array.

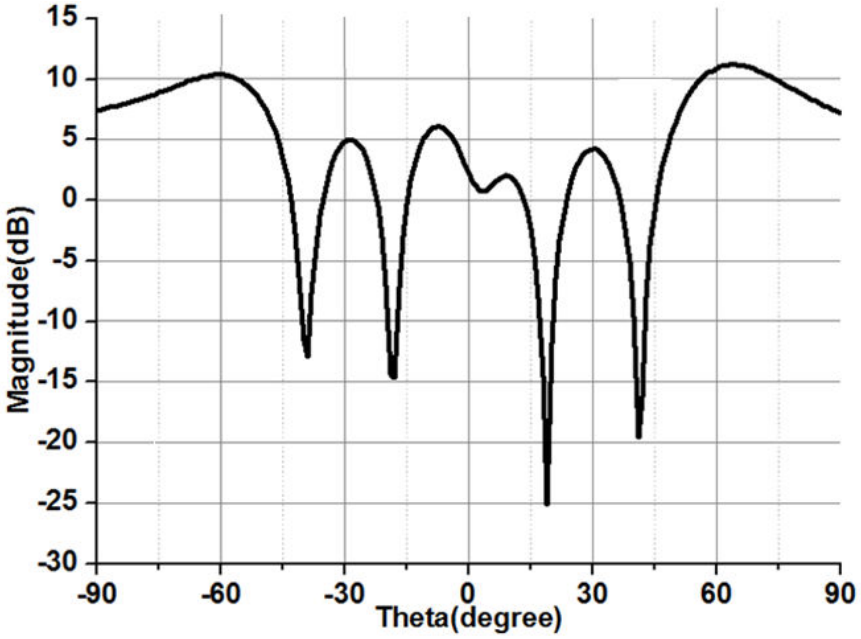

Fig.4.17 Directivity pattern in E-plane (E_θ) for 6-groove array with *w*=15mm

To do so, the width *w* is enlarged from 2.5mm to 15mm (total size of 15mm×15mm). The successive grooves have heights h_1=0.7mm and h_2=2.32mm as optimized from last section. The directivity pattern in E-plane (E_θ) is depicted in Fig.4.17. Three remarks can be made after comparing this pattern to that of the smaller array (red curve in Fig.4.15):

1).The directivity level at endfire has been raised from 2.2dB to 7.5dB (ΔD =5.3dB).

2).The field at broadside is not minimum anymore (current Ψ=5dB instead of 17.8dB when *w*=2.5mm).

3).The maximum beam is obtained at θ=±60° instead of ±90° (expected for the endfire radiation).

Regarding the increase of directivity, it directly results from the larger size of the radiating aperture (increased by 6 times) and could be expected. However, we can note the improvement is below expectation: the theoretical increase ΔD should be 10log6=7.78dB since the field at maximum angle is multiplied by 6 (i.e. radiated power at maximum multiplied by 36) while the incident power (i.e. total radiated power) is multiplied by 6 in the same time.

Then, the poor performance at broadside suggests the groove heights have to be re-optimized again. It could also partly explain why the directivity is not as high as it should.

Finally, the shift of the maximum beam from ±90° to ±60° is a bit tricky and will be addressed later.

In this section, we will mainly focus on the cancellation of the radiation at broadside. To do so, we repeat the optimization of the grooves height. A synthesis is given where the variation range is narrowed down to [0.5, 1] mm for h_1 and [2.1, 2.4] mm for h_2. The corresponding patterns are shown in Fig.4.18-21.

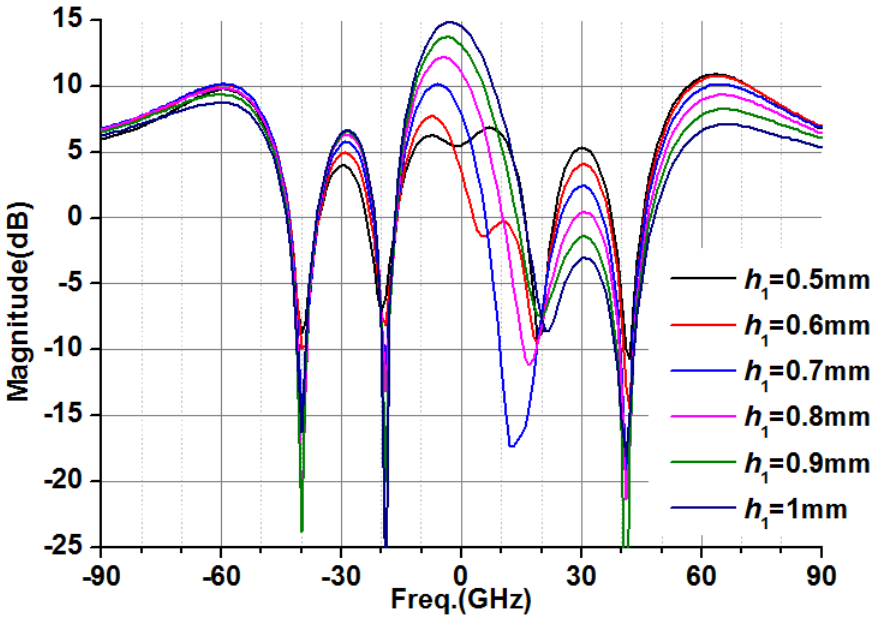

Fig.4.18 Directivity pattern in E-plane (E_θ) for h_1=0.5-1mm and h_2=2.1mm

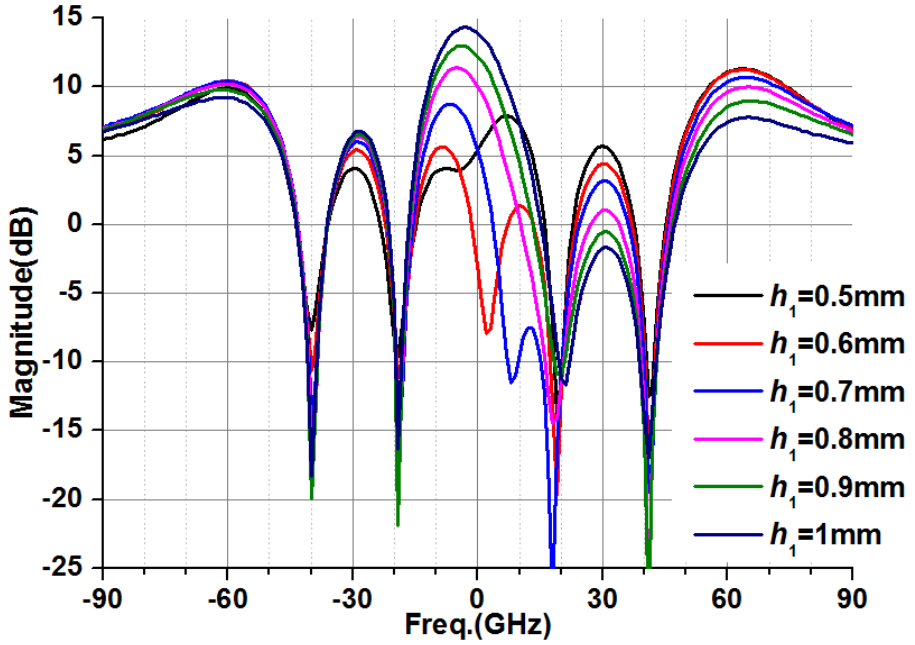

Fig.4.19 Directivity pattern in E-plane (E_θ) for h_1=0.5-1mm and h_2=2.2mm

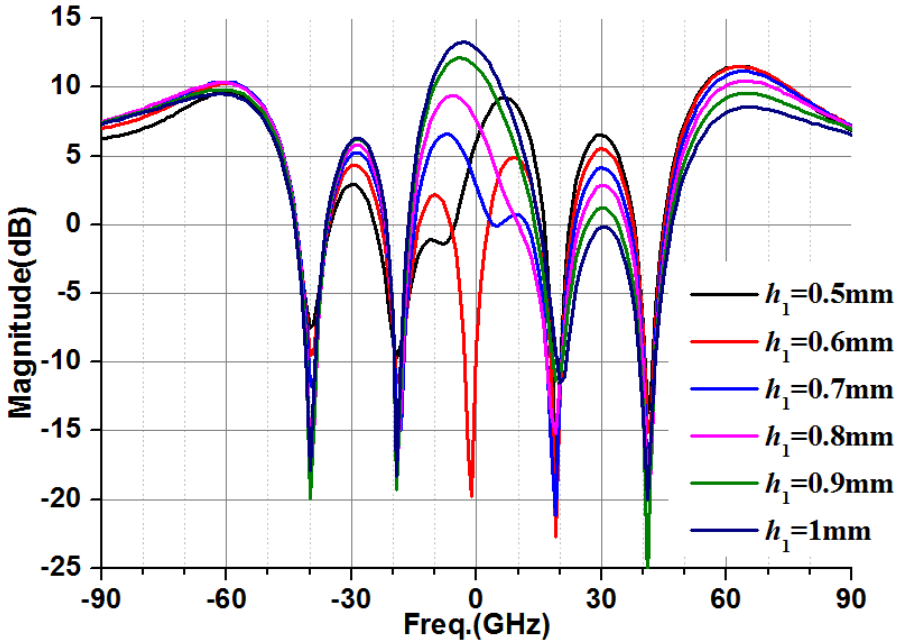

Fig.4.20 Directivity pattern in E-plane (E_θ) for h_1=0.5-1mm and h_2=2.3mm

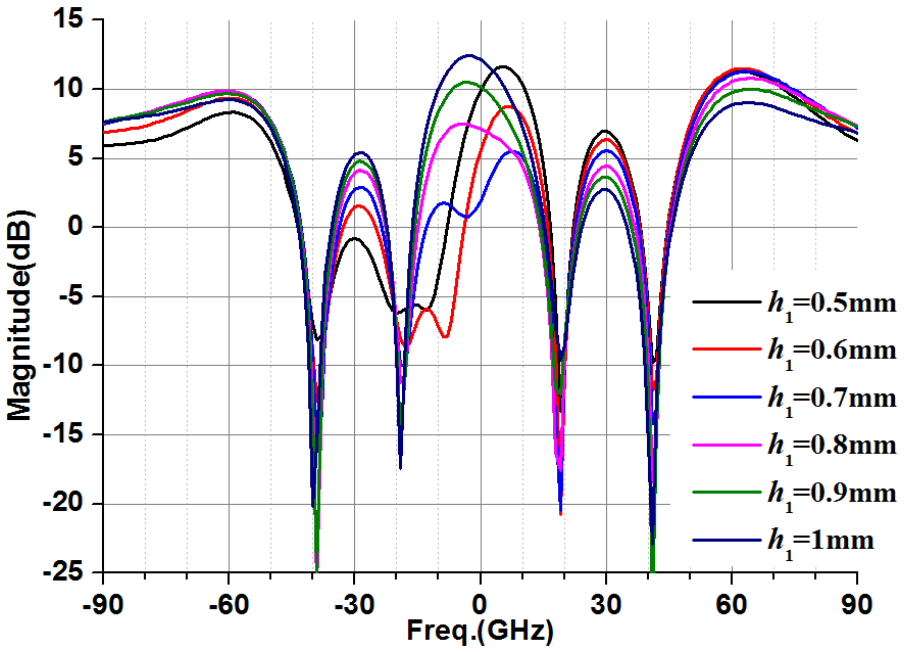

Fig.4.21 Directivity pattern in E-plane (E_θ) for h_1=0.5-1mm and h_2=2.4mm

Ψ extracted from Fig.4.18-21 is plotted in Fig.4.22.

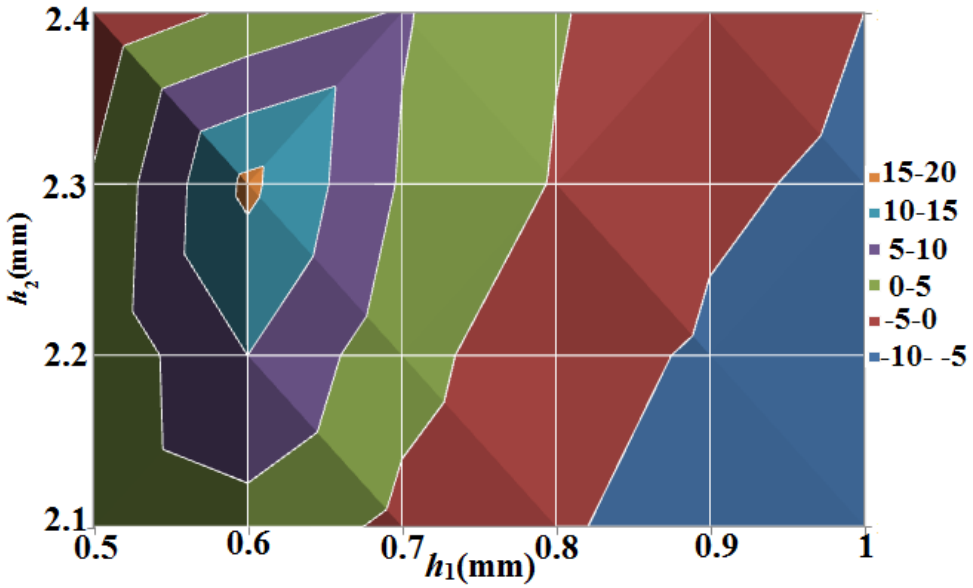

Fig.4.22 2D contour plot of Ψ when h_1= [0.5, 1] mm and h_2= [2.1, 2.4] mm

The best value of Ψ is reached when h_1 in [0.6, 0.7] mm and h_2 in [2.2, 2.3] mm. In this range, a further optimization with a smaller step (which is 0.02mm) is taken. Finally, the optimal dimension is localized as h_1=0.62mm and h_2=2.28mm and the corresponding results are shown in Fig.4.23. As before, the optimization succeeds in cancelling radiation at broadside. However, the subsequent improvement of directivity close to endfire is negligible. Moreover, as already pointed out, the main lobe is

located at ±60° and not at endfire.

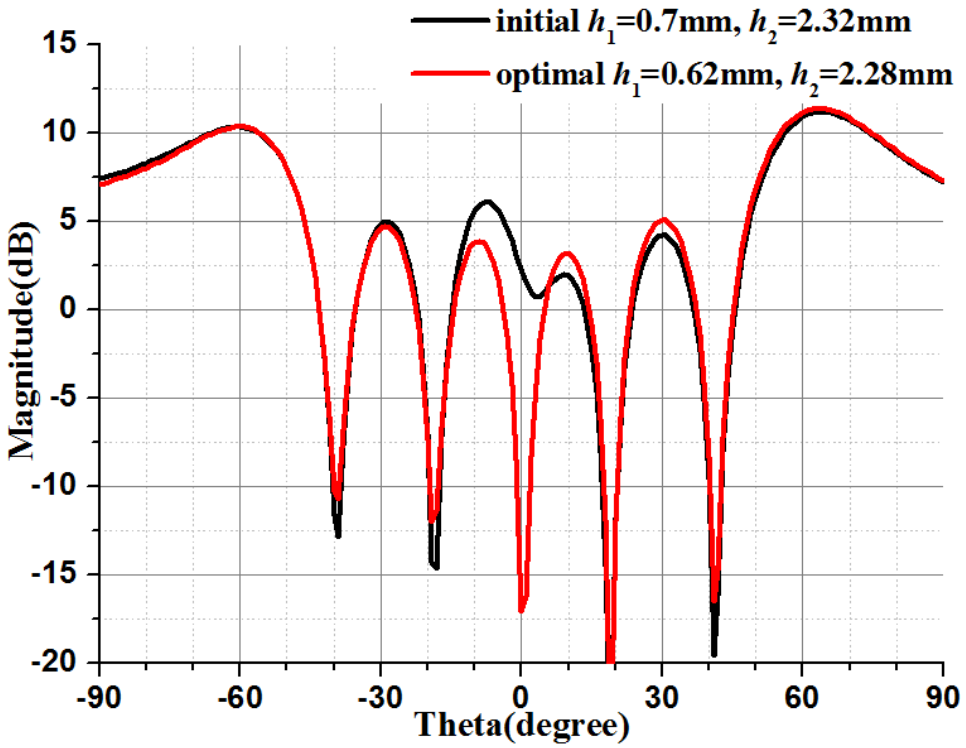

(a)

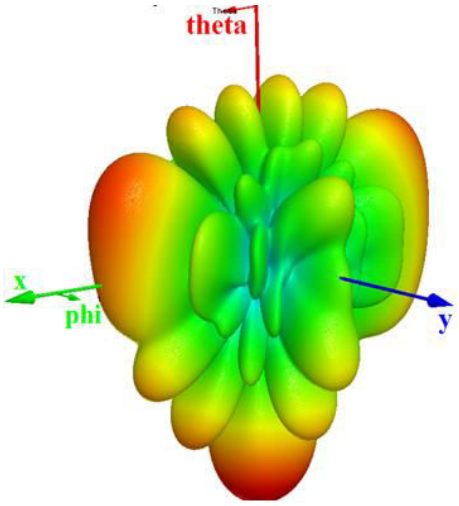

(b)

Fig.4.23 (a) comparison of initial and optimized results of directivity patterns in E-plane (E_θ), and (b) 3D directivity plot for 6-groove array with w=15mm

The 3D pattern in Fig.4.23 gives a more global overview of the obtained radiation. First, it is important to point out that the strong observed back radiation (bottom lobe) is meaningless. Indeed, it results from the simulation conditions: what we plot is the total field. Then, as we excite the reflector with an ideal plane wave, a

large incident field exists behind the reflector. Apart from this artefact, we clearly see that most power is reflected back close to endfire and backfire with a tilt towards the upper half space.

Finally, we see that the initial dimensions (h_1=0.7mm and h_2=2.32mm) are quite close to the final optimized ones (h_1=0.62 mm and h_2=2.28 mm). Indeed, the two patterns in Fig. 4.23 (a) exhibit no great difference, especially regarding radiation in the main lobes. Only the radiation at broadside has been improved, which shows that it is quite sensitive to the geometrical dimensions. In the next sections when we expand the grooves along the *y*-axis further (for a bigger *w*), we will rely on the initial dimensions because the level of radiation at endfire is our main concern. In applications where no radiation at broadside is mandatory, the additional optimization step will be required. With the guidance of these conclusions, a bigger array for practical fabrication will be investigated in the next section.

4.4 Final Array Validation (with 24 grooves and *w*=60mm)

Considering the need for practical fabrication and measurement, a bigger array is necessary. In this section, a 24-groove array with *w*=60mm (overall size is thus 60mm×60mm) is designed. This array is then considered for further investigations about bandwidth and incidence.

4.4.1 24-groove Array Simulation

The 24-groove array has been simulated and optimized. Since the optimization process is the same as before, it is not presented in detail here (more detail can be found in appendix). Just note that, due to the increased array size, simulations become quite time-consuming and it is essential to use a reduced optimization range to vary h_1 and h_2. The final optimal dimensions for this 24-groove array with *w*=60mm are as h_1=0.48mm, and h_2=2.3mm. Fig.4.24 shows its radiation pattern in E-plane (E_θ) and the 3D pattern.

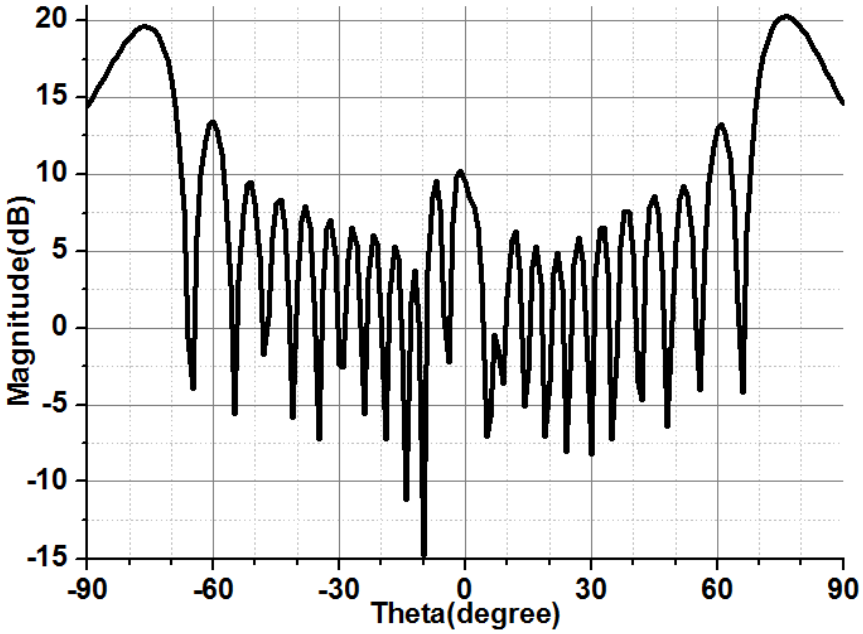

(a)

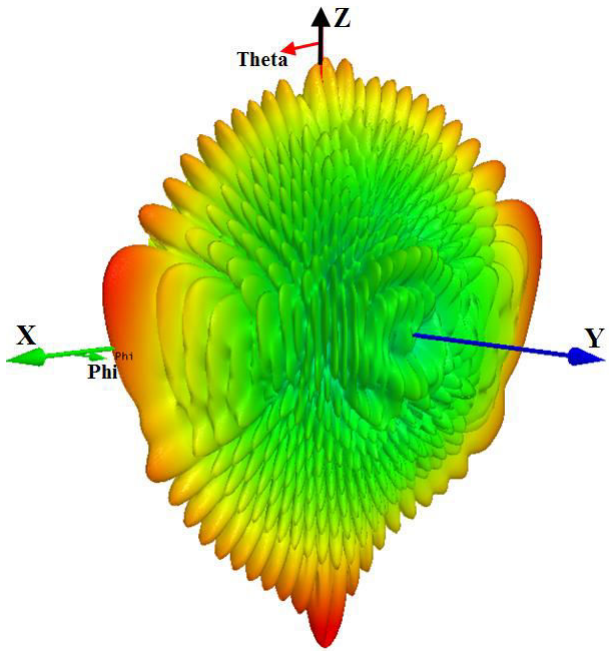

(b)

Fig.4.24 (a) Comparison of initial and optimized results in E-plane (E_θ) and (b) 3D directivity radiation pattern of the optimized result for 24-groove array with *w*=60mm

Based on the final optimal result, the 24-groove array with *w*=60mm exhibits quasi-endfire radiation at 60GHz. The broadside reflection has also been reduced to an acceptable level (10dB below max). The 3D radiation pattern confirms the endfire

radiation performance, in which most part of the power is radiated orthogonally to the incident direction (here, the maximum radiation is obtained close to θ=±75°). In next section, explorations will be carried out concerning the array's bandwidth.

4.4.2 Bandwidth Investigations

Until now, radiation patterns have only been given at the central frequency (f_0=60GHz). In this section we address bandwidth issues. Following simulations are taken based on the 24-groove array with w=60mm, with the optimal dimensions from previous section (h_1=0.48mm and h_2=2.3mm for the successive grooves).

4.4.2.1 Bandwidth for 24-groove Array with w=60mm

For the 24-groove array with w=60mm , the incident wave frequency is varied from 57GHz to 66GHz. The corresponding directivity patterns in E-plane (E_θ) are shown in Fig.4.25.

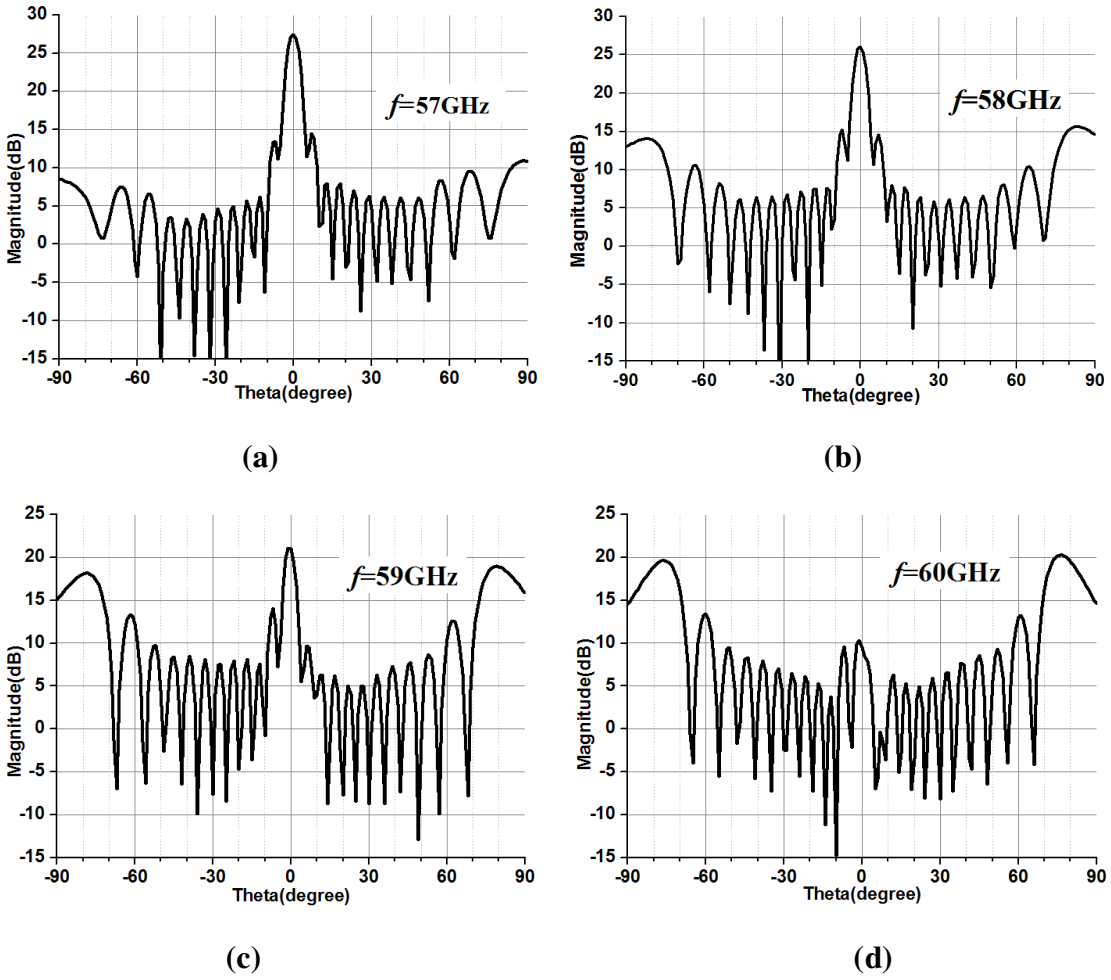

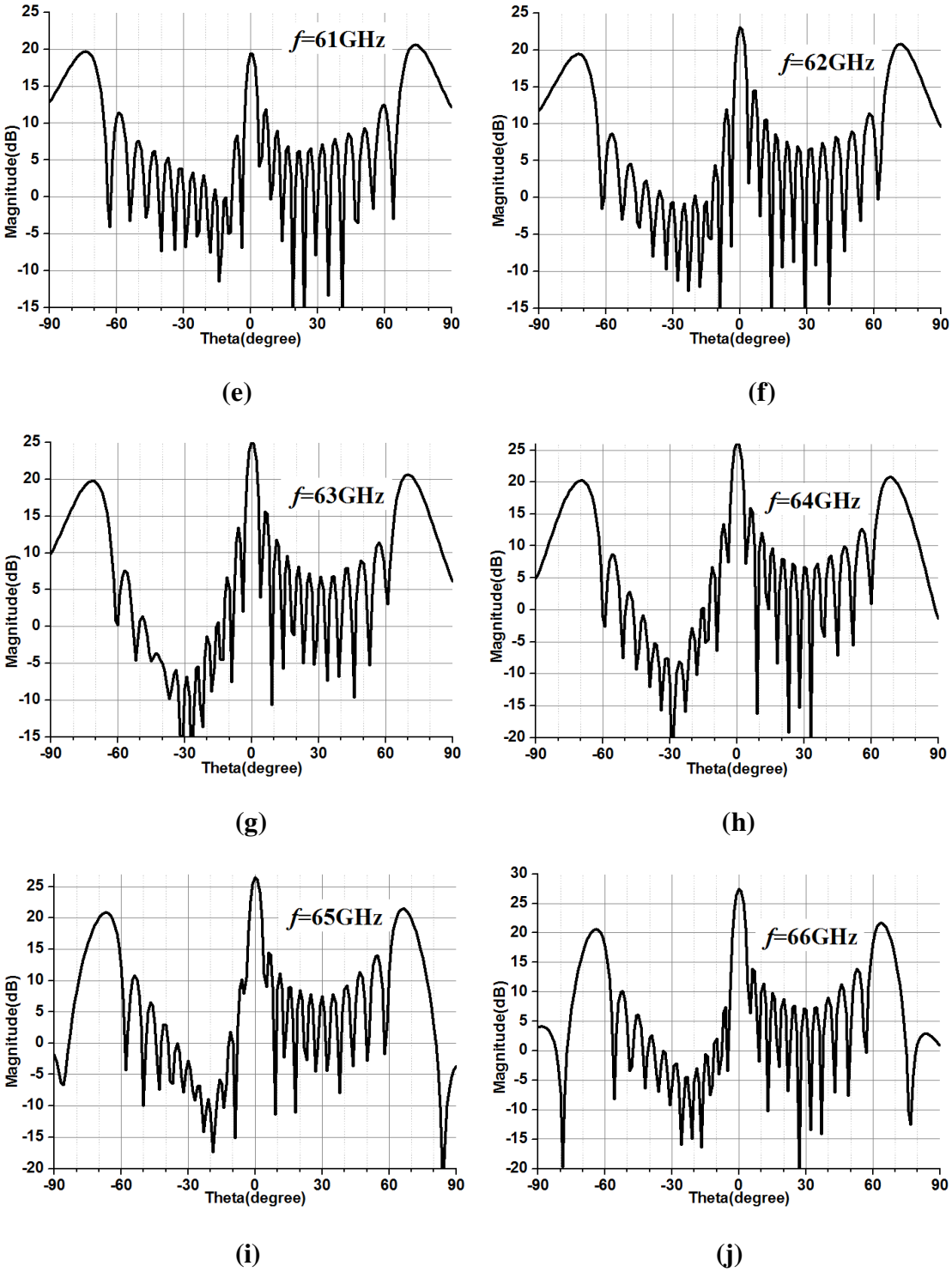

Fig.25 Comparison of directivity patterns in E-plane (E_θ) for 24-groove array from (a) 57GHz to (j) 66GHz

Furthermore, in order to get a clear view of the bandwidth, magnitude in the direction of maximum beam (θ_{max}=±75°) at f_0=60GHz is collected in Fig.4.26. It should be noted that, since there are two magnitudes corresponding to θ=75° and -75° respectively, the calculations in Fig.4.26 are made with the average value of them.

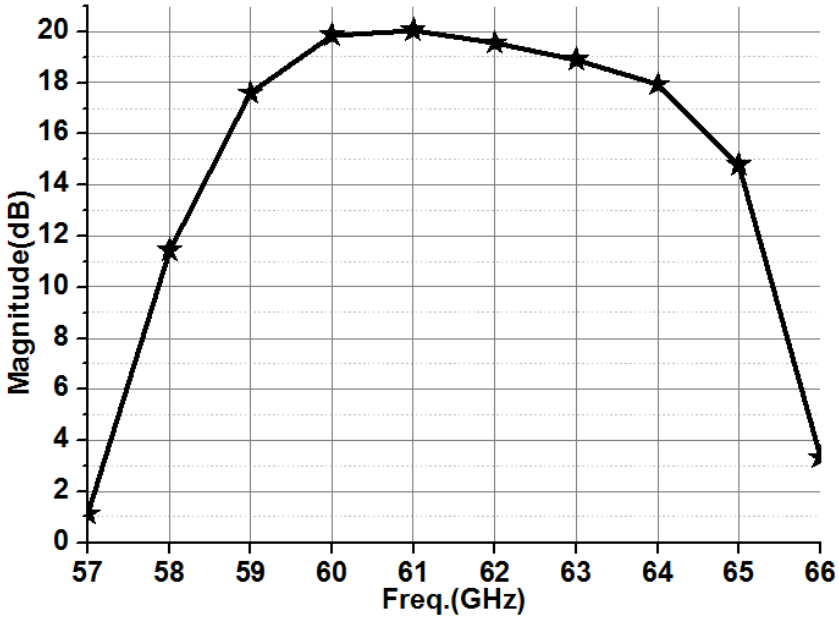

Fig.4.26 Comparison of directivity at θ=±75° from57GHz to 66GHz

Based on the results, three remarks can be done:

1) The initial maximum beam for f_0=60GHz, close to endfire (precisely at θ=±75°), stays quite stable when f varies from 59GHz to 64GHz. In the following, the reference frequency is defined at 61 GHz (which corresponds to the largest directivity at θ=±75°, i.e. 20.1dB) rather than at 60GHz (which corresponds to only 19.8dB). The xdB-bandwidth is then defined as $BW_{x\text{dB}} = \dfrac{f_H - f_L}{f_{reference}}$ where f_{H} and f_{L} define the frequencies for which the directivity encounter an x dB-drop compared to reference ($\left|D(f) - D\left(f_{reference}\right)\right|$=$x$dB). Typically, the variation versus frequency is less than 1dB from 59.3GHz to 62.7GHz, which corresponds to the 1dB-bandwidth $BW_{1\text{dB}}$=5.6%. Similarly, the 3dB-bandwidth is $BW_{3\text{dB}}$=8.9% (from 58.9GHz to 64.3GHz).

2) The beam at broadside is much more sensitive to frequency and a low radiation level at broadside is only possible at 60GHz. As $\Delta f = |f - f_0|$ increases, the broadside reflection magnitude grows rapidly.

3) The bandwidth is not symmetrical around 60GHz. Instead, it seems it is shifted rightwards. In other words, the performance of the array is better above 60 GHz than underneath.

For the next step, we will try to give theoretical explanations about the effect of

frequency by analyzing the array factor.

4.4.2.2 Analysis on Frequency Variation using Array Factor Theory

In this section, we will discuss the frequency variation's effect on the array performance by using array factor theory.

Fig.4.27 gives the general situation of the groove array.

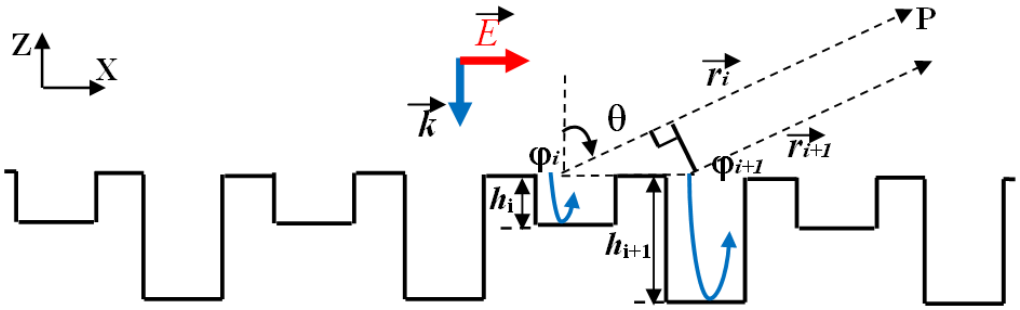

Fig.4.27 General schematic of groove array

For a normal incident wave, the phase of the reflection coefficient at the entrance of the *i*th (*i*=1, 2, 3…) groove element can be expressed as:

$$\varphi_i = 2kh_i + \pi \tag{4-1}$$

The first term stands for the wave path within the groove element: it propagates from the entrance of the groove to the shorted end at z=-h_i and then is reflected back to the entrance. The second term (π) is the phase-shift brought by the short circuit itself.

The ideal height should be $h_i = \frac{\lambda_0}{4} = \frac{c}{4f_0}$ when i is an odd number (i=1, 3, 5…) and $h_i = \frac{\lambda_0}{2} = \frac{c}{2f_0}$ when i is an even number (i=2, 4, 6…), where f_0=60GHz. Therefore, (4-1) can be expressed as:

$$\varphi_i = \begin{cases} \pi(\frac{f}{f_0}+1) & i = 1,3,5... \\ \pi(2\frac{f}{f_0}+1) & i = 2,4,6... \end{cases}$$

If we denote the normalized incident frequency as f_n= $\frac{f}{f_0}$, then the reflected phase can

be obtained as:

$$\varphi_i = \begin{cases} \pi(f_n + 1), & i = 1,3,5... \\ \pi(2f_n + 1), & i = 2,4,6... \end{cases} \tag{4-2}$$

When the incident wave frequency changes, the element phases in (4-2) exhibit linear variations correspondingly.

The array factor at arbitrary normalized frequency f_n can be expressed as

$$F(\theta) = \sum_{i=1}^{N} e^{j\varphi_i} e^{jkd(i-1)\sin\theta} = \sum_{i=1}^{N} e^{j\varphi_i} e^{j\pi f_n (i-1)\sin\theta} \tag{4-3}$$

in which $k = \frac{2\pi f}{c}, d = \frac{\lambda_0}{2} = \frac{c}{2f_0}$. Here we assume the number of elements N is even, which meets the depiction in Fig.4.27. So we can write N=2M, and the array factor can be expressed as

$$F(\theta) = \sum_{i=1}^{2M} e^{j[\varphi_i + f_n (i-1)\sin\theta]} \tag{4-4}$$

By separating odd and even indices, we expand (4-4) into two parts. When i is odd, i=2p-1 (p=1, 2, 3…), and when i is even, i=2p (p=1, 2, 3…), so (4-4) can be expressed as:

$$\begin{aligned} F(\theta) &= \sum_{p=1}^{M} e^{j\pi(f_n+1)} e^{j\pi f_n (2p-2)\sin\theta} + \sum_{p=1}^{M} e^{j\pi(2f_n+1)} e^{j\pi f_n (2p-1)\sin\theta} \\ &= \left[e^{j\pi(f_n+1)} e^{-j2\pi f_n \sin\theta} + e^{j\pi(2f_n+1)} e^{-j\pi f_n \sin\theta} \right] \sum_{p=1}^{M} e^{jp2\pi f_n \sin\theta} \end{aligned} \tag{4-5}$$

If we denote $\psi = 2\pi f_n \sin\theta$, (4-5) can be simplified as

$$\begin{aligned} F(\theta) &= e^{j\pi(f_n+1)} e^{-j\psi} \left[1 + e^{j\left(\pi f_n + \frac{\psi}{2}\right)} \right] \sum_{p=1}^{M} e^{jp\psi} = 2e^{j\left(\frac{3}{2}\pi f_n + \pi - \frac{3\psi}{4}\right)} \cos\left(\frac{\pi f_n + \frac{\psi}{2}}{2} \right) \sum_{p=1}^{M} e^{jp\psi} \\ &= 2e^{j\left(\frac{3}{2}\pi f_n + \pi - \frac{3\psi}{4}\right)} \cos\left[\frac{\pi f_n}{2}(1 + \sin\theta) \right] \sum_{p=1}^{M} e^{jp\psi} \end{aligned} \tag{4-6}$$

Therefore, we have

$$|F(\theta)| = 2\left|\cos\left[\frac{\pi f_n}{2}(\sin\theta+1)\right]\frac{\sin\left(\frac{M\psi}{2}\right)}{\sin\left(\frac{\psi}{2}\right)}\right|$$

$$= 2\left|\cos\left[\frac{\pi f_n}{2}(\sin\theta+1)\right]\frac{\sin(M\pi f_n \sin\theta)}{\sin(\pi f_n \sin\theta)}\right| \quad (4\text{-}7)$$

(4-7) gives the overall array factor for the proposed groove array, which is a function of the normalized frequency f_n. It can be used to analyze the changes the incident frequency f cause in the array's radiation pattern (as shown in Fig.4.25 and Fig.4.26).

At endfire radiation, we have θ=90°, and the array factor in (4-7) becomes

$$F(90^\circ) = 2\left|\cos\pi f_n \frac{\sin(M\pi f_n)}{\sin(\pi f_n)}\right| \quad (4\text{-}8)$$

When θ=75°, the array factor in (4-7) becomes

$$F(75^\circ) = 2\left|\cos(0.983\pi f_n)\frac{\sin(0.966M\pi f_n)}{\sin(0.966\pi f_n)}\right| \quad (4\text{-}9)$$

For the 24-groove array, we have M=12. Results for F(75°) and F(90°) are plotted as a function of the normalized frequency f_n, and are compared in Fig.4.28.

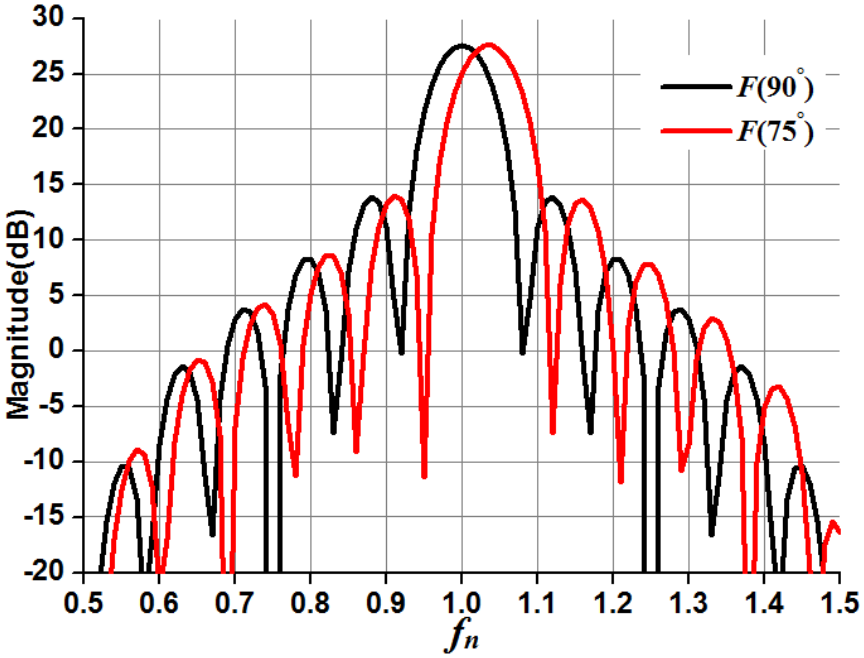

Fig.4.28 Comparison of F(θ) when θ=75° and 90°

For $F(90^\circ)$, the peak value is 27.6dB when f_n=1.0. If we take f_n=1.0 as reference, the 1-dB bandwidth is 4.3%, and the 3dB-bandwidth is 7.2%.

For $F(75^\circ)$, the peak value locates at f_n=1.03 (it corresponds to a magnitude of 27.5dB) instead of f_n=1.0 (that corresponds to a magnitude of 25.1dB), so the array factor witnesses a small shift rightwards, which is in coincidence with Fig.4.26. Based on (4-9), we can clearly tell this shift results from observation angle θ variation. Furthermore, if we take f_n =1.03 as reference here (like what we done in Fig.4.26), the 1dB-bandwidth is about 4.5% and 3dB-bandwidth is 8%. This result is very close to $F(90^\circ)$ and is also consistent with our simulation results in Fig.4.26.

For the next step, we can consider the broadside reflection, which means θ=0°. Based on (4-7), we have:

$$F\left(0^\circ\right) = 2M\left|\cos\frac{\pi f_n}{2}\right| \tag{4-10}$$

Once again, result for $F(0^\circ)$ is depicted in dB in Fig.4.29.

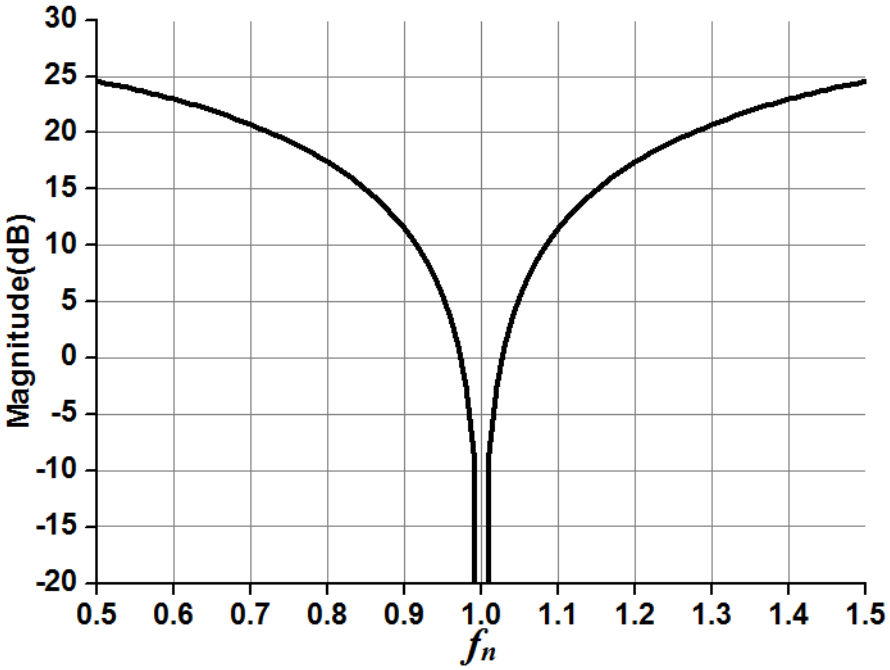

(a)

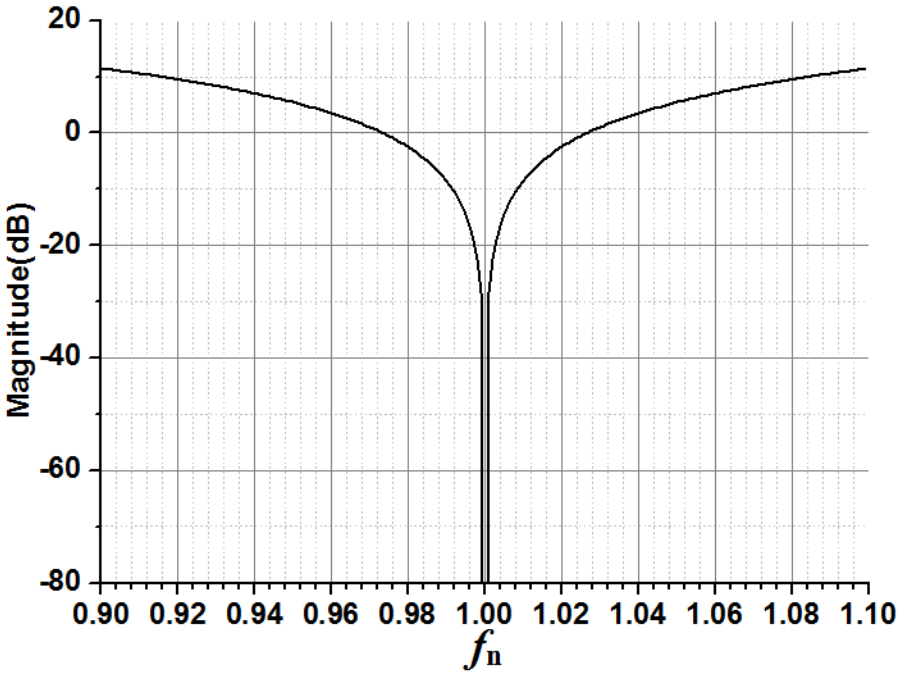

(b)

Fig.4.29 Result for $F(\theta)$ (a) when θ=0° and (b) zoom at f_n=0.9-1.1

In Fig.4.29, the array factor at broadside $F(0^\circ)$ is presented. This curve clearly shows that a low broadside reflection can only be obtained at f_n=1. Any small frequency variation would make the magnitude increase quickly (when f_n=1, $F(\theta)$<-100dB, and when f_n=0.99 or 1.01, $F(\theta)$ grows to -8.5dB). This tendency also matches our simulation results in Fig.4.29: at central frequency f_0=60GHz, a small broadside reflection can be achieved. When f changes between 57GHz to 66GHz (corresponding to f_n=0.95-1.1), the broadside reflection grows rapidly as Δf increases.

Note that since cancellation of the specular reflection is not ideally realized, the simulated magnitudes at broadside are bigger than the theoretical ones.

Conclusion

In this section, we have investigated the bandwidth of the 24-groove array with w=60mm. By changing the incident wave frequency between 57GHz to 66GHz, the array shows a narrow bandwidth. We tried to explain the obtained results with array factor $F(\theta)$. By comparing the theoretical array factor $F(\theta)$ at θ=90°, 75° and 0° with the simulation results, the array's bandwidth performance is well understood.

4.4.3 Oblique Incidence

Previous tasks until now were all undertaken assuming normal incidence. In a practical situation, a good tolerance to oblique incidence will be helpful if the source is not perfectly localized normally to the reflector. So the oblique incidence problem is discussed in this section.

Fig.4.30 depicts the general configuration, with φ_{inc} and θ_{inc} defining the direction of the incoming wave. A normally incident wave corresponds to $\theta_{inc}=0^{\circ}$. When $\theta_{inc}\neq 0^{\circ}$ and $\varphi_{inc}=0^{\circ}$, the oblique incidence occurs in XOZ plane; when $\theta_{inc}\neq 0^{\circ}$ and $\varphi_{inc}=90^{\circ}$, the oblique incidence occurs in YOZ plane. We will consider these two specific configurations.

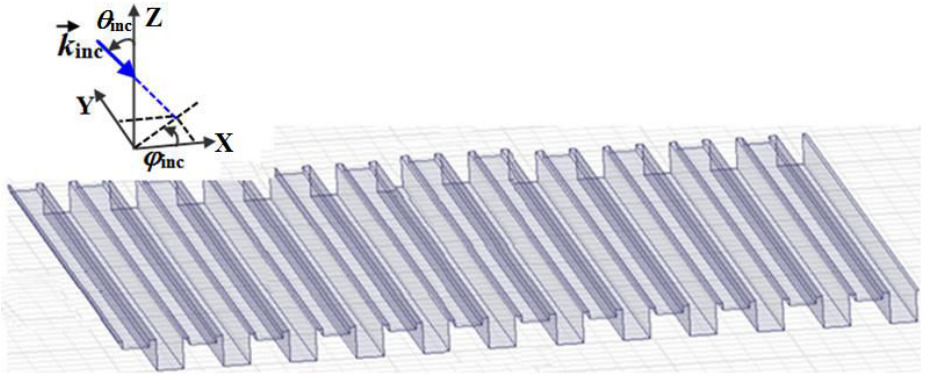

Fig.4.30 Configuration of oblique incidence

4.4.3.1 Oblique in XOZ plane

If $\theta_{inc}\neq 0^{\circ}$ and $\varphi_{inc}=0^{\circ}$, the incident wave is oblique in XOZ plane, which is also the E-plane. Fig.4.31 shows the general configuration. Note that the polarization of the E-field is TM ($\vec{E}_{inc}$ lies within the XOZ plane).

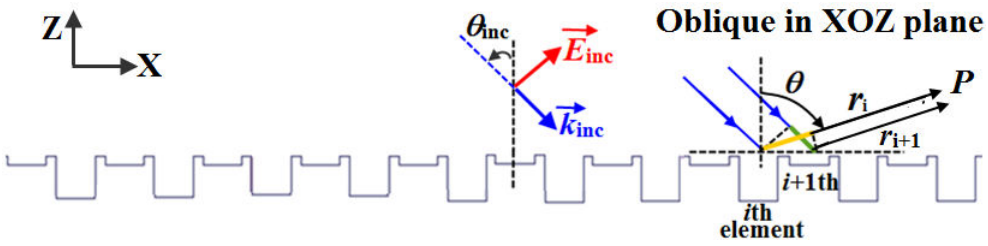

Fig.4.31 Oblique incidence in XOZ plane

When θ_{inc} varies from 0° to -30°, the simulated far-field patterns of directivity in E-plane (E_{θ}) are compared in Fig.4.32.

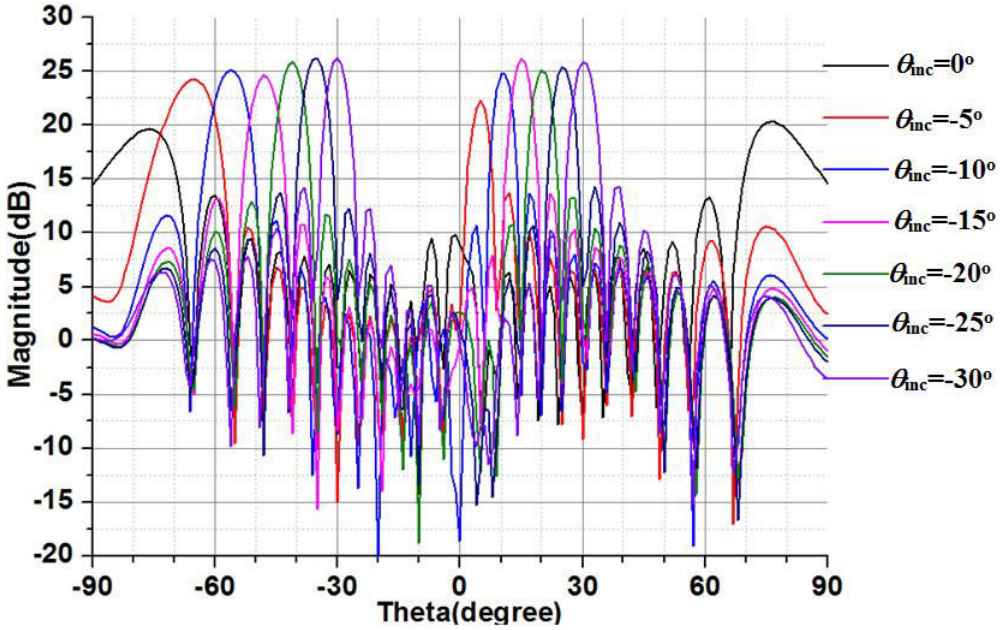

Fig.4.32 Comparison of simulated directivity patterns in E-plane (E_θ), when θ_{inc} varies from 0° to -30° for oblique incidence in XOZ plane

Based on Fig.4.32, three remarks can be made.

1) As the oblique incident angle θ_{inc} varies from 0° to -30°, the initial maximum beam at -75° is shifted gradually to -30°.

2) In the meantime, the initial maximum beam at 75° quickly disappears.

3) Finally, a new lobe appears near the broadside direction and it is shifted gradually from 0° to +30°.

In order to get a better understanding of the obtained oblique incidence performance, we will try to analyze the result by using an array factor analysis, as we did previously for the bandwidth.

4.4.3.2 Result Analysis Based on Array Factor

In this section, we explore the array's performance with oblique incidence in XOZ plane by analyzing its array factor.

Based on the general configuration in Fig.4.31, the phase for *i*th groove element at center frequency can be written as:

$$\varphi_i = -\pi(i-1) + k_0(i-1)d\sin\theta_{inc} \tag{4-11}$$

In (4-11), the first term $-\pi(i\text{-}1)$ stands for the initial phase difference required for endfire (in practice, we could express the phase of successive elements as 0, π, 0, π…

instead of 0,- π, -2π, -3π..., but these two sets of phase are equivalent). The second term $k_0(i-1)d\sin\theta_{inc}$ denotes the additional phase difference introduced by the oblique incidence (the marked green line in Fig.31). By convention, this incident angle is chosen negative (θ_{inc}<0) based on the coordinate system. Considering the E-field in far-field point *P*, the array factor *F*(θ) can be expressed as:

$$F(\theta)=\sum_{i=1}^{N}e^{j\varphi_i}e^{jkd(i-1)\sin\theta}=\sum_{i=1}^{N}e^{j\left[-\pi(i-1)+kd(i-1)\sin\theta_{inc}\right]}e^{jkd(i-1)\sin\theta}$$

$$=\sum_{i=1}^{N}e^{j(i-1)(-\pi+kd\sin\theta_{inc}+kd\sin\theta)}=\sum_{i=1}^{N}e^{j(i-1)\psi} \tag{4-12}$$

The array factor records its maximum value when ψ=2$p\pi$ (*p*=-2, -1, 0, 1, 2…), and then we have

$$\left|F(\theta)\right|=\left|\frac{\sin\left(\frac{N\psi}{2}\right)}{\sin\left(\frac{\psi}{2}\right)}\right| \tag{4-13}$$

in which, $\psi=k_0d\sin\theta_{inc}+k_0d\sin\theta-\pi$ and $d=\lambda/2$, so

$$\psi=\pi\left(\sin\theta+\sin\theta_{inc}-1\right) \tag{4-14}$$

$$\sin\theta+\sin\theta_{inc}=2p+1 \tag{4-15}$$

(4-15) offers a clear illustration of the oblique incidence's effect on the proposed array's far-field beam direction.

When θ_{inc}=0°, the problem corresponds to normal incidence. The maximum radiation beam appears at $\sin\theta$-1=2*p*. So the maximum beam is at $\theta_{\max}=\theta$=90° when *p*=0 or $\theta_{\max}=\theta$=-90° when *p*=-1. Then, (4-13) can be written as

$$\left|F(\theta)\right|_{\text{normal incident}}=\left|\frac{\sin\left[\frac{N\pi}{2}\left(\sin\theta-1\right)\right]}{\sin\left[\frac{\pi}{2}\left(\sin\theta-1\right)\right]}\right| \tag{4-16}$$

This means, with the prescribed 180° phase difference between successive elements

and element spacing $d=\lambda/2$, the array will achieve endfire radiation, and it will produce two main beams symmetrically.

On the other hand, if $\theta_{inc}\neq 0^{\circ}$, this problem corresponds to what we discussed in Fig.4.31. For instance, when $\theta_{inc}=-5^{o}$, we have $\sin\theta=1+\sin 5^{\circ}+2p$. So the maximum beam would direct towards $\theta_{max}=\theta=-65.9^{\circ}$ with $p=-1$. This is the location we observed in Fig.4.31 for the left main beam.

Fig.4.33 depicts the array factors $F(\theta)$ for different incidence angles. The magnitudes are given in dB. Note that the maximum value for $F(\theta)$ is 27.6dB (=20log24, where 24 is the number of the grooves).

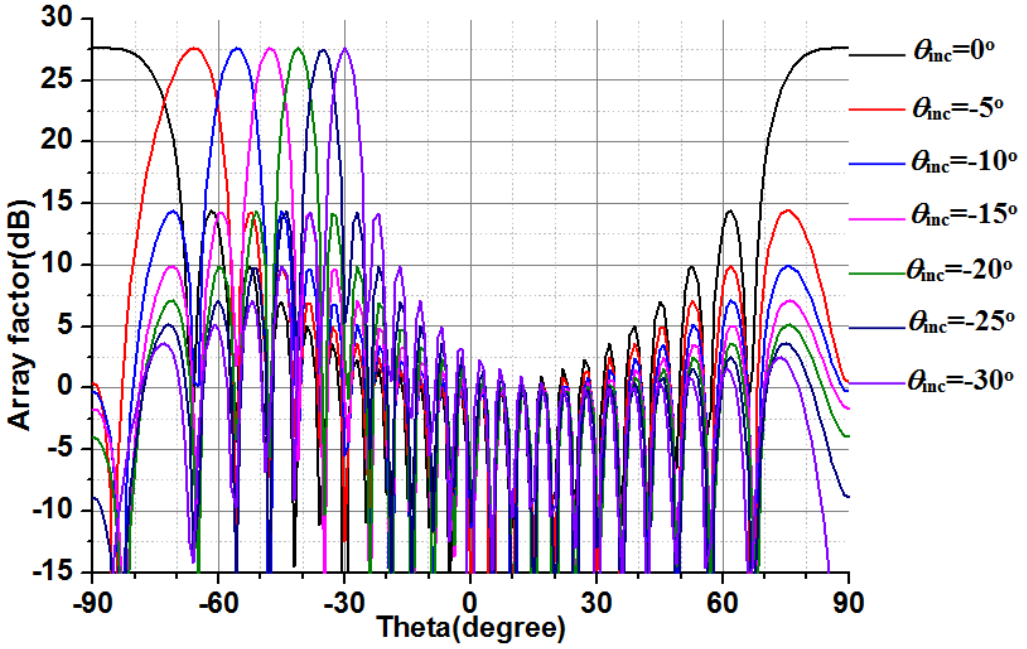

Fig.4.33 Array factor $F(\theta)$ for different θ_{inc} from 0° to -30°

In order to get an easy understanding, the theoretical values for maximum left beam direction θ_{max} are collected in Table 4.1 and compared with the simulation results in Fig.4.31.

Table 4.1 Comparison of theoretical and simulation results of θ_{max}

		$\theta_{inc}(^{\circ})$						
		0	**-5**	**-10**	**-15**	**-20**	**-25**	**-30**
θ_{max} (°)	Theoretical Value	±90	-65.9	-55.7	-47.8	-41.4	-35.3	-30
	Simulation Results	±75	-65	-56	-48	-42	-35	-30

As shown in Fig.4.33 and Table 4.1, apart from the normal incidence situation (θ_{inc}=0°), all θ_{max} for oblique incidence are matching our simulation results. This means, due to the introduction of oblique incidence angle θ_{inc}, the array aiming for endfire radiation suffers a beam shift, and the maximum beam direction θ_{max} is controlled by the incidence angle θ_{inc}.

Meanwhile, compared with the simulated results (Fig.4.31), only one main beam is observed in the theoretical predictions (Fig.4.33). The beam at θ<0° is kept, while the other beam at θ>0° disappears. Finally, if we take observation of the second lobe, we can notice that this lobe directly coincides with $-\theta_{inc}$. When θ_{inc}=-5°, the lobe directs to 5°, when θ_{inc}=-10°, the lobe directs to 10°…. Therefore, this lobe can be believed as the specular reflection from the array. The specular reflection gets cancelled initially at broadside direction. However, when oblique incidence occurs, the symmetry conditions in the excitation mechanism are lost, and the sensitive cancellation can't be kept any more. Thus the specular reflection arises and is steered as the oblique incidence scans. As a consequence, the positioning of the reflector with respect to the illuminating source in the E-plane is a critical issue for this topology.

4.4.3.3 Oblique in YOZ plane

As shown in Fig.34, if $\theta_{inc}\neq0^{o}$ and $\varphi_{inc}=90^{o}$, the oblique incidence occurs in YOZ plane. The situation for an oblique incidence in H-plane is very different from the one we encountered in E-plane. Now, the expected 180° phase difference between consecutive grooves is preserved whatever the incidence angle θ_{inc}. The phase delay brought by the incidence angle is converted into a linear phase variation along the grooves themselves. As a consequence, the beam is tilted in the YOZ plane. Then, in the following, we plot the radiation pattern in the plane where the maximum radiation is expected, i.e. in the θ_{obv} =-θ_{inc}.

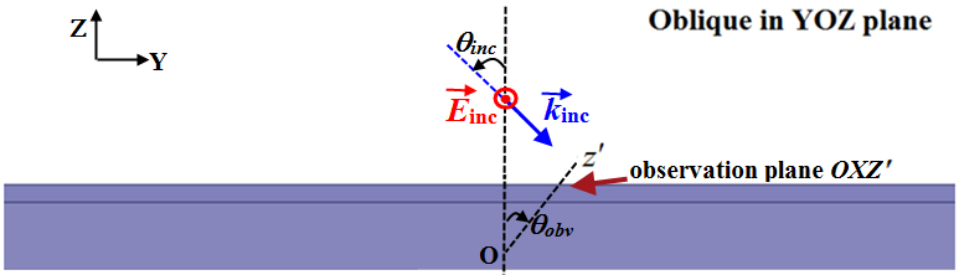

Fig.4.34 Oblique incidence in YOZ plane

When the oblique incidence angle θ_{inc} scans from 0° to -30°, the corresponding

directivity in the observation plane OXZ' (which is the new E-plane) E_θ are depicted in Fig.4.35.

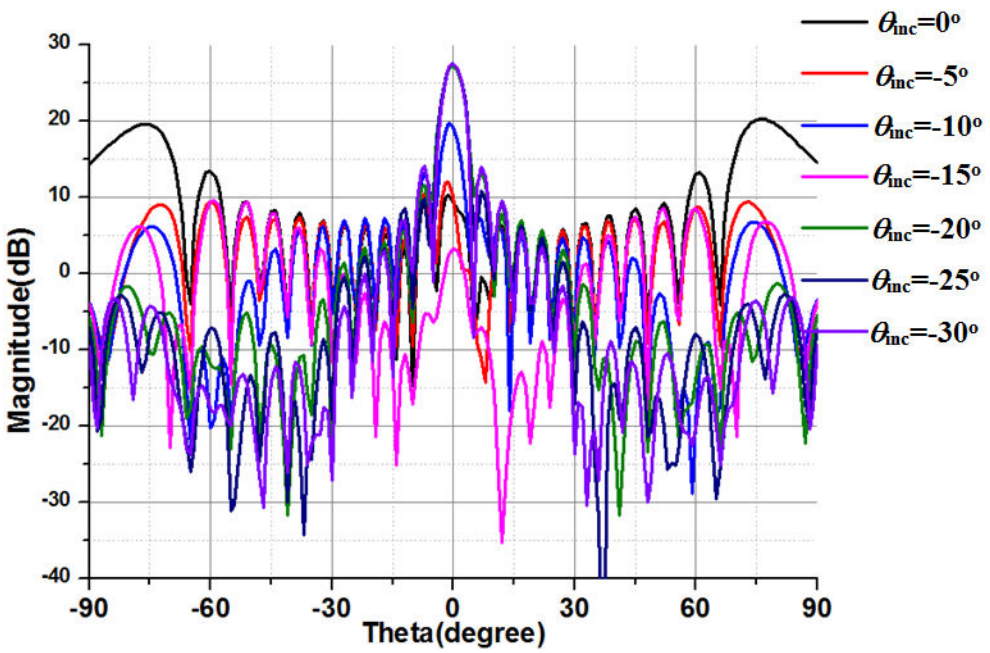

Fig.4.35 E-plane (E_θ) comparison when θ_{inc} varies from 0°to -30° for oblique incidence in YOZ plane

The figure shows that the pattern rapidly degrades as the incidence angle increases. A large broadside radiation is observed which demonstrates again the sensitivity of the broadside cancellation. Meanwhile, the initial endfire radiation (at θ=±75°) level decreases greatly, though the out-phase reflection between successive elements is still kept.

Conclusion

In this section, we took detailed investigations on a 24-groove array with w=60mm. At first, such array was designed and optimized. Then, the array's bandwidth has been studied and its performance versus frequency variation has been explained by analyzing its array factor. At last, the array's performances under oblique incidence have been explored. The oblique incidence problems can be divided into two specific situations. When the oblique incidence occurs in XOZ plane, additional phase difference is introduced by the incidence angle θ_{inc}. The relations between θ_{inc} and maximum beam direction θ_{max} have been investigated using simple array theory. When the oblique incidence occurs in YOZ plane, the 180° reflection phase between

successive groove elements can theoretically be preserved. However, simulations have shown that the patterns deteriorate rapidly. For the next section, we will attempt to address the issue of maximum beam shift under normal incidence.

4.5 Investigation on Maximum Beam Shift

In previous sections, arrays with various sizes have been investigated and discussed. We still have one unsolved issue. Though our design aimed at endfire radiation, the obtained main beam directions could not be precisely steered at $\pm 90^{\circ}$. To illustrate this issue, Fig.4.36 compares 3 different arrays (w=15mm) when N varies from 6 to 24. It clearly shows that the main beam is closer to endfire when N gets larger.

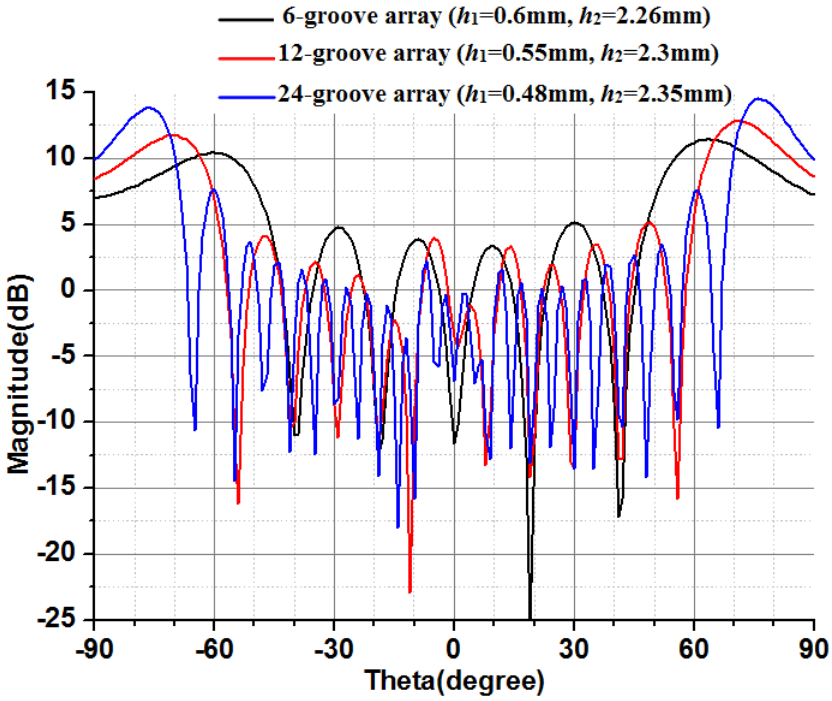

Fig.4.36 Comparison of main beam pointing for array in different sizes

In order to get a better understanding of this problem, investigation is taken based on array theory, at least to get a qualitative insight. More precisely, we propose to evaluate the radiation pattern of the array using pattern multiplication. To do so, we will first estimate the radiation pattern of the unit-cell and then multiply it by the array factor.

The primary radiation pattern of a single groove element is simulated first. As shown in Fig.4.37, the element is excited with lumped port, and is surrounded with

PML boundary to avoid undesired back-radiation. Its pattern in E-plane (rE_θ) is recorded in Fig.38. Note that this is a quite rough evaluation as it does not account for coupling between grooves. However, we will show it is sufficient to explain most phenomena.

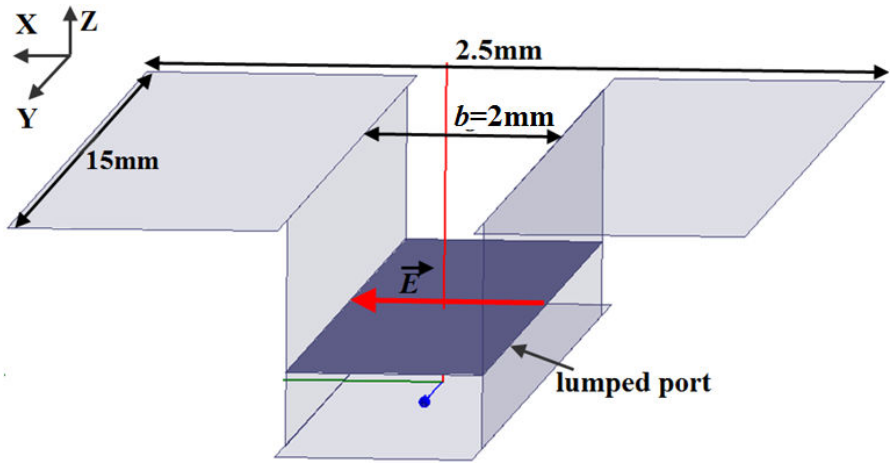

Fig.4.37 Simulation of single groove element with lumped port excitation

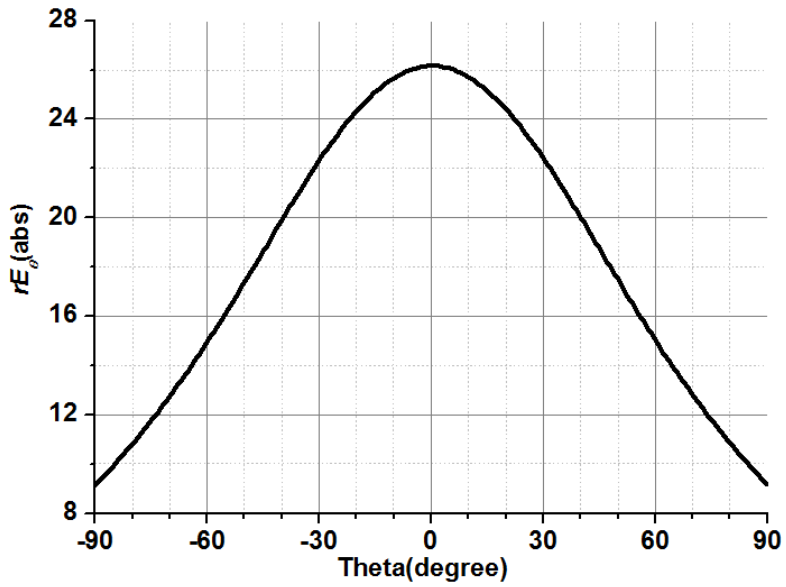

Fig.4.38 Primary groove element's far-field in E-plane rE_θ

In Fig.4.38, we refer to the parameter *rE,* which is the product of the far-field *E* and the distance *r* since in the far-field, $r \to \infty$ and E→0. Meanwhile, as discussed in previous section, (4-16) gives the array factor for normal incidence as $|F(\theta)| = \left| \frac{\sin\left[\frac{N\pi}{2}(\sin\theta - 1)\right]}{\sin\left[\frac{\pi}{2}(\sin\theta - 1)\right]} \right|$. Here we take *N*=6, 12 and 24 respectively, and then the

corresponding array factors $F(\theta)$ are obtained and shown in Fig.4.39.

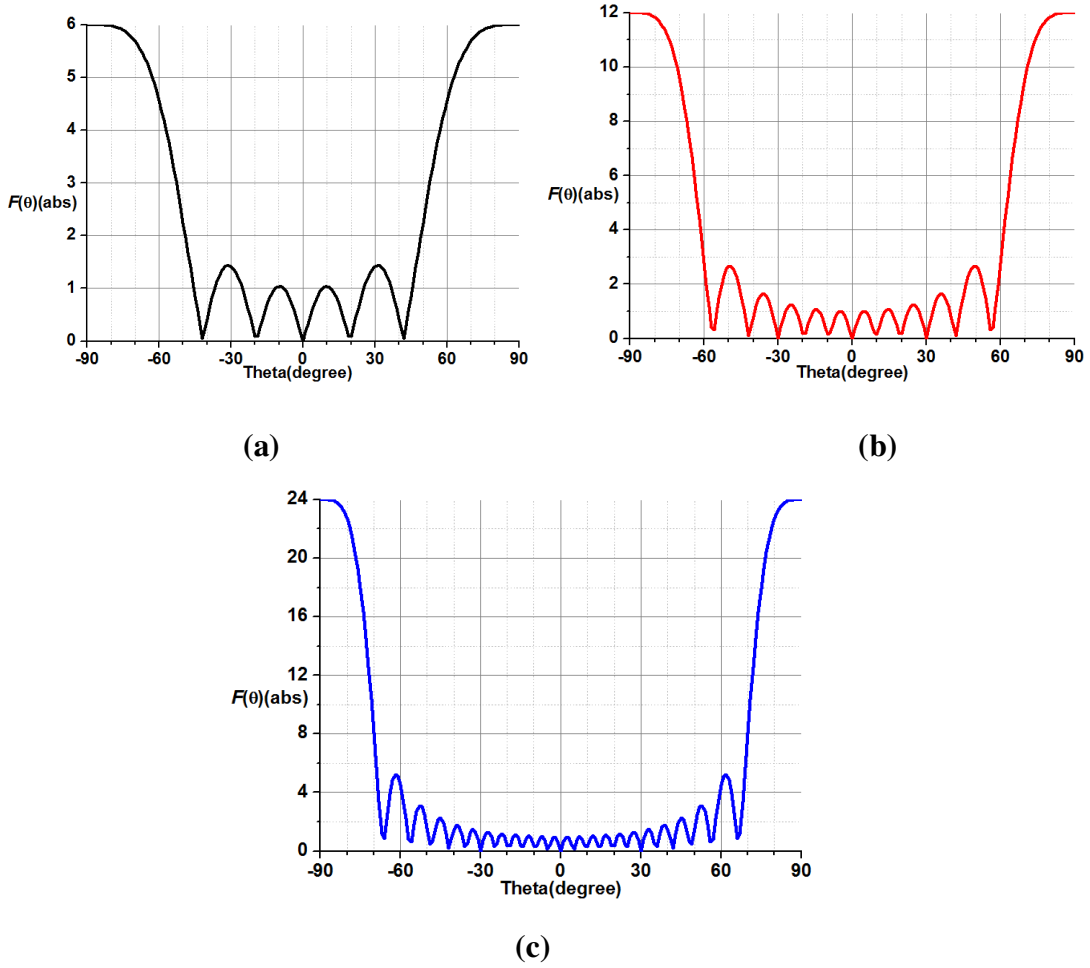

Fig.4.39 Endfire array factor for (a) *N*=6, (b) *N*=12 and (c) *N*=24

We can now calculate out the theoretical directivity based on the primary pattern in Fig.4.38 and array factor $F(\theta)$ in Fig.4.39. The theoretical E-field in far-field can be calculated out through pattern multiplication:

$$rE_{\text{overall}} = rE_{\text{primary}} \cdot F(\theta) \tag{4-17}$$

For the next step, the corresponding results of far-field directivity patterns can be obtained as:

$$D = 10\log\frac{4\pi \cdot U}{P_{\text{rad}}} = 10\log\frac{4\pi\left(rE_{\text{overall}}\right)^2}{120\pi P_{\text{rad}}} = 20\log\left(\frac{rE_{\text{overall}}}{\sqrt{30NP_0}}\right) \tag{4-18}$$

In (4-18), U is the radiation intensity, P_{rad} represents the total radiated power. We assume it is identical to the incident power on the reflector P_{inc}. Then, we can express

P_{inc} as NP_0 where N is the number of element and P_0 the incident power on one element. The theoretical directivity patterns are compared with simulated ones (from Fig. 4.36) in Fig.4.40.

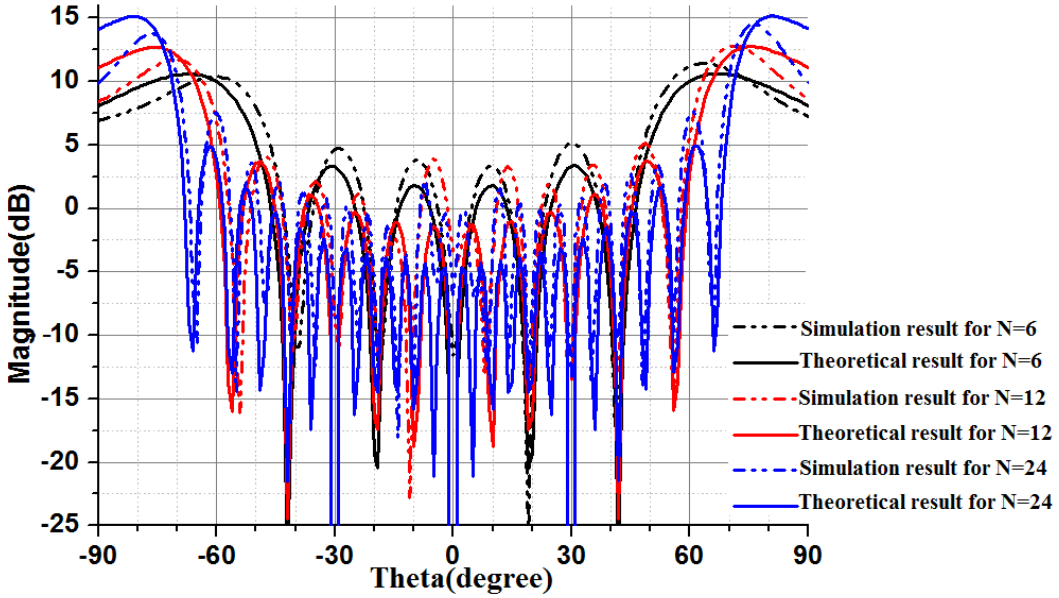

Fig.4.40 Directivity patterns comparison when *N* increases from 6 to 24

Two remarks can be done based on Fig.4.40:

1) Fig.4.40 gives a clear demonstration about the main beam shift. When N=6, the theoretical directivity records its maximum beam at θ_{max}=66°, and when N increases to 24, it finally points towards θ_{max}=81°, which is close to the endfire direction. This tendency is in good coincidence with our simulated results. The small disagreement may be explained by the rough evaluation of the unit-groove pattern.

2) Theoretically, when N increases from 6 to 12, or from 12 to 24, the magnitude level growth at ±90° should be 10log2=3dB, as shown in Fig.4.40 for the theoretical patterns. However, we can notice in the simulation results, the magnitude level growth is around 1.5dB. Meanwhile, we can find out that the simulation values at θ_{max} and ±90° are smaller than the theoretical ones. On the contrary, the simulated side lobes are higher than the theoretical ones. Once again, this may be due to the rough evaluation of the primary pattern. The "filtering" brought by this pattern is essential in the final performance. Our coarse evaluation was sufficient to bring a qualitative insight in the observed phenomena but it is not precise enough to predict the field levels accurately.

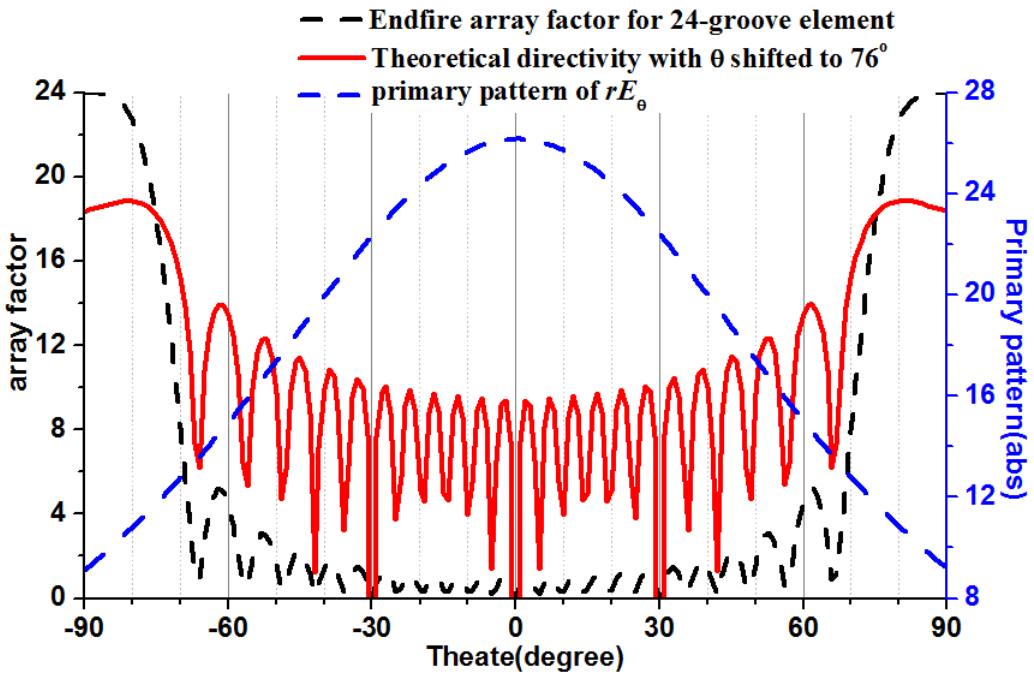

Fig.4.41 Illustration of the main beam shift when *N*=24

Fig.4.41 illustrates in more details the main beam shift for the *N*=24 configuration. Due to the primary pattern (in blue), the expected main beams at $\pm 90^\circ$ are "filtered out". If we imagine the array factor (in black) as the input, it provides a quite wide beamwidth (the single 1dB-beamwidth is 9° from -90° to -81°). In this range, the primary pattern (which can be regarded as a bandpass filter) grows with a steep slope (the magnitude increases by 22.5%). After multiplying the two curves, the maximum beam (in red) appears at $\theta_{max}=\pm 81^\circ$ rather than $\pm 90^\circ$. When *N* reduces, the array factor's beamwidth gets wider. As the primary pattern goes on growing, θ_{max} is continuingly shifted by the primary pattern. In short, there are two elements that contribute to the main beam shift: a wide beamwidth for the array factor (especially as *N* decreases) and a primary pattern with positive growth in this beamwidth range. In Fig.4.33 with oblique incidence in XOZ plane, all the array factors when $\theta_{inc}\neq 0$ share a quite small beamwidth (less than 3°). So it is interesting to notice that the main beams do not suffer any shift (as can be seen in Table 4.1 where the maxima of the theoretical array factor coincide with those of the simulated array pattern). Only the magnitude of the simulated main beams exhibit a little increase as θ_{inc} varies from 0° to -30°, which is of course due to the effect of the primary pattern.

4.6 Additional Simulations about Array Material

In this section, extra simulations are done as preparations before fabrication, since we should get a good assessment of the material loss. Indeed, for the sake of simplicity, the metal in previous HFSS simulations was treated as perfect electric conductor (PEC), which means no conductor loss was considered. However, when it comes to the practical fabrication, the ideal situation cannot be realized. Considering the computer-numerical-control (CNC) technique and fabrication cost, we may choose aluminum (conductivity=37.8×10^6 S/m and relative permeability=0.99) as the potential material candidate. Therefore, simulations based on the 24-groove array (w=60mm) with aluminum are taken.

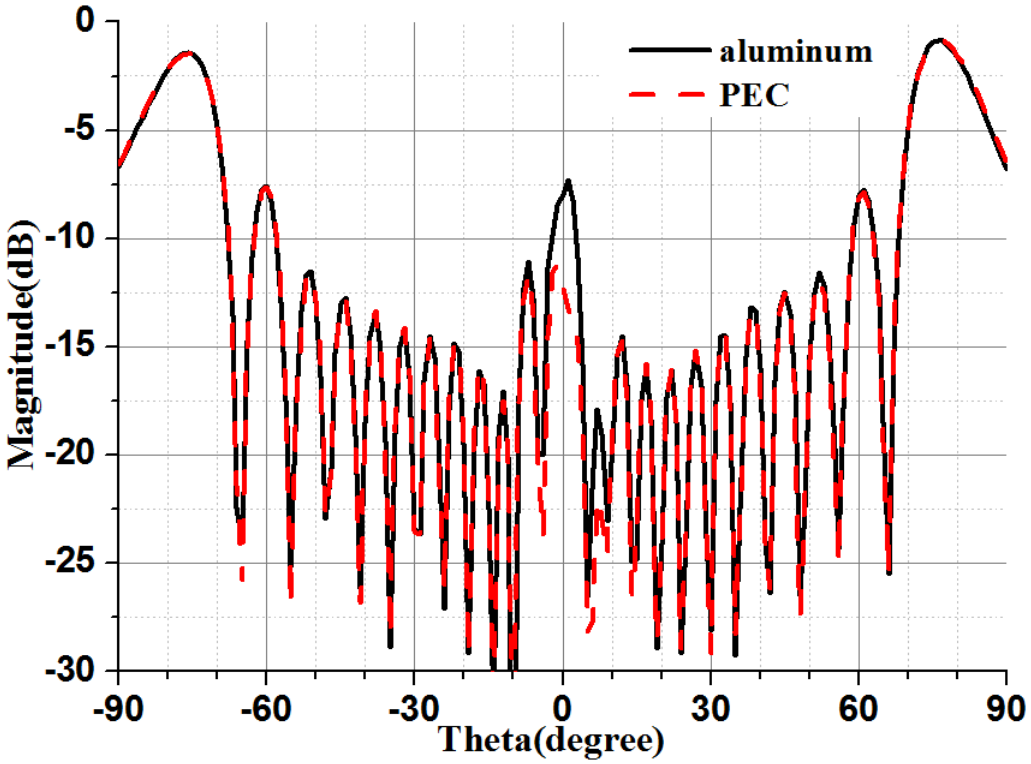

Fig.4.42 Bistatic RCS comparisons of 24-groove array when w=60mm with the material of Perfect E and with aluminum

Since the simulation uses planar wave excitation, the array's gain cannot be directly measured. So Fig.4.42 compares the array's Bistatic RCS in E-plane (E_θ) in aluminum (black solid line) and in PEC (red dotted line), respectively. At the broadside direction, the aluminum array produces bigger RCS (4dB bigger) than the PEC array. This can only be explained that the sensitive broadside reflection is affected by the varied current distribution. More important, in the direction of main beams (θ=±75°), the array in aluminum produces magnitude greatly close to the PEC array. This means the conductor loss at 60GHz for the array's main beam can be

neglected in our structure.

Conclusion

In this chapter, an array based on metal parallel plate groove elements has been studied. It derives from the rectangular waveguide element but provides a much simpler structure and easier design for fabrication. By properly choosing the groove's parameters in aperture length *b* and height *h*, a 6-groove array and a 24-groove array have been simulated and optimized respectively. The far-field radiation pattern demonstrates that the array could lead to the expected endfire radiation. Further investigations have explored the array bandwidth and its performance in oblique incidence. Theoretical explanations have been given based on array theory. At last, the array's main beam shift problem has been studied. For the next step, one array will be fabricated, and its practical performance will be measured in the indoor communication environment.

Chapter 5 Implementation and Measurement

Contents

Chapter 5 Implementation and Measurement

5.1 Introduction

In last chapter, the array based on metal groove elements is proposed to realize a reflector breadboard at 60GHz. Based on preliminary investigations about the 24-groove array (chapter 4), a bigger reflector with 80 grooves is fabricated. Related measurements of this array are then achieved in a NLOS environment and its performance for the communication improvement is verified.

As shown in Fig.5.1, a 200mm×200mm array (corresponding to 80 groove-cells) has been fabricated. We chose a bigger size than the simulated ones in chapter 4 in order to improve the power budget during the measurement campaign. These dimensions are also more realistic regarding a practical scenario. Unfortunately, such a large array cannot be simulated completely using HFSS and the performance has to be extrapolated with simple array theory.

(a)

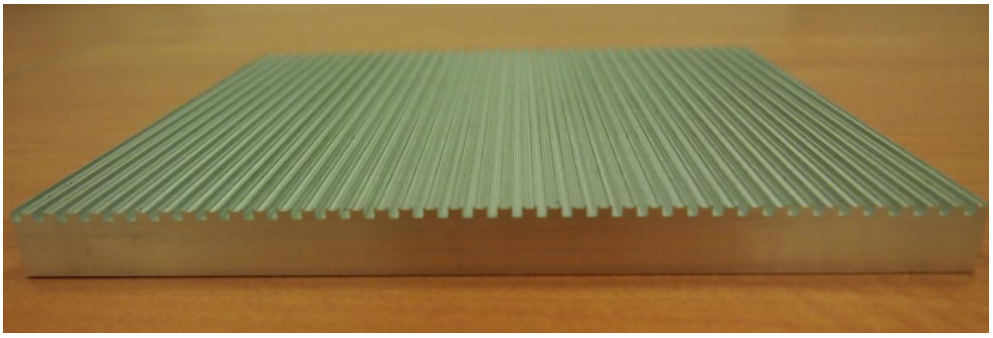

(b)

Fig.5.1 Fabricated 200mm×200mm array in (a) top view and (b) side view

5.2 Introduction about Measurement System

In this section, the measurement system at 60GHz is introduced. The whole measurement system is explained in Fig.5.2 (a). It was developed in a previous study for a 60GHz channel sounder [159-161].

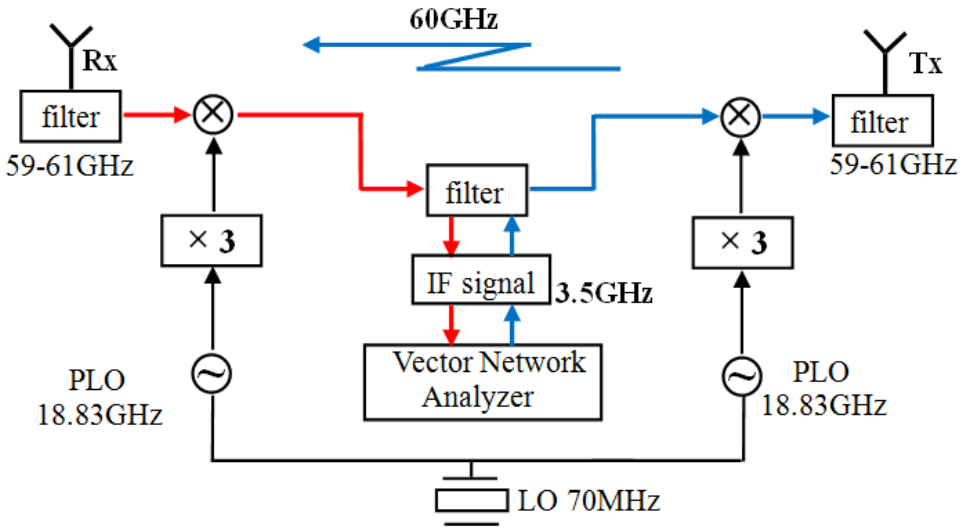

(a)

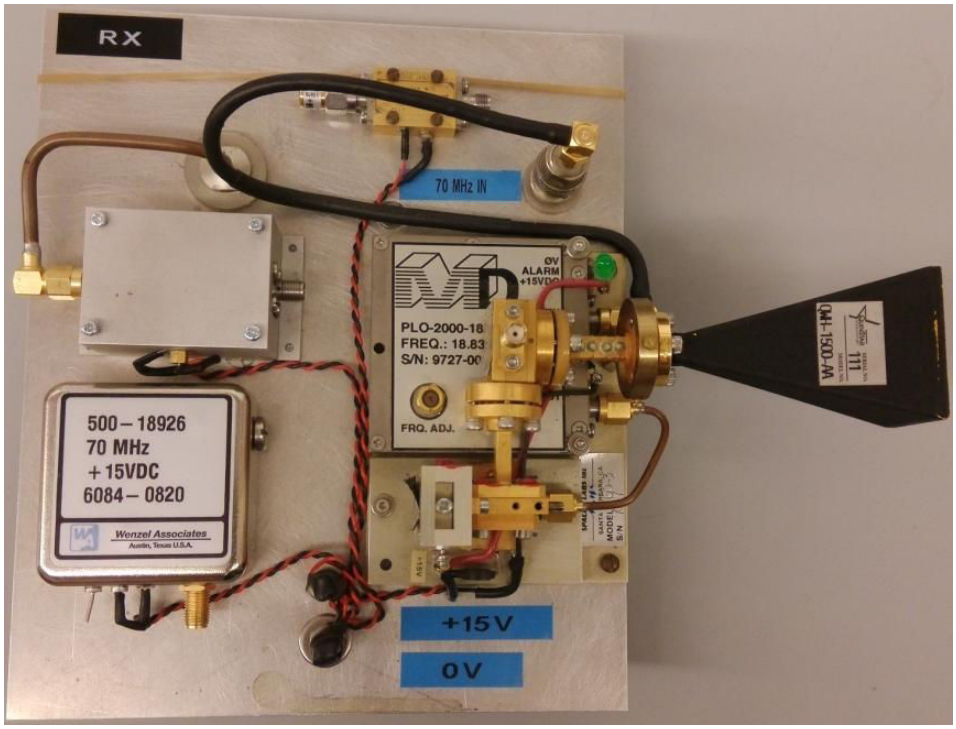

(b)

Fig.5.2 (a) Schematic of the measurement system and (b) picture of the Rx front-end (antenna, down-conversion and baseband modules)

The main experiment system includes three parts: the RF front-end (horn antenna at 60GHz for Tx and Rx), baseband modules (PLOs, up/down convertors, frequency multiplier and filters) and acquisition and control modules (Vector Network Analyzer or VNA). Taken the signal transmitted from Tx part as one example, baseband signal at 18.83GHz is generated based on 70MHz local reference LO, and then frequency-tripled to 56.5GHz carrier-frequency. Afterwards, the IF signal at 3.5GHz is up-converted by the carrier frequency to the 60GHz RF, and transmitted from Tx antenna to free space. As for the signal in Rx part, the working principle is totally reciprocal, and the IF signal is finally analyzed by the VNA.

The Tx and Rx antennas are identical horn antennas with 22.4dBi gain and around 10° 3dB-beamwidth (10° for H-plane and 12° for E-plane). The measured gain patterns are given in Fig.5.3.

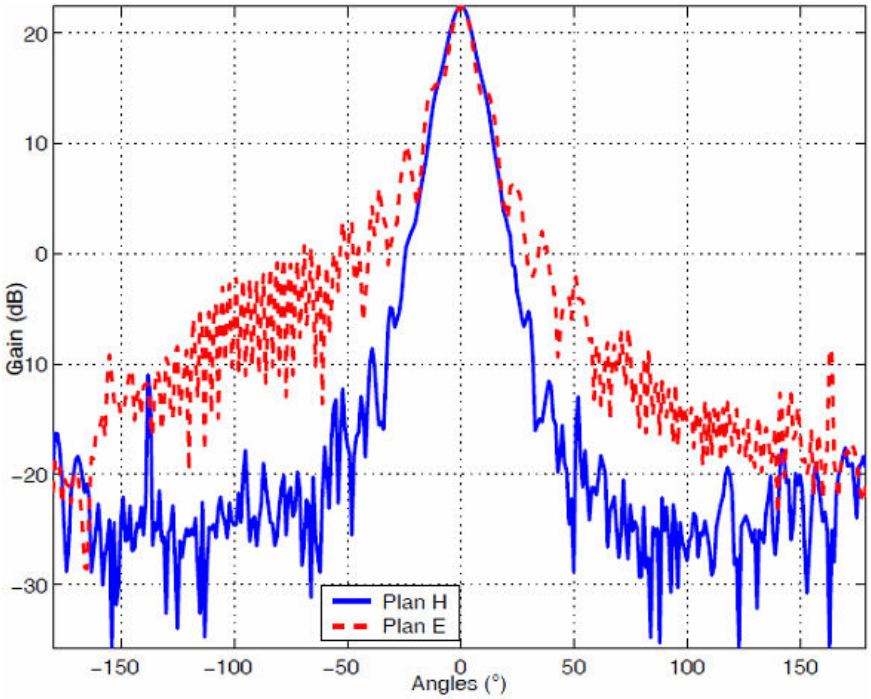

Fig.5.3 Gain pattern of horn antenna in experiment system at 60GHz

The modelling of the horn pattern is necessary for the power budget estimation in the following. In order to facilitate the calculation, an analytical model will be derivied to numerically approximate the gain pattern in Fig.5.3.

For the power transmitted from the horn antenna, the power density is

$$W(r,\theta,\varphi)=\frac{1}{\eta_0}\left\|\vec{E}(r,\theta,\varphi)\right\|^2 \tag{5-1}$$

in which η_0=120π is the wave impedance in free space. For simplicity, we assume the field produced by the horn is

$$\left\|\vec{E}(r,\theta,\varphi)\right\|=\frac{E_0}{r}\cos^N\theta \tag{5-2}$$

In (5-2), $\theta\in[0,\ \pi/2]$ and $\varphi\in[0,\ 2\pi]$, and the field is supposed to be 0 elsewhere. It should be noted that E_0 here is root mean square value of the magnitude (not the maximum value).

So, the total power radiated by the horn antenna can be written as

$$P_{\mathrm{Tx}}=\int_0^{2\pi}\int_0^{\pi/2}W(r,\theta,\varphi)r^2\sin\theta d\theta d\varphi$$

$$=\int_0^{2\pi}\int_0^{\pi/2}\left(\frac{E_0}{\eta_0 r}\cos^N\theta\right)^2 r^2\sin\theta d\theta$$

$$= \frac{2\pi}{\eta_0} E_0^2 \int_0^{\pi/2} \cos^{2N}\theta \sin\theta d\theta$$

$$= \frac{2\pi}{\eta_0 (2N+1)} E_0^2 \tag{5-3}$$

Assuming there is no loss for the horn antenna, its maximum gain (when θ=0) is given by

$$G_{horn} = \frac{E^2}{\eta_0} \Big/ \frac{P_{Tx}}{4\pi r^2} = \frac{4\pi E^2}{\eta_0 P_{Tx}} = 2(2N+1) \tag{5-4}$$

As introduced before, G_{horn}=22.4dB. Therefore, (5-4) can be solved out that *N* should be set to 43 in the analytical model.

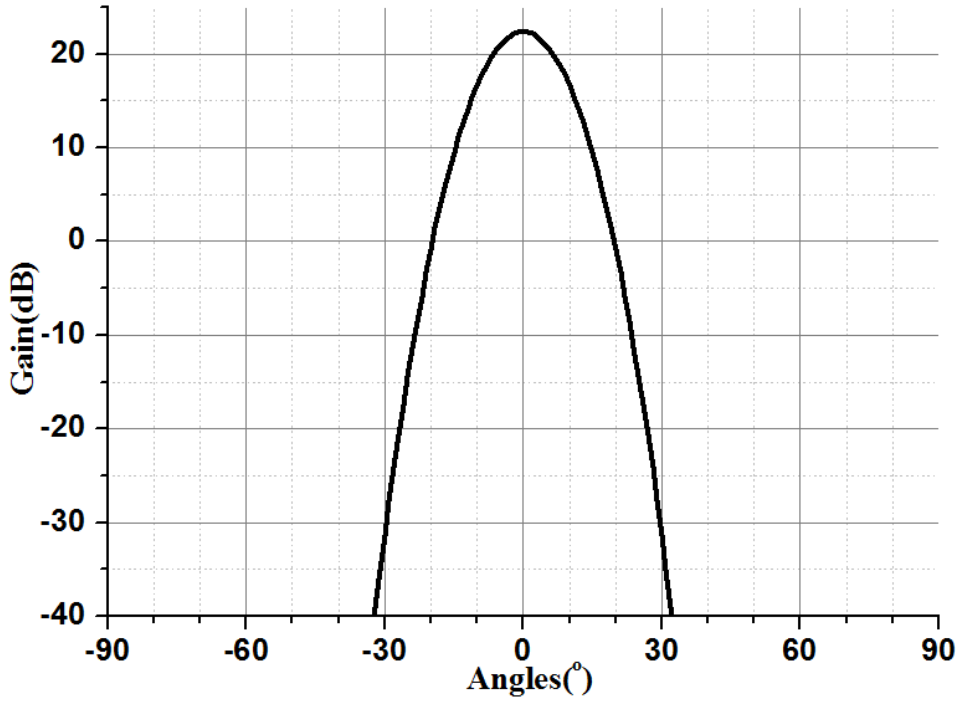

Fig.5.4 Derived gain pattern based on analytical model

Fig.5.4 depicts the derived gain pattern of the analytical model. It should be emphasized that, since this model is only an approximation, its E-plane and H-plane are assumed to be identical. According to Fig.5.4, the 3dB-beamwidth is 14° ([-7°, 7°]), which is 2° bigger than the practical result in Fig.5.3. Then, though this model does not demonstrate precisely accurate fitting to Fig.5.3, it is acceptable for power budget estimation.

Last but not least, as the important acquisition and control center, the VNA used

in our system is Rohde & Schwarz ZVB 14 (No. 1145.1010.17) [162], whose specification parameters are listed in Table 5.1.

Table 5.1 Parameter specifications for VNA

Ports	**2**
response frequency range	**10MHz-14GHz**
dynamic range (at 10 Hz IF bandwidth)	**>120 dB**
Power sweep range	**–40 dBm to +13 dBm**
Inherent noise	**< –110 dBm**

5.3 Measurement Plan and Related Parametric Investigations

In this section, we will introduce the procedure for the measurement campaign and investigations on important parameters. In order to validate the groove-based array's performance in NLOS environment, the whole measurement is done in two steps.

5.3.1 Rx and Tx are Placed Face to Face

In the beginning, the two antennas (Rx and Tx) are placed face to face, as shown in Fig.5.5.

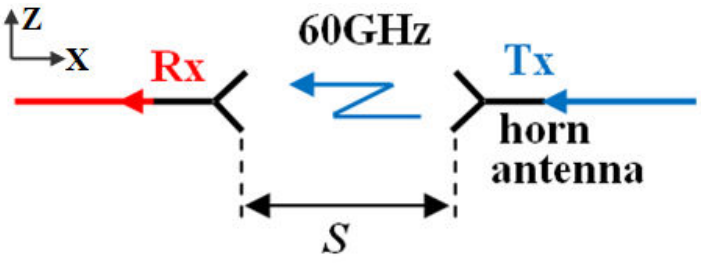

Fig.5.5 Rx and Tx placed face to face

By measuring the received power P_{Rx} at Rx antenna, the whole measurement system's loss (denoted as $Loss_{sys}$), which mainly comes from the circuit loss (e.g. up/down convert) of the sounder system, can be calculated based on Friis formula [163].

If we record the gain of the Tx and Rx antennas as G_{horn}, the power transmitted from Tx antenna as P_{Tx}, and the free space path loss [164] as $Loss_{air}$, then we have:

$$P_{Rx} = P_{Tx} + 2G_{horn} - Loss_{sys} - Loss_{air} \tag{5-5}$$

Meanwhile, the $Loss_{air}$ at 60GHz in (5-1) can be expressed as:

$$Loss_{air} = 68 + 20\log S \tag{5-6}$$

The unit for S is m in (5-6). And the combination of (5-5) and (5-6) can lead to the expression of $Loss_{sys}$:

$$Loss_{sys} = P_{Tx} + 2G_{horn} - P_{Rx} - 68 - 20\log S \tag{5-7}$$

5.3.2 Rx and Tx are Placed in NLOS Environment

For the next step, the Rx and Tx antennas are placed in NLOS environment, where the direct radio linkage does not exist. As depicted in Fig.5.6 (a), the distance between the two orthogonal antennas along *x*-axis is *S*, and the distance along y-axis is *F*, and all the other parameters and equipments are kept the same. With the same transmitted power P_{Tx}, the received power at Rx is recorded.

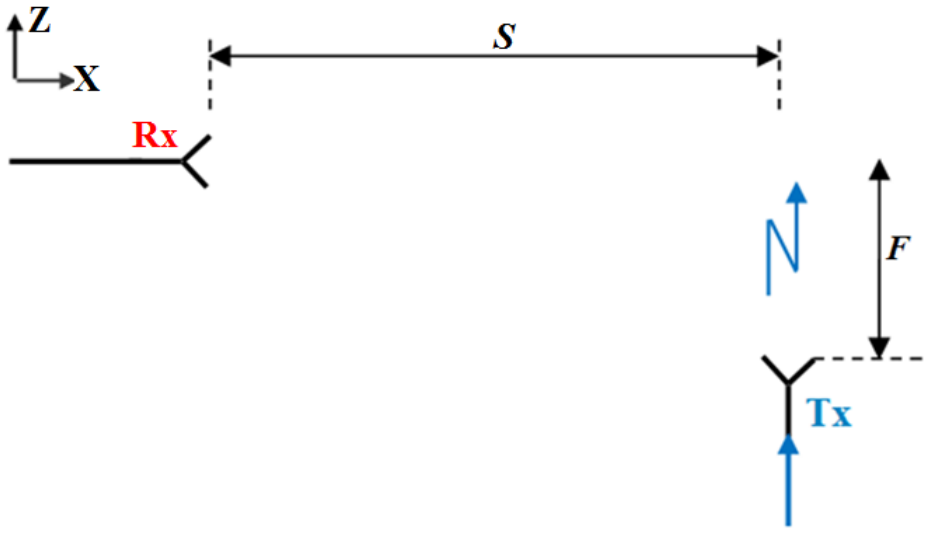

(a)

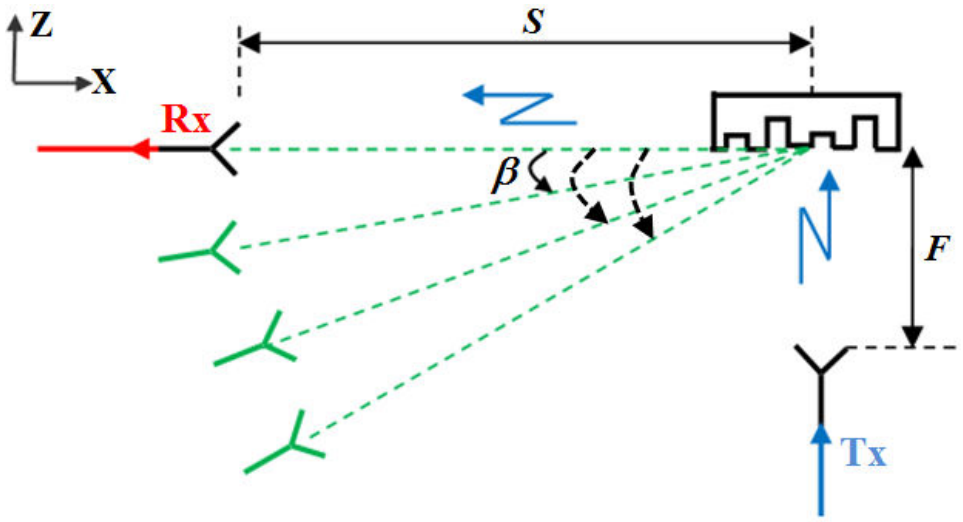

(b)

Fig.5.6 Rx and Tx are placed in NLOS environment with (a) no reflecting array and (b) reflecting array in the size of 200mm×200mm

Then, the groove-based array is added at the intersection point, as Fig.5.6 (b) shows. The array is in the size of $L \times w$ (L=w=200mm in this case). The Tx antenna is perpendicular to the array. Different positions are considered for the Rx antenna: more precisely, it is rotated around the array center (angle β) at distance S. For all positions, it points to the array center.

Based on our conception, the power transmitted from Tx will be captured by the reflecting array, and then re-radiated towards the Rx antenna. So the power received at Rx antenna can be expressed as:

$$P_{\mathrm{Rx}} = P_{array} + G_{horn} + G_{array} - \mathrm{Loss}_{sys} - \mathrm{Loss}_{air} \tag{5-8}$$

From which, G_{array}, the array gain, can be derived as:

$$G_{array} = P_{\mathrm{Rx}} + \mathrm{Loss}_{sys} + \mathrm{Loss}_{air} - P_{array} - G_{horn} \tag{5-9}$$

In (5-9), P_{array} is the amount of power captured and re-radiated by the array, which is a function of the distance F. As can be seen, G_{array} can be calculated out if we know P_{array}. Therefore, calculations of P_{array} will be explored in next section. Finally, a corner reflector with the same dimensions (200mm×200mm) will be used in the same measurement configuration for comparison.

5.3.2.1 Interpretation of P_{array}

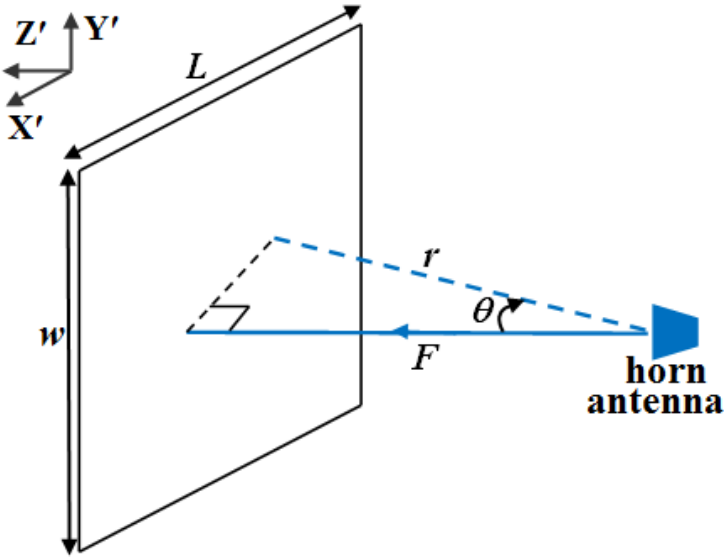

Fig.5.7 Power intercepted by the array

Fig.5.7 depicts the scenario involving the horn antenna and the array, to show how the power is intercepted. Based on the derived analytical model from (5-1) and (5-2) in last section, P_{array} can be calculated as:

$$P_{array} = \int_{-w/2}^{w/2}\int_{-L/2}^{L/2} W(r,\theta,\varphi)\vec{e}_r\vec{e}_z dxdy$$

$$= \frac{E^2}{\eta_0}\int_{-w/2}^{w/2}\int_{-L/2}^{L/2} \frac{\cos^{2N}\theta}{r^2}\cos\theta dxdy$$

$$= \frac{E^2}{\eta_0}F^{2N+1}\int_{-w/2}^{w/2}\int_{-L/2}^{L/2} \frac{1}{\left(x^2+y^2+F^2\right)^{N+3/2}}dxdy \qquad (5\text{-}10)$$

When we apply L=w=0.2m and N=43 into (5-10), P_{array} can be obtained. Fig.5.8 presents the curve of P_{array} when F varies in the range [0, 5] m.

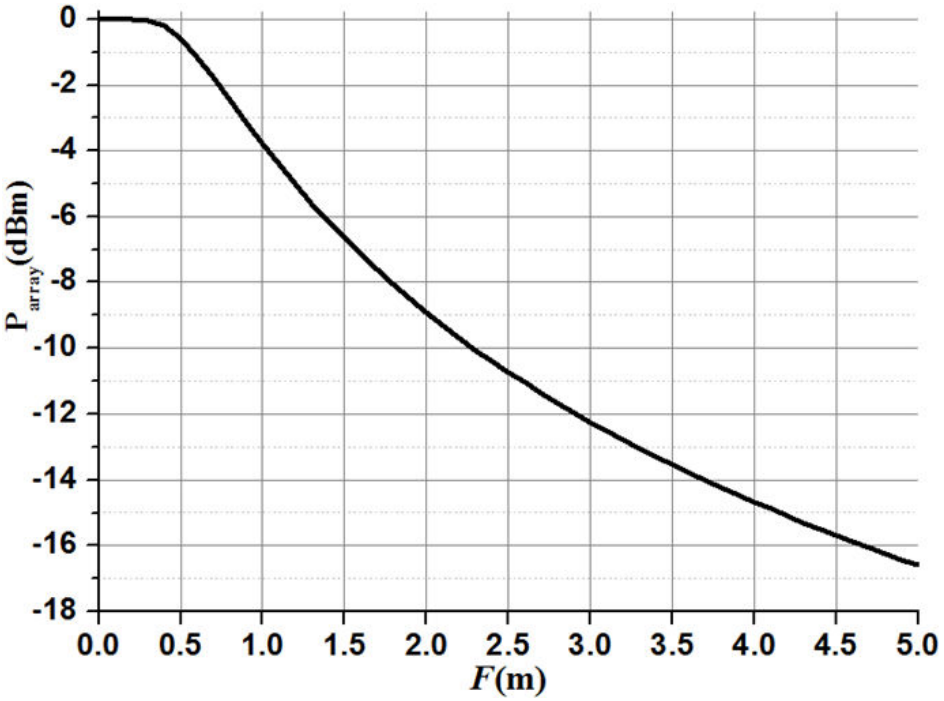

Fig.5.8 P_{array} for different *F*

5.3.2.2 Prediction of G_{array} based on *F*

Thanks to (5-9) and (5-10), G_{array} can be calculated easily based on the measured results. On the other hand, the theoretical value of G_{array} is also needed for comparison. Therefore, in this section, theoretical analysis is developed to predict the gain G_{array}.

The proposed analysis is more accurate than the simple pattern multiplication used in chapter 4. Indeed, it now accounts for the spherical nature of the wave illuminating the reflector. Considering the scenario in Fig.5.6 (b), the wavepath error related to *F* has to be introduced. This error comes from the feeding difference between an ideal plane incident wave (as used in chapter 4) and the actual spherical wave produced by the horn in the measurement. As seen in Fig.5.9, extra wavepaths (e.g. *F'* denoted in orange line) are inevitably introduced.

In order to assess the effect of this situation, the radiating aperture is first discretized in $\lambda_0/2\times\lambda_0/2$ cells, each of them corresponding to a short section of the successive grooves and reflecting the incident power with an ideal phase shift (0° or 180°). Then, the radiation is calculated from the contributions of all cells by accounting for the exact phase and magnitude of the incident wave on each one. Two aspects are thus addressed: 1), first of all, the impinging waves arriving at groove elements are no longer in-phase, thus an extra phase error is added to the initial

phase of these elements; 2), since the incident E-field on the groove elements is in inverse ratio with the distance F ($E \propto \frac{1}{F}$), the initial excitation magnitude M on each groove is also interfered.

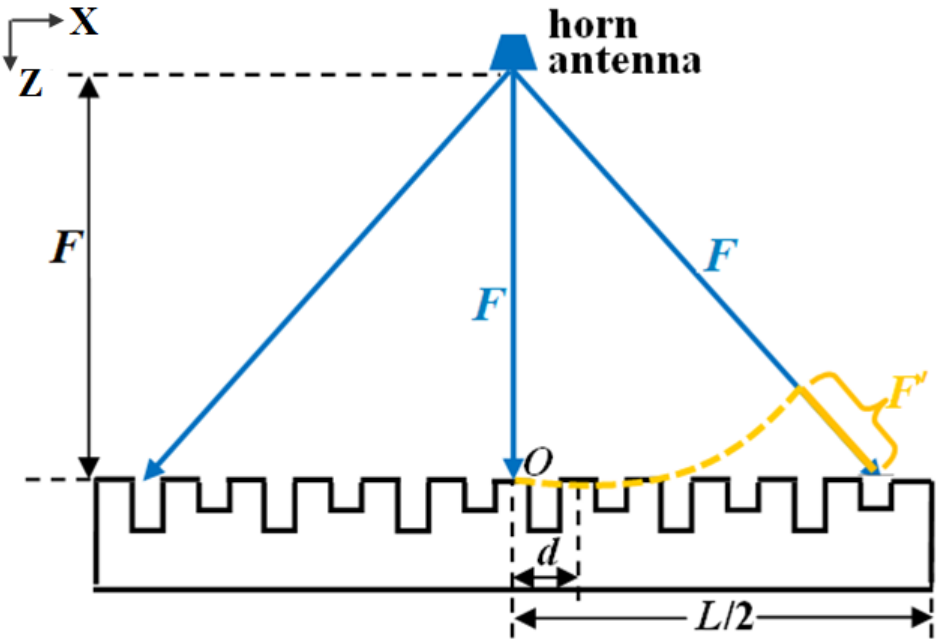

Fig.5.9 Schematic of spatial wavelength error from feeding

Fig.5.9 depicts the extra wavepaths on the side view in XOZ plane. Considering the array's symmetrical geometry, it is not difficult to imagine the same scenario in YOZ plane, which makes it a 2D problem. Therefore, the 80-groove array is discretized along x-axis and y-axis into an 80×80-element array as shown in Fig.5.10, and the corresponding phase error and magnitude error is calculated individually for each element $a_{i,j}$.

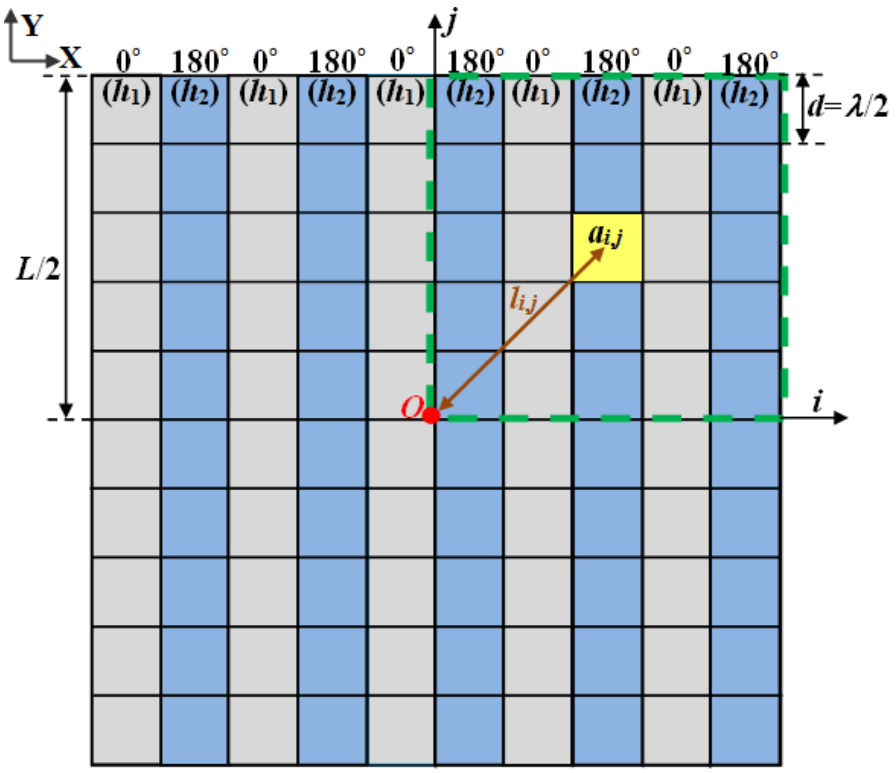

Fig.5.10 Array 2D discretization

The geometry centre of the array is at O, which is also the horn antenna's projection on the array. Thanks to the array symmetry, we only need to consider one-quarter block for simplification. Taken the right-up block (encircled with green dashed line) as example, for arbitrary element $a_{i,j}$, its distance to O can be expressed as:

$$l_{i,j} = \sqrt{\left[(i-0.5)d\right]^2 + \left[(j-0.5)d\right]^2}, \quad 1 \le i, j \le 40 \tag{5-11}$$

So the corresponding spatial wavepath error F' for $a_{i,j}$ can be expressed as:

$$F'_{i,j} = \sqrt{l_{i,j}^2 + F^2} - F = \sqrt{\left[(i-0.5)d\right]^2 + \left[(i-0.5)d\right]^2 + F^2} - F \tag{5-12}$$

If we use $\varphi'_{i,j}$ to denote the phase error of element $a_{i,j}$, and $M'_{i,j}$ for magnitude error, then we have:

$$\varphi'_{i,j} = F'_{i,j}\frac{2\pi}{\lambda} = \frac{2}{\lambda}\left\{\sqrt{\left[(i-0.5)d\right]^2 + \left[(i-0.5)d\right]^2 + F^2} - F\right\}\pi$$

$$= \frac{2\pi}{\lambda} \frac{\left[(i-0.5)d\right]^2 + \left[(i-0.5)d\right]^2}{\sqrt{\left[(i-0.5)d\right]^2 + \left[(i-0.5)d\right]^2 + F^2} + F} \tag{5-13}$$

$$M'_{i,j} = \frac{F}{F + F'_{i,j}} - 1 = \frac{F}{\sqrt{\left[(i-0.5)d\right]^2 + \left[(i-0.5)d\right]^2 + F^2}} - 1 \tag{5-14}$$

In (5-13), $\varphi'_{i,j} > 0$, this is easy to understand since the extra wavepath adds excess phases, compared with reference O. In (5-14), $M'_{i,j} < 0$, because the incident E-field is attenuated due to the extra wavepath, compared with reference O.

When F varies from 0.5m to 5m, the corresponding phase error $\varphi'_{i,j}$ is calculated based on (5-13). The results are compared in Fig.5.11 in degrees.

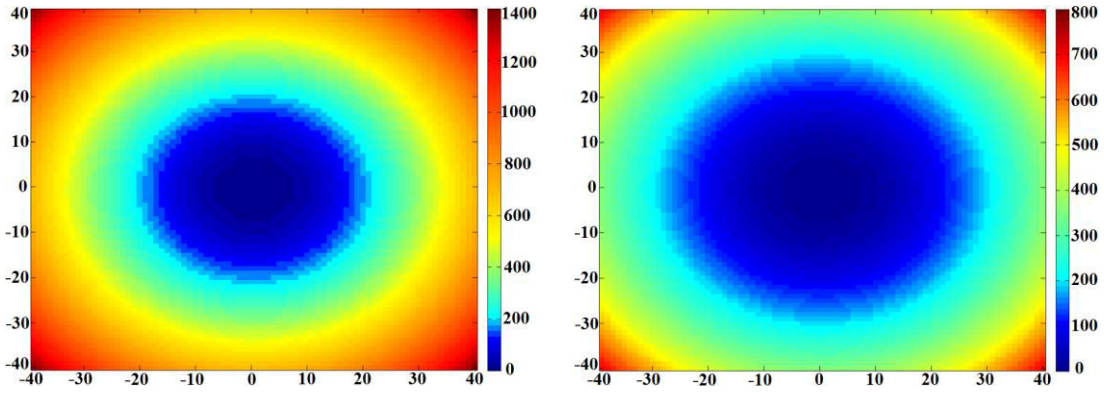

(a) F=0.5m **(b) F=1m**

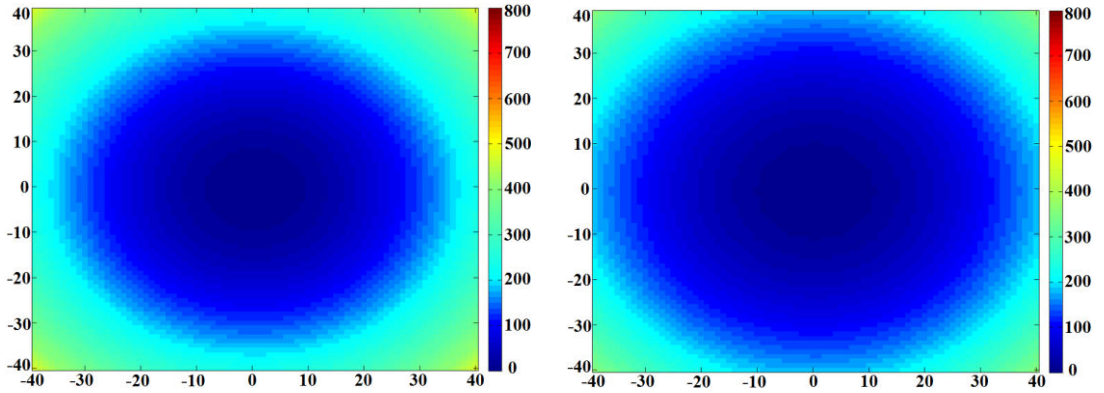

(c) F=1.5m **(d) F=2m**

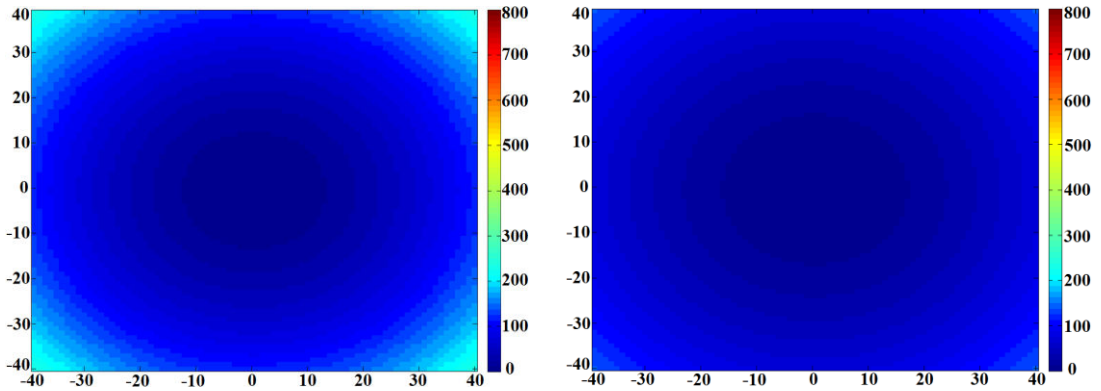

(e) *F*=3m **(f) *F*=5m**

Fig.5.11 Color plot comparison of $\varphi'_{i,j}$ when *F* varies from 0.5m to 5m

Since $\varphi'_{i,j}$ witnesses a maximum around 1400° when F=0.5m in Fig.5.11 (a), which is far beyond other situations' range, the scale in Fig.5.11 (a) is different from the other ones.

For all cases, the maximum error is of course obtained for the four corner elements (the furthest from O), which corresponds to $\varphi'_{\pm 40,\pm 40}$. Then, the larger F, the smaller $\varphi'_{40,40}$. To illustrate this logical evolution, Fig.5.12 gives a more detailed comparison of $\varphi'_{40,40}$ when F varies from 0.5m to 5m.

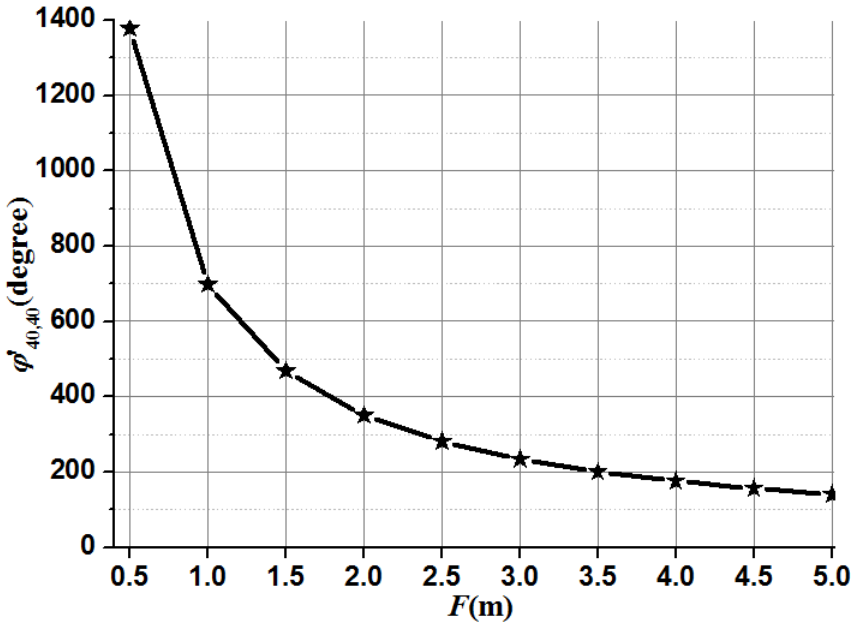

Fig.5.12 Schematic of $\varphi'_{40,40}$ when *F* varies from 0.5m to 5m

According to Fig.5.12, the maximum phase error $\varphi'_{40,40}$<200° when $F\geq$3.5m. We will see later (in Fig.5.14) that such an error on the corner of the reflector is compatible with a gain drop lower than 3 dB.

Similarly, the comparisons of magnitude error $M'_{i,j}$ are shown in Fig.5.13.

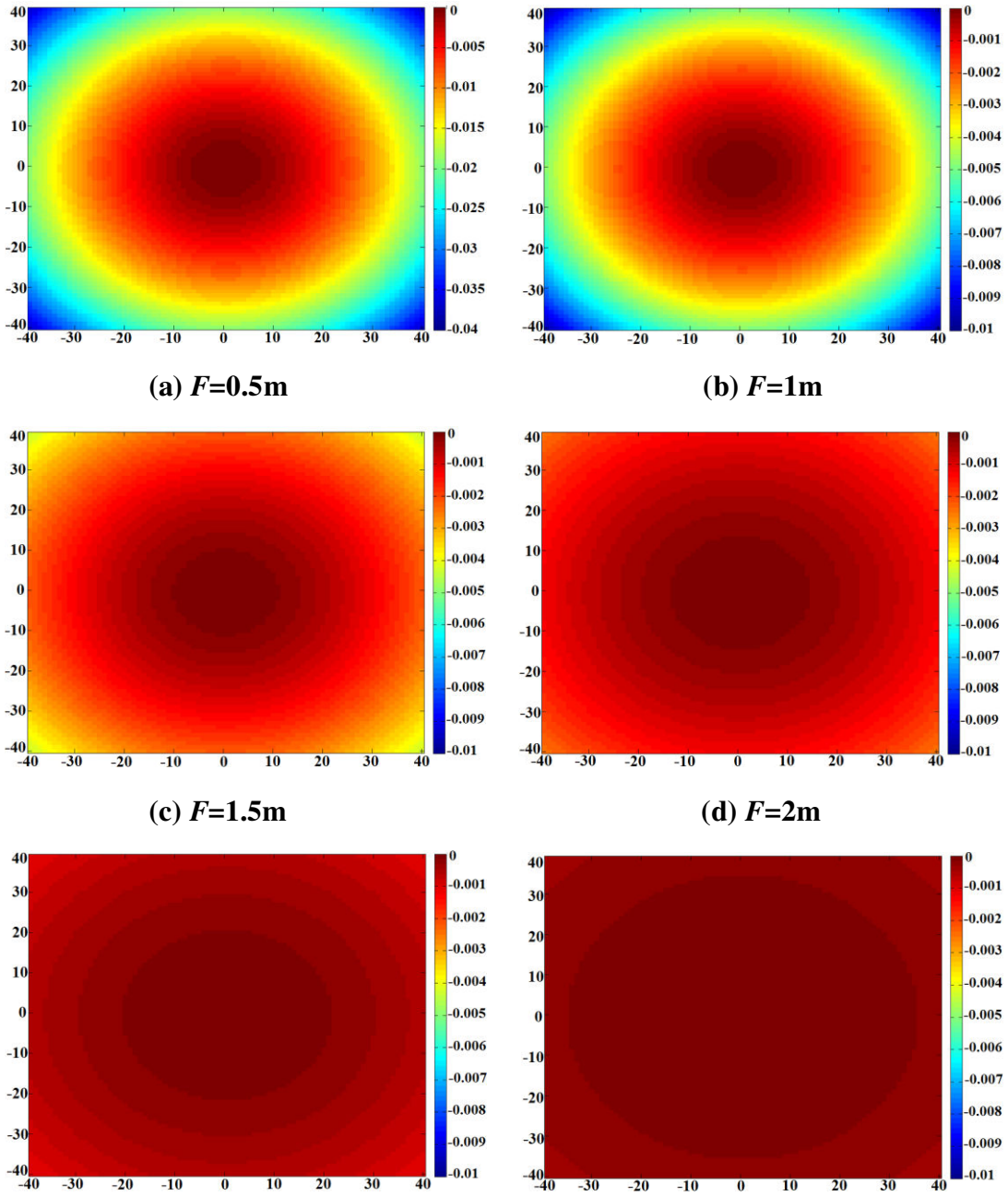

(a) F=0.5m **(b) F=1m**

(c) F=1.5m **(d) F=2m**

(e) F=3m **(f) F=5m**

Fig.5.13 Color plot comparison of $M'_{i,j}$ when F varies from 0.5m to 5m

According to Fig.5.13, the magnitude error is not significant. Even for the worst situation when F=0.5m, the maximum error is below -0.04, and when F increases to 2m, the maximum error is limited to around -0.01. Therefore, it can be concluded the error effect mainly comes from $\varphi'_{i,j}$.

Due to the existence of $\varphi'_{i,j}$ and $M'_{i,j}$, the elements in Fig.5.10 are updated in the

fed magnitude and phase as :

$$M_{i,j} = 1 + M'_{i,j} \tag{5-14}$$

$$\psi_{i,j} = \begin{cases} \varphi'_{i,j}, & i = -40,-38,\ldots -2,1,\ldots 39 \\ \pi + \varphi'_{i,j}, & i = -39,-37,\ldots -1,2,\ldots 40 \end{cases} \tag{5-15}$$

Based on (5-14) and (5-15), the theoretical directivity pattern of the array for different distances F can be calculated assuming simple array theory. This procedure is quite similar with what has been done in chapter 4: the theoretical directivity is obtained from multiplication of the array factor (now including phase and magnitude errors) and the primary pattern of a single groove element. The calculated result is depicted in Fig.5.14.

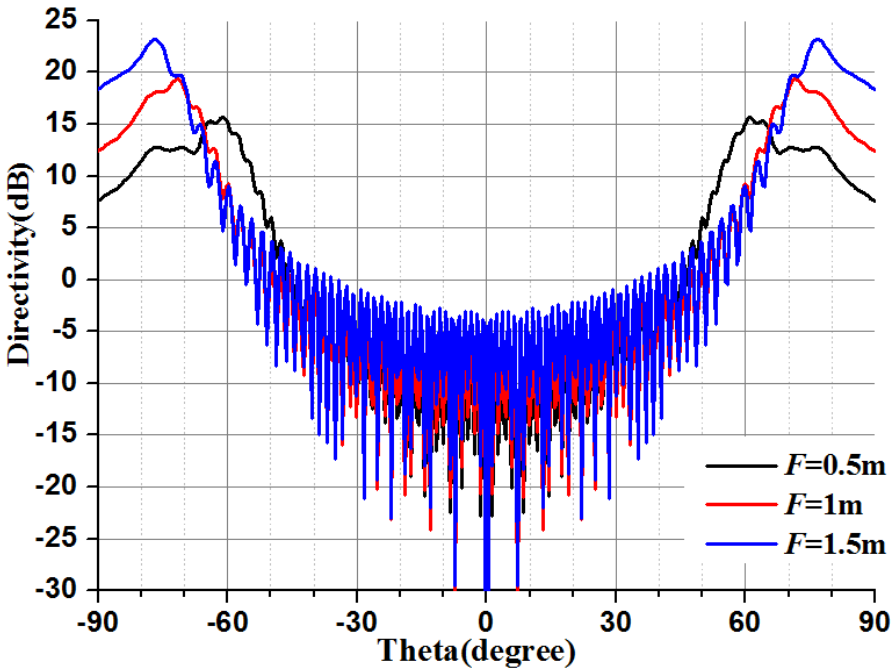

(a)

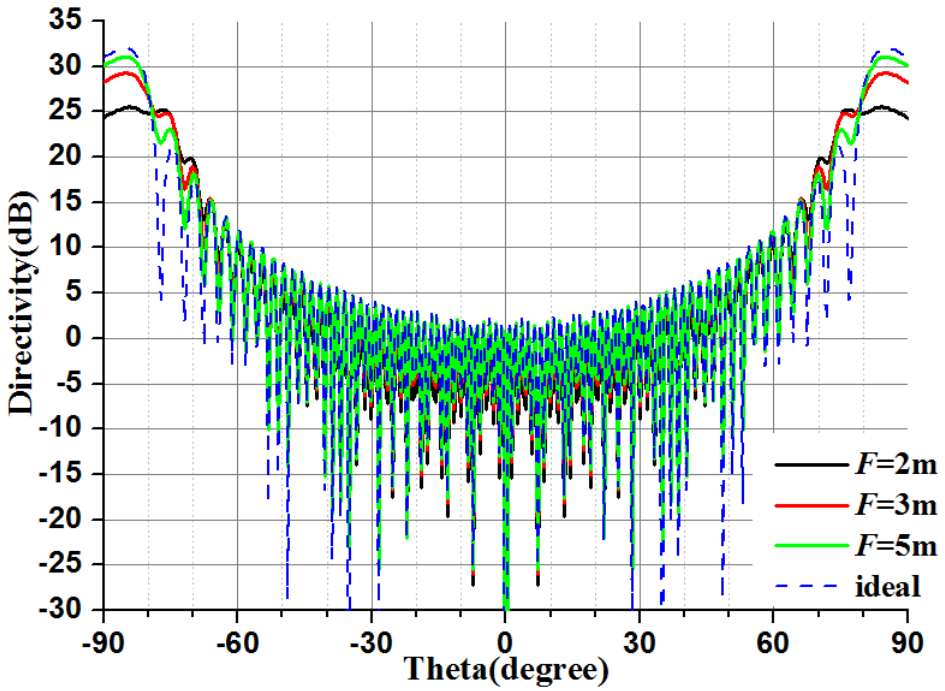

(b)

Fig.5.14 Theoretical Directivity of the array considering $\varphi'_{i,j}$ and $M'_{i,j}$ when (a) F=0.5-1.5m and (b) F=2m-5m plus ideal situation

Fig.5.14 compares the theoretical directivities corresponding to different F, and the last one (blue dotted line in Fig.5.14 (b)) indicates an ideal situation without phase error, or it can be regard as $F=+\infty$. When F is smaller than 2m, the array performance witnesses a great deterioration. Even when F=2m, the maximum directivity still exhibits 6dB difference.

For the next step, these theoretical investigations will be confronted with measurement results.

5.4 Analysis and Comparison of Measurement Results

In this section, the measured results from the two steps shown in Fig.5.6 will be analyzed and compared with theoretical calculations.

Through the whole measurement, the transmitted power is always fixed as P_{Tx} =0dBm. As the first step, $Loss_{sys}$ is determined based on (5-7) using the configuration described in Fig. 5.6a. In order to diminish undesired errors in the experiment (e.g. imperfect antenna positioning), measurements are repeated several times and averaged for each tested position (S moving from 0.5m to 1.5m).

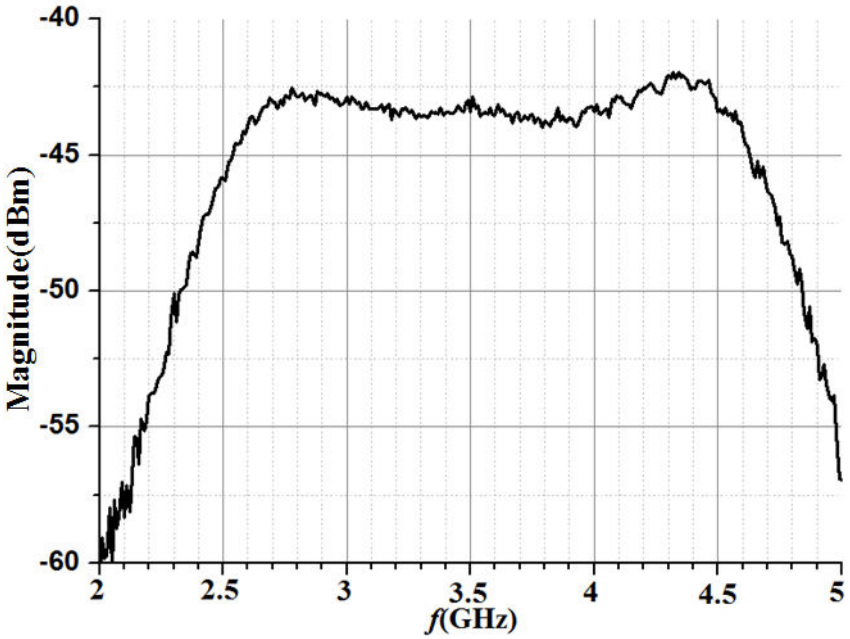

Fig.5.15 Measured P_{Rx} when S=1m

Fig.5.15 gives one example of the received P_{Rx} when S=1m. As explained in Fig.5.3, the center frequency f=3.5GHz (IF) corresponds to the desired 60GHz signal. The measured received power at 60 GHz is recorded in table 5.2 for different S. The corresponding theoretical path loss is also given and the system loss can thus be derived.

Table 5.2 Measured P_{Rx} and calculation for $Loss_{sys}$ at 60GHz

	S(m)		
	0.5	**1**	**1.5**
Measured P_{Rx} (dBm)	-37	-43.4	-45.9
Theoretical $Loss_{air}$ (dB)	62	68	71.5
Calculated $Loss_{sys}$ (dB)	19.8	20.2	19.1

According to Table 5.2, the average value of the system loss is $Loss_{sys}$=19.7dB. Then, the second step of the measurement involving the two antennas in NLOS environment is taken, and the measurement setting is shown in Fig.5.16.

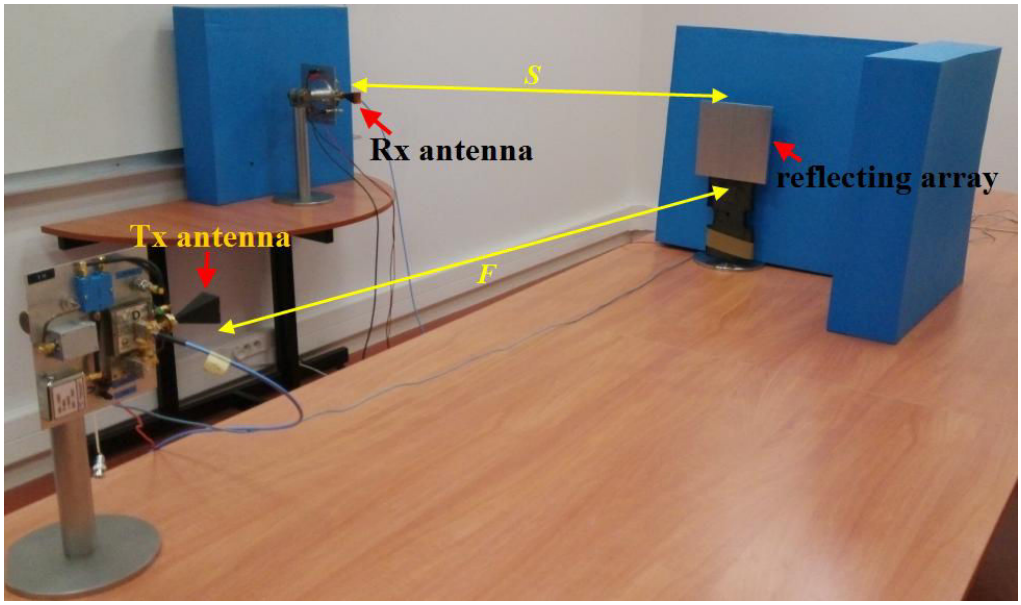

Fig.5.16 Measurement setting for two antennas in NLOS environment

At first, only the two orthogonal antennas (β=0°) are utilized with no array. Different configurations have been tested where S changes between 0.5 and 1.5m while F varies between 1.5 and 2m. Note that the values for F have been chosen as a tradeoff between the maximum avoidance of phase errors and the hardware limit such as cable lengths. In all cases, the received P_{Rx} remains around -85dBm which is close to noise floor. Fig.5.17 exhibits one example when S=1m and F=2m, which is representative of P_{Rx} with no array. This demonstrates there is almost no power received by the Rx antenna in this situation, which is consistent with the NLOS environment.

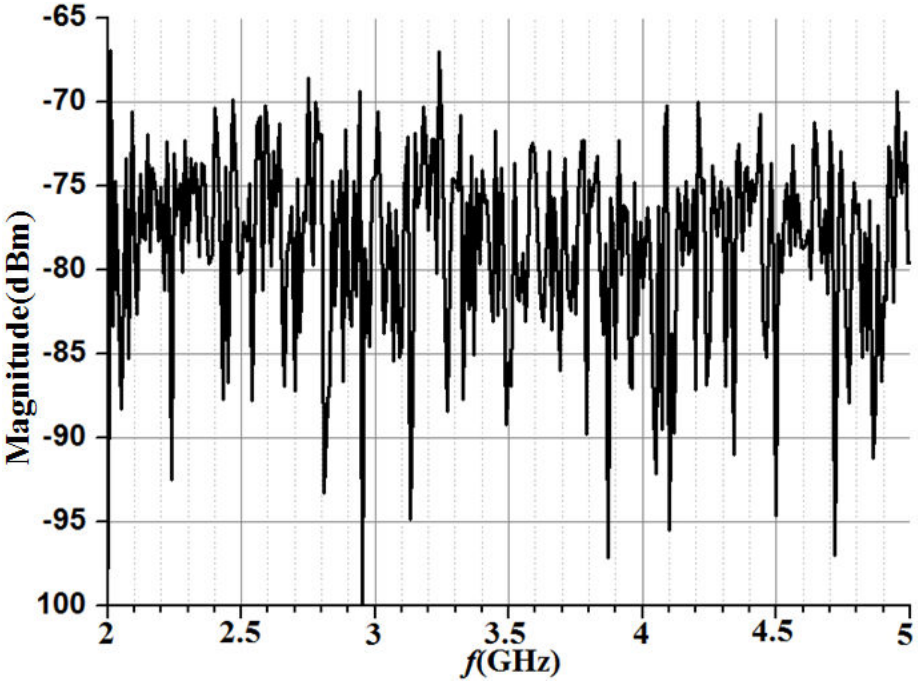

Fig.5.17 Measured P_{Rx} when S=1m and F=2m at β=0° for Rx and Tx antennas in NLOS environment with no array.

Then, the reflecting array is added. Similarly, the different configurations are measured when S and F are still varied in the same range. For each configuration, the rotation angle β is altered between [0°, 30°], and the measured P_{Rx} is recorded in Table 5.3.

Table 5.3 Measured P_{Rx} with reflecting array at 60GHz

		Measured P_{Rx} (dBm)					
		F=1.5m			F=2m		
		S=0.5m	S=1m	S=1.5m	S=0.5m	S=1m	S=1.5m
β(°)	0	-57.5	-62.9	-65.1	-57.7	-62.1	-64.3
	5	-53.4	-58.9	-60.9	-52.8	-58	-59.1
	10	-51.3	-56.1	-59	-49	-54.2	-56.4
	15	-47.4	-51.9	-53.8	-48.5	-52.6	-55.2
	20	-48.5	-53.6	-56.4	-52.5	-56.7	-59.5
	25	-54.7	-59.9	-61.6	-56	-62.2	-64.1
	30	-56.4	-62.9	-64.9	-61.5	-69.1	-70.1

For a better comparison, the results in Table 5.3 are schematized in Fig.5.18. The received power (purple dashed line), is also given as a reference.

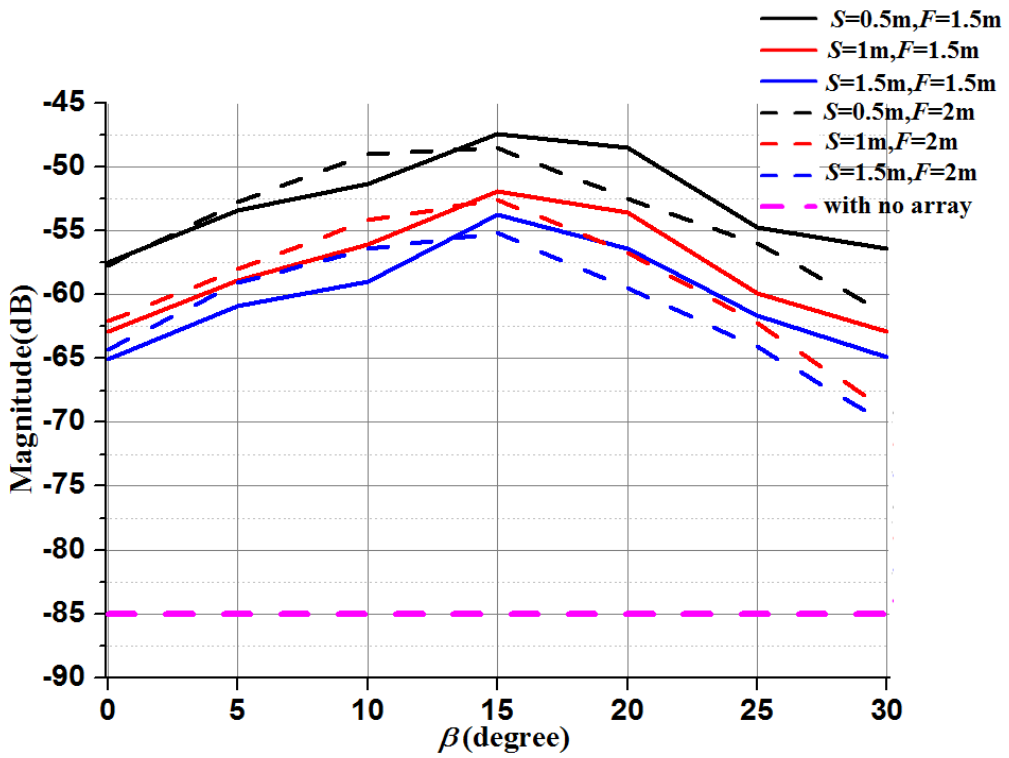

Fig.5.18 Comparison of measured P_{Rx} when *S* varies between 0.5m and 1.5m, and *F* between 1.5m and 2m, together with the initial result with no array.

It clearly demonstrates that, thanks to the utilization of the reflecting array, the received power at the Rx terminal is significantly increased. The maximum is always obtained for $10°<\beta<20°$, which is quite consistent with the theoretical main lobe position in Fig. 5.14. The growth depends on *S* and *F*, e.g. when *S*=1.5m and *F*=2m, the growth is 20dB at $\beta=0°$ and 30dB at $\beta=15°$. In conclusion, the signal level at Rx terminal is greatly improved by the array, and the 60GHz communication relay in NLOS environment is successfully established as anticipated.

At last, for comparison, a 200mm×200mm (same size as our array) corner reflector is also taken into measurement as a reference, a photo of this corner reflector is presented in Fig.5.19.

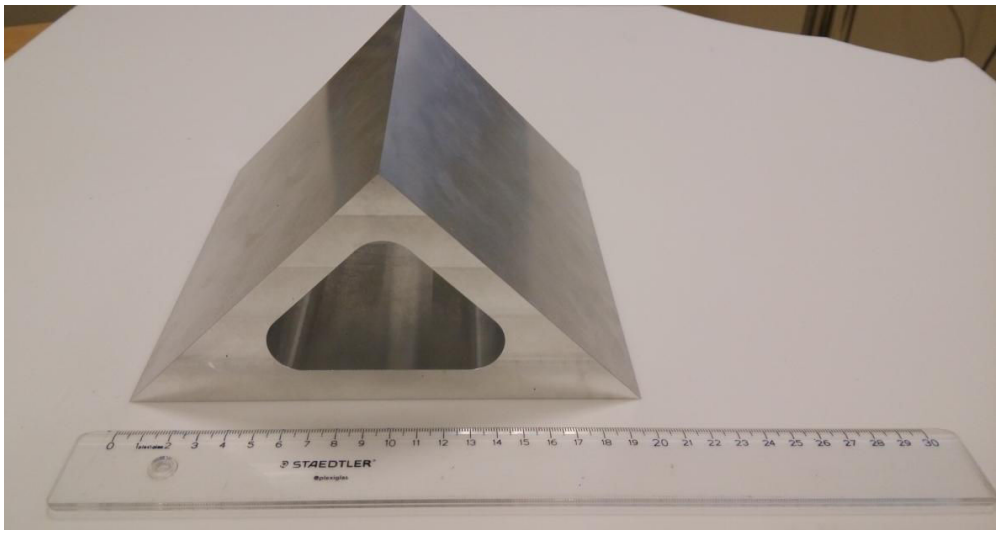

Fig.5.19 Photo of 200mm×200mm corner reflector

Measurement involving the corner reflector is shown in Fig.5.20. The distance from the half height of the reflector to Tx antenna is F, and the distance from the bottom centre to Rx antenna is S. In this experiment, Rx is always set parallel to x-axis (β=0) since the corner reflector does not produce any tilt in the reflected beam.

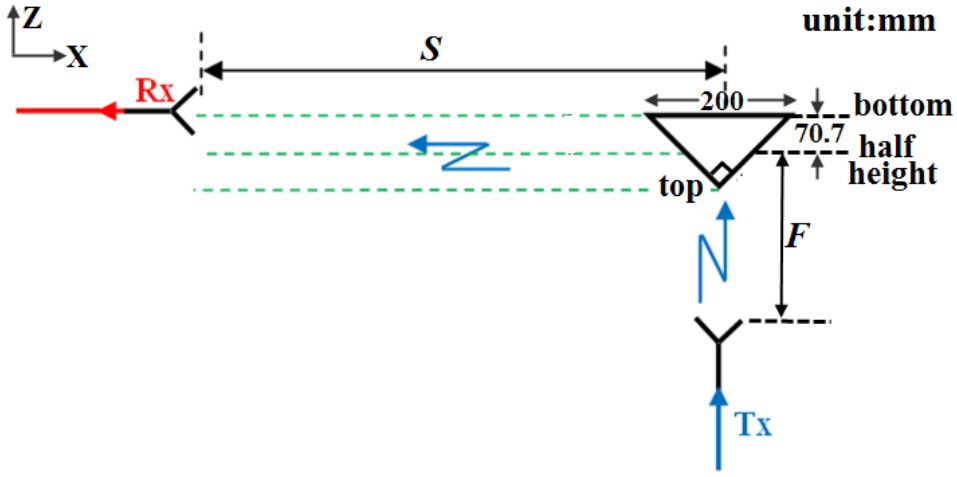

Fig.5.20 Measurement configuration for corner reflector

On the other hand, it has been noticed that the z-translation of the RX antenna with regards to the center of the corner reflector (defined as half height in the figure) had a significant impact on the received power. Different z-positions (denoted with green dashed line) have then been tested. In the following, we only record the result when Rx is located at the half height line, which roughly corresponds to the maximum. Fig.5.21 gives a typical comparison with three curves showing the received power: with no array, with reflecting array when S=1.5m, F=2m and β=15°, and with corner

reflector when S=1.5m, F=2m.

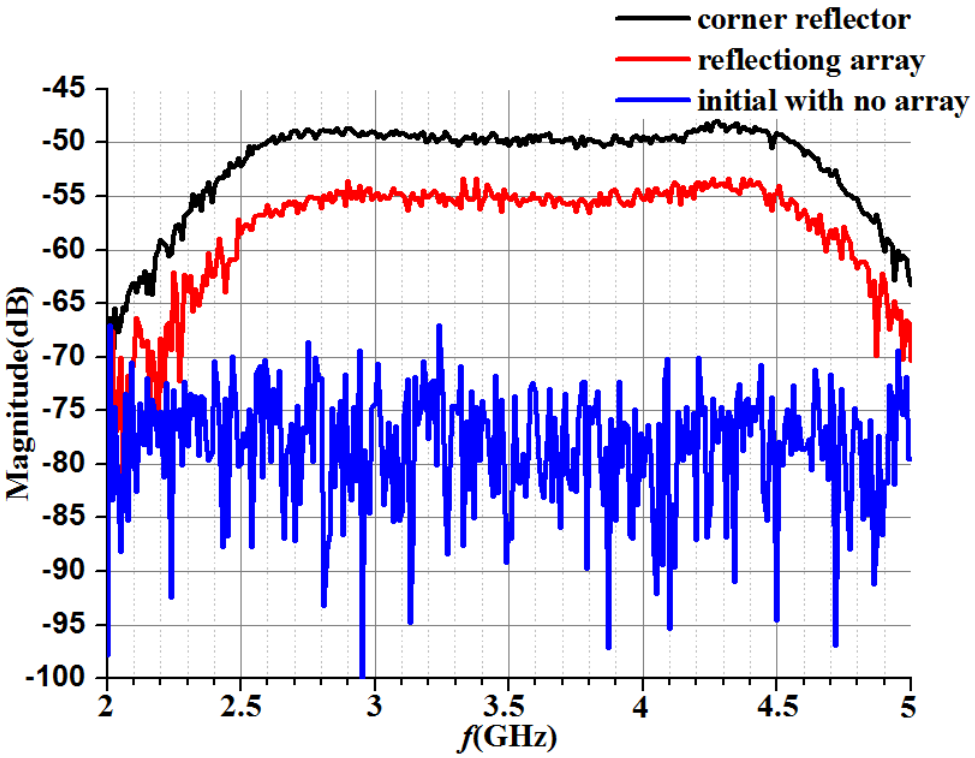

Fig.5.21 P_{Rx} comparison with corner reflector and reflecting array when S=1.5m, F=2m

At 60GHz, both the corner reflector and our planar reflector provide high improvement to the signal. The result with the corner reflector is 5dB bigger than those of the reflecting array. However, much lower profile makes the reflecting array an acceptable good choice when flatness is a requirement.

Finally, the array's gain is also estimated from the measurements. Based on Fig.5.8, when F=1.5m, P_{array}=-6.6dB; and when F=2m, P_{array}=-8.9dB. After applying P_{array} and the results in Table 5.3 into (5-9), G_{array} is obtained and listed in Table 5.4 for different F and β.

In theory, the gain should not be dependent on S. In practice, Table 5.4 shows that it is (about 2dB improvement when S varies from 0.5 to 1.5m). This is due to the fact that achievable S are not large enough to be in the Fraunhoffer zone. As the size of the reflector is D=0.2m and the wavelength at 60GHz is λ_0=5mm, the Fraunhoffer limit is $2D^2/\lambda_0$=16m, which is much larger than the typical S we use. Then the concept of gain is a bit misleading as we do not comply with far field assumptions. Definitively, what is important is the demonstrated improvement of transmitted power (not gain), whether we work in far field or not.

Table 5.4 Calculated G_{array}

		Calculated G_{array} (dB)					
		***F*=1.5m**			***F*=2m**		
		***S*=0.5m**	***S*=1m**	***S*=1.5m**	***S*=0.5m**	***S*=1m**	***S*=1.5m**
$\beta(^\circ)$	**0**	8.4	9	10.3	10.7	12.3	13.6
	5	12.5	13	14.5	15.6	16.4	18.8
	10	14.6	15.8	16.4	19.2	20	21.3
	15	18.5	20	21.6	19.9	21.8	22.7
	20	17.4	18.3	19	15.9	17.7	18.4
	25	11.2	12	13.8	12.4	12.2	13.8
	30	9.5	9	10.5	6.9	5.3	7.8

Now, having this in mind, we will compare the value of "gain" derived from measurement with the theoretical directivity (as plotted in Fig. 5.14). The results are given in Fig.5.21 (a). For this comparison, we select the calculated "gain" obtained with larger *S* to better approach the Fraunhoffer limit. The comparison is given in the range θ=[60°, 90°] (θ=90°-β). The agreement is quite good up to θ=75°. For larger angles, the theoretical predictions are too optimistic. As we already discussed in chapter 4, this may be due to the rough estimation of the groove elementary pattern.

In Fig.5.22 (b), extra comparisons of the array's gain performance are included for the array's bandwidth exploration. Limited by the measurement sounder which only shares 2GHz bandwidth, the results are demonstrated in *f*= [59, 61] GHz.

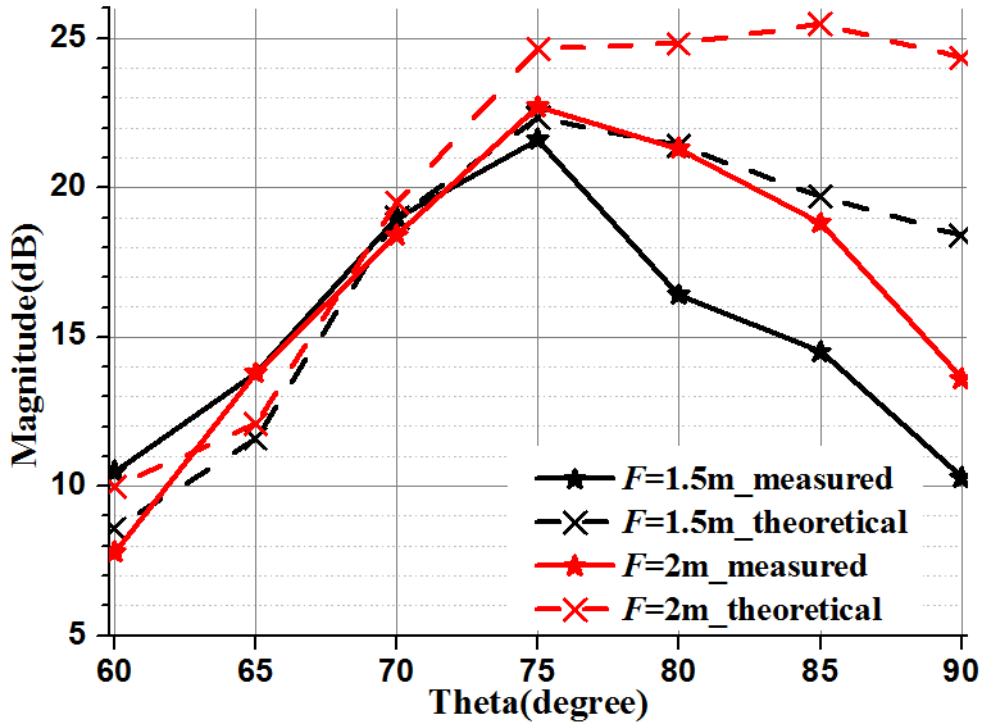

Fig.5.22 Comparisons between measured gain and theoretical directivity when *S*=1.5m and *F* varies between 1.5m and 2m.

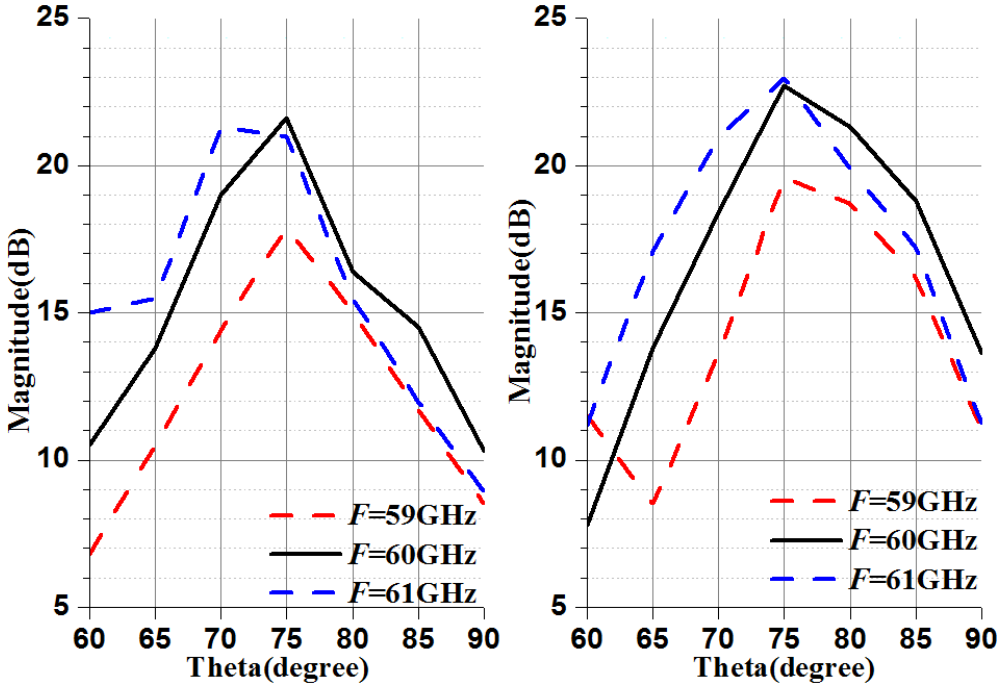

(a) **(b)**

Fig.5.23 Gain comparisons for *f*=59-61GHz and *θ*= [60°, 75°], when *S*=1.5m and (a) *F*=1.5m and (b) *F*=2m.

The measured gain is around 2-3dB less than the theoretical directivities in the maximum beam direction. When F=1.5m, the maximum beam direction is θ=75° for measured value of 20dB, and the theoretical result records its maximum at the same direction as 21.6dB (the difference is 2.3dB). When F=2m, the maximum beam direction is θ=75° for the average measured value of 22.7dB, and the theoretical result records its maximum at θ=85° as 25.5dB (the difference is 3.2dB). Actually, we can notice the two results are in coincidence in the range θ=[60°, 75°], but the magnitude difference grows quickly when θ=[75°, 90°].

As for the gains in 59GHz and 61GHz in Fig.5.21 (b), observations can be made as below:

1). the gain difference between 59GHz and 60GHz is scaling through almost the whole range of [60°, 90°] (Δgain_59=gain_59GHz-gain_60GHz is growing): the minimal Δgain_59=-4.6dB for F=1.5m at θ=65°, and -5.3dB for F=2m at θ=70°; and when θ=90°, Δgain _59=-1.8dB for F=1.5m and -2.6dB for F=2m.

2). the gain difference between 61GHz and 60GHz is diminishing through almost the whole range of [60°, 90°] (Δgain_61=gain_61GHz-gain_60GHz is decreasing): when θ=60°, the maximum Δgain _61=4.5dB for F=1.5m and 3.4dB for F=2m; and when θ=90°, Δgain_61=-1.4dB for F=1.5m and -2.4dB for F=2m. Moreover, the 3dB bandwidth is kept 2GHz (59-61GHz) or 6.7% at least in the range [75°, 90°].

Actually, the observations have validated the investigations in chapter 4. Based on (4-7) and Fig.4.28, when the observation angle θ moves away the endfire direction from 90° to 60°, the array factor $2\left|\cos\left[\frac{\pi f_n}{2}(\sin\theta+1)\right]\frac{\sin(M\pi f_n\sin\theta)}{\sin(\pi f_n\sin\theta)}\right|$ would see its maximum beam shifted towards higher frequency. Therefore, the gain at 59GHz would drop and the gain at 61GHz would increase, and the overall bandwidth would not be affected much.

Conclusion

In this chapter, a 200mm×200mm array based on the metal groove structure has been fabricated and measured in practical NLOS environment. Parameters investigations are conducted on the distance F, by calculating the power intercepted by the array, and by analyzing its effect on the array's theoretical Directivity. Thanks to the array, the power received at Rx terminal is increased by around 30dBm in the

measurement. This greatly improves the communication between Tx and Rx terminals, and successfully establish the desired 60GHz communication for indoor NLOS environment. Further explorations have compared the array's measured directivity with theoretical values.

General Conclusion

Aiming to enable the 60GHz signal transmission in NLOS environment and improve the link budget for indoor communication, a solution based on passive repeater with quasi-endfire radiation is proposed in this thesis with systematic investigations and theoretical analyses. The typical foreseen application is the radio-coverage of a T-shaped corridor.

A planar reflector made of two different phase-shifting cells is proposed as the fundamental module of the repeater. It uses out-of-phase elements with $\lambda/2$ inter-element spacing to suppress the specular the broadside reflection at broadside while producing main beams close to endfire direction.

Different topologies and technologies are investigated to address this problem. The first solutions are based on DRA elements. It is first shown that all DRAs in the array should be identical so that they radiate similarly, which is essential for the proper operation of the reflecting system. Based on this constraint, notched DRAs are first investigated. By combining two such DRAs with notches on opposite diagonals it is possible to generate polar conversion together with out-of-phase reflection. Simulations with HFSS are used to optimize the design of the structure. Different simulation strategies are proposed, using either a single cell or a couple of them. Finally, optimizations are carried out at the array level of to address finiteness effects. Considering our design objective, a factor of merit involving the endfire to broadside radiation ratio is defined and utilized to help localizing the optimal dimensions.

A second topology is also studied that involves a square DRA coupled to an open-circuited phase-delay stub. Although both structures demonstrate strong scattering of the power close to endfire direction, they raise challenges for the fabrication process, considering their relative complexity at 60GHz. Therefore, an alternative technology using dielectric filled short-circuited metallic waveguides is then considered. Once again, the feasibility of the concept is shown in simulation at the array level. Finally, a last technology is selected that can be seen as an evolution of the metallic waveguide structure. It is made of short-circuited parallel-plate waveguides. The structure can be fabricated from a simple metallic plate in which grooves are drilled. This simplifies the design to a quasi-2D problem with no need to

use any dielectric material. Simulations are taken on a 6-groove and 24-groove array to explore the endfire radiation performances. Theoretical derivations based on array theory are provided in details to explore the 24-groove array's performance in bandwidth and oblique incidence. Explanations are also given concerning the phenomenon of the main beam shift, which is a problem observed in all the four topologies.

Finally, a metal groove array in the size of 200mm×200mm is fabricated and measured. Practical measurements for 60GHz communications in NLOS environment are carried out to test the array's performance, and analyses on the experimental results are presented. In the experiment, when the array is 1.5m away from the transmitted antenna and 2m away from the receiving antenna, the received power is improved by 30dB (from noise floor), and the maximum beam appears around 75° in the E-plane. This greatly improves the communication between transmitting and receiving terminals, and successfully establishes the desired 60GHz communication for indoor NLOS environment.

For future work, prospective studies could be taken in the following aspects:

1) Improving the passive repeater's bandwidth should be pursued. The groove array's 1dB-bandwidth ($BW_{1dB} = \frac{f_H - f_L}{f_{reference}}$) is close to 5%, which is not an ideal result. Actually, the groove array is a tradeoff between fabrication cost and bandwidth, when we consider the fabrication cost at 60GHz is priority. So to construct a simple enough structure with wide bandwidth would be quite promising breakthrough.

2) As introduced before, the optimizations at array level is quite necessary and important, based on our simulation strategy. However, the optimization procedure is relatively complicated, and the calculation burden is very heavy, especially when the array size gets larger. Therefore, simplifying the optimization procedure would be quite helpful and efficient. One idea, as referred in chapter 4, is to optimize a corresponding small linear array at first to reduce the parameter scanning range. More implementations for the simulations will be explored.

3) The different solutions proposed for the design of the reflector could be used for other applications. For instance, the structure made of grooves could be tested for the design of cylindrical (or even planar) reflectarrays at millimeter waves. The application to the reduction (or raise) of the RCS of scatterers could also be considered.

4) Finally, other technologies could be considered such as those offered by additive fabrication. For instance, it could be interesting to assess the possibility to design a reflector made of a dielectric layer with variable permittivity backed by a ground plane. The variation of permittivity could be achieved by drilling holes in the dielectric layer or by a more advanced structuring of the dielectric material using 3D printing.

Reference

[1] A. Raniwala, and T. C. Chiueh, "Architecture and algorithms for an IEEE 802.11-based multi-channel wireless mesh network", 24th Annual Joint Conference of the IEEE Computer and Communications Societies (INFOCOM 2005), vol.3, pp. 2223-2234, Mar. 2005.

[2] N. Guo, R. C. Qiu, S. S. Mo, and K. Takahashi, "60-GHz millimeter-wave radio: principle, technology, and new results", EURASIP Journal on Wireless Communications and Networking, 2007.

[3] M. Marcus, B. Pattan, "Millimeter wave propagation: spectrum management implications", IEEE Microwave Magazine, vol. 6, no. 2, pp. 54-62, Jun., 2005.

[4] http://www.wirelesshd.org

[5] "Introducing the UltraGig 6400, the ultimate wireless video solution for smartphones and tables", [Online] Available: http://www.siliconimage.com/ultragig/

[6] "Wi-Fi Alliance and Wireless Gigabit Alliance finalize unification", [Online] Available: http://www.wi-fi.org/news-events/newsroom/wi-fi-alliance-and-wireless-gigabit-alliance-finalize-unification.

[7] "Snapdragon 810 Processors", [Online] Available: https://www.qualcomm.com/products/snapdragon/processors/810

[8] A. Valentino, and P. P. Toulios, "Fields in the focal region of offset parabolic antennas", IEEE Transactions on Antennas and Propagation, vol. 24, no. 6, pp. 859-865, 1976.

[9] A. W. Rudge, and N.A. Adatia, "Offset-parabolic-reflector antennas: A review", Proceedings of the IEEE, vol. 66, no. 12, pp. 1592-1618, Dec., 1978.

[10] J. D. Kraus, "The square corner reflector", Radio, pp. 19-24, Mar., 1939.

[11] J. D. Kraus, and R. J. Marhefka, *Antennas for all applications*, *Third Edition*. McGraw-Hill, 2002.

[12] M. T. Jusoh, O. Lafond, F. Colombel, and M. Himdi, "Performance and radiation patterns of a reconfigurable plasma corner-reflector antenna", IEEE Antennas and Wireless Propagation Letters, vol. 12, pp. 1137-1140, 2013.

[13] R. Yang, "Passive repeater using double flat reflectors", IRE International Convention Record, vol. 5, pp. 36-41, Mar., 1966.

[14] R. A. Isberg, and R. L. Chufo, "Passive reflectors as a means for extending UHF signal down intersecting cross in mines or large corridors", IEEE Vehicular Technology Conference, vol. 28, pp. 267-272, Mar., 1978.

[15] H. M. Elkamchouchi, and M. N. A. El-Salam, "Linear dipole with parallelepiped metallic reflector", IEEE Antenna and Propagation Society International Symposium, vol. 3, pp. 1298-1301, 2000.

[16] A. Ali, A. Coustou, and H. Aubert, "Wide band passive repeaters: design and measurements", IEEE Antennas and Propagation Society International Symposium (APSURSI2009), pp. 1-4, 2009.

[17] QUALCOM Engineering Group, "Repeaters for indoor coverage in CDMA networks", QUALCOM White Paper, 2003.

[18] R. Lytle, and S. Strom, "A new carrier current protocol utilizing an active repeater for consumer and industrial applications", IEEE Transactions on Consumer Electronics, vol. CE-31, no. 4, pp. 700-705, 1985.

[19] http://www.transition.com

[20] H. D. Hristov, W. Grote, and R. Feick, “Antenna passive repeaters for indoor recovery of microwave cellular signals”, Microwave Journal, vol. 51, no. 9, pp. 160-179, 2008.

[21] L. Wang, S. W. Qu, J. F. Li, Q. Chen, Q. W. Yuan, and S. K, “Experimental investigation of MIMO performance using passive repeater in multipath environment”, IEEE Antennas and Wireless Propagation Letters, vol. 10, pp. 752-755, 2011.

[22] L. Li, Q. Chen, Q. W. Yuan, T. Maruyama, T. Furuno, and S. Uebayashi, “Novel broadband planar reflectarray with parasitic dipoles for wireless communication applications”, IEEE Antennas and Wireless Propagation Letters, vol. 8, pp. 881-885, 2009.

[23] H. D. Hristov, R. Feick, and W. Grote, “Improving indoor signal coverage by use of through-wall passive repeaters”, IEEE Antenna and Propagation Society International Symposium, vol. 2, pp. 158-161, 2014.

[24] N. Honma, Y. Takahashi, and Y. Tsunekawa, “Maximizing SNR using tunable passive repeater: Deterministic control method”, IEEE Antenna and Propagation Society International Symposium, vol. 2, pp. 158-161, 2011.

[25] D. G. Berry, R. G. Malech and W. A. Kennedy, “The reflectarray antenna”, IEEE Transactions on Antenna and Propagation, vol. AP-11, pp. 645-651, Nov. 1963.

[26] D. M. Pozar, S. D. Targonski, and H. D. Syrigos, “Design of millimeter wave microstrip reflectarrays”, IEEE Transactions on Antenna and Propagation, vol. 45, no. 2, pp. 287-296, 1997.

[27] X. Chen, Y. J. Zhang, Z. Z. Chen, and C. Yang, “Development of a ka-band wideband circularly polarized 64-element microstrip antenna array with double application of the sequential rotation feeding technique”, IEEE Antennas and Wireless Propagation Letters, vol. 10, pp. 1270-1273, Nov., 2011.

[28] R. C. Hansen, *Phased array antennas*. Wiley, 1998.

[29] D. Parker, and D. C. Zimmermann, “Phased arrays - part 1: theory and architectures”, IEEE Transactions on Microwave Theory and Techniques, vol. 50, no. 3, pp. 678-687, 2002.

[30] C. S. Malagisi, “Microstrip disc element reflect array”, Electronics and Aerospace Systems Convention, pp.186-192, Sept., 1978.

[31] J. P. Montgomery, “A microstrip reflectarray antenna element”, Proceedings of the Antenna Applications Symposium, Sept. 1978.

[32] A. G. Roederer, “Reflectarray antennas”, 3rd European Conference on Antennas and Propagation (EuCAP2009), pp.18-22, Mar. 2009.

[33] R. D. Javor, X. D. Wu, and K. Chang, “Design and performance of a microstrip reflectarray antenna”, IEEE Transactions on Antenna and Propagation, vol. 43, no. 9, pp. 932-939, Sept., 1995.

[34] T. A. Metzler, “Stub loaded microstrip reflectarrays”, Antennas and Propagation Society International Symposium, AP-S. Digest, vol. 1, pp. 574-577, 1995.

[35] M. E. Bialkowski, and H. J. Song, “Investigations into a power-combining structure using a reflectarray of dual-feed aperture-coupled microstrip patch antennas”, IEEE Transactions on Antennas and Propagation, vol. 55, no. 3, pp. 841-849, Jun., 2002.

[36] E. Carrasco, B. Alfageme, and J. A. Encinar, “Design of a multilayer aperture-coupled cell used as phase shifter in reflectarrays”, 13th Journées Internationales de Nice sur les Antennes (JINA), pp.194-195, Nov., 2004.

[37] E. Carrasco, M. Barba, and J. A. Encinar, “Reflectarray element based on aperture-coupled patches with slots and lines of variable length”, IEEE Transactions on Antennas and Propagation,

vol. 55, no. 3, pp. 820-825, Mar., 2007.

[38] D. M. Pozar, and T. A. Metzler, "Analysis of a reflectarray antenna using microstrip patches of variable size", Electronics Letters, vol. 29, no. 8, pp. 657-658, 1993.

[39] S. D. Tagonski, and D. M. Pozar, "Analysis and design of a microstrip reflectarray using patches of variable size", Antennas and Propagation Society International Symposium, AP-S. Digest, vol. 3, pp. 1820-1823, 1994.

[40] J. Huang, and R. J. Pogorzelski, "Microstrip reflectarray with elements having variable rotation angles", IEEE Antennas and Propagation Society International Symposium, Digest, vol. 2, pp. 1280-1283, 1997.

[41] J. Huang, and R. J. Pogorzelski, "A Ka-band microstrip reflectarray with elements having variable rotation angles", IEEE Transaction on Antenna and Propagation, vol. 46, no. 5, pp. 650-656, 1998.

[42] M. R. Chaharmir, J. Shaker, M. Cuhaci, and A. Sebak, "Reflectarray with variable slots on ground plane", IEE Proceedings on Microwaves, Antennas and Propagation, vol. 150, no. 6, pp. 436-439, 2003.

[43] M. R. Chaharmir, J. Shaker, M. Cuhaci, and A. Sebak, "Circularly polarised reflectarray with cross-slot of varying arms on ground plane", Electronics Letters, vol. 38, no. 24, pp. 1492-1493, 2002.

[44] M. R. Chaharmir, J. Shaker, M. Cuhaci, and A. Sebak, "Reflectarray with slots of varying length on ground plane", IEEE Antennas and Propagation Society International Symposium, vol. 3, 2002.

[45] D. C. Chang, and M. C. Huang, "Microstrip reflectarray antenna with offset feed", Electronics Letters, vol. 28, no. 16, pp. 189-1491, 1992.

[46] R. D. Javor, X. D. Wu, and K. Chang, "Offset-fed microstrip reflectarray antenna", Electronics Letters, vol. 30, no. 17, pp. 1363-1365, 1994.

[47] J. A. Encinar, "Design of two-layer printed reflectarrays using patches of variable size", IEEE Transactions on Antennas and Propagation, vol. 49, no. 10, pp. 1403-1410, Oct., 2001.

[48] J. A. Encinar, and J. A. Zornoza, "Broadband design of three-layer printed reflectarrays", IEEE Transactions on Antennas and Propagation, vol. 49, no. 10, pp. 1403-1410, Jul., 2003.

[49] J. A. Encinar and J. A. Zornoza, "Three-layer printed reflectarrays for contoured beam space applications", IEEE Transactions on Antennas and Propagation, vol. 52, no. 5, pp. 1138-1148, May, 2003.

[50] F. C. E. Tsai, and M. E. Bialkowski, "Designing a 161-element Ku-band microstrip reflectarray of variable size patches using an equivalent unit cell waveguide approach", IEEE Transactions on Antennas and Propagation, vol. 51, no. 10, pp. 2953-2962, Oct., 2003.

[51] M. R. Chaharmir, J. Shaker, M. Cuhaci, and A. Ittipiboon, "A broadband reflectarray antenna with double square rings as the cell elements", 1st European Conference on Antennas and Propagation (EuCAP2006), pp.1-4, Nov. 2006.

[52] M. E. Bialkowski, and K. H. Sayidmarie, "Investigations into phase characteristics of a single-layer reflectarray employing patch or ring elements of variable size", IEEE Transactions on Antennas and Propagation, vol. 56, no. 11, pp. 3366-3372, Nov., 2008.

[53] D. M. Pozar, and S. D. Targonski, "A microstrip reflectarray using crossed dipoles", IEEE Antennas and Propagation Society International Symposium, vol. 2, pp. 1008-1011, Jun. 1998.

[54] J. Huang, and K. Chang, "Ka-band reflectarray using ring elements", Electronics Letters, vol. 39, no. 6, pp. 491-493, 2003.

[55] C. Han, C. Rodenbeck, J. Huang, and K. Chang, "A C/Ka dual frequency dual layer circularly polarized reflectarray antenna with microstrip ring elements", IEEE Transaction on Antenna and Propagation, vol. 52, no. 11, pp. 2871-2876, 2004.

[56] B. Strassner, C. Han, and K. Chang, "Circularly polarized reflectarray with microstrip ring elements having variable rotation angles", IEEE Transaction on Antenna and Propagation, vol. 52, no. 4, pp. 1122-1125, 2004.

[57] C. Han, J. Huang, and K. Chang, "A high efficiency offset-fed X/Ka-dual-band reflectarray using thin membranes", IEEE Transaction on Antenna and Propagation, vol. 53, no. 2, pp. 2792-2798, 2005.

[58] C. Han, C. Rodenbeck, J. Huang, and K. Chang, "A C/ka dual frequency dual Layer circularly polarized reflectarray antenna with microstrip ring elements", IEEE Transaction on Antenna and Propagation, vol. 52, no. 11, pp. 2871-2876, 2004.

[59] D. Cadoret, A. Laisne, R. Gillard, and L. Le Coq, "Design and measurement of new reflectarray antenna using microstrip patches loaded with slot", Electronics Letters, vol. 41, no. 11, pp. 623-624, 2005.

[60] L. Moustafa, R. Gillard, F. Peris, and R. Loison, "The Phoenix Cell: A New reflectarray cell with large bandwidth and rebirth capabilities", IEEE Antennas and Wireless Propagation Letters, vol. 10, pp. 71-74, 2011.

[61] S. Adel, and H. Hammad, "Modified phoenix cell for microstrip reflectarray antennas", Middle East Conference on Antennas and Propagation (MECAP2012), pp. 1-3, 2012.

[62] K. Sarabandi, and N. Behdad, "A frequency selective surface with miniaturized elements", IEEE Transactions on Antennas and Propagation, vol. 55, no. 5, pp. 1239-1245, 2007.

[63] A. Edalati, and K. Sarabandi, "Wideband, wide angle, polarization independent RCS reduction using nonabsorptive miniaturized-element frequency selective surfaces", IEEE Transactions on Antennas and Propagation, vol. 62, no. 2, pp. 747-754, Nov., 2013.

[64] A. Edalati, and K. Sarabandi, "Reflectarray antenna based on grounded loop-wire miniaturised-element frequency selective surfaces", IET Microwaves, Antennas & Propagation, vol. 8, no. 12, pp. 973-979, 2014.

[65] A. Edalati, and K. Sarabandi, "Wideband reflectarray antenna based on miniaturized element frequency selective surfaces", 6th European Conference on Antennas and Propagation (EUCAP2012), pp. 362-364, 2012.

[66] M. Jiang, W. Hong, Y. Zhang, S. H. Yu, and H. Zhao, "A folded reflectarray antenna with a planar SIW slot array antenna as the primary source", IEEE Transactions on Antennas and Propagation, vol. 62, no. 7, pp. 3575-3583, 2014.

[67] W. Menzel, D. Pilz, and M. Al-Tikriti, "Millimeter-wave folded reflector antennas with high gain, low loss, and low profile", IEEE Antennas and Propagation Magazine, vol. 44, no. 3, pp. 24-29, Jun., 2002.

[68] J. A. Zornoza, R. Leberer, J. A. Encinar, and W. Menzel, "Folded multilayer microstrip reflectarray with shaped pattern", IEEE Transactions on Antennas and Propagation, vol. 54, no.2, pp. 510-518, Jun., 2006.

[69] A. Zeitler, J. Lanteri, C. Pichot, C. Migliaccio, P. Feil, and W. Menzel, "Folded reflectarrays with shaped beam pattern for foreign object debris detection on runways," IEEE Transactions on Antennas and Propagation, vol. 58, no.9, pp. 3065-3068, Sept., 2010.

[70] B. D. Nguyen, J. Lanteri, J. Y. Dauvignac, and C. Pichot, "94 GHz folded Fresnel reflector using

C-patch elements", IEEE Transactions on Antennas and Propagation, vol. 56, no. 11, pp. 3373-3374, Nov., 2008.

[71] J. Lanteri, C. Migliaccio, J. Y. Dauvignac, and C. Pichot, "Reflectarray using an offset prolate feed at 94 GHz", IEEE Antennas and Propagation Society International Symposium, pp. 1-4, 2008.

[72] R. Soummera, C. Aimea, and P. E. Falloona, "Prolate apodized coronography: numerical simulations for circular apertures", EAS Publications Series vol. 8, pp. 93-105, 2003.

[73] J. Lanteri, C. Migliaccio, J. Y. Dauvignac, and C. Pichot, "Improvement of reflectarrays and lenses radiation pattern by prolate spheroidal functions in W band", 1st European Conference on Antennas and Propagation (EuCAP2009), pp. 826-830, Mar., 2009.

[74] J. Lanteri, A. Zeitler, J. Y. Dauvignac, C. Pichot, C. Migliaccio, P. Feil, and W. Menzel, "Investigation of wideband millimetre-wave reflectarrays for radar applications operating in the W Band", 3rd European Conference on Antennas and Propagation (EuCAP2006), Nov., 2006.

[75] P. Nayeri, M. Liang, R. A. S. Garcia, M. G. Tuo, F. Yang, M. Gehm, H. Xin, and A. Z. Elsherbeni, "3D Printed Dielectric Reflectarrays: Low-Cost High-Gain Antennas at Sub-Millimeter Waves", IEEE Transactions on Antennas and Propagation, vol. 62, no. 4, pp. 2000-2008, Jan., 2014.

[76] A. Sabban, "A Comprehensive study of losses in mm-wave microstrip antenna arrays", 27th European Microwave Conference, vol. 1, pp. 163-167, 1997.

[77] J. C. Rautio, "An investigation of microstrip conductor loss", vol. 1, no. 4, pp. 60-67, IEEE Microwave Magazine, 2000.

[78] J. R. James, S. P. Hall, and C. Wood, "The skin-effect at high frequencies", IEEE Transactions on Microwave Theory and Techniques, vol. 33, no. 10, pp. 1076-1082, 2003.

[79] D. Sievenpiper, L. J. Zhang, R. F. J. Broas, N. G. Alexopolous, and E. Yablonovitch, "High-impedance electromagnetic surfaces with a forbidden frequency band", IEEE Transactions on Microwave Theory and Techniques, vol. 47, no. 11, pp. 2059-2074, 1999.

[80] A. P. Feresidis, G. Goussetis, A. Yakovlev, and C. Simovski, "High impedance surfaces: Applications", in *Metamaterial Handbook*. London, U. K.: Taylor and Francis, vol. II, ch.22.

[81] L. Akhoondzadeh-Asl, D. J. Kern, P. S. Hall, and D. H. Werner, "Wideband dipoles on electromagnetic bandgap ground planes", IEEE Transactions on Antennas and Propagation, vol. 55, no. 9, pp. 2426 - 2434, Sept. 2007.

[82] D. C. Li, F. Boone, M. Bozzi, L. Perregrini, and K. Wu, "Concept of virtual electric/magnetic walls and its realization with artificial magnetic conductor technique", IEEE Microwave and Wireless Components Letters, vol. 18, no. 11, pp. 743-745, 2008.

[83] D. F. Sievenpiper, J. H. Schaffner, H. J. Song, and R. Y. Loo, "Two-dimensional beam steering using an electrically tunable impedance surface", IEEE Transactions on Antennas and Propagation, vol. 51, no. 10, pp. 2713-2722, Oct. 2003.

[84] F. Costa and A. Monorchio, "Closed-Form analysis of reflection losses in microstrip reflectarray antennas", IEEE Transactions on Antennas and Propagation, vol. 60, no. 10, pp. 4650-4660, Oct. 2012.

[85] D. M. Pozar, "Wideband reflectarrays using artificial impedance surfaces", Electronics Letters, vol. 43, no. 3, Feb. 2007.

[86] A. Barakat, A. Allam, R. K. Pokharel, H. Elsadek, M. El-Sayed, and K. Yoshida, "60 GHz triangular monopole Antenna-on-Chip over an Artificial Magnetic Conductor", 6th European Conference on Antennas and Propagation (EuCAP2012), pp. 972-976, Mar., 2012.

[87] G. Mikhail, Y. Quere, C. Quendo, and C. Person, "A novel THz-enhanced dipole antenna using second-order high impedance surface resonance for MM imaging and sensing", IEEE Topical Meeting on Silicon Monolithic Integrated Circuits in Rf Systems (14th SiRF), pp. 19-23, 2014.

[88] M. R. Chaharmir, J. Shaker, and H. Legay, "Dual-band Ka/X reflectarray with broadband loop elements", IET Microwaves, Antennas & Propagation, vol. 4, no. 2, pp. 225-231, 2010.

[89] L. Li, Q. Chen, Q. W. Yuan, K. Sawaya, T. Maruyama, T. Furuno, and S. Uebayashi, "Frequency selective reflectarray using crossed-dipole elements with square loops for wireless communication applications", IEEE Transactions on Antennas and Propagation, vol. 59, no. 1, pp. 89-99, Nov., 2000.

[90] R. D. Richtmeyer, "Dielectric resonator", Journal of Applied Physics, vol. 10, no. 6, pp. 391-398, 1939.

[91] M. Gastine, L. Courtois, and J. L. Dormann, "Electromagnetic resonances of free dielectric spheres", IEEE Transactions on Microwave Theory and Techniques, vol. 15, no.. 12, pp. 694-700, 1963.

[92] D. Kajfez, and P. Guillon, *Dielectric Resonators*. Norwood, MA: Artech House, 1986.

[93] S. A. Long, M. McAllister, and S. Liang, "The resonant cylindrical dielectric cavity antenna", IEEE Transactions on Antennas and Propagation, vol. 31, no. 3, pp. 406-412, May, 1983.

[94] M. W. McAllister, and S. A. Long, "Resonant hemispherical dielectric antenna", Electronics Letters, vol. 20, no. 16, pp. 657-659, Aug., 1984.

[95] K. M. Luk, K. W. Leung, and J. R. James, (editors), *Dielectric Resonator Antennas (Antennas Series)*. Research Studies Press, 2002.

[96] A. Petosa, and A. Ittipiboon, "Dielectric Resonator Antennas: A historical review and the current state of the art", IEEE Antennas and Propagation Magazine, vol.52, no.5, pp.91-116, Oct., 2010.

[97] K. W. Leung, E. H. Lim, and X. S. Fang, "Dielectric resonator antennas: from the basic to the aesthetic", Proceedings of the IEEE, vol. 100, no. 7, pp. 2181-2193, Jul., 2012.

[98] M. W. McAllister, S. A. Long, and G. L. Conway, "Rectangular dielectric resonator antenna", Electronics Letters, vol. 19, no. 6, pp. 218-219, Mar., 1983.

[99] W. M. Abdel Wahab, D. Busuioc, and S. Safavi-Naeini, "Low cost planar waveguide technology-based dielectric resonator antenna (DRA) for millimeter-wave applications: analysis, design, and fabrication," IEEE Transaction on Antennas and Propagation, vol. 58, no. 8, August, 2010.

[100] R. K. Mongia, and A. Ittipiboon, "Theoretical and experimental investigations on rectangular dielectric resonator antennas," IEEE Transactions on Antennas Propagation, vol. 45, no. 9, pp. 1348-1356, Sept., 1997.

[101] R. K. Mongia, and P. Bhartia, "Dielectric resonator antennas - a review and general design relations for resonant frequency and bandwidth," International Journal of Microwave and Millimeter-Wave Computer-Aided Engineering, vol. 4, issue 3, pp. 230-247, July 1994.

[102] X. S. Fang, and K. W. Leung, "Designs of Single-, Dual-, Wide-Band Rectangular Dielectric Resonator Antennas," IEEE Transaction on Antennas and Propagation, vol.59, no. 6, pp. 2409-2414, Jun. 2011.

[103] R. C. Hansen. *Microwave Scanning antennas (Array theory & practice)*. Peninsula Pub, 1966, 2:322.

[104] S. Ebadi, R.V. Gatti, and R. Sorrentino, “Linear reflectarray antenna design using 1-bit digital phase shifters,” European Conference on Antennas and Propagation (EuCAP2009), Berlin, Germany, March 2009.

[105] S. Montori, L. Marcaccioli, R.V. Gatti, “Constant-phase dual polarization MEMS-based elementary cell for electronic steerable reflectarrays,” Microwave Conference (EuMC2009), pp. 33-36, 2009.

[106] M. G. Keller, J. Shaker, A. Petosa, and A. Ittipiboon, “A Ka-band dielectric resonator antenna reflectarray”, 30th European Microwave Conference, pp. 1-4, 2000.

[107] M. H. Jamaluddin, R. Gillard, R. Sauleau, L. Le Coq, X. Castel, R. Benzerga, and T. Koleck, “A dielectric resonator antenna (DRA) reflectarray”, European Microwave Conference (EuMC2009), pp. 25-28, 2009.

[108] M. H. Jamaluddin, R. Gillard, R. Sauleau, P. Dumon, and L. Le Coq, “Reflectarray element based on strip-loaded dielectric resonator antenna”, Electronics Letters, vol. 44, no. 11, pp. 664-665, 2008.

[109] M. H. Jamaluddin, *Réseau réflecteur à base de résonateurs diélectriques - Conception et caractérisation en bande Ka.* Thèse de doctorat, Institut National des Sciences Appliquées, 2009.

[110] D. M. Pozar, “Microstrip antenna aperture coupled to a microstrip line”, Electronics Letters, vol. 21, Jan. 1985.

[111] R. N. Simons, and R. Q. Lee, “Effect of Parasitic Dielectric Resonators on CPW/Aperture-Coupled Dielectric Resonator Antennas”, IEE Proceedings Part-H, vol. 140, pp. 336-338, Oct. 1993.

[112] J. T. H. St. Martin, Y. M. M. Antar, A. A. Kishk, A. Ittipiboon, and M. Cuhaci, “Dielectric resonator antenna using aperture coupling”, Electronics Letters, vol. 26, no. 24, Nov. 1990.

[113] D. M. Pozar, “Review of Aperture Coupled Microstrip Antenna: History, Operation, Development, and Application”, Microwave Online System Company world wide web site, July, 1996.

[114] A. Ittipiboon, R. K. Mongia, Y. M. M. Antar, P. Bhartia, M. Cuhaci, “Aperture fed rectangular and triangular dielectric resonators for use as magnetic dipole antennas”, IEE Electronics Letters, Vol. 29, No. 23, Nov. 1993, pp. 2001-2002.

[115] R. K. Mongia, A. Ittipiboon, Y. M. M. Antar, P. Bhartia, M. Cuhaci, “A half-split cylindrical dielectric resonator antenna using slot coupling”, Microwave and Guided Wave Letters, Vol. 3, No. 2, Feb. 1993, pp. 38-39.

[116] G. P. Junker, A. A. Kishk, and A. W. Glisson, “Input impedance of aperture-coupled dielectric resonator antennas”, IEEE Transactions on Antennas and Propagation, vol. 44, no. 5, 1996.

[117] K. P. Esselle, “A low-profile rectangular dielectric-resonator antenna”, IEEE Transactions on Antennas and Propagation, vol. 44, no. 9, pp. 1296-1297, Sep. 1996.

[118] K. W. Leung, K. M. Luk, K. Y. A. Lai, L. Deyun, “Theory and experiment of an aperture-coupled hemispherical dielectric resonator antenna”, IEEE Transactions on Antennas &

Propagation, vol. 43, no. 1, pp. 1192-1198, Nov. 1995.

[119] S. H. Zainud-Deen, A. M. Abd-Elhady, A. A. Mitkees, and A. A. Kishk, "Slot-loading rectangular dielectric resonator elements reflectarray", IEEE Middle East Conference on Antennas and Propagation (MECAP2010), pp. 1-3, Oct., 2010.

[120] S. H. Zainud-Deen, A. M. Abd-Elhady, A. A. Mitkees, and A. A. Kishk, "Dielectric Resonator Reflectarray with Two DRA Sizes and Varying Slot Loading", IEEE Antennas and Propagation Society International Symposium (APSURSI2010), pp. 1-4, 2010.

[121] A. M. Abd-Elhady, A. A. Mitkees, and A. A. Kishk, "X-band linear polarized aperture-coupled DRA reflectarray", International Conference on Microwave and Millimeter Wave Technology (ICMMT2010), pp. 1042-1044, May, 2010.

[122] Y. H. Cho, W. J. Byun, and M. S. Song , "High gain metal-only reflectarray antenna composed of multiple rectangular grooves", IEEE Transactions on Antennas and Propagation, vol. 59, no. 12, pp. 4559-4568, Nov. 2010.

[123] T. Baykas, S. C. Sean, L. Zhou, Y. Wang, M.A. Rahman, H. Harada, and S. Kato, "IEEE 802.15.3c: the first IEEE wireless standard for data rates over 1Gb/s", IEEE Communications Magazine, vol. 49, no. 7, pp. 114-121, Jul., 2011.

[124] P. Minyoung, C. Cordeiro, E. Perahia, and L. L. Yang, "Millimeter-wave multi-Gigabit WLAN: Challenges and feasibility", IEEE International Symposium on Personal, Indoor and Mobile Radio Communications (PIMRC), pp. 1-5, Sept., 2008.

[125] H. Xu, V. Kukshya, T. S. Rappaport, "Spatial and temporal characteristics of 60-GHz indoor channels", IEEE Journal on Selected Areas in Communications, vol.20, pp.620-630, Apr., 2002.

[126] N. Moraitis and P. Constantinou, "Indoor channel measurements and characterization at 60 GHz for wireless local area network applications", IEEE Transactions on Antennas and Propagation, vol. 52, pp. 3180-3189, Dec., 2004.

[127] S. Marano, W. M. Gifford, H. Wymeersch, and M. Z. Win, "NLOS identification and mitigation for localization based on UWB experimental data", IEEE Journal on Selected Areas in Communications, vol. 28, pp. 1026-1035, Aug., 2010.

[128] L. Wang, S. W. Qu, J. F. Li, and Q. Chen "Experimental Investigation of MIMO Performance Using Passive Repeater in Multipath Environment", IEEE Antennas and Wireless Propagation Letters, vol. 10, pp. 752-755, Aug., 2011.

[129] J. Huang, J. Encinar, *Reflectarray Antennas*. Wiley, 2007.

[130] S. Mener, *Conception d'une cellule déphaseuse pour réseau réflecteur reconfigurable à deux polarisations circulaires indépendantes*. Thèse de doctorat, Institut National des Sciences Appliquées, 2013.

[131] T. Makdissy, *Nouvelles topologies de cellules déphaseuses à coût et complexité réduits pour les antennes réseaux réflecteurs large bande*. Thèse de doctorat, Institut National des Sciences Appliquées, 2013.

[132] T. Makdissy, R. Gillard, E. Fourn, E. Girard, and H. Legay, "A patch-slot combination approach for large band reflectarrays", 42nd European Microwave Conference (EuMC2012), pp.759-762, Oct., 2012.

[133] Y. H. Cho, S. K. Lim, S. W. Lee, M. W. Yi, W. S. Lee, and J. H. So, "A Metal-Only Reflectarray (MOR) Antenna Excited by Equivalent Surface Current Sources to Model Arbitrary Feeds", European Conference on Antennas and Propagation (EuCAP2014), pp. 1921-1923, Apr., 2014.

[134] J. Thomson, *Notes on Recent Researches in Electricity and Magnetism*. Oxford: Clarendon, 1893, (reprinted London: Dawsons, 1968), pp. 344-347.

[135] Lord Rayleigh, "On the passage of electric waves through tubes, or the vibrations of dielectric cylinders", Phil. Mag., vol. XLIII, pp. 125-132, 1897.

[136] N. W. McLachlan, *Theory and Applications of Mathieu Functions*, pp. 8, 1947 (reprinted by Dover: New York, 1964).

[137] A.Sommerfeld, "Fortpflanzung elektrodynarnischer Wellen an einenzylindrischen Leiter", Ann. d. Phys., vol. 67, pp. 223, ser. 3, 1899.

[138] A. Sommerfeld, "Über die Fortpflanzung elektrodynamisches wellen langes eines drahtes", Ann. der Phys. Chem. 67, 233, 1899.

[139] E. Karplus, "Communication with quasi optical waves", Proceedings of IEEE, vol. 19, pp. 1715, 1931.

[140] J. R. Carson, S. P. Mead, and S. A. Schelkunoff, "Hyperfrequency waveguides-mathematical theory", Bell Syst. Tech. J. 15, 310, 1936.

[141] G. C. Southworth, "Hyperfrequency waveguides-general considerations and experimental results", Bell Syst. Tech. J. 15, 284, 1936.

[142] C. H. Chandler, "An investigation of dielectric rod as waveguides", Journal of Applied Physics, 20, 1188, 1949.

[143] S. Sensiper, "Electromagnetic wave propagation on helical conductors", Research Laboratory for Electronics, Mass. Inst. of Tech., Rept No. 194, May 16(1951); Proc. IRE 43. 149, 1955.

[144] R. E. Collin, *Field Theory of Guided Waves*. McGraw-Hill, 1960.

[145] K. S. Packard, "The Origin of Waveguides: A Case of Multiple Rediscovery", IEEE Transaction on Microwave Theory and Techniques, vol. 32, pp. 961-969, Sept. 1984.

[146] D. M. Pozar, *Microwave Engineering, Forth edition*. Willey, pp. 961-969, Nov. 2011.

[147] J. Huang, "Bandwidth study of microstrip reflectarray and a novel phased reflectarray concept," IEEE Transaction on Antennas Propagation, vol. 45, pp. 287-295, Feb. 1997.

[148] D. M. Pozar, and S. D. Targonski, "A shaped-beam microstrip patch reflectarray," IEEE Transaction on Antennas Propagation, vol. 47, no. 7, pp.1167-1173, Jul. 1999.

[149] S. V. Hum, and M. Okoniewski, "A technique for predicting specular reflections from reflectarrays", Proc. IEEE Antennas and Propagation Soc. Symp. , pp. 2116-2119, Jun. 2007.

[150] M. R. Chaharmir, J. Shaker, N. Gagnon, and D. Lee, "Design of broadband, single layer dual-band large reflectarray using multi open loop elements," IEEE Transaction on Antennas Propagation, vol. 58, no. 9, pp. 2875-2883, 2010.

[151] W. J. Byun, Y. H. Cho, M. S. Kang, K. S. Kim, B. S. Kim, and B. S. Song, "Millimeter-wave metallic-rectangular-grooves based reflectarray antenna and its applications to E-band multi-Gbps system," Asia-Pacific Microwave Conference Proceedings (APMC), vol. 59, no. 12, pp. 4559-4568, 2013.

[152] Y. H. Cho , W. J. Byun, and M. S. Song, "Metallic-rectangular-grooves based 2D reflectarray antenna excited by an open-ended parallel-plate waveguide," IEEE Transaction on Antennas

Propagation, vol. 58, no. 5, pp. 1788-1972, 2010.

[153] K. Barkeshli, and J. L. Volakis, "Electromagnetic scattering from an aperture formed by a rectangular cavity recessed in a ground plane," Journal of Electromagnetic Waves and Applications, vol. 5, no. 7, pp. 715-734, 1991.

[154] H. H. Park, and H. J. Eom, "Electromagnetic scattering from multiple rectangular apertures in a thick conducting screen," IEEE Transaction on Antennas Propagation, vol. 47, no. 6, pp. 1056-1060, 1999.

[155] S. Y. Geng, and P. Vainikainen, "Millimeter-wave propagation in indoor corridors," IEEE Antennas and Wireless Propagation Letters, vol. 8, pp. 1242-1245, 2009.

[156] H. A. Muqaibel, A. Safaai-Jazi, A. M. Attiya, and A. Bayram, "Measurement and characterization of indoor ultra-wideband propagation," IEEE conference on Ultra Wideband Systems and Technologies, pages: 295-299, 2003.

[157] L. Talbi, and J. Lebel, "Extending 60GHz UWB coverage to medium distances under NLOS conditions," International Conference on Wireless Communications in Unusual and Confined Areas (ICWCUCA), pp. 1-6, 2012.

[158] R. A. Isberg, and R. L. Chufo, "Passive reflectors as a means for extending UHF signals down intersecting cross cuts in mines or large corridors", 28th IEEE Vehicular Technology Conference, vol. 28, pp. 267-272, 1978.

[159] S. Collonge, *Caractérisation et modélisation de la propagation des ondes électromagnétiques à 60 GHz à l'intérieur des bâtiments*. Thèse de doctorat, Institut National des Sciences Appliquées, 2003.

[160] S. Collonge, G. Zaharia, and G. E. Zein, "Wideband and dynamic characterization of the 60 GHz indoor radio propagation-future home WLAN architectures", Annales Des Télécommunications, vol. 58, pp. 417-447, 2003.

[161] S. Guillouard, G. E. Zein, and J. Citerne, "High time domain resolution indoor channel sounder for the 60 GHz Band", Proceedings of the 28th European Microwave Conference, vol. 2, pp. 341-344, Oct. 1998.

[162] http://www.rohde-schwarz.com/en/product/zvb-productstartpage_63493-7990.html

[163] H. T. Friis, "A Note on a Simple Transmission Formula", Proceedings of the IRE, vol. 34, no. 5, pp. 254-256, 1946.

[164] B. Sklar, *Digital Communications: Fundamentals and Applications*, *Second Edition.* Prentice Hall, 2011.

Acknowledgement

This thesis is accomplished under the guidance of my supervisor, prof. Raphaël Gillard. I would like to extend my sincerest thanks for his patient and inspiring help on my academic work, which I benefit quite a lot. I also want to attribute my gratitude to prof. Renaud Loison, who always offered me warm encouragement, and greatly helped me on the improvement and correction of my paper and thesis.

Moreover, I want to thank the reviewers of my thesis: prof. Xavier Begaud, prof. Claire Migliaccio, prof. Jean-Marc Laheurte, and prof. Ghaïs El Zein. It's my great honor to have you be the juries of my thesis defense, and your constructive comments and suggestions are very important to improve the thesis.

I would like to further thank Jérôme SOL and Dr. Laurent Le Coq, who helped me patiently for many measurements of the prototype with good results.

To my friends and colleagues, who have already left INSA de Rennes or who are right now fighting for their thesis, I want to acknowledge their help during my stay in INSA de Rennes. Dr. Cong Bai, Dr. Jinglin Zhang, Dr. Yi Liu, Dr. Tony Makdissy, Zhigang Yao, Jiali Xu and who I forgot to mention here, you made my days happier and easier, and I wish you all good luck in your fruitful careers and the best upcoming future.

I want to thank China Scholarship Council (CSC) for the financial support, which make me could concentrate on my Ph.D. studies. Thanks for providing me this opportunity to pursue my dreams.

Finally, I want to thank my family and my girlfriend. You have always supported me with strong confidences and comprehensive understandings. This is the most important faith for me to sustain all these years.

I have spent 23 years to come to my doctor degree, which I think would be the highest degree I can ever earn. I have learned so many in academic investigations, and also so many about the life. I hope this thesis and degree, being a new starting point of both my career and my life, would lead to my promising future.

Publication

[1] D. Wang, R. Gillard, and R. Loison, “A 60GHz Passive Repeater Array with Quasi-Endfire Radiation Based on Metal Groove Unit-Cells”, International Journal of Microwave and Wireless Technologies, submitted.

[2] D. Wang, R. Gillard, and R. Loison, “Un répéteur passif utilisant un réflecteur plan rainuré pour les communications indoor à 60 GHz”, 19èmes Journées Nationales Micro-ondes (JNM2015), Bordeaux, France, 2015.

[3] D. Wang, R. Gillard, and R. Loison, “A 60GHz passive repeater array with endfire radiation based on metal groove unit-cells”, 9th European Conference on Antennas and Propagation (EuCAP2015), Apr., 2015.

[4] D. Wang, R. Gillard, and R. Loison, “A notched dielectric resonator antenna unit-cell for 60GHz passive repeater with endfire radiation”, 8th European Conference on Antennas and Propagation (EuCAP2014), pp. 3167-3170, Apr., 2014.

[5] D. Wang, R. Gillard, and R. Loison, “A 60GHz passive repeater with endfire radiation using dielectric resonator antennas”, IEEE Radio and Wireless Symposium, pp. 31-33, Jan., 2014.

INSA de RENNES
Service des Formations

AVIS DU JURY SUR LA REPRODUCTION DE LA THESE SOUTENUE

Titre de la thèse:
Analyse et conception de répéteurs passifs plans à rayonnement quasi-latéral pour communications « indoor » à 60 GHz

Nom Prénom de l'auteur : WANG DUO

Membres du jury :
- Monsieur BEGAUD Xavier
- Monsieur GILLARD Raphaël
- Monsieur LOISON Renaud
- Madame MIGLIACCIO Claire
- Monsieur LAHEURTE Jean-Marc

Président du jury : Xavier Begaud

Date de la soutenance : 06 Mai 2015

Reproduction de la these soutenue

Thèse pouvant être reproduite en l'état
~~Thèse pouvant être reproduite après corrections suggérées~~

Fait à Rennes, le 06 Mai 2015

Signature du président de jury

Le Directeur,

M'hamed DRISSI

Résumé

Le développement rapide de l'industrie des systèmes sans fil suscite une demande urgente pour des communications à haut débit, notamment en environnement « indoor ». Toutefois, les protocoles traditionnels de communications sont incapables de supporter de très hauts débits et, surtout, il n'y a pas de ressources spectrales disponibles à basse fréquence. Comme une alternative, la bande des 60GHz est préconisée parce qu'elle permet un débit de plus de 5Gbit/s, grâce à son large spectre (57GHz à 64 GHz). Toutefois, en pratique, l'environnement « indoor » est complexe et, dans les situations d'absence de visibilité directe, la couverture radio est difficile à assurer à cause des fortes atténuations. Afin de remédier à ce problème, l'utilisation de répéteurs est possible. Dans cette thèse, l'intérêt est porté sur les répéteurs passifs, plus simples à installer et compatibles avec une réalisation faible coût. Le cas critique de la couverture radio d'un couloir en T est choisi comme fil conducteur, tout au long de cette étude. Les solutions préconisées visent aussi la compacité, ce qui justifie l'utilisation de réflecteurs plans.

A partir de la théorie des réseaux d'antennes, une structure périodique générique pour le répéteur est proposée. Elle implique deux cellules réfléchissantes élémentaires (espacées de $\lambda/2$), produisant des ondes en opposition de phase. Plusieurs topologies et technologies sont ensuite envisagées et étudiées pour la mise en œuvre.

La première utilise des antennes à résonateur diélectrique (DRA). Deux topologies différentes sont étudiées et comparées, le DRA à encoche et le DRA couplé à une ligne déphaseuse en circuit ouvert. Différentes stratégies de modélisation sont également étudiées en utilisant une cellule unique, un couple de 2 cellules avec phases opposées ou un petit réseau. Pour chaque topologie, un réseau canonique de 6×6 éléments est simulé.

La deuxième technologie étudiée utilise des guides d'ondes rectangulaires chargés par un matériau diélectrique et court-circuités. Des analyses paramétriques sont effectuées et un 6 ×6 réseau est conçu et optimisé pour valider la faisabilité de la solution.

Finalement, une structure en guide à plaques métalliques parallèles est analysée. Dérivant de la solution précédente, elle permet une fabrication plus simple. Pour cette dernière solution, une analyse plus complète est menée incluant des considérations sur la bande passante, les performances en incidence oblique et la direction de rayonnement maximal.

Enfin, un réseau à base de cet élément rainuré est fabriquée présentant une taille de 200 mm×200 mm. Des mesures expérimentales à 60GHz sont réalisées pour tester les performances du réseau. La preuve de concept est ainsi donnée et les résultats expérimentaux sont analysés.

Mots-clés: communications à 60 GHz, environnement « indoor », rayonnement latéral, répéteur passif, réflecteur passif, DRA, guide rectangulaire chargé, plaque rainurée.

Abstract

The fast development of information and consumer electronics industries creates a pressing demand for high-speed indoor communications. Traditional communication protocols are unable to support such high transmission rate, and there are no radio bands available at lower frequency. As an alternative, 60GHz communications have sparked great attention, since it enables a maximum data transmission rate more than 5Gbit/s based on its wide unlicensed bandwidth. However, practical indoor environment is usually complicated (e.g. walls, corridors, stairs, etc.), thus the non-line-of-sight (NLOS) areas cannot be covered due to the significant attenuation. Considering the requirements for signal recovery in the NLOS environment, a planar passive repeater with endfire radiation and high directivity, low profile and low cost is investigated and designed in this thesis.

Based on array theory, a periodic structure for the foreseen printed repeater is derived out. It involves two reflector elements (in the spacing of 2) to provide 0° and 180° reflection phases respectively. In order to construct a proper reflector element, four topologies are proposed and analyzed.

In the first part of the study, DRA (Dielectric Resonator Antenna) technology is the main focus. Two different topologies are investigated and compared, including notched DRA and DRA coupled to phase-shift stub. Different modeling strategies are also studied using either a single cell, a couple of cells with opposite phases or a small array. For each topology, a preliminary 6×6 array is simulated. Optimization at the array level is emphasized through the whole thesis.

In the second part, investigations are taken on a rectangular dielectric filled waveguide element. Parametric analyses are carried out and possible fabrication technologies are discussed. Once again, a preliminary 6×6 array is designed and optimized to validate the feasibility of such a structure.

In the third part, a parallel-plate groove structure is analyzed. It evolves from the rectangular waveguide, and enjoys more simplification. Further work is taken to explore the arrays' bandwidth, oblique incidence performance and maximum radiation direction. Detailed theoretical analysis based on the simulation results are demonstrated in the end.

Finally, an array based on the groove elements is fabricated in the size of 200mm×200mm. Practical measurements for 60GHz communications in NLOS environment are designed to test the array's performance. Analyses on the experiment results are given.

Key words: 60GHz communications, indoor NLOS environment, endfire radiation, passive repeater, planar reflector, DRA, dielectric filled waveguide, parallel-plate groove

N° d'ordre : **15ISAR 12 / D15 - 12**
Institut National des Sciences Appliquées de Rennes
20, Avenue des Buttes de Coëmes • CS 70839 • F-35708 Rennes Cedex
Tel : 02 23 23 82 00 - Fax : 02 23 23 83 96